

THE UNIVERSITY OF HULL

**ENHANCED OIL RECOVERY BY FLOODING WITH AQUEOUS  
SURFACTANT SOLUTION: A MODEL STUDY AND  
COMPARISON WITH THEORY**

being a Thesis submitted for the Degree of Doctor of Philosophy  
in the University of Hull

by

Luke Daniel Savory  
BSc (University of Hull)

March 2015

## ACKNOWLEDGEMENTS

I would like to express great thanks to Professor Paul D.I. Fletcher for his never ending help, guidance, support and encouragement in all of the work presented here, I certainly would not have been able to come this far without it. My thanks also go to the members of the Surfactant and Colloid Group (past and present), especially the ‘inhabitants’ of lab C107, namely Andrew Johnson and Ioannis Marinopoulos, for the useful discussions and passing off of ideas over a coffee.

I would also like to thank Schlumberger Cambridge Research Ltd. (Cambridge, U.K.) for their financial support and Dr. Andrew M. Howe for his input as my industrial supervisor and his invaluable help in proof reading this thesis. I would also like to thank his colleague Dr. Andrew Clarke who also attended the industrial meetings and provided further insightful discussions. My thanks also go to the University of Hull for their provision of a tuition fee waiver.

Specific thanks are due to a number of undergraduate students whose 4<sup>th</sup> year MChem research projects or 3<sup>rd</sup> year group research projects I co-supervised. Firstly, Freya Woods (4<sup>th</sup> Year MChem research project) for obtaining all of the experimental results for the AOT system in Chapter 4 containing 40 mM NaCl and 10 mM Na<sub>2</sub>CO<sub>3</sub>. Secondly, Fabian Stelzer (4<sup>th</sup> Year MChem research project) for obtaining the experimental results for the preliminary experiments for foam flooding in Chapter 6. Finally, Adam Young, Birsen Somuncuoghlu, Callum Holness, Charlotte Rowland and Isabella Wynn (3<sup>rd</sup> year group research project) for obtaining the experimental results for the visualising of the oil recovery in Chapter 6.

Last, but by no means least I would like to thank my incredible wife, Nicky, for her un-failing support and encouragement throughout this PhD and her tea making expertise whilst writing this thesis, and I would like to thank my daughter, Melody, who was not around for the start of this PhD, who often brightened up my day with her smiles when I most needed it.

TO NICKY AND OUR FAMILY

‘The works of the Lord are great, studied by all who have pleasure in them.’

Psalm 111v2

“By investigating God’s majestic and awesome creation, science can actually be a means of worship.”

Francis Collins – ex-director of the Human Genome Project

“Plurality must never be posited without necessity.”

William of Occam

## PUBLICATIONS AND PRESENTATIONS

The work contained in this thesis has contributed to the following publications and presentations.

1. Paper: Fletcher, P.D.I., Savory, L.D., Woods, F., Clarke, A., Howe, A.M., A model study of enhanced oil recovery by flooding with aqueous surfactant solution and comparison with theory, *Langmuir*, **2015**, *31*, 3076.
2. Award winning oral presentation: ‘Enhanced oil recovery: overcoming parasitic surfactant adsorption’, University of Hull Research Colloquium, 27<sup>th</sup> June 2014, Hull, UK.
3. Poster presentation: ‘Enhanced oil recovery: overcoming parasitic surfactant adsorption’, University of Hull Research Colloquium, June 2013, Hull, UK. (Authors: A.M. Howe, P.D.I. Fletcher, L.D. Savory).
4. Poster presentation: ‘Enhanced oil recovery: overcoming parasitic surfactant adsorption’, Science PhD Scholarship Showcase, 9<sup>th</sup> May 2012, Hull, UK. (Authors: A.M. Howe, P.D.I. Fletcher, L.D. Savory).

## ABSTRACT

The aim of the work within this thesis is to elucidate the details of enhanced oil recovery by surfactant solution flooding. This was achieved by determining the detailed surface chemistry and flow behaviour of model systems consisting of a packed column of calcium carbonate particles as the porous rock with interstices filled with a pure oil, and aqueous solutions of three different surfactants (an anionic, cationic and nonionic) as the displacing phase. Each three phase system is characterised in detail in terms of its surface chemistry properties, including; water-rock adsorption, water-oil interfacial tensions, water-oil-rock contact angles, aqueous phase behaviour, microemulsion phase behaviour and water-oil partitioning.

Two models are derived to enable modelling of the oil recovery performance of the aqueous surfactant solutions being pumped through the powder packed columns with interstices filled with the oil. The first model enables the concentration of free surfactant,  $[\text{surf}]_{\text{free}}$ , present within the packed columns during flooding to be calculated from the initial concentration pumped in,  $[\text{surf}]_{\text{init}}$ . This allows a direct comparison between surface chemistry characterisation results (which relate to  $[\text{surf}]_{\text{free}}$ ) and %oil recovery results (which relate to  $[\text{surf}]_{\text{init}}$ ). The second two-part model shows how, based on the hypothesis that the residual oil is trapped in the form of liquid bridges between contacting calcite particles, the measured %oil recovery variation with surfactant concentration can be understood and predicted for concentrations of surfactant both below and above the  $c_{\text{uc}}$  in terms of the characterisation results.

It was found that, for surfactant concentrations  $< c_{\text{uc}}$ , the oil recovery depends on the contact angle alone (when capillary forces are dominant over viscous forces, i.e. low capillary number regime). The predictions show that the oil recovery varies from 58 % with a  $0^\circ$  contact angle through the water to 82 % with a contact angle of  $90^\circ$  or greater. When surfactant concentration  $> c_{\text{uc}}$ , additional oil is recovered by a solubilisation plus emulsification mechanism. Experimental results were in reasonable agreement with those predicted from the model.

# ENHANCED OIL RECOVERY BY FLOODING WITH AQUEOUS SURFACTANT SOLUTION: A MODEL STUDY AND COMPARISON WITH THEORY

## CONTENTS

<b>CHAPTER 1 – INTRODUCTION</b> .....	15
<b>1.1 General background and the main aim of this work</b> .....	15
<b>1.2 Single-phase and two-phase flow through porous media</b> .....	18
<i>1.2.1 Single-phase flow through porous media: Reynolds number and Darcy's law</i> .....	18
<i>1.2.2 Two-phase flow: Oil field dimensionless numbers and relative permeability</i> .....	20
<b>1.3 Interfacial tension and the three-phase contact angle</b> .....	24
<i>1.3.1 Interfacial tension</i> .....	24
<i>1.3.2 The three-phase contact angle</i> .....	25
<b>1.4 Surfactants and their use in enhanced oil recovery</b> .....	27
<i>1.4.1 What are surfactants?</i> .....	27
<i>1.4.2 Aqueous phase behaviour</i> .....	28
<i>1.4.3 Behaviour of surfactants in an oil and water system - microemulsions</i> .....	30
<i>1.4.4 How surfactants can be used to overcome the capillary forces</i> .....	31
<i>1.4.4.1 Adsorption and the corresponding effect on the interfacial tensions</i> .....	32
<i>1.4.4.2 Effect on the three-phase contact angle</i> .....	34
<i>1.4.4.3 Effect on emulsification</i> .....	35
<i>1.4.4 Summary of the use of surfactants in enhanced oil recovery</i> .....	36

<b>1.5</b>	<b>Current opinions in enhanced oil recovery by flooding with surfactant solution</b>	37
1.5.1	<i>Wettability alteration and spontaneous imbibition</i>	39
1.5.2	<i>Modelling of the complex oil recovery process</i>	39
1.5.3	<i>Computer modelling/history mapping</i>	39
1.5.4	<i>Visualisation of oil recovery</i>	39
1.5.5	<i>Screening tests and generic flooding experiments</i>	40
1.5.6	<i>Loss of surfactant due to adsorption at the rock-water interface</i>	40
1.5.7	<i>Common factors in oil recovery studies</i>	40
1.5.8	<i>Aims of and the novel features of the current study</i>	41
<b>1.6</b>	<b>Presentation of thesis</b>	42
<b>1.7</b>	<b>References</b>	44
<b>CHAPTER 2 – EXPERIMENTAL</b>		54
<b>2.1</b>	<b>Materials</b>	54
2.1.1	<i>Water</i>	54
2.1.2	<i>Oils</i>	54
2.1.3	<i>Surfactants</i>	55
2.1.4	<i>Calcium carbonate powders and calcite crystals</i>	57
2.1.5	<i>Other materials</i>	61
<b>2.2</b>	<b>Methods</b>	62
2.2.1	<i>Determination of surfactant concentrations</i>	62
2.2.2.1	<i>Epton titration</i>	62
2.2.2.2	<i>UV-visible spectrophotometry</i>	63
2.2.2	<i>Water-oil-calcite contact angles</i>	65
2.2.3	<i>Water-oil interfacial tensions</i>	66

2.2.3.1	<i>du Noüy ring</i> .....	66
2.2.3.2	<i>Spinning drop</i> .....	68
2.2.4	<i>Water-air interfacial tensions</i> .....	69
2.2.5	<i>Adsorption isotherms of surfactants from aqueous solution to the calcite-water interface</i> .....	70
2.2.6	<i>Partition coefficients of surfactants between water and oil phases</i> .....	71
2.2.7	<i>Determination of microemulsion phase inversion</i> .....	71
2.2.8	<i>Calcite packed column experiments</i> .....	72
2.2.8.1	<i>Reproducibility of oil recovery floods</i> .....	76
2.2.8.2	<i>Testing the pressure sensor</i> .....	77
2.2.9	<i>Other techniques</i> .....	84
<b>2.3</b>	<b>References</b> .....	<b>85</b>
 <b>CHAPTER 3 – CHARACTERISATION OF THE CALCITE PACKED COLUMNS</b>		
<b>3.1</b>	<b>Introduction</b> .....	<b>86</b>
<b>3.2</b>	<b>Porosity, permeability and pore sizes within the packed columns</b> .....	<b>87</b>
3.2.1	<i>Porosity</i> .....	87
3.2.2	<i>Permeability</i> .....	87
3.2.3	<i>Pore size</i> .....	92
3.2.4	<i>Comparison of experimental model conditions to field conditions</i> .....	95
<b>3.3</b>	<b>Effect of flow rate and gravity on oil recovery – capillary and bond numbers</b> .....	<b>96</b>
<b>3.4</b>	<b>Conclusions</b> .....	<b>98</b>
<b>3.5</b>	<b>References</b> .....	<b>99</b>

## CHAPTER 4 - MODELLING DECANE REMOVAL FROM A CALCITE PACKED COLUMN USING AQUEOUS SOLUTIONS OF THE ANIONIC SURFACTANT AOT

<b>4.1</b>	<b>Introduction</b>	101
<b>4.2</b>	<b>Microemulsion phase inversion and aqueous phase composition in the presence and absence of decane</b>	103
<b>4.3</b>	<b>Effect of AOT concentration on adsorption to the calcite-water interface, and the altering of the decane-water interfacial tension and calcite-decane-water contact angle</b>	108
4.3.1	<i>Adsorption of AOT to the calcite-water interface</i>	108
4.3.2	<i>Effect of AOT concentration on the decane-water interfacial tension</i>	111
4.3.3	<i>Effect of AOT concentration on the water-calcite-decane contact angle</i>	113
4.3.4	<i>Modelling the effect of AOT adsorption on the interfacial tensions and three phase contact angle</i>	114
4.3.5	<i>Overview of systems to be used for oil recovery experiments</i>	119
<b>4.4</b>	<b>Decane removal from calcite packed columns</b>	120
4.4.1	<i>Experimental results and the need for a model</i>	120
4.4.2	<i>Derivation of model to calculate concentration of free (non-adsorbed) surfactant in particle packed columns</i>	122
4.4.3	<i>Two-part model to calculate effect of interfacial tension, contact angle and solubilisation on %oil recovered</i>	129
4.4.3.1	<i>Principles of the model for oil recovery with <math>[surf] &lt; cac</math></i>	129
4.4.3.2	<i>Additional oil recovery when <math>[surf] &gt; cac</math></i>	133
4.4.3.3	<i>Comparison of experimental results to the derived model</i>	134
<b>4.5</b>	<b>Conclusions</b>	142
<b>4.6</b>	<b>References</b>	145

## CHAPTER 5 - MODEL VALIDATION USING A CATIONIC AND A NONIONIC SURFACTANT

<b>5.1</b>	<b>Introduction</b>	150
<b>5.2</b>	<b>Characterisation of and oil recovery performance of a system consisting of water, toluene, calcite and the cationic surfactant C14BDMAC</b>	152
5.2.1	<i>Microemulsion phase inversion and surfactant partitioning</i>	152
5.2.2	<i>cac and aqueous phase behaviour of C14BDMAC</i>	156
5.2.3	<i>Adsorption of the C14BDMAC to the water-calcite and toluene-calcite interfaces</i>	159
5.2.4	<i>Effect of C14BDMAC concentration on the toluene-water interfacial tensions</i>	162
5.2.5	<i>Effect of C14BDMAC concentration on the water-calcite-toluene contact angles</i>	163
5.2.6	<i>Toluene removal from a calcite packed column using aqueous solutions of C14BDMAC: experimental results and comparison to the model</i>	168
<b>5.3</b>	<b>Characterisation of and oil recovery performance of a system consisting of water, heptane, calcite and the commercial nonionic surfactant CW-100S</b>	170
5.3.1	<i>Aqueous phase behaviour, microemulsion phase inversion, surfactant partitioning and the cac</i>	170
5.3.2	<i>Adsorption of the CW-100S to the water-calcite and heptane-calcite interfaces</i>	174
5.3.3	<i>Effect of CW-100S concentration on the heptane-water interfacial tensions</i>	177
5.3.4	<i>Effect of CW-100S concentration on the water-calcite-heptane contact angles</i>	179
5.3.5	<i>Heptane removal from a calcite packed column using aqueous solutions of CW-100S: experimental results and comparison to the model</i>	182

5.4	Conclusions	185
5.5	References	187
<b>CHAPTER 6 - SUMMARY OF CONCLUSIONS, FUTURE WORK AND PRELIMINARY EXPERIMENTS</b>		
6.1	Summary of conclusions	189
6.2	Future work and preliminary experiments	193
6.2.1	<i>Future work</i>	193
6.2.2	<i>Visualisation of the oil recovery using a glass-bead micromodel</i>	193
6.2.3	<i>Foam flooding</i>	195
<b>APPENDIX A - DEGRADATION OF AOT IN AQUEOUS SOLUTIONS</b>		
<b>APPENDIX B - EQUATIONS FOR THE LIQUID BRIDGE MODEL</b>		
<b>APPENDIX C - CONTACT ANGLE MODELLING AND [SURF]<sub>FREE</sub> MODEL FITTING PARAMETERS AND GRAPHS FOR ALL SYSTEMS INVESTIGATED</b>		
<b>APPENDIX D - SUMMARY OF DRIVING PRESSURE PLOTS FOR VARIOUS FLOODS</b>		
<b>APPENDIX E - CALCITE BET NITROGEN ADSORPTION ISOTHERM PLOTS AND XRD PATTERNS</b>		

## LIST OF COMMON SYMBOLS AND ABBREVIATIONS

Where one symbol can have multiple variations of a subscript/superscript, here it is denoted as an arbitrary letter.

### *English letters*

A	overall packed column cross-sectional area
AOT	anionic surfactant bis-2-ethyhexylsulfosuccinate sodium salt
B <sub>o</sub>	Bond number (Eötvös number), ratio of gravity to capillary forces
C <sub>L</sub>	Capillary length
C <sub>N</sub>	Capillary number, ratio of viscous to capillary forces
cac	critical aggregation concentration
c <sub>μc</sub> <sub>a</sub>	critical microemulsion concentration in phase a (absence of a indicates c <sub>μc</sub> in aqueous phase)
CW-100	surfactant component of the CW-100 mixture, the (non-ionic) surfactant is Coconut diethanolamide.
C14BDMAC	cationic surfactant alkylbenzyldimethylammonium chloride with a 14 carbon chain length tail
DEA	diethanolamine
EOR	Enhanced oil recovery
f	fraction of the particle surface accessible to water
FCX	FordaCal calcium carbonate (calcite) sample from Minelco, where X can be 10, 30 or 200
g	acceleration due to gravity on the earth's surface
K <sub>D</sub>	Darcy permeability coefficient
K <sub>L</sub>	a constant reflecting the strength of adsorption in the Langmuir or Langmuir-type adsorption isotherms
K <sub>P-ow</sub>	oil water partition coefficient of surfactant monomer

$k_B$	Boltzmann constant
$L$	packed column length in the direction of the fluid flow
$N_{AV}$	Avogadro's number
$n$	number of pore volumes pumped through the column
$p_v$	pore volumes (volume of phase pumped/volume of pores in column)
$Q$	volumetric flow rate
$R_{em}$	moles of oil emulsified per mole of aggregated AOT, equal to [emulsified oil]/([AOT] – $c_{\mu c}$ )
$Re_p$	reynolds number for flow through packed beds of spherical particles
$R_{sol}$	moles of oil emulsified per mole of aggregated AOT, equal to [solubilised oil]/([AOT] – $c_{\mu c}$ )
$r_a$	radius of 'a'
$T$	absolute temperature
$U$	linear flow velocity ( $U = Q/\phi_{pore}A$ )

*Greek letters*

$\beta$	The cooperativity parameter for the Langmuir-type adsorption isotherm
$\Delta P_a$	Pressure drop across a (can be Laplace pressure or driving pressure drop)
$\phi_a$	volume fraction of a. When a = pores, then $\phi_a$ = porosity.
$\Gamma_{a-b}$	surface concentration (adsorbed amount) of surfactant at the interface between phases a and b, where a and b can be substituted by the symbols/names of the phases (or left out for general usage)

$\Gamma_{\max a-b}$	maximum surface concentration (adsorbed amount) of surfactant at the interface between phases a and b, where a and b can be substituted by the symbols/names of the phases (or left out for general usage).
$\gamma_{a-b}$	interfacial tension (or surface energy) between phases a and b, where a and b can be substituted by the symbols/names of the phases (or left out for general usage).
$\mu$	dynamic viscosity
$\nu$	kinematic viscosity ( $\mu/\rho$ )
$\rho$	density
$\theta$	rock-water-oil contact angle measured through the water

### *Symbols*

$[\text{surf}]_{\text{non-adsorbed}}$	concentration of surfactant not adsorbed at an interface (also called $[\text{surf}]_{\text{free}}$ )
% oil recovery	percent of the original oil in place recovered

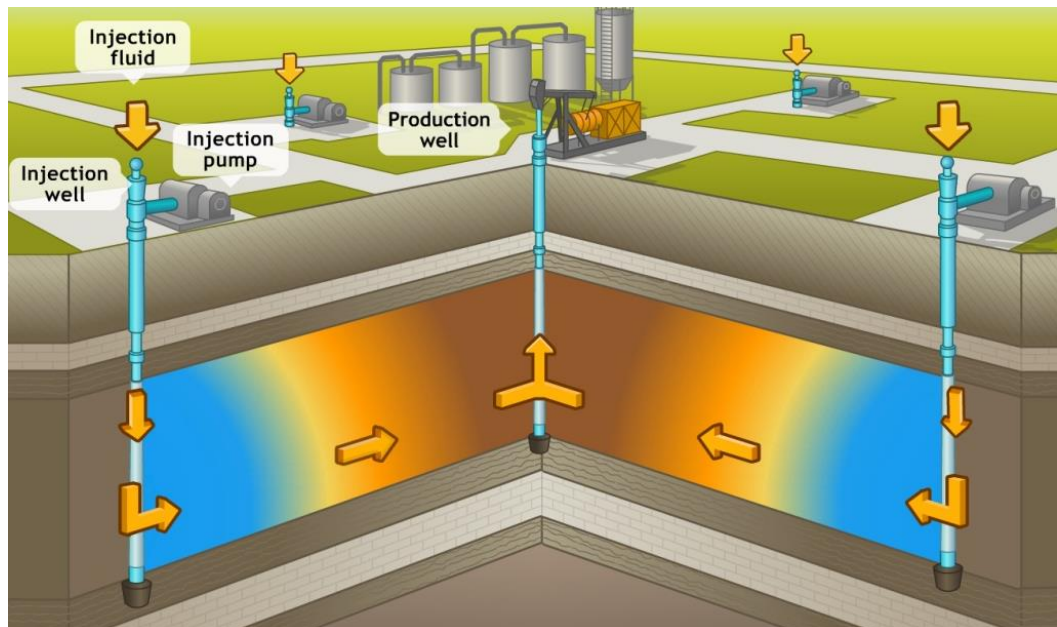
# CHAPTER 1

## INTRODUCTION

### 1.1 General background and the main aim of this work

The first fraction of oil extracted from an oil reservoir is done so by simply drilling a production well and allowing the oil to flow out under its own pressure (it is under pressure as the oil is saturated with natural gas), this stage is known as primary oil recovery. Over time the natural pressure decreases and the oil recovery rate slows. Secondary oil recovery is then used in which injection wells are drilled around the production well and (usually) brine is pumped down in order to raise the pressure in the reservoir (Figure 1.1); these two processes together can recover up to approximately 40 % of the total oil in place in the reservoir. After secondary oil recovery has taken place much of the remaining oil is trapped in the porous reservoir rock by capillary forces (discussed in section 1.2)<sup>1,2</sup>, and other effects such as flow bypassing due to heterogeneous permeability can also be important.

**Figure 1.1.** The process of secondary and tertiary oil recovery, where the injection fluid would be brine for secondary and something other than brine for tertiary (e.g. CO<sub>2</sub>, steam, surfactant solutions etc.).<sup>3</sup>



Although fossil fuels will probably eventually be replaced by renewable fuels, the current demand for crude oil is high and is not expected to decrease any time soon<sup>4</sup>. As the initial oil recovery techniques typically recover less than half of the total oil present in a reservoir it is essential to increase these yields in order to keep up with the high demand. Tertiary (or enhanced) oil recovery techniques involve the injection of something other than the brine used in secondary oil recovery with the aim of overcoming the capillary forces (or prevent flow bypassing) in order to release the trapped oil<sup>5,6</sup>. The work throughout this thesis focuses on the injection of aqueous surfactant solutions.

Because of its obvious economic importance, enhanced oil recovery (EOR) techniques with the use of surfactants have been investigated extensively in the literature since the early 1900's, with one of the first patents published in 1927 describing how interfacial tensions between crude oil, the reservoir rock and water can be reduced through the addition of 'soap' to the water<sup>7</sup>. Since then, an extensive literature on the interrelated aspects of this complex process has been developed; including many reviews<sup>8-20</sup>, general measurements of the EOR performance of different surfactant systems<sup>21-25</sup>, studies of how exposure of the porous network to crude oil and water leads to complex "mixed wettabilities" in which the pores are partially wetted by both oil and water and how surfactant addition alters the wettability state of the reservoir<sup>26-34</sup>, visualisation of the complex, multiphase flow<sup>35-52</sup> and modelling of how the oil recovery depends on the pore network structure, wettability state, relative permeabilities to oil and water, flow rates and other conditions<sup>53-67</sup>. However, this literature does not contain clear, systematic information on how the rock/oil/water contact angle varies with surfactant concentration and how this relates to surfactant adsorption at the various surfaces present, how surfactant adsorption causes its depletion in the EOR aqueous phase, and how these factors relate to the fraction of oil recovered.

The main aim of the work within this thesis is to elucidate the details of enhanced oil recovery by flooding with aqueous solutions of surfactant. This was done with the use of an experimental model system consisting of a pure rock (calcium carbonate), a pure oil (decane, heptane or toluene) and pure water containing surfactant (an anionic, cationic or a nonionic) and salt. Each system was characterised in detail in terms of the surface chemistry properties and the results of this characterisation used to understand the amount of oil recovered from a packed column of the calcium carbonate.

This chapter introduces the fundamental topics which are of most relevance to the research discussed throughout the rest of this thesis. As each area introduced has an enormous amount of theory and literature behind it, only the parts of the theories of particular relevance to this research are introduced. In some cases, topics are discussed in more detail as and when appropriate in the results chapters. In many cases the reader will be referred to other books and reviews if a further understanding is being sought after.

As oil recovery processes involve the flow of fluids through a porous medium, the first section introduces the basics of single-phase and two-phase flow through porous media. The two-phase flow discussion focuses mainly on the three main ‘forces’ which are thought to play a role in the trapping and/or displacement of one phase by another. Following this, the concepts of interfacial tension and the three-phase contact angle are introduced. Up to this point the text involves no discussions about surfactants and their use in the oil recovery process.

Since the fundamentals of how the oil is trapped within a porous medium will be established by this point, the discussion will turn surfactants and how they can be used to aid the recovery of oil from a porous medium. Initially it is important to establish an understanding of the basic principles of the behaviour of surfactants both in aqueous solutions and in an oil and water system. Hence, the topic of surfactant aggregation and microemulsions is introduced. Following this it is shown how surfactants can be used to alter interfacial tensions and the three-phase contact angles, and further the effect that surfactants have on the emulsification of one immiscible phase within another.

Finally, a brief overview of the literature related to this work is discussed, followed by a discussion about the way in which this work aims to bring new clarity and insight in to this area of research.

## 1.2 Single-phase and two-phase flow through porous media

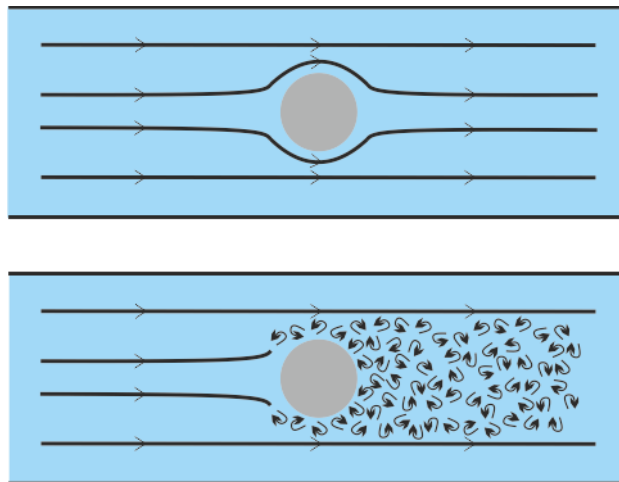
Before an understanding of how the oil left trapped in a porous rock can be removed is developed, it is first necessary to have a basic understanding of the flow characteristics of fluids through a porous medium. Due to the nature of oil recovery where one phase is used to displace another, there will always be at least two fluid phases present in the porous medium (in the work here, an aqueous phase and an oil). However, as two-phase flow is a much more complex situation than single-phase flow, the discussion here will begin with the basics of single-phase flow. As the aims of the current work is to understand the effects of the surface science involved in aqueous surfactant flooding on the oil recovery, only a brief discussion on some of the fundamentals of single-phase and two-phase flow in relation to oil recovery will be had. If the reader wants to learn more about the complexities of this area, there are many books and online resources to which they can refer to.

### 1.2.1 *Single-phase flow through porous media: Reynolds number and Darcy's law*

Single-phase flow through porous media is, in many ways, a far more simple situation than two-phase flow. Before any discussions about the characteristics of single phase flow can be had, it is first necessary to define what is meant by this term. Throughout the following discussions, single-phase flow through porous media refers to the flow of one single un-reactive fluid through an incompressible porous medium, in this case a packed bed of particles. Thus, within the flow system there are only two components present, the solid particles and the fluid which is flowing through the interstices between the particles. Limiting the discussions to such a system enables the focus to be more towards the type of systems used throughout this work. The distinction of an un-reactive fluid and an incompressible porous medium is so that it can be assumed that the flow properties of the system, such as permeability and connectivity between pore space, remains constant during the flow of the fluid. If the porous medium is compressible or the fluid reacts with the porous medium, the complexities of single-phase flow are greatly increased<sup>68-69</sup>.

For single-phase flow through a porous medium, there are two main flow regimes which are possible: i) laminar flow and ii) turbulent flow. Laminar flow is the case in which the fluid flows smoothly in ‘layers’ and there is no mixing between the layers. In laminar flow, flow properties such as the velocity remain constant at each point within the flowing region of the fluid. In turbulent flow the velocity of the fluid at any point in the flowing region may vary in direction and speed, and often circular currents are observed. How these situations look changes depending on the type of system through which the fluid is flowing. Figure 1.2 shows the example of a single sphere in the middle of a cylindrical pipe. The general observation for laminar flow is that the fluid moves smoothly around the sphere without mixing with the other layers of the fluid. For turbulent flow the flow may be laminar in nature before the fluid comes in to contact with the sphere, but in the process of flowing around the sphere the flow turns to become turbulent in nature. In flow through a packed bed (where there are many spheres), the principles are similar .

**Figure 1.2** Diagrammatic representation of laminar (top) and turbulent (bottom) flow of a liquid through a cylindrical pore containing a sphere. The black lines with arrows indicate the flow direction of the fluid at each point.



For single-phase flow through a packed bed of particles, the calculation of the Reynolds number (equation 1.1) is useful in order to determine which flow regime is expected to be present under a specific set of conditions.

$$\text{Re}_p = \frac{U_{\text{particle}}}{(1 - \phi_{\text{pore}})v} \quad (1.1)$$

where  $Re_p$  is the Reynolds number for flow through packed beds of spherical particles,  $U$  the linear velocity of the flowing liquid,  $r_{particle}$  the radius of the particles making up the bed,  $\phi_{pore}$  the porosity of the packed bed (volume of pores / total volume of object) and  $\nu$  the kinematic viscosity (dynamic viscosity / density). Whilst the transition from laminar to turbulent flow has been debated, Çarpınlioğlu *et al.* have shown that for flow through vertical packed beds of spherical particles with a  $\phi_{pore}$  of 0.36 - 0.56, the transition from laminar to turbulent flow occurs at an  $Re_p$  of approximately 2000<sup>70</sup>.

There are a number of useful equations for systems which are in the Laminar flow regime. One of these equations is Darcy's law (equation 1.2).

$$\Delta P = \frac{Q\mu L}{AK_D} \quad (1.2)$$

where  $K_D$  is the permeability coefficient,  $\Delta P$  is the pressure drop across the packed column,  $Q$  is the volumetric flow rate,  $\mu$  is the fluids dynamic viscosity,  $L$  is the packed column length in the direction of the fluid flow and  $A$  is the overall packed column cross-sectional area. The Darcy permeability coefficient,  $K_D$ , is useful as a measure of the ease at which a fluid can flow through the porous medium (and is routinely determined in the oil field literature).

### *1.2.2 Two-phase flow through porous media - capillary, viscous and gravity forces and flow bypassing*

As previously mentioned, the addition of a second fluid in to a flow system significantly complicates a situation, and hence amplifies the amount of theories and equations related to the area. Since the work here is mainly interested in how one phase is displaced by another (in these discussions, oil being displaced by water), this introduction will be limited to discussing the parameters which effect such a displacement.

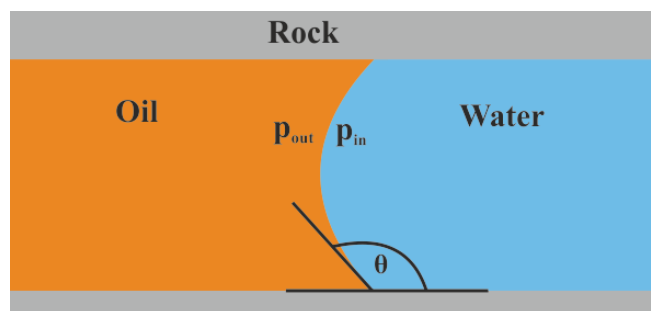
The residual oil remaining in an oil reservoir is thought to be mainly trapped by the capillary forces which arise as a consequence of the curvature at the oil-water interface and the oil-water interfacial tension. In surface science terms, the capillary force is more commonly discussed in terms of the Laplace pressure across a curved interface. For an

oil-water interface with a spherical cap within a cylindrical pore (Figure 1.3), the Laplace pressure is given by equation 1.3.

$$\Delta P_L = p_{in} - p_{out} = \frac{2\gamma_{ow} \cos \theta}{r_{pore}} \quad (1.3)$$

where  $\gamma_{ow}$  is the interfacial tension between the oil and the water,  $\theta$  the three phase contact angle measured through the water and  $r_{pore}$  the radius of the pore.

**Figure 1.3** Diagrammatic representation of a curved oil-water interface within a cylindrical pore which gives rise to the Laplace pressure/capillary forces.



Thus, in order to release the trapped oil the capillary forces need to be overcome. There are three main ways in which this is thought possible: i) reversing the sign of the Laplace pressure, ii) forcing the oil out by overcoming the capillary forces with viscous forces and iii) using gravity forces to cause the oil to separate out to the top of the reservoir<sup>71-72</sup>.

Depending on the value of the contact angle, the capillary forces can either help or hinder the imbibition of water in to the pore. The whole focus of the wettability alteration literature (mentioned at the start of this chapter) is on lowering the contact angle (measured through the water) to below 90 ° to enable the water phase to spontaneously imbibe in to pores and release the trapped oil. While this may initially appear to be the best option for releasing the trapped oil in reservoirs, the process can be extremely slow. It is partly for this reason that forced imbibition is often employed, the aim of which is to overcome the Laplace pressure (capillary forces) by increasing the viscous forces. The ratio between viscous and capillary forces, known as the capillary number ( $C_N$ , equation 1.4), is often used to understand the point at which viscous forces overcome the capillary forces and hence displace the oil.

$$C_N = \frac{\text{viscous forces}}{\text{capillary forces}} = \frac{\mu U}{\gamma_{ow}} \quad (1.4)$$

where  $\mu$  is the dynamic viscosity of the displacing phase. Many studies have focussed on the effect of flow rate, viscosity, the oil-water interfacial tension and the three-phase contact angle on oil recovery by forced imbibition with some attempting to model the critical capillary number at which oil becomes mobilised<sup>73-74</sup>. The critical capillary number is expected to be  $> 1$ , however, problems arise with estimating the viscous and capillary forces over identical and correct length scales. This is discussed in further detail in Chapter 3.

The last type of displacement mechanism that may be employed to release trapped oil is that of when gravity forces overcome the capillary forces, a process often called gravity drainage. The ratio between gravity and capillary forces, known as the Bond number (sometimes also called the Eötvös number), is given in equation 1.5.

$$B_o = \frac{\text{gravity forces}}{\text{capillary forces}} = \frac{\Delta\rho g (2r_{\text{pore}})^2}{\gamma_{ow}} \quad (1.5)$$

where  $\Delta\rho$  is the density difference between the two phases and  $g$  the acceleration due to gravity. Despite the fact that oil recovery by raising the bond number (usually by lowering the oil-water interfacial tension) can be high<sup>75</sup>, there is not as much literature found as compared to either wettability alteration for spontaneous imbibition or overcoming the capillary forces with viscous forces. This may be as a consequence of oil recovery through gravity drainage being very slow<sup>76</sup>.

All the above relationships are useful for understanding the oil recovery on a pore-scale level. However, the effect they may have on the oil recovery at a macroscopic level depends on, among other parameters, the nature of the permeability of the rock, i.e. is it homogenous or heterogeneous permeability. For a rock with homogenous permeability any of the above relationships may sufficiently explain the oil recovery mechanisms observed, however, for a rock with heterogeneous permeability effects such as flow bypassing may be observed<sup>50,69</sup>. Flow bypassing is where the flowing liquid preferentially passes through some pores over others (usually due to size differences). Thus, although the oil recovery from some pores may be close to 100 %, if some parts of the reservoir are not reached by the flooding phase no oil can be recovered from those areas. The effectiveness of a flood on flowing through the whole reservoir is often

discussed in terms of the sweep efficiency, which is the volume of the reservoir contacted by the displacing fluid. As the current work uses a largely homogeneously permeable porous material, the sweep efficiency is not considered to have a significant effect, and as such is not discussed any further.

Overall it can be seen that pore-level trapping by capillary forces (Laplace pressure) can be overcome by changing the sign of the Laplace pressure through wettability alteration, overcoming the capillary forces through forced imbibition (by adjusting the oil-water interfacial tension, the viscosity of the displacing phase or the flow rate) and lowering the oil-water interfacial tension to increase the relative effects of gravity leading to gravity drainage. Further, the oil recovery from heterogeneous porous media is likely to be affected by other factors such as sweep efficiency.

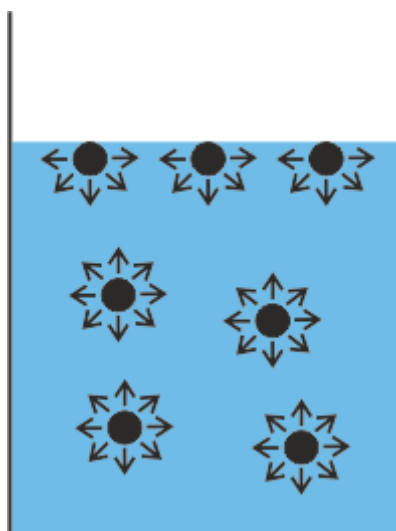
The following section discusses the basic principles of interfacial tension and the three-phase contact angle, the two main parameters which define the Laplace pressure (the main cause for oil becoming trapped in the rock).

### 1.3 Interfacial tension and the three-phase contact angle

#### 1.3.1 Interfacial tension

Without the effect of external forces such as gravity, liquids have a tendency to form shapes which minimise their surface area to volume ratio. The cause for this can be understood by looking at the intermolecular forces that occur between the molecules which make up the liquid and how these are affected when a molecule is at the surface of the liquid. There are two main categories of intermolecular forces, these being polar and dispersive. The types of intermolecular forces between the molecules within a liquid depends on the structure of the molecules. Molecules with polar entities, such as water, have both polar and dispersive forces between the molecules, whereas molecules which are non-polar only have dispersion forces between the molecules. Every molecule, regardless of polarity, within the bulk of the liquid experiences attractions to other molecules in all directions. For molecules on the surface of the liquid (at an air-liquid interface), however, there are no (or negligible) attractive interactions between the molecules and the air, and hence the surface molecules experience a net force of attraction in to the bulk of the liquid (Figure 1.4). It is this phenomenon which gives rise to the surface tension of a liquid.

**Figure 1.4** Diagram of the forces of attraction between molecules in both the bulk of and the surface of a liquid.



Surface (or interfacial) tension is defined as the energy required to increase the surface (or interfacial) area by unit area, commonly quoted in  $\text{J m}^{-2}$ . It is more commonly quoted in the equivalent units of  $\text{N m}^{-1}$ , i.e. the force acting over the surface per unit length of

the surface perpendicular to the force<sup>77</sup>. The term surface tension is often used to discuss the tension between air and a liquid, whereas interfacial tension often used for the tension between two liquids. It is worth noting, however, that the term interfacial tension can be used for both air-liquid and liquid-liquid tensions.

If the liquid in Figure 1.4 is water and the air replaced with a non-polar phase such as an alkane, the water molecules at the interface still experience an inward pull in to the bulk of the water phase despite the presence of some interactions between the water molecules and the alkane molecules. There are multiple reasons for this, though one significant reason is that the hydrogen bonds (a type of polar force) between water molecules are stronger than the permanent-dipole-induced-dipole interactions between the water molecules and the non-polar phase. Hence, the tendency for water to minimise its interfacial area under air giving rise to surface (or interfacial tension) also occurs for water in the presence of a non-polar liquid. If the reader wants to read further about the intermolecular forces between molecules in a liquid and how they affect interfacial tensions there are many good books available, such as that in ref 78.

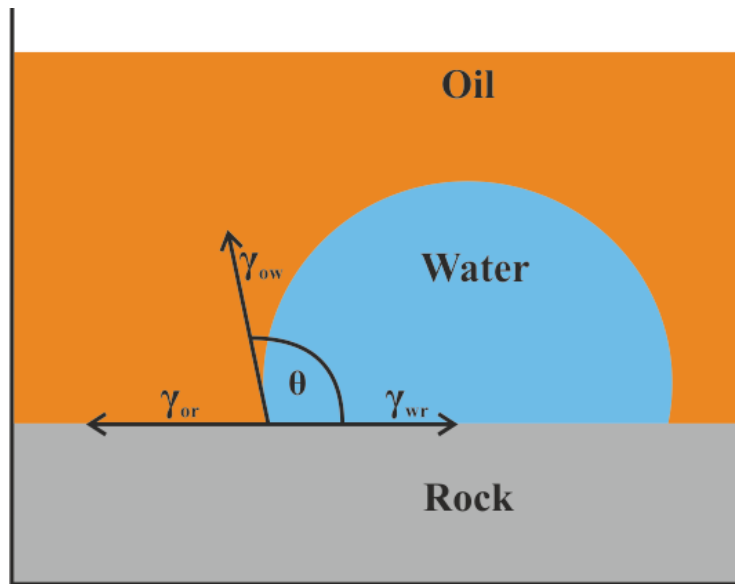
### 1.3.2 *The three-phase contact angle*

When a liquid contacts a solid in the presence of another fluid (gas or liquid), the equilibrium three-phase contact angle (Figure 1.5) is determined as a function of the three interfacial tensions. The relationship between the equilibrium contact angle and the three interfacial tensions for a liquid in contact with an incompressible solid under another fluid is given by Youngs equation (1.6). Figure 1.5 shows the case of a water drop in contact with a flat surface of a rock under an oil.

$$\cos \theta = \frac{\gamma_{ro} - \gamma_{wr}}{\gamma_{ow}} \quad (1.6)$$

where  $\gamma_{ro}$  is the rock-oil interfacial tension,  $\gamma_{wr}$  the water-rock interfacial tension,  $\gamma_{ow}$  the oil-water interfacial tension and  $\theta$  the rock-water-oil contact angle measured through the water phase.

**Figure 1.5** Diagram of the three-phase contact angle between sessile drop of water on a rock under and oil.



Whether or not a true equilibrium contact angle is attained and various parameters which may effect this is discussed in more detail in the results chapters.

When the effect of gravity on the water drop is negligible the drop will have a spherical cap (minimising the interfacial area), which is the case when the oil-water interfacial tension is reasonably high. However, when the oil-water interfacial tension is reduced to low values the drop spreads out due to the effect of gravity. The length a meniscus can be before gravity effects the curvature of that meniscus is given by the capillary length (equation 1.7).

$$C_L = \sqrt{\frac{\gamma_{ow}}{\Delta\rho g}} \quad (1.7)$$

where  $C_L$  is the capillary length. The effect of this is easily seen by observing the meniscus of water in a glass. The capillary length is the length of the meniscus from the point of contact with the glass to the point at which the water surface becomes flat.

It is worth noting here that the Bond number (equation 1.5) is equivalent to the square of the product of the pore diameter (of Figure 1.3) divided by the capillary length. Hence, the point at which gravity causes the oil-water interface to no longer have a spherical cap within the pore is the same point at which gravity forces become dominant over the capillary forces.

## 1.4 Surfactants and their use in enhanced oil recovery

### 1.4.1 What are surfactants?

Before any discussion can be had on the use of surfactants in enhanced oil recovery, it is first necessary to define what a surfactant is. Surfactants are molecules which consist of two regions, one of which is hydrophilic and the other hydrophobic. It is due to this amphiphilic nature that surfactants are often observed to adsorb at various different interfaces. It is this property which gives rise to their name of surfactant which comes from the phrase surface active agent. Figure 1.6 shows a schematic representation of the generic structure of a surfactant.

**Figure 1.6** Schematic diagram of the generic structure of a surfactant, where the green circle is the hydrophilic ‘head’ and the black line the hydrophobic ‘tail’.



The structure in Figure 1.6 shows a surfactant with one ‘head’ and one ‘tail’. This doesn’t always have to be the case however, and surfactants can have multiple head or tail regions.

A common way to group surfactants is by the charge present on the head group when dissolved in water. Very broadly, surfactants are grouped in to nonionic and ionic surfactants. In practise, the generic term ionic is not often used, and instead the specific charge on the head group is used, i.e. anionic and cationic. There are also examples of surfactants with zwitterionic headgroups.

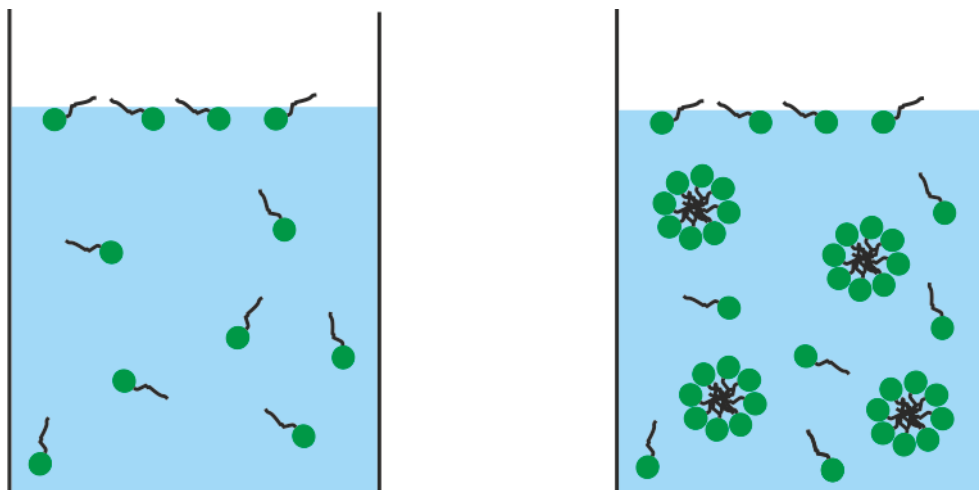
The tail groups of surfactants can also consist of different components and configurations. Tails made up of alkane chains are commonly encountered (branched or straight). Other examples of surfactant tail groups are alkylbenzenes and fluoroalkyl chains.<sup>79-80</sup>

### 1.4.2 Aqueous phase behaviour

Due to their amphiphilic nature, surfactants often display some interesting characteristics in aqueous solutions. One such characteristic is their tendency to form aggregated structures above a certain concentration (the critical aggregation concentration, cac). Often these aggregates are in the form of spherical micelles, hence why it is common to see this critical concentration denoted as the cmc, or critical micelle concentration. However, sometimes the aggregates can be in other forms such as lamellar liquid crystal phases (which are observed for some of the systems in this current work). Hence, throughout this work the term cac is used as this encompasses the formation of all aggregates, including micelles. In aqueous solutions, the aggregates form with the hydrophilic heads on the outside and the hydrophobic tails on the inside. The opposite can occur in oil solutions where the heads are on the inside of the aggregates and the tails on the outside, in this case if the aggregates formed are spherical they are denoted as reverse micelles.

As mentioned, the formation of aggregates often occurs at a critical concentration known as the cac. Below this concentration the surfactants dissolve as monomers, and above this concentration the excess monomers (the concentration above the cac) form aggregates. Another characteristic of surfactants in aqueous solutions is the adsorption of the monomers at the air-water interface (discussed further in section 1.4.4.1). These situations are shown schematically in Figure 1.7.

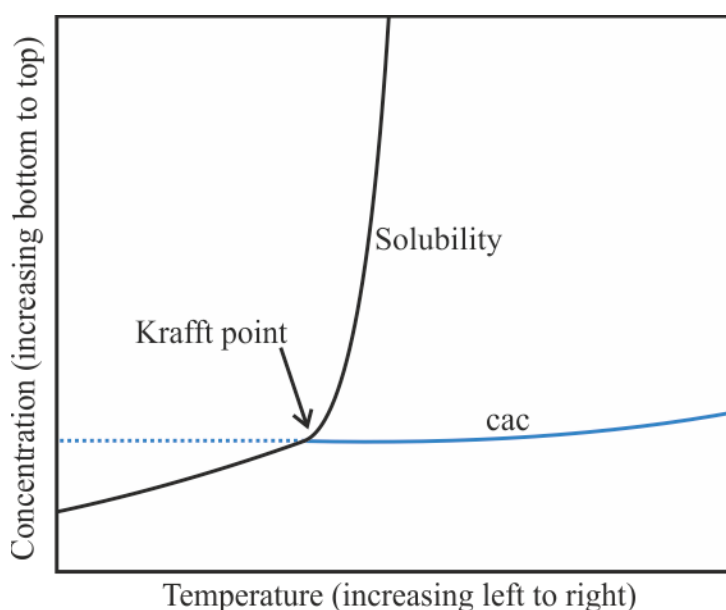
**Figure 1.7** 2D diagrammatic representation of surfactants in aqueous solutions both below (left) and above (right) cac. The concentration of monomers in the right diagram is equal to the cac.



The cause for both the adsorption at the air-water interface and the formation of aggregates is often discussed in terms of the removal of the hydrophobic tails from contact with the water. Opposing this process is the repulsion between the head groups of the surfactants, a situation more prevalent with ionic surfactants. If the reader is interested there are many good books available on the thermodynamics of the adsorption and aggregation processes<sup>79-81</sup>. It is worth mentioning that the formation of aggregates is a dynamic and reversible process. Hence, individual monomers in aggregates can be removed from aggregates and replaced by other monomers, and aggregates can fully dissociate and another aggregate formed.

An important phenomenon that is commonly observed for ionic surfactants is that of a sudden increase in the solubility of the surfactant in water at a certain temperature. The reason for this is that the solubility of ionic surfactant monomers is generally quite low (due to the hydrophobic tails), however the solubility of the aggregates is significantly higher as the hydrophobic regions are not in contact with the water. Thus, at temperatures where the solubility concentration is below that of the cac, only monomers can dissolve and hence the solubility is low. When the temperature is such that the solubility becomes roughly equal to the cac (known as the Krafft point/temperature) there is a sudden rise in the solubility (Figure 1.8) as all the excess surfactant forms aggregates which as previously stated are much more soluble than the monomers.

**Figure 1.8** Diagrammatic representation of the Krafft point for the dissolution of ionic surfactants in water.

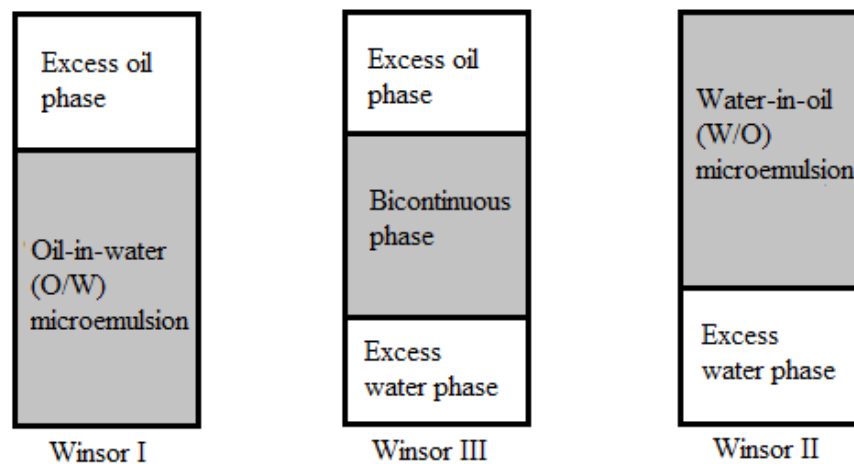


Interestingly the opposite occurs with nonionic surfactants, i.e. the solubility decreases with increasing temperature. At a temperature known as the cloud point the surfactants form large aggregates forming a separate phase, causing the solution to become cloudy.

#### 1.4.3 Behaviour of surfactants in an oil and water system - microemulsions

When surfactant is added to a system consisting of oil and water (whereas above only water was present), below a critical concentration (the critical microemulsion concentration,  $c_{\mu c}$ ) the surfactant is present as monomers which may be present in one or both of the phases and will adsorb at the interface between the two phases. Above the  $c_{\mu c}$ , aggregates may again be formed. The formed aggregates (which can be in either phase, or in a separate middle phase) have the ability to solubilize small amounts of the opposite phase to which the aggregates are in. For a system consisting of a 1:1 volume ratio of water:oil and a surfactant concentration above the  $c_{\mu c}$  there are three different multiphase systems containing microemulsions which can occur. These systems are usually discussed in terms of the Winsor naming system (Figure 1.9).

**Figure 1.9** Diagrammatic representation of the three Winsor systems.



The type of microemulsion formed is determined by the preferred curvature of the surfactant aggregates. For an O/W microemulsion the preferred curvature of the aggregates is positive (with the heads on the outside of the aggregates), for a bicontinuous microemulsion the preferred curvature is zero, and for a W/O microemulsion the preferred curvature is negative (with the heads on the inside of the aggregates). A factor considered in predicting the preferred curvature of a surfactant

system is the hydrophile-lipophile balance (HLB) of the surfactant<sup>82</sup>. This provides a measure of the balance between the hydrophilic and hydrophobic entities of a surfactant molecule.

For a system consisting of water, alkane and an ionic surfactant, the inversion from a Winsor I to a III to a II can be caused through the addition of salt. This is due to the addition of salt shielding the charge between the head groups of the surfactant (which lowers the HLB) thus allowing them to become closer together. This in turn leads to a decrease in the preferred curvature of the aggregates. The addition of salt can be used to cause microemulsion phase inversion with nonionic surfactant as well, though often larger amounts salt are needed. If the reader would like to read more about the nature of the preferred curvature of surfactant aggregates and how other parameters affect this, they are referred to reference 81.

#### *1.4.4 How surfactants can be used to overcome the capillary forces*

As the residual oil left behind in an oil reservoir is mainly trapped by capillary forces, the magnitude of which are define by the Laplace pressure, it is necessary to understand how surfactants can be used to overcome them. The following two sections (1.4.4.1 and 1.4.4.2) discuss how surfactants can alter the interfacial tensions of the three-phase system and how in turn this alters the three-phase contact angle, both of which are involved in determining the value of the Laplace pressure. The final section (1.4.4.3) briefly discusses how the lowering of the oil-water interfacial tension leads easier emulsification between the two-phases, which in some respects negates the need to overcome the Laplace pressure.

#### 1.4.4.1 *Adsorption and the corresponding effect on the interfacial tensions*

As previously mentioned, surfactant monomers have the tendency to adsorb at air-water and oil-water interfaces. Further, they are often found also to adsorb at solid-liquid interfaces. The driving force for adsorption at the air-water or oil-water interfaces is often that of removing the hydrophobic tails from being in contact with the water. The driving forces for adsorption at the solid-liquid interface, however, are not limited to the hydrophobic driving forces but can also be due to other effects such as electrostatic interactions. Although it can be useful to understand the mechanisms of surfactant adsorption to the solid-liquid interface, in this current work the focus is mainly on modelling how much adsorbs and how this affects the interfacial tensions, contact angles and the amount of surfactant lost due to adsorption in the EOR process. The following discusses how surfactant adsorption can be modelled and how the adsorption affects the interfacial tensions and contact angles, leaving the discussion about how adsorption leads to loss of surfactant in the EOR process to Chapter 4.

The amount of surfactant adsorption to an interface can be expressed in terms of an adsorption isotherm where the amount of surfactant adsorbed per unit area is plotted vs. the concentration of non-adsorbed surfactant in solution. These plots can be analysed quantitatively by fitting an adsorption isotherm model to the data. There are many models that have been derived, with probably the most common being the Langmuir isotherm (equation 1.8).

$$\Gamma = \frac{\Gamma_{\max} K_L [\text{surf}]_{\text{non-adsorbed}}}{1 + K_L [\text{surf}]_{\text{non-adsorbed}}} \quad (1.8)$$

where  $\Gamma$  is the adsorbed amount per unit area,  $K_L$  a constant reflecting the strength of adsorption and  $[\text{surf}]_{\text{non-adsorbed}}$  the concentration surfactant not adsorbed. The assumptions of the Langmuir isotherm are; i) the solid has specific binding sites, ii) all of the adsorption sites are of equal energy, iii) there are no interactions between the adsorbed species, and iv) adsorption only takes place up to a monolayer<sup>83</sup>. Despite these assumptions the Langmuir isotherm can often be used to fit experimental data where these assumptions are known not to be true. The suitability of the Langmuir isotherm for fitting to experimental data is discussed further in the results chapters.

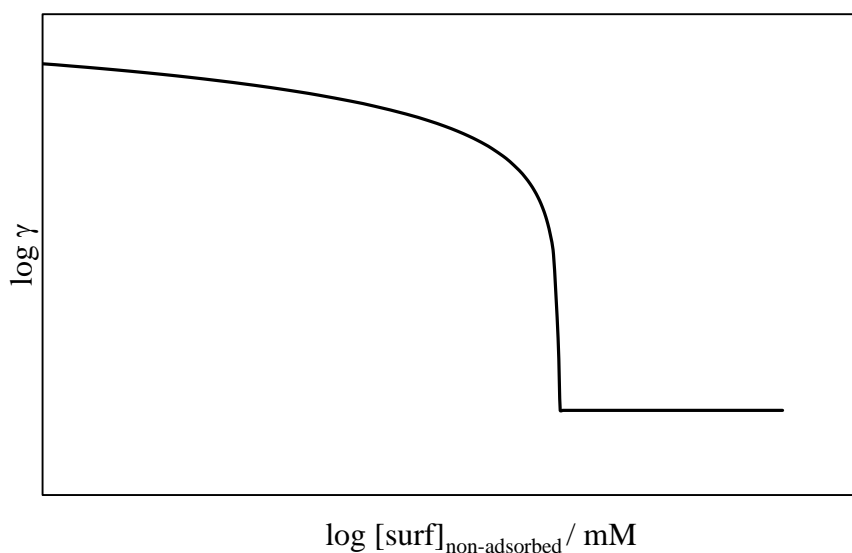
As a consequence of surfactants adsorbing at interfaces, the interfacial tension decreases. The relationship between the adsorbed amount and the change in interfacial

tension is given by the Gibbs adsorption equation. Equation 1.9 is the Gibbs adsorption equation for nonionic surfactants or ionic surfactants in swamping electrolyte.

$$\Gamma = -\frac{1}{kT} \frac{d\gamma}{d \ln a} \quad (1.9)$$

where  $k$  is the Boltzmann constant,  $T$  the absolute temperature,  $\gamma$  the interfacial tension and  $a$  the activity of the surfactant monomers. If the interfacial tension between two phases is plotted vs. the surfactant concentration on a log-log scale graph, the interfacial tension is seen to progressively decrease down to certain value, at which point there is no further decrease in the tension with an increase in surfactant concentration (Figure 1.10). The concentration at which this break point occurs is the  $c_{ac}$  or  $c_{\mu c}$  (depending on if it is the air-water or oil-water interfacial tension being measured). The reason for this breakpoint occurring is that the activity of the surfactant monomers no longer increases with increasing surfactant concentration above the  $c_{ac}/c_{\mu c}$  as the excess surfactant forms aggregates which do not adsorb at the interface.

**Figure 1.10** Diagrammatic example of the decrease in interfacial tension between two phases with an increase in surfactant concentration where both axis are on a logarithmic scale.



For an oil-water system with  $[\text{surf}] > c_{\mu c}$  (as in Figure 1.9), the post- $c_{\mu c}$  oil-water interfacial tension is seen to reach a minimum in the Winsor III region of microemulsion phase inversion and can often approach ultra-low values of around  $1 \times 10^{-3} \text{ mN m}^{-1}$ . This trend will be seen in Chapter 4. Thus, for surfactants in an oil and water system a large

variation in the oil-water interfacial tension can be achieved through the addition of salt and the varying of the surfactant concentration (from the value without surfactant, typically approximately  $40 \text{ mN m}^{-1}$ , to ultra-low values of approx.  $1 \times 10^{-3} \text{ mN m}^{-1}$ ).

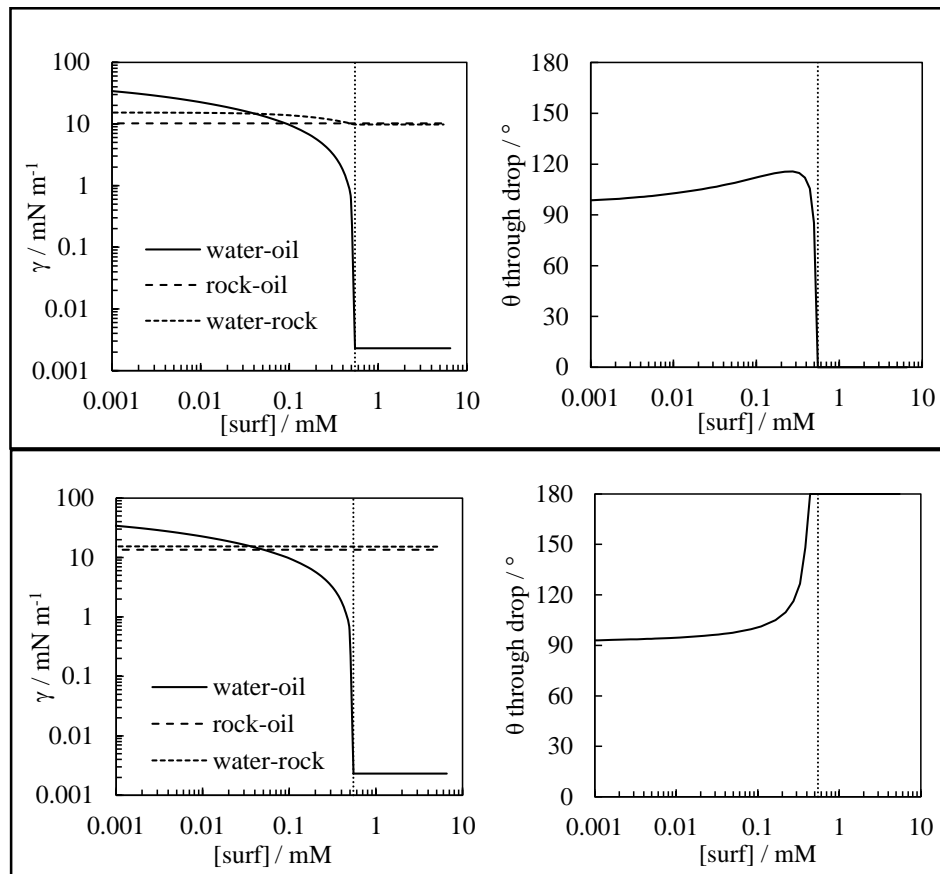
#### 1.4.4.2 *Effect on the three-phase contact angle*

As the three-phase contact angle (section 1.3.2) is determined by the relative magnitudes of the three interfacial tensions, it is clear that the addition of surfactant to the system can alter the contact angle through adsorption at the interfaces causing a change in the interfacial tensions. The ways in which the tensions, and hence the contact angles can vary with surfactant concentration are many. By creating ‘dummy’ tension data and calculating the contact angles (with Youngs equation, 1.6), it is easy to understand how much of a variation in the contact angle the addition of surfactant to a system can cause. Figure 1.11 shows two such situations.

The two theoretical systems shown in Figure 1.11 have the same decrease in the water-oil tension down to an ultra-low value and an unchanging rock-oil tension. The only difference between the two systems is the change in the water-rock interfacial tension. The top system is the case where the water-rock tension drops down to a value less than the rock-oil tension at a concentration approximately equal to the  $c_{\mu c}$ , whereas the bottom system the water-rock tension stays above the rock-oil tension at all concentrations of surfactant. The slight difference in the variation of the water-rock tension results in a significant change in the calculated contact angles, where the top system sharply drops to a contact angle of  $0^\circ$  and the bottom system sharply rises to  $180^\circ$ .

Thus, it can be seen that the addition of surfactant to a water-oil-rock system can cause the contact angle to vary from  $0$  to  $180^\circ$ .

**Figure 1.11** Theoretical representations of the effect of surfactant concentration on the interfacial tensions in a water-rock-oil system and the corresponding effect on the three-phase contact angle (tensions on left give rise to the contact angles on the right). The vertical dotted lines represents the  $c_{\mu c}/c_{ac}$ . The only difference between the two systems is the change in the water-rock interfacial tension.



#### 1.4.4.3 *Effect on emulsification*

It is due to their tendency to adsorb at oil-water interfaces that surfactants are often used as emulsifiers for stabilising macroscopic emulsions. Emulsions, in general, are defined as a system in which small droplets of one immiscible phases is dispersed in another. Microemulsions (section 1.4.3) are thermodynamically stable emulsions which form spontaneously upon the mixing together of the different components of the system. Macroscopic emulsions, on the other hand, are thermodynamically unstable and require work to be done to cause one phase to become dispersed within the other. The reason

for this can be understood by looking at the free energy of emulsion formation from two separate immiscible phases.

$$\Delta G = \gamma\Delta A - T\Delta S$$

where  $\gamma$  is the interfacial tension between the two immiscible liquids,  $\Delta A$  the change in the interfacial area between the two immiscible liquids,  $\Delta S$  the change in the entropy of the system and  $T$  the temperature of the system. With a large interfacial tension between the water and the oil, it is clear that the  $\Delta G$  will be positive, and hence the system is thermodynamically unstable. If the interfacial tension is lowered by the addition of surfactant the  $\Delta G$  becomes smaller, and hence the emulsified system will become more stable. Thus, the addition of surfactant to an oil and water system decreases the work required for one phase to be emulsified by the other. Thus, the curved oil-water interface may be removed through the emulsification of one phase in the other (though the emulsion drops may become trapped in pores).

#### *1.4.4 Summary of the use of surfactants in enhanced oil recovery*

The addition of surfactant to an oil-water-rock system can lead to large variations in the oil-water interfacial tensions and the water-rock-oil three-phase contact angle. As both the parameters are highly linked to the trapping/releasing of the oil in a porous medium by the three forces discussed in section 1.2.1 (capillary, viscous and gravity forces), it is obvious to see how surfactants can be utilised in the releasing of the trapped oil. Further, the solubilisation capabilities of a microemulsion system and the decreased amount of work required to form an emulsion between water and oil probably also plays an important role in the oil recovery performance of aqueous surfactant solutions.

As briefly mentioned, the adsorption of surfactant at the rock surface can lead to significant depletion of the surfactant in an EOR process. This is discussed in more detail in Chapter 4.

## **1.5 Current opinions in enhanced oil recovery by flooding with surfactant solution**

As previously mentioned, the literature on the interrelated aspects of enhanced oil recovery by flooding with aqueous surfactant solutions is vast. Over the years there have been multiple reviews on enhanced oil recovery, which, despite some great efforts still often do not manage to encompass the totality of the oil recovery literature<sup>8-20</sup>. Further, it is not easy to find reviews or papers which discuss with a great degree of clarity the specifics of how various surface chemistry properties affect oil recovery performance.

One issue which does not help the complexity of this research area is the great degree of overlap between the multiple disciplines and research areas which are involved. Due to this there are many ways in which any one single aspect of this research area can be approached by different researchers. As this is the case, a simple overview of the current opinions in enhanced oil recovery seems best to be approached in the form of a table. Table 1.2 summarises the main areas of research which are of interest to the current study, and the key ideas (and in some cases key authors) associated with each area. The key authors are by no means the only authors worth a mention, they are simply the authors which appear most common or whose ideas have endured over the years. A brief discussion about each area can be found following the table. The reader should bear in mind that this overview is by no means exhaustive, it serves simply to show the wide variety of research areas involved in the oil recovery literature.

Following this, the common factors between many of the research areas are discussed, and how the current study aims to bring new clarity and insight in to this complex area of research.

**Table 1.2** An overview of the main areas of research in the oil-recovery literature.

<b>Main areas of research</b>	<b>Key ideas/authors</b>
Wettability alteration and spontaneous imbibition <sup>29-34</sup>	<ul style="list-style-type: none"> <li>• Using surfactants to alter the wettability of oil filled rocks causing the water to imbibe (without a driving pressure) due to the Laplace pressure. <i>Key authors, T. Austad and D. Standnes.</i></li> <li>• Studies on how components in crude oil alter the wettability of the rock under different conditions. <i>Key author, J. Buckley.</i></li> </ul>
Modelling of the complex oil recovery process <sup>52-66</sup>	<ul style="list-style-type: none"> <li>• Modelling how the oil recovery depends on the pore network structure, wettability state, relative permeabilities to oil and water, flow rates and other conditions <i>Key authors, S. Buckley, M. Leverett, W. Rose, M. Blunt., P. Hammond.</i></li> </ul>
Computer modelling / history mapping <sup>83-85</sup>	<ul style="list-style-type: none"> <li>• Using complex computer algorithms to model the oil recovery performances under different conditions using mainly history mapping/forecasting techniques.</li> </ul>
Visualisation of oil recovery - glass micromodels, x-ray tomography and more <sup>35-51</sup>	<ul style="list-style-type: none"> <li>• Using glass micromodels to enable visualisation of the oil recovery process under different conditions. <i>Key author, R. Lenormond.</i></li> <li>• Using x-ray tomography, low field NMR and other techniques to visualise oil recovery in rock cores.</li> </ul>
Screening tests and generic flooding experiments <sup>21-25</sup>	<ul style="list-style-type: none"> <li>• Taking new surfactant systems and carrying out pre-screening tests, followed by determining the oil recovery from rock core samples.</li> </ul>
Loss of surfactant due to adsorption at the rock-water interface <sup>86-88</sup>	<ul style="list-style-type: none"> <li>• Rock core flooding experiments with aqueous surfactant solution to determine the amount of surfactant depleted during a flooding process.</li> </ul>

### *1.5.1 Wettability alteration and spontaneous imbibition*

As mentioned previously, the wettability alteration literature is mainly focussed on attempting to understand the effect of the water-rock-oil three phase contact angle on oil recovery by spontaneous imbibition. As well as attempting to understand how the oil recovery depends on the contact angle, many studies are carried out to see how both surfactant in the aqueous phase and natural surfactants in crude oil can effect this contact angle.

### *1.5.2 Modelling of the complex oil recovery process*

This is the section of the literature which comes closest to the aims of the current research. The main aims are to understand how multiple parameters affect the oil recovery from various different types of porous media. The longest enduring ideas within this area are perhaps those of Buckley and Leverett<sup>53</sup>. They attempted to extend Darcy's law to enable its use for two-phase flow in an attempt to bring predictive capabilities in understanding how much oil will be recovered. Rose, however, has published multiple papers refuting these ideas<sup>90-91</sup>.

Despite the vast amount of literature related to this topic, it is not easy to find a generic consensus on how these various parameters effect oil recovery.

### *1.5.3 Computer modelling/history mapping*

In these studies, many of the same parameters related to oil recovery which are incorporated in to the models from the previous section are used in highly complex computer simulations. A common program used is UTCHEM, which is developed at the University of Texas. The principles of such programs is similar to that of a weather forecast, whereby a large amount of parameters are input and the outcome calculated based on previous examples.

### *1.5.4 Visualisation of oil recovery*

This area is split into two main categories; i) using glass micromodels to image oil recovery using optical techniques, and ii) using more complex techniques such as x-ray tomography and NMR to image oil recovery within rock cores. From these experiments, the effect of varying the capillary and Bond number on the macroscopic oil recovery can be visualised.<sup>52</sup>

### *1.5.5 Screening tests and generic flooding experiments*

Much of this area of the literature is taken up with designing and synthesizing new surfactants with properties which aim to overcome common problems encountered in EOR processes. Problems such as surfactant precipitation and degradation are common for researches to aim to reduce.

Aqueous solutions of the new surfactants are then used in screening tests to assess their viability for oil recovery. This may include interfacial tension, contact angle and various other physiochemical measurements. Many of the surfactants are used in conjunction with a co-surfactant. The solutions are then used in rock core flooding experiments to see how effective they are at recovering the oil.

### *1.5.6 Loss of surfactant due to adsorption at the rock-water interface*

It is well established that due to the large surface area to volume ratio during flooding processes large amounts of surfactant can be lost due to adsorption at the rock-water interface. Some researches carry out aqueous floods through rock cores and measure the amount of surfactant lost, and how it can also be desorbed and recovered.

### *1.5.7 Common factors in oil recovery studies*

Despite the huge variation in research topics, there are a few common factors between many of the studies, such as;

1. The use of rock cores cut from outcrop rocks near oil producing reservoirs
2. The use of crude oil which contains many impurities
3. Similar pre-flood routines
4. Water-floods before surfactant floods

Pre-flood routines often consist of cleaning the rock core, filling it with brine, displacing the brine with oil until residual brine saturation is obtained, followed by the oil displacement floods of interest. This is thought necessary as this process is supposed to closely resemble the processes which actually occur in a real reservoir. It is thought that reservoirs were initially filled with water, this water was then displaced over millions of years as the oil was made and flowed up in to the rock slowly (displacing the water) due to gravity, then oil engineers drill a hole and pump down the displacing solutions. It is for a similar reason that many studies carry out a water-flood before surfactant

flooding, as this is closer to how tertiary oil recovery processes occur in an actual oil field.

#### *1.5.8 Aims of and the novel features of the current study*

As mentioned at the beginning of this chapter, the main aim of the work discussed within this thesis is to elucidate the details of enhanced oil recovery by flooding with aqueous solutions of surfactant in terms of surface chemistry properties. In order to do this it was necessary to use a pure experimental system to minimise the amount of parameters involved in the oil recovery process. Therefore, all experiments were carried out using a pure rock (calcium carbonate), a pure oil (decane, heptane or toluene) and pure water containing surfactant (an anionic, cationic or a nonionic) and salt. Each system was characterised in detail in terms of the surface chemistry properties. All packed columns were filled with the pure oil first (with no pre water-flood), and the oil subsequently displaced using the surfactant solution (i.e. no ‘secondary’ oil recovery process with water). The results of the characterisation were used to develop an understanding of the amount of oil recovered from a packed column of the calcium carbonate (with the aid of two models, both derived in Chapter 4).

For the current work surfactant floods are carried out at a flow rate corresponding to the low capillary number regime (i.e. capillary forces dominate, at least for low surfactant concentrations), but with a pressure drop imposed so that the flow is not by spontaneous imbibition. It is hypothesised that the oil left behind after such a flood is trapped as liquid bridges between contacting particles in the packed bed. Much of the theory involved in the considerations of the amount of fluid retained when a particle bed is flooded with a second fluid are also important in the prediction of so-called “liquid holdup” in distillation columns and catalyst particle bed reactors and other applications<sup>92-98</sup>.

Thus, although each individual aspect of the current study may not itself be classified as novel, the novel aspect comes from the full systematic characterisation of many of the system parameters thought to be involved in oil recovery, and the linking of these to the oil recovery performance. The full systematic characterisation was made possible through the use of all pure components, not often encountered in the literature.

## 1.6 Presentation of thesis

Chapter 2 describes the main experimental techniques used throughout this work. As the flooding experiments did not use a standard technique, there is a discussion about development and testing of the set-up used for these experiments.

Chapter 3 discusses the properties and characterisation of the calcite packed columns. This involves describing the packed bed characteristics, such as porosity, and the flow properties of fluids through the packed bed, such as permeability. Using the experimental results from these sections a discussion about the estimation of the pore radii within the packed bed is had. The characterised parameters are then compared to some examples of field conditions. Following this, the effect of flow rate and gravity on the oil recovery from the packed beds are discussed in terms of the capillary and bond numbers.

The work discussed in Chapter 4 starts with the characterisation of a system consisting of water, decane, calcite, and the anionic surfactant AOT with three different salt concentrations, in terms of the equilibrium microemulsion behaviour, aqueous phase behaviour, adsorption at the water-calcite interface, changes in the water-decane interfacial tension and the change in the three-phase contact angle as a function of AOT concentration. Following this characterisation, it is shown how the %oil recovery from the packed columns (from Chapter 3) varies with surfactant concentration. At this point, a model is derived to enable the determination of the concentration of surfactant that is left in the bulk of the water phase during a column flood after adsorption to the calcite-water interface has occurred. The model is then used to convert the initial concentrations of surfactant pumped in to the column to the concentration that is free (or non-adsorbed), which enables the oil recovery results to be related to the characterisation results. Finally, a second two-part model is derived to show how, based on the hypothesis that the residual oil is trapped in the form of liquid bridges between contacting calcite particles, the measured %oil recovery variation with surfactant concentration can be understood and predicted for concentrations of surfactant both below and above the  $c_{\mu c}$  in terms of the characterisation results.

With the aim of further testing the models derived in Chapter 4, Chapter 5 discusses the characterisation of and the oil recovery performance of two different systems, one with a cationic surfactant and one with a nonionic surfactant. The first system consists

of water, toluene, calcite and the pure cationic surfactant C14BDMAC. The second system consists of water, heptane, calcite and the un-pure commercial (technical grade) nonionic surfactant CW-100S. Most of the discussion within this chapter is aimed at understanding how the difference in behaviour of the surfactant leads to a difference in the oil recovery performance compared to the AOT containing system, and whether or not the models from Chapter 4 are still able to be used to model the oil recovery performance.

Chapter 6 summarises the conclusions from Chapters 3 to 5 and compares them with the aims of the study from this chapter. Following this, possible future work is discussed along with some preliminary experiments and results.

Appendix A briefly discusses the degradation kinetics of the anionic surfactant AOT in basic solutions. Appendix B contains the main equations involved in the liquid bridge calculations discussed in Chapter 4, and the CD attached to the cover of this thesis has the spreadsheet used for these calculations. Appendix C contains tables and graphs showing the fitting parameters used for the modelling of the interfacial tensions and the first model in Chapter 4. Appendix D briefly summarises the observations made from the pressure plots obtained from various column flood experiments, with representative examples of such pressure plots. Finally, Appendix E shows the BET graphs and XRD patterns for the three calcium carbonate samples used in this work.

## 1.7 References

1. Dawe, R.A. and Wall, C., An engineer's view of enhanced oil recovery. In *Enhanced Oil Recovery by Displacement with Saline Solutions*, Britannic House, London, 1977, p1.
2. Hesselink, F. Th., Effect of surfactant phase behaviour and interfacial activity on the recovery of capillary-trapped oil, In *Enhanced Oil Recovery by Displacement with Saline Solutions*, Britannic House, London, 1977, p11.
3. <http://www.2b1stconsulting.com/eor/> accessed 5th March 2015.
4. *World Energy Outlook 2012 Executive Summary*, International Energy Agency, Paris, 2012.
5. Sheng, J.J., *Modern Chemical Enhanced Oil Recovery: theory and practice*, 2011, Elsevier, Amsterdam.
6. Melrose, J.C. and Brandner, C.F., Role of capillary forces in determining microscopic displacement efficiency for oil recovery by waterflooding *J. Can. Pet. Technol.*, **1974**, 13, 54.
7. *US Pat.*, 1 651 311, **1927**.
8. Reed, R.L.; Healy, R.N. Some physicochemical aspects of microemulsion flooding: a review. In "Improved oil recovery by surfactant and polymer flooding", Eds. Shah, D.O.; Schechter, R.S., Academic Press, **1977**, pp. 383.
9. Taber, J.J. Research on enhanced oil recovery: past, present and future. *Pure & Appl. Chem.*, **1980**, 52, 1323.
10. Morrow, N.R.; Mason, G. Recovery of oil by spontaneous imbibitions. *Curr. Opin. Colloid Interface Sci.*, **2001**, 6, 321.
11. Babadagli, T. Evaluation of the critical parameters in oil recovery from fractured chalks by surfactant injection. *J. Petroleum Sci. Eng.*, **2006**, 54, 43.
12. Babadagli, T. Development of mature oil fields – a review. *J. Petroleum Sci. Eng.*, **2007**, 57, 221.
13. Jamaloei, B.Y. Insight into the chemistry of surfactant-based enhanced oil recovery processes. *Rec. Patents Chem. Eng.*, **2009**, 2, 1.

14. Nazar, M.F.; Shah, S.S.; Khosa, M.A. Microemulsions in enhanced oil recovery: a review. *Petroleum Sci. Technol.*, **2011**, *29*, 1353.
15. Soll, W.M.; al Shureqi, H.; Finol, J.; Al-Harthy, S.A.A.; Oyemade, S.; de Kruijf, A.; van Wunnik, J.; Arkesteijn, F.; Bouwmeester, R.; Faber, M.J. Alkaline/surfactant/polymer flood: from the laboratory to the field. *Soc. Petroleum Eng. J.*, **2011**, *14*, 702.
16. Hirasaki, G.J.; Miller, C.A.; Puerto, M. Recent advances in surfactant EOR. *Soc. Petroleum Eng. J.*, **2011**, *16*, 889.
17. Lu, J.; Liyanage, P.J.; Solairaj, S.; Adkins, S.; Arachchilage, G.P.; Kim, D.H.; Britton, C.; Weerasooriya, U.; Pope, G.A. Recent technology developments in chemical enhanced oil recovery. *Int Petroleum Technol. Conf.*, **2013**, paper IPTC 16425, 1.
18. Jeirani, Z.; Mohamed Jan, B.; Si Ali, B.; See, C.H.; Saphanuchart, W. Pre-prepared microemulsion flooding in enhanced oil recovery: a review. *Petroleum Sci. Technol.*, **2014**, *32*, 180.
19. Jeirani, Z.; Mohamed Jan, B.; Si Ali, B.; See, C.H.; Saphanuchart, W. In situ prepared microemulsion-polymer flooding in enhanced oil recovery: a review. *Petroleum Sci. Technol.*, **2014**, *32*, 240.
20. Sheng, J.L. A comprehensive review of alkaline-surfactant-polymer (ASP) flooding. *Asia-Pac. J. Chem. Eng.*, **2014**, *9*, 471.
21. Bi, Z.; Zhang, Z.; Xu, F.; Qian, Y.; Yu, J. Wettability, oil recovery and interfacial tension with an SDBS-dodecane-kaolin system. *J. Colloid Interface Sci.*, **1999**, *214*, 368.
22. Babadagli, T.; Boluk, Y. Oil recovery performances of surfactant solutions by capillary imbibitions. *J. Colloid Interface Sci.*, **2005**, *282*, 162.
23. Puerto, M.; Hirasaki, G.J.; Miller, C.A.; Barnes, J.R. Surfactant systems for EOR in high-temperature, high-salinity environments. *Soc. Petroleum Eng. J.*, **2012**, *17*, 11.

24. Al-Sulaimani, H.; Al-Wahaibi, Y.; Al-Bahry, S.; Elshafie, A.; Al-Benani, A. Residual-oil recovery through injection of biosurfactant, chemical surfactant and mixtures of both under reservoir temperatures: induced-wettability and interfacial-tension effects. *SPE Reservoir Eval. Eng.*, **2012**, *15*, 210.
25. Var, A.Z.; Bastani, D.; Badakhshan, The impact of surfactants on wettability change and level of water imbibitions in relation to EOR in carbonate reservoirs. *Petroleum Sci. Technol.*, **2013**, *31*, 2098.
26. Standnes, D.C.; Austad, T. Wettability alteration in chalk. 2. Mechanism for wettability alteration from oil-wet to water-wet using surfactants. *J. Petroleum Sci. Eng.*, **2000**, *28*, 123.
27. Standnes, D.C.; Austad, T. Wettability alteration in carbonates. Interaction between cationic surfactant and carboxylates as a key factor in wettability alteration from oil-wet to water-wet conditions., *Colloids Surfaces A*, **2003**, *216*, 243.
28. Standnes, D.C., Austad, T., Wettability alteration in carbonates. Low -cost ammonium surfactants based on bio-derivatives from the coconut palm as active chemical to change the wettability from oil-wet to water-wet conditions, *Colloids Surfaces A*, **2003**, *218*, 161.
29. Milner, J. Austad, T. Chemical flooding of oil reservoirs. 6. Evaluation of the mechanism for oil expulsion by spontaneous imbibitions of brine with and without surfactant in water-wet, low-permeable, chalk material. *Colloids & Surfaces A*, **1996**, *113*, 269.
30. Austad, T., Matre, B., Milner, J, Sævareid, A., Øyno, L., Chemical flooding of oil reservoirs 8. Spontaneous oil expulsion from oil- and water-wet low permeable chalk material by imbibition of aqueous surfactant solutions, *Colloids Surfaces A*, **1998**, *137*, 117.
31. Buckley, J.S., Effective wettability of minerals exposed to crude oil, *Curr. Opin. Colloid Interface Sci.*, **2001**, *6*, 191.

32. Wu, Y.; Shuler, P.J.; Blanco, M.; Tang, Y.; Goddard, W.A. An experimental study of wetting behaviour and surfactant EOR in carbonates with model compounds. *Soc. Petroleum Eng. J.*, **2008**, March, 262000.
33. Yefei, W.; Huaimin, X.; Weizhao, Y.; Baojun, B.; Xinwang, S.; Jichao, Z. Surfactant induced reservoir wettability alteration: recent theoretical and experimental advances in enhanced oil recovery. *Petroleum Sci.*, **2011**, 8, 463-476.
34. Jarrahian, Kh.; Seiedi, O.; Sheykhani, M.; Sefti, M.V.; Ayatollahi, Sh. Wettability alteration of carbonate rocks by surfactant: a mechanistic study. *Colloids Surfaces A*, **2012**, 410, 1-10.
35. Rashidi, M.; Peurrung, L.; Tompson, A.F.B.; Kulp, T.J. Experimental analysis of pore-scale flow and transport in porous media. *Adv. Water Resources*, **1996**, 19, 163-180.
36. Stohr, M.; Roth, K.; Jahne, B. Measurement of 3D pore-scale flow in index-matched porous media. *Exp. Fluids*, **2003**, 35, 159-166.
37. Cheng, L-C.; Chen, H-H.; Shan, H-Y.; Tsai, J-P. Effect of connectivity and wettability on the relative permeability of NAPLs. *Environ. Geol.*, **2009**, 56, 1437-1447.
38. Jamaloei, B.Y.; Asghari, K.; Kharrat, R.; Ahmadloo, F. Pore-scale two-phase filtration in imbibitions process through porous media at high- and low-interfacial tension flow conditions. *J. Petroleum Sci. Eng.*, **2010**, 72, 251-269.
39. Jamaloei, B.Y.; Asghari, K.; Kharrat, R. Pore-scale flow characterization of low-interfacial tension flow through mixed-wet porous media with different pore geometries. *Exp. Thermal Fluid Sci.*, **2011**, 35, 253-264.
40. Gunda, N.S.K.; Bera, B.; Karadimitriou, N.K.; Mitra, S.K.; Hassanizadeh, S.M. Reservoir-on-a-chip (ROC): a new paradigm in reservoir engineering. *Lab Chip*, **2011**, 11, 3785-3792.
41. Jamaloei, B.Y.; Kharrat, R. Pore-scale description of surfactant-enhanced waterflooding for heavy oil recovery. *J. Petroleum Sci. Eng.*, **2012**, 92-93, 89-101.

42. Mitchell, J.; Staniland, J.; Chassagne, R.; Fordham, E.J. Quantitative in situ enhanced oil recovery monitoring using nuclear magnetic resonance. *Transp. Porous Media*, **2012**, *94*, 683-706.
43. Karadimitriou, N.K.; Hassanizadeh, S.M. A review of micromodels and their use in two-phase flow studies. *Vadose Zone J.*, **2012**, *11*, DOI: 10.2136/vzj2011.0072
44. Dong, M.; Liu, Q.; Li, A. Displacement mechanisms of enhanced heavy oil recovery by alkaline flooding in a micromodel. *Particuology*, **2012**, *10*, 298-305.
45. Ma, K., Lontas, R., Conn, C.A., Hirasaki, G.J., Biswal, S.L., Visualization of improved sweep with foam in heterogeneous porous media using microfluidics, *Soft Matter*, **2012**, *8*, 10669.
46. Mohammadi, S.; Ghazanfari, M.H.; Masihi, M. A pore-level screening study on miscible/immiscible displacements in heterogeneous models. *J. Petroleum Sci. Eng.*, **2013**, *110*, 40-54.
47. Chen, L.; Zhang, G.; Ge, J.; Jiang, P.; Tang, J.; Liu, Y. Research of the heavy oil displacement mechanism by using alkaline/surfactant flooding system. *Colloids Surfaces A*, **2013**, *434*, 63-71.
48. Krummel, A.T.; Datta, S.S.; Munst, S.; Weitz, D.A. Visualizing multiphase flow and trapped fluid configurations in a model three-dimensional porous medium. *AIChE J.*, **2013**, *59*, 1022-1029.
49. Datta, S.S.; Ramakrishnan, T.S.; Weitz, D.A. Mobilization of trapped non-wetting fluid from a three-dimensional porous medium. *Phys. Fluids*, **2014**, *26*, 022002-1- 13.
50. Conn, C.A., Ma, K., Hirasaki, G.J., Biswal, S.L., Visualizing oil displacement with foam in a microfluidic device with permeability contrast, *Lab Chip*, **2014**, *14*, 3968.
51. Zhang, J.Y., Nguyen, Q.P., Flaaten, A.K., Pope, G.A., Mechanisms of Enhanced Natural Imbibition With Novel Chemicals, *SPE Reservoir Eval. Eng.*, **2009**, *12*, 912.
52. Lenormand, R., Liquids in porous media, *J. Phys. Condens. Matter*, **1990**, *2*, SA79.

53. Buckley, S.E.; Leverett, M.C. Mechanism of fluid displacement in sands. *Trans. Amer. Inst. Mining & Metallurg. Eng.*, **1942**, *146*, 107-116.
54. Warren, J.E.; Calhoun, J.C. A study of waterflood efficiency in oil-wet systems. *Petroleum Trans.*, **1955**, *204*, 22.
55. Chatzis, I.; Morrow, N.R., Correlation of capillary number relationships for sandstone. *Soc. Petroleum Eng. J.*, **1984**, *24*, 555-562.
56. Huang, D.D.; Honarpour, M.M. Capillary end effects in coreflood calculations. *J. Petroleum Sci. Eng.*, **1998**, *19*, 103-117.
57. Rose, W. Modeling forced versus spontaneous capillary imbibitions processes commonly occurring in porous sediments. *J. Petroleum Sci. Eng.*, **2001**, *30*, 155-166.
58. Valvatne, P.H.; Blunt, M.J. Predictive pore-scale modelling of two-phase flow in mixed wet media. *Water Resour. Res.*, **2004**, *40*, WO7406, 1-21.
59. Hammond, P.S. Unsal, E. Spontaneous and forced imbibition of aqueous wettability altering surfactant solution in an initially oil-wet capillary. *Langmuir*, **2009**, *25*, 12591-12603.
60. Hammond, P.S. Unsal, E. Forced and spontaneous imbibitions of surfactant solution in an oil-wet capillary: the effects of surfactant diffusion ahead of the advancing meniscus. *Langmuir*, **2010**, *26*, 6206-6221.
61. Zhao, X.; Blunt, M.J.; Yao, J. Pore-scale modeling: effects of wettability on waterflood oil recovery. *J. Petrol. Sci. Eng.*, **2010**, *71*, 169-178.
62. Hammond, P.S. Unsal, E. Spontaneous imbibition of surfactant solution in an oil-wet capillary: wettability restoration by surfactant-contaminant complexation. *Langmuir*, **2011**, *27*, 4412-4429.
63. Stukan, M.R.; Ligneul, P.; Boek, E.S. Molecular dynamics simulation of spontaneous imbibitions in nanopores and recovery of asphaltenic crude oils using surfactants for EOR applications. *Oil & Gas Sci. Technol.*, **2012**, *67*, 737-742.

64. Hammond, P.S. Unsal, E. A dynamic pore network model for oil displacement by wettability-altering surfactant solution. *Transp. Porous Med.*, **2012**, *92*, 789-817.
65. Schmid, K.S.; Geiger, S. Universal scaling of spontaneous imbibitions for arbitrary petrophysical properties: water-wet and mixed-wet states and Handy's conjecture. *J. Petroleum Sci. Eng.*, **2013**, *101*, 44-61.
66. Sheng, J.L. Comparison of the effects of wettability alteration and IFT reduction on oil recovery in carbonate reservoirs. *Asia-Pacific J. Chem. Eng.*, **2013**, *8*, 154-161.
67. Blunt, M.J.; Bijeljic, B.; Dong, H.; Gharbi, O.; Iglauer, S.; Mostaghimi, P.; Paluszny, A.; Pentland, C. Pore-scale imaging and modelling. *Adv. Water Res.*, **2013**, *51*, 197-216.
68. Ott, H., de Kloe, K., van Bakel, M., Vos, F., van Pelt, A., Legerstee, P., Bauer, A., Eide, K., van der Linden, A., Berg, S., Makurat, A., Core-flood experiment for transport of reactive fluids in rocks, *Rev. Sci. Instrum.*, **2012**, *83*, 084501.
69. Sahimi, M., Flow phenomena in rocks: from continuum to fractals, percolation, cellular automata, and simulated annealing, *Rev. Mod. Phys.*, **1993**, *65*, 1393.
70. Çarpınlioğlu, M.Ö., Özahi, E. and Gündoğdu, M.Y., Determination of laminar and turbulent flow ranges through vertical packed beds in terms of particle friction factors, *Adv. Powder Technol.*, **2009**, *20*, 515.
71. Grattoni, C.A., Jing, X.D., Dawe, R.A., Dimensionless groups for three-phase gravity drainage flow in porous media, *J. Pet. Sci. Eng.*, **2000**, *29*, 53.
72. Løvoll, G., Méheust, Y., Måløy, K.J., Aker, E., Schmittbuhl, J., Competition of gravity, capillary and viscous forces during drainage in a two-dimensional porous medium, a pore scale study, *Energy*, **2005**, *30*, 861.
73. Abrams, A., The influence of fluid viscosity, interfacial tension, and flow velocity on residual oil saturation left by waterflood, *SPE. J.*, **1975**, *15*, 437.
74. Chatzis, I., Morrow, N.R., Correlation of capillary number relationships for sandstone, *SPE. J.*, **1984**, *24*, 555.

75. Adibhatla, B., Mohanty, K.K., Oil recovery from fractured carbonates by surfactant-aided gravity drainage: laboratory experiments and mechanistic simulations, *SPE Reservoir Eval. Eng.*, **2008**, *11*, 119.
76. Austad, T., Milner, J., Spontaneous imbibition of water into low permeable chalk at different wettabilities using surfactants. International Symposium on Oilfield Chemistry, Houston, 18<sup>th</sup>-21<sup>st</sup> February 1997, SPE, 1997, 257.
77. *Oxford dictionary of science*, Daintith, J. and Martin, E., Eds.; Oxford University Press, Oxford, 2010.
78. van Oss, C.J. *Interfacial forces in aqueous media*, New York: Marcel Dekker, **1994**.
79. Fainerman, V.B., Möbius, D. and Miller, R. (eds.), *Surfactants: Chemistry, Interfacial Properties, Applications*, Elsevier, Amsterdam, **2001**.
80. Barnes, G.T., Gentle, I.R., *Interfacial science: an introduction*, Second edition, Oxford University Press, New York, **2011**.
81. Mitchell, J. and Ninham, B.W., Micelles, vesicles and microemulsions, *J. Chem. Soc. Faraday Trans. 2*, **1981**, *77*, 601.
82. Griffin, W.C., Classification of surface-active agents by “HLB”, *J. Soc. Cosmet. Chem.*, **1949**, *1*, 311.
83. Young, D. M., and Crowell, A.D., *Physical Adsorption of Gases*, First Edition, Butterworth & Co. Ltd., London, **1962**.
84. Qi, L.Q., Liu, Z.Z., Yang, C.Z., Yin, Y.J., Hou, J.R., Zhang, J., Huang, B., Shi, F.G., Supplement and optimization of classical capillary number experimental curve for enhanced oil recovery by combination flooding, *Sci. China-Technological Sci.*, **2014**, *57*, 2190.
85. AlSofi, A.M., Liu, J.S., Han, M., Aramco, S., Numerical simulation of surfactant-polymer coreflooding experiments for carbonates, *J. Pet. Sci. Eng.*, **2013**, *111*, 184.

86. Zerpa, L.E., Queipo, N.V., Pintos, S., Salager, J.L., An optimization methodology of alkaline-surfactant-polymer flooding processes using field scale numerical simulation and multiple surrogates, *J. Pet. Sci. Eng.*, **2005**, *47*, 197.
87. Gogoi, S.B., Adsorption-desorption of surfactant for enhanced oil recovery, *Transp. Porous Med.*, **2011**, *90*, 589.
88. Liu, Q., Dong, M., Zhou, W., Ayub, M., Zhang, Y.P., Huang, S., Improved oil recovery by adsorption-desorption in chemical flooding, *J. Pet. Sci. Eng.*, **2004**, *43*, 75.
89. Curbelo, F.D.S., Garnica, A.I.C., Neto, E.L.B., Enhanced oil recovery and adsorption of ionic surfactant, *J. Pet. Sci. Technol.*, **2013**, *31*, 663.
90. Rose, W., Myths about later-day extensions of Darcy's law, *J. Pet. Sci. Eng.*, **2000**, *26*, 187.
91. Rose, W., Rose, D.M., "Revisiting" the enduring Buckley–Leverett ideas, *J. Pet. Sci. Eng.*, **2004**, *45*, 263.
92. Wammes, W.J.A.; Mechielsen, S.J.; Westerterp, K.R. The influence of pressure on the liquid hold-up in a concurrent gas-liquid trickle-bed reactor operating at low gas velocities. *Chem. Eng. Sci.*, **1991**, *46*, 409.
93. van der Merwe, W.; Maree, C.; Nicol, W. Nature of residual liquid holdup in packed beds of spherical particles. *Ind. Eng. Chem. Res.*, **2004**, *43*, 8363.
94. Zeinal Heris, S.; Hamad Mosavian, M.T.; White, E.T. Capillary holdup between vertical spheres. *Brazilian J. Chem. Eng.*, **2009**, *26*, 695.
95. Schwidder, S.; Schnitzlein, K. Predicting the static liquid holdup for cylindrical packings of spheres in terms of the local structure of the packed bed. *Chem. Eng. Sci.*, **2010**, *65*, 6181.
96. Haines, W.B. Studies in the physical properties of soils. II A note on the cohesion developed by capillary forces in an ideal soil. *J. Agric. Sci.*, **1925**, *15*, 529.
97. Fisher, R.A. On the capillary forces in an ideal soil; correction of formulae given by W.B. Haines. *J. Agric. Sci.*, **1926**, *16*, 492.

98. Kralchevsky, P.A.; Nagayama, K. Capillary bridges and capillary-bridge forces. In “Particles at fluid interfaces and membranes”, Elsevier, Amsterdam, **2001**, chap. 11, pp. 469.

## CHAPTER 2

### EXPERIMENTAL

#### 2.1 Materials

##### 2.1.1 Water

Water for washing and making up solutions was purified by passing through an Elgastat Prima reverse osmosis unit followed by a Millipore Milli-Q reagent water system with one carbon filter and two ion-exchange filters fitted. The water consistently had a resistivity of  $\sim 16 \text{ M}\Omega \text{ cm}^{-1}$  at  $25 \text{ }^\circ\text{C}$  and a surface tension of  $71.9 \text{ mN m}^{-1}$  (determined using the du Noüy ring method), in good agreement with the value given in literature<sup>1</sup>.

##### 2.1.2 Oils

The oils were selected for each surfactant system so that microemulsion phase inversion could be achieved using NaCl as the inversion parameter at  $25 \text{ }^\circ\text{C}$ . The three oils used were, n-decane (Sigma, 99% pure or TCI, 99% pure), n-heptane (Fisher, 99% pure) and toluene (Fisher, Analytical reagent grade). The measured interfacial tensions between Milli-Q water and all three un-purified oils (table 2.1) were within approximately 3% of the values calculated from the literature values of the polar and dispersive surface energy components (see Chapter 4, section 4.3.4 and Chapter 5 sections 5.2.5 and 5.3.4). Purification of the oils by passing over a column of basic alumina was found to not have a noticeable effect on the interfacial tensions, contact angles or the column flood experiments within the experimental errors. As purification of the oils did not significantly affect the key results, the majority of experiments were carried out with the oils as received.

**Table 2.1** Comparison between the measured water-oil interfacial tensions and the values calculated from the literature values of the polar and dispersive surface energy components (see Chapter 4, section 4.3.4).

<b>Oil</b>	<b>Measured pure water-un-purified oil interfacial tension / mN m-1</b>	<b>Calculated pure water-oil interfacial tension / mN m-1</b>	<b>%difference compared to calculated value</b>
n-decane	49.2	50.5	2.6
n-heptane	48.8	50.5	3.4
toluene	30.5	31.4	2.9

### 2.1.3 Surfactants

The anionic surfactant sodium bis-2-ethyhexyl sulfosuccinate (AOT) was obtained from Sigma Aldrich as 98% pure and was used as received. Solutions of AOT in water were used within a couple of weeks of preparation, but those in aqueous sodium carbonate solutions were used within 2 days. This is due to the degradation of AOT in the presence OH<sup>-</sup> ions, and the presence of sodium carbonate raising the natural pH of the solutions from ~9 in solutions of AOT in pure water to ~10.8 in solutions of AOT in water containing 10 mM of sodium carbonate (thus speeding up degradation). The kinetics of AOT degradation is discussed in more detail in Appendix A. All measurements with AOT were made at 25 °C and pH of 10.8, unless otherwise stated. To ensure that the effect of degradation was accounted for, selected measurements were carried out at pH 9.3 ± 0.3 to ensure there was no significant difference.

The cationic surfactant benzyldimethyltetradecylammonium chloride (C14BDMAC) was purchased from Fluka Analytical as > 99 % pure and was used as received.

The non-ionic surfactant was obtained from Pilot Chemical Company under the trade name Calamide CW-100. It was supplied as a mixture of the surfactant bis-2-hydroxyethyl acetamide with an alkyl chain attached to the R group seen in Table 2.2 and diethanolamine (DEA) in an approximate mass ratio of 8:2 respectively (mole ratio approx. 1.3:1). Due to the chain length distributions of the surfactant component<sup>2</sup>, a molecular mass of the surfactant with a C<sub>13</sub> chain length was used to enable calculation

of the approximate surfactant concentration in terms of mM instead of weight percent. All further calculations and discussions (other than in section 2.2.1.2) consider only the surfactant component (80 wt.%) and disregard the DEA component, and will be referred to as CW-100S (when the overall mixture is being referred to it will be named CW-100). This enables better comparisons between the behaviour of this surfactant, the AOT and the C14BDMAC. The CW-100 was used as supplied, so the surfactant was always part of a mixture with DEA.

The structures of all three surfactants are shown in table 2.2.

**Table 2.2** The structures of the three surfactants used throughout this work.

Surfactant	Structure
AOT	
C14BDMAC ( $R_2 = n\text{-C}_{14}\text{H}_{30}$ )	
CW-100  ( $R_1 = \text{mainly } n\text{-C}_{12}\text{H}_{26} - n\text{-C}_{14}\text{H}_{30}$ )  Top: surfactant component (CW-100S)  Bottom: diethanolamine (DEA)	

#### 2.1.4 Calcium carbonate powders and calcite crystals

Three calcium carbonate powders of different mean particle sizes were obtained from Minelco UK. The powders are part of their FordaCal product range, which consists of natural ground calcium carbonate particles of different particle size distributions. Figure 2.1 shows the sieve analysis size-distribution data provided by Minelco, Figure 2.2 the SEM images of the three powders and Table 2.3 gives the average particle sizes from the SEM images and sieve analysis data and the specific surface areas, porosities and average pore diameters obtained from BET analysis of nitrogen adsorption isotherms.

**Figure 2.1** Cumulative size distributions for the calcium carbonate powders obtained from sieve analysis (Manufacturer's information) and SEM images. The vertical solid lines indicate the mean particle sizes corresponding to the averages of the sieve aperture size at 50% of the cumulative distributions and the mean sizes estimated from analysis of the SEM images.

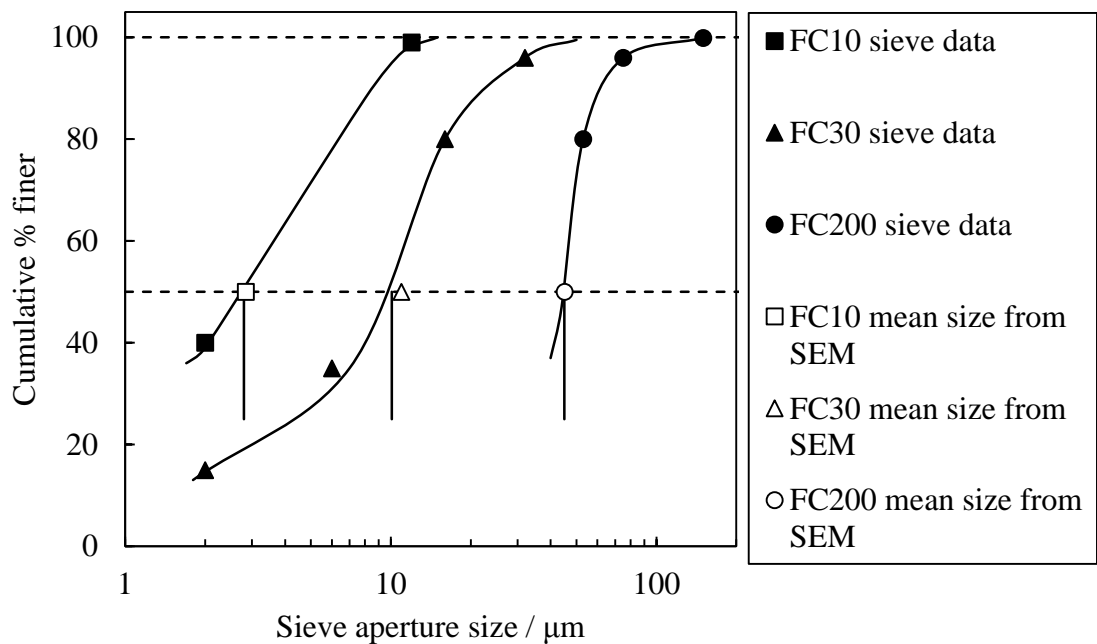


**Figure 2.2** SEM images of the three calcium carbonate powders used here: FC10 (top), FC30 (middle) and FC200 (bottom). The scale bar represents a length of 20  $\mu\text{m}$ .

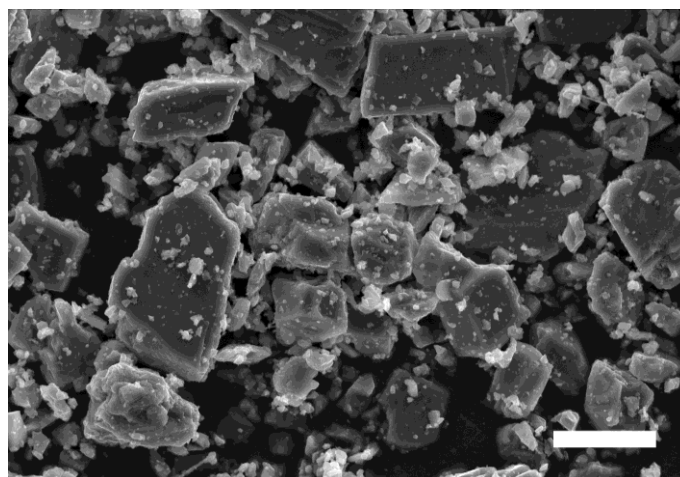
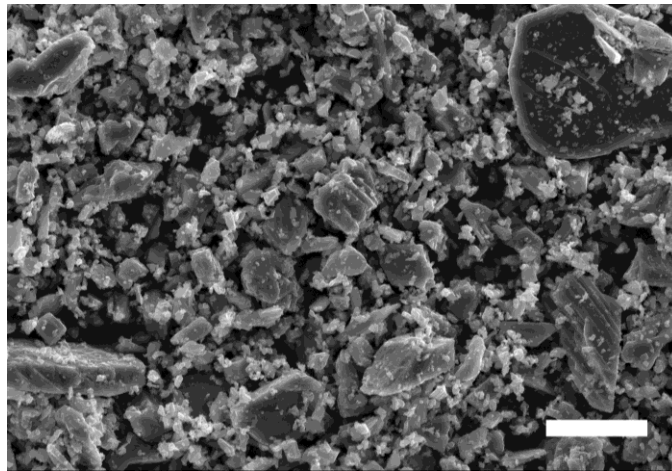
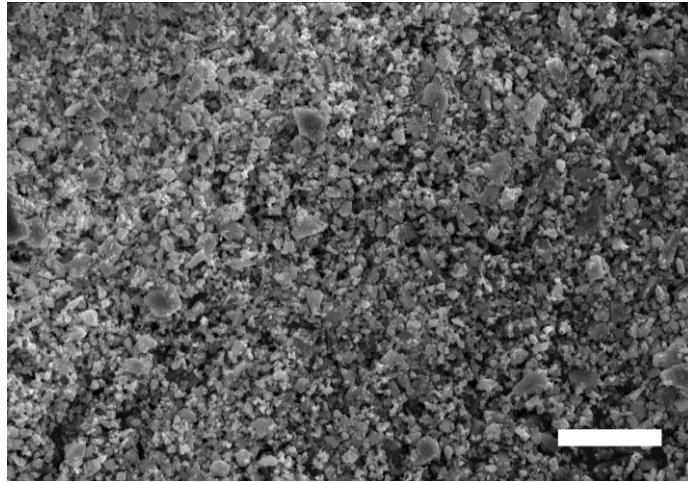


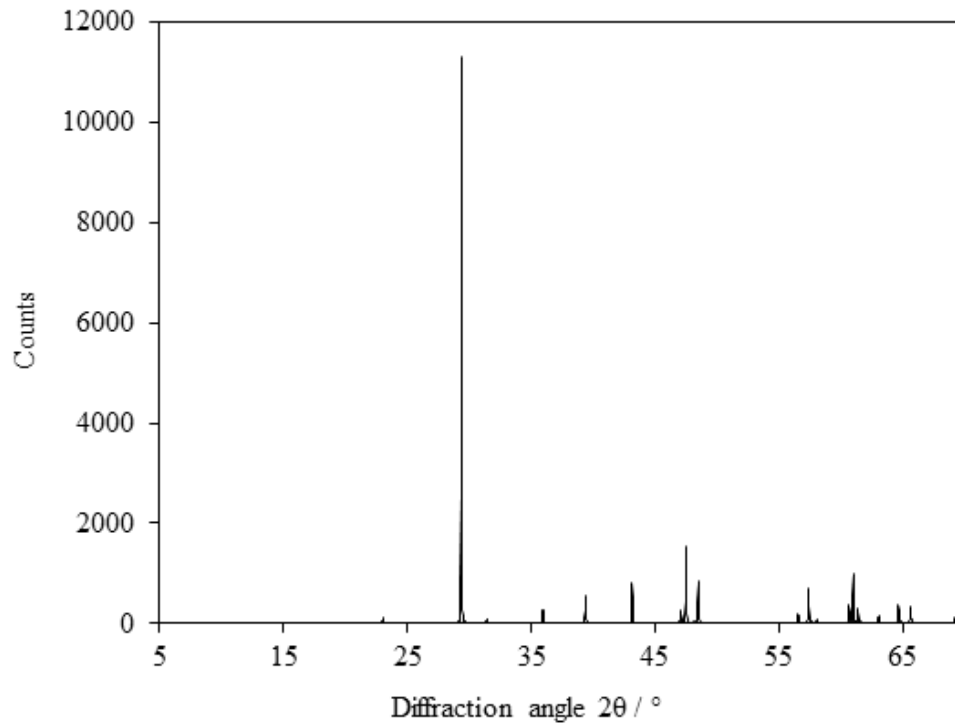
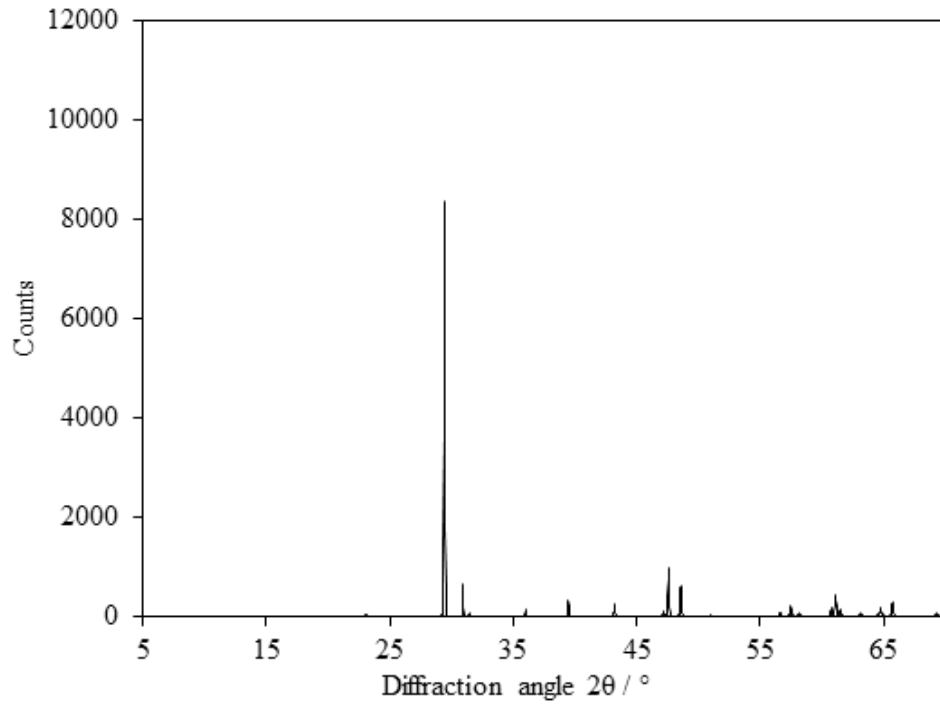
**Table 2.3** Properties of the calcium carbonate powders used. The average particle radii correspond to the average of the radii at 50% of the cumulative distribution from sieving analysis and the mean radii derived from SEM images.

<b>Powder</b>	<b>Average particle radius / <math>\mu\text{m}</math></b>	<b>BET specific surface area / <math>\text{m}^2 \text{g}^{-1}</math></b>	<b>Powder particle internal pore volume fraction</b>	<b>Powder particle internal pore radius/nm</b>
FC10	1.4	8.6	0.08	110
FC30	5.0	10	0.04	49
FC200	23	19	0.05	26

The SEM images show the particles are irregularly-shaped and polydisperse. X-ray diffraction (XRD) measurements confirmed that the powders all consist virtually exclusively of the calcite polymorph of calcium carbonate (Figure 2.3). The X-ray diffraction pattern was compared to the literature using the instruments software and found to have a 99% match to a sample in the Panalytical HighScore database. The nitrogen adsorption/desorption isotherms (which can be seen in Appendix E) showed no significant hysteresis in the case of FC10 but significant hysteresis was observed for FC30 and FC200. The total specific surface areas measured using BET are 10-400 fold larger than those estimated for monodisperse, non-porous spheres of the corresponding mean particle size ( $0.8 \text{ m}^2 \text{g}^{-1}$  for FC10,  $0.2 \text{ m}^2 \text{g}^{-1}$  for FC30 and  $0.05 \text{ m}^2 \text{g}^{-1}$  for FC200) and hence are dominated by internal (or micro) porosity of the particles. As seen in Table 2.3, the particles have an internal pore volume fractions from 0.08 to 0.04 with average internal pore diameters from 110 to 26 nm.

Calcite crystals for contact-angle measurements were obtained from John Brommeland ([www.brommeland.com](http://www.brommeland.com)) in Norway. They were cut to size (9 x 9 x 5 mm) and the top surface was polished using abrasive paper with a particle size of 4.5 microns. One of the crystals was ground up in a pestle and mortar and the x-ray diffraction pattern determined and compared to that of the pre-ground calcium carbonate obtained from Minelco and were found to match with reasonable accuracy (Figure 2.3).

**Figure 2.3** Powder XRD pattern for the FC200 calcium carbonate (top) and the ground up calcite crystal (bottom). The complete set of patterns for all the Fordacal samples can be seen in Appendix E.



### 2.1.5 Other materials

Other materials used with source and purity and what they were used for are shown in Table 2.4.

**Table 2.4** Other materials used throughout the work in this thesis.

<b>Material</b>	<b>Use</b>	<b>Source and purity</b>
Sodium Chloride (NaCl)	In surfactant solutions to cause different Winsor system behaviours	Fisher, 99 %
Sodium Carbonate (Na <sub>2</sub> CO <sub>3</sub> )	In surfactant solutions to help buffer the pH	Fisher, 99 %
Hyamine 1622	Cationic titrant in Epton titration for determining AOT concentration	Fluka, 98 %
Dimidium bromide	Cationic dye in Epton titration	Sigma Aldrich, 95 %
Disulfine blue	Anionic dye in Epton titration	Sigma Aldrich, 50 % dye content
Chloroform	Epton titration	Fisher, analytical reagent grade
Ethanol	Washing of glassware	VWR Chemicals, 99 %
Acetone	Washing of glassware and columns	Fisher Scientific, 99.97 %
Hydrochloric acid (HCl) aqueous solution	Reducing solution pH	Fisher Scientific UK, ~ 37 wt.% HCl in water
Sodium hydroxide (NaOH)	Increasing solution pH	Fisher Scientific UK, ~ 99 %

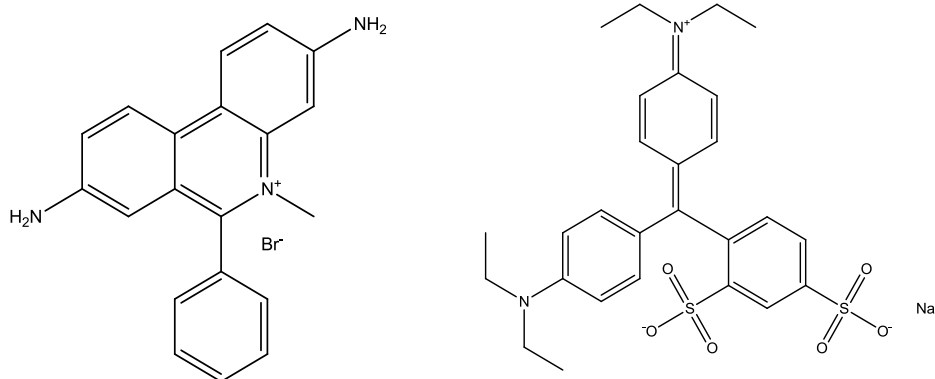
## 2.2 Methods

### 2.2.1 Determination of surfactant concentrations

#### 2.2.1.1 Epton titration

For both the AOT (anionic) and the C14BDMAC (cationic) surfactants, the concentrations were determined using the two-phase Epton titration as described by Reid et al<sup>3</sup>. The theory of how the titration works is as follows. Initially, water and chloroform are added to an appropriate vessel followed by an acidified aqueous solution of two dyes, dimidium bromide (cationic) and disulfine blue (anionic), the structures of which are shown in Figure 2.4.

**Figure 2.4** Structures of dimidium bromide (left) and disulfine blue (right).



When, for example, an aliquot of an anionic surfactant solution is added as the titrand to the vessel, it forms a complex with the cationic dye (dimidium bromide) which partitions in to the chloroform layer to give a pink colour. To aid the partitioning of the complex to the chloroform, vigorous shaking is needed to increase the water-chloroform surface area. As the cationic surfactant titrant is added from the burette a colourless complex is formed with the anionic surfactant which resides in the chloroform layer, whilst the cationic dye partitions back to the water layer. At the point of excess, the cationic surfactant titrant forms a complex with the anionic dye which subsequently partitions in to the chloroform layer giving a blue colour. Thus, the chloroform layer changes from pink to colourless to blue. The titre value is taken to be the point at which the chloroform turns blue minus the value of the blank titration (the amount of the cationic surfactant titrant it takes to see a blue colour without the anionic surfactant titrand present). The titration can be carried out in the reverse direction if the titrand is

required to be a cationic surfactant, in this case the colour change would be from blue-pink. Reid *et al.* claim that this method provides much greater clarity of the end point than any of the similar titrations which use only dye.

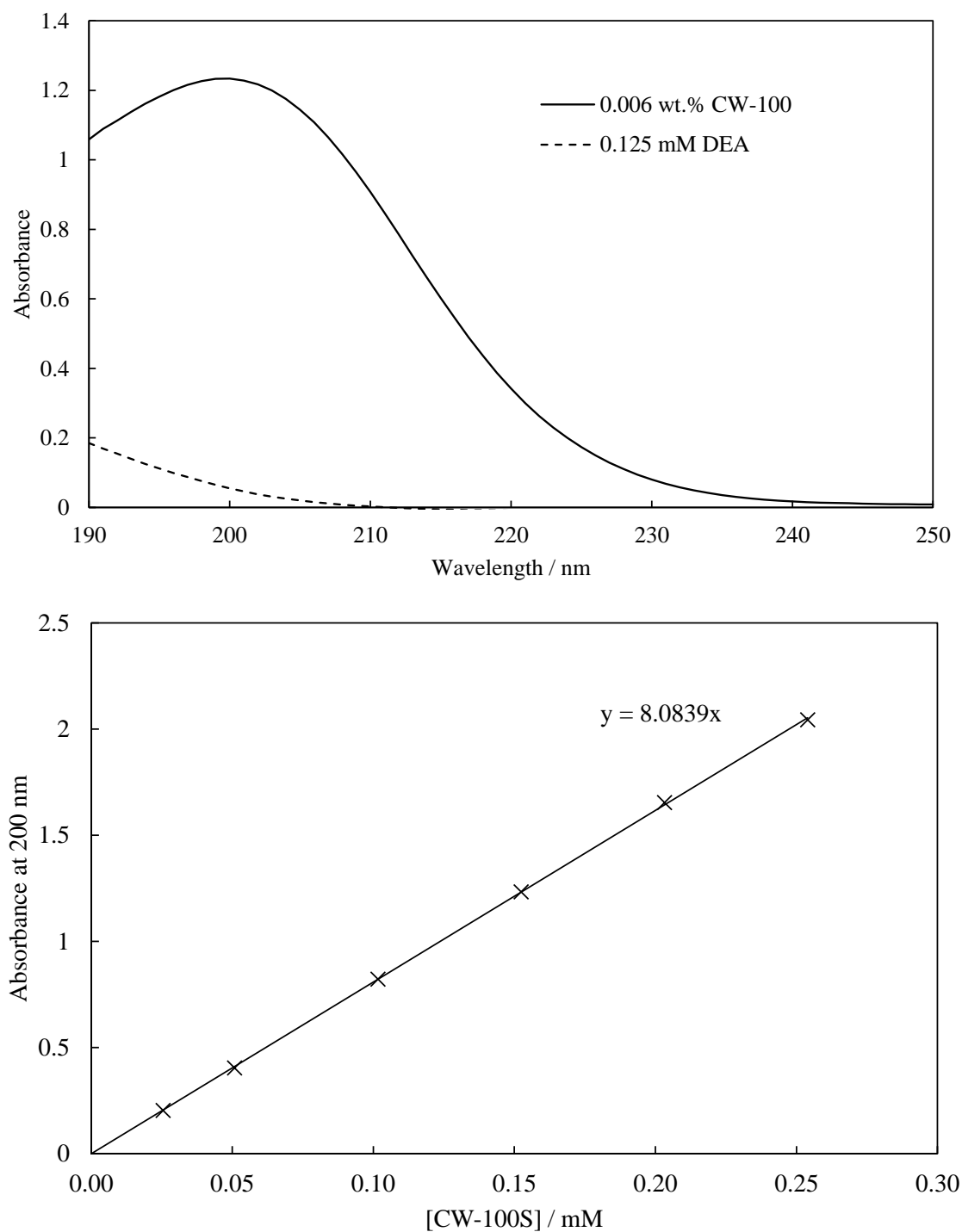
In this work, 10 ml of water, 15 ml chloroform and 2.5 ml of the acidified indicator solution are used. Due to excessive emulsion build up during shaking, samples with an initial surfactant concentration of  $> \sim 10$  mM were first diluted by a factor of 10 prior to analysis. At surfactant concentrations  $< 1$  mM solutions were placed in a viewing cabinet with a white light to determine more precisely the point of change from pale pink to clear. Titrations were carried out without any titrand present to determine the blank volume for each surfactant concentration (the volume of the titrant required to give a visible colour change with the dye), and this value subsequently subtracted from the corresponding titration values.

#### 2.2.1.2. *UV-visible spectrophotometry*

The non-ionic surfactant used (CW-100S) cannot be analysed using the Epton titration as this method relies on a surfactant with a charged head group forming a complex with the oppositely charged dye and partitioning to the chloroform layer. Hence, a different technique was required to analyse the concentration of surfactant present. The UV-visible spectrum of the CW-100 mixture in aqueous solutions showed that there was an absorbance maximum ( $\lambda_{\text{max}}$ ) at approximately 200 nm (Figure 2.5, top). In Figure 2.5 (top) the concentration is shown as the wt.% CW-100, the mixture 80 wt.% surfactant (CW-100S) and 20 wt.% DEA. The spectrum of pure DEA at the concentration expected to be present in the CW-100 mixture is also shown. The absorption at 200 nm by DEA is  $\leq 5$  % of that from the CW-100 mixture, and hence the adsorbance of the mixture is dominated by the surfactant component. Thus, the calibration plot (Figure 2.5, bottom) can be used to determine the concentration of the surfactant component, CW-100S in the CW-100 mixture. The same process was used for this surfactant in heptane solutions.

Throughout the following work the spectrometer used was a Perkin Elmer Lambda 25. It was configured so that the absorbance of the cuvette and the aqueous phase without surfactant present was subtracted from the overall spectrum, thus the absorbance seen should purely be due to the surfactant present.

**Figure 2.5** Upper plot: Absorbance spectrum of a solution of 0.006 wt.% CW-100 (the mixture, approx. 0.15 mM surfactant component, 0.11 mM DEA) in water and 0.125 mM pure DEA in water, both in a 10 mm path length cuvette. Lower plot: UV absorbance calibration plot for different concentrations of CW-100S in water (wt.% of mixture converted to mM of the surfactant component) in a 10 mm path length cuvette at 200 nm. The background water spectrum has been subtracted.

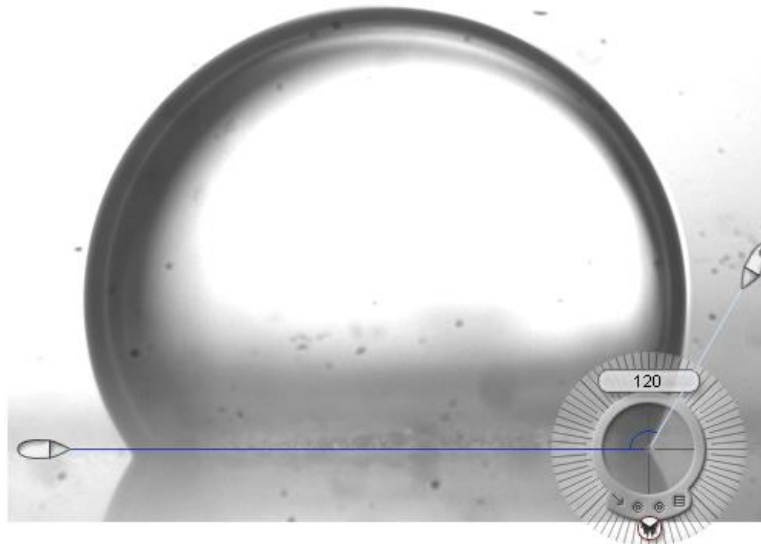
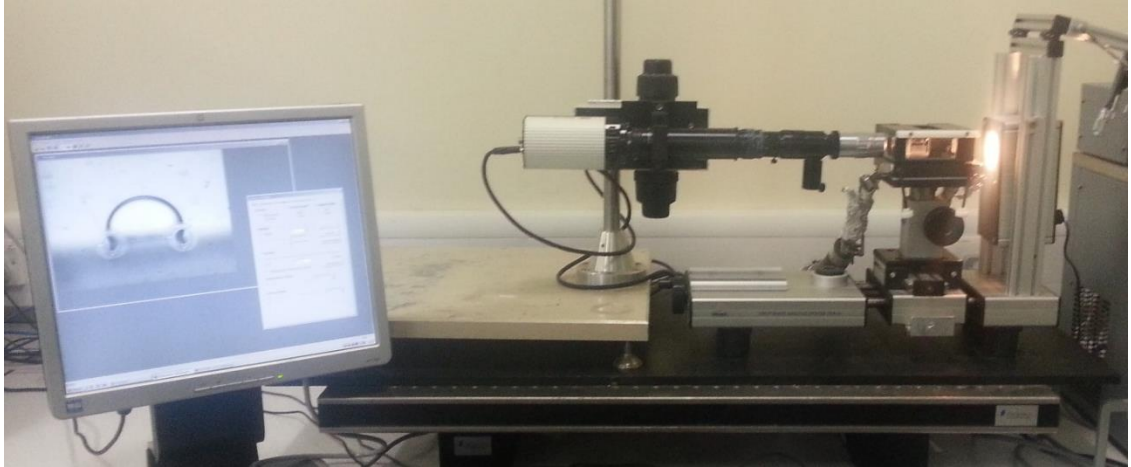


### 2.2.2 Water-oil-calcite contact angles

Contact angles (static, advanced),  $\theta$ , of drops of aqueous solutions on calcite crystals under oil were measured as follows. The calcite crystals were cleaned with heptane, dried using compressed air and placed in a glass 10 mm path length cuvette. The cuvette containing the crystal was filled with the oil of study and placed in the thermostatted cell of a Krüss DSA 10 instrument (Figure 2.6). A 0.2-0.5  $\mu\text{l}$  sessile drop of the aqueous solution was carefully injected on to the calcite surface, making sure to avoid any voids or cracks on the crystal. To obtain reliable values of  $\theta$ , it is important that the field of view size of the three-phase contact line of the sessile drop is similar to or smaller than the capillary length of the oil-water interface ( $= (\gamma/\Delta\rho g)^{1/2}$  where  $\gamma$  is the oil-water tension,  $\Delta\rho$  is the density difference between the two fluid phases and  $g$  is acceleration due to gravity). Systems with an ultra-low oil-water interfacial tension consequently have a very small capillary length (approx. 0.02 mm with  $\gamma_{ow} = 0.001 \text{ mN m}^{-1}$  for water under decane) and thus require small drop volumes and high magnification to determine the contact angle. The small drop size is to minimise excessive spreading of the drop due to the effect of gravity. The horizontal microscope used here consisted of a Navitar 1-60350 zoom system equipped with a Mitutoyo M Plan Apo 5 objective lens (magnification 5X, numerical aperture 0.14, working distance 34.0 mm) and a QImaging QICam digital camera which enabled overall magnification of approximately 100X. This magnification enabled clear visualisation of the three-phase contact line at the edge of the sessile drop. Micrographs were taken of the static advanced sessile drop and the contact angle measured with an on-screen protractor using Iconico software (New York, Version 4.0) (Figure 2.6). For Winsor III systems containing three fluid phases, small drops of the third (surfactant-rich phase) were observed to separate from the main water drop. In all cases, the contact angle measured corresponded to the calcite-(water-rich)-(decane-rich) three-phase contact line.

Where partitioning of the surfactant between the water and the oil phases occurs, most of the measurements were made with either partition equilibrated phases (surfactant starting in water and equilibrated with the oil, as in section 2.2.6) or with pseudo equilibrated phases (where the concentrations are made up in the water and oil phases individually as calculated from the partition coefficient).

**Figure 2.6** Picture of the experimental set-up for the determination of the water-oil-calcite contact angle (top), and a screenshot showing the use of the onscreen protractor (bottom).



### 2.2.3 Water-oil interfacial tensions

#### 2.2.3.1 *du Noüy ring*

The interfacial tensions between oil and water were determined using the static maximum pull (or push in some cases) method through use of a Krüss K12 processor tensiometer and a Pt-Ir du Noüy ring<sup>4</sup>. In this method the du Noüy ring starts off in the more dense phase and is pulled up through the less dense phase forming a meniscus around the ring. The force exerted on the ring by the meniscus increases until a maximum is reached, at which point the force decreases and soon after the meniscus

breaks off. Figure 2.7 depicts the change in the force exerted on the ring as the height of the ring above the surface is increased and shows the corresponding shapes of the meniscus at the different points of the graph. The interfacial tension is calculated from the force exerted on the ring at the maximum (point labelled b in Figure 2.7) by using equation 2.1.

$$\gamma = \frac{F_{\max} P}{4\pi r_{\text{ring}}} \quad (2.1)$$

where  $\gamma$  is the interfacial tension,  $F_{\max}$  is the force exerted on the ring at maximum pull and  $r_{\text{ring}}$  the mean radius of the ring. The denominator ( $4\pi r_{\text{ring}}$ ) is the wetted length. The correction factor,  $P$ , is calculated automatically by the tensiometer using the Zuidema and Waters equation (2.4)<sup>5</sup>.

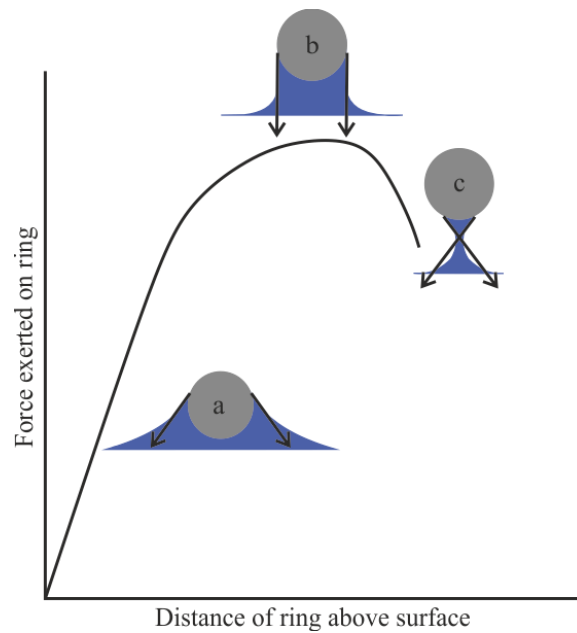
$$P = 0.725 + \sqrt{\frac{0.01452\gamma^*}{(4\pi r_{\text{ring}})^2} + 0.04534} - \frac{1.679}{r_{\text{ring}}/r_{\text{wire}}} \quad (2.2)$$

where  $\gamma^*$  is the uncorrected (measured) tension,  $\Delta\rho$  the density difference between the two phases and  $r_{\text{wire}}$  the cross sectional radius of the wire of the ring. Other correction factors have been determined, such as those by Harkins and Jordan<sup>6</sup> and Huh and Mason<sup>7</sup>, though the Zuidema and Waters correction was deemed suitable for the work carried out here. The correction factor is needed for two main reason; firstly due to the weight of the column of the more dense phase being pulled up underneath the ring along with the meniscus on either side of the ring, and secondly due to fact that the contact angle on the inside of the ring tends to be greater than 0 °.

The tensiometer allows the ring to be left at just under maximum pull and the measurement repeated. This allows the repeat measurements to be made over time (without significantly changing the interfacial area) to ensure that the equilibrium value of tension is determined.

As with the contact angles, where partitioning of the surfactant between the water and the oil phases occurs, most of the measurements were made with either partition equilibrated phases or with pseudo equilibrated phases (also the case for spinning drop measurements).

**Figure 2.7** The variation of the force exerted on the ring with the distance of the ring above the surface, and the corresponding shapes of the meniscus attached to the ring at the different points of the graph. The meniscus labelled b is the point of the maximum pull exerted on the ring used in the equations. The arrows indicate the direction of the forces exerted on the ring due to the interfacial tension. The grey circles are a cross section of one part of the ring.



### 2.2.3.2 Spinning drop

When interfacial tensions were below  $\sim 5 \text{ mN m}^{-1}$  the du Noüy ring method becomes unsuitable as the meniscus can easily detach from the ring. In this case, the spinning drop method was employed. Using this technique, a small droplet of the oil is injected in a spinning capillary that contains the more dense water phase. In the spinning drop technique, the shape of the drop is determined while the capillary is spinning. The shape is a balance between interfacial tension (minimising interfacial area) and centrifugal forces (elongating the drop to a narrow cylinder). The interfacial tension is calculated from the drop shape using the equation derived by Vonnegut (2.3)<sup>8</sup>.

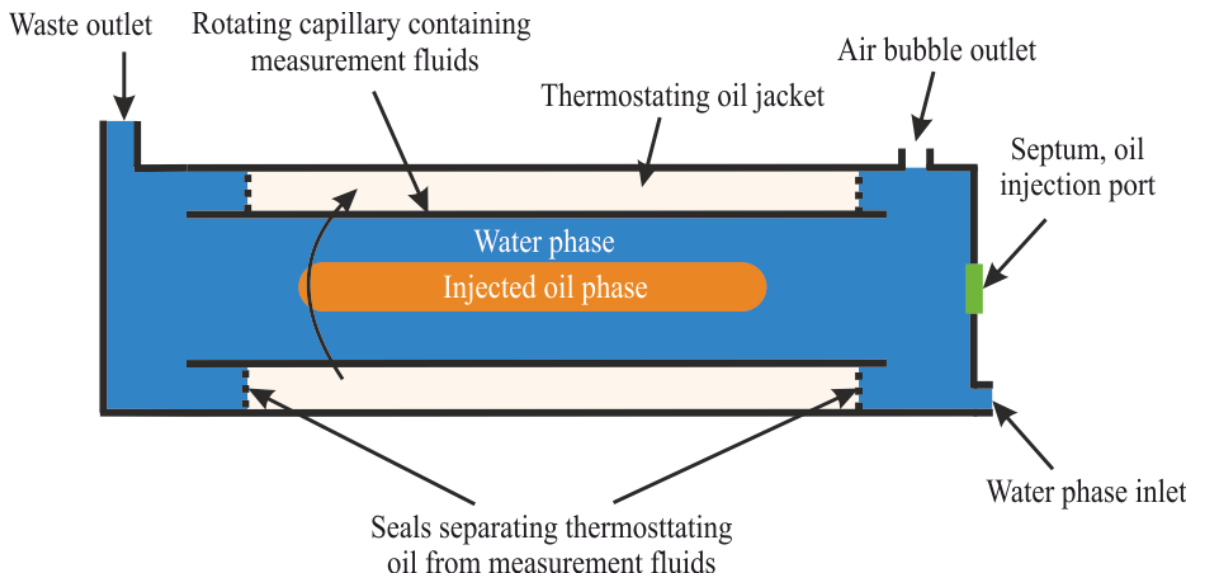
$$\gamma = (\omega^2 r_{\text{drop}}^3 \Delta\rho / 4)(1 + 2r_{\text{drop}} / 3L) \quad (2.3)$$

where  $\omega$  is the angular velocity (in radians per second),  $r_{\text{drop}}$  the radius of the oil drop,  $\Delta\rho$  the density difference between the oil and the water and  $L$  the length of the drop (not

including the hemispherical ends). Figure 2.8 shows a schematic of the spinning drop apparatus.

In the work here a Krüss Site 04 spinning drop tensiometer was used with a Grant LTD 6G thermostat bath filled with silicone oil attached.

**Figure 2.8** Schematic of the spinning drop apparatus.



#### 2.2.4 Water-air interfacial tensions

The Wilhelmy plate method, rather than the du Noüy ring method (described in 2.2.3.1) was used to determine the liquid-air interfacial tensions. The Wilhelmy plate method is a static method, so there are fewer complications in determining the equilibrium value of the interfacial tension. The principles of the two methods is similar in that one phase wets the plate/ring with a contact angle close to  $0^\circ$  and the force exerted on the plate/ring is determined. The interfacial tension is calculated using equation 2.4, where  $x$  is the horizontal length of the plate and  $y$  the thickness of the plate. Jordan *et al.*<sup>9</sup> have shown that despite the complex shape of the meniscus around the plate, equation 2.4 is still valid (and hence no correction factor is needed).

$$\gamma = \frac{F}{2(x + y)} \quad (2.4)$$

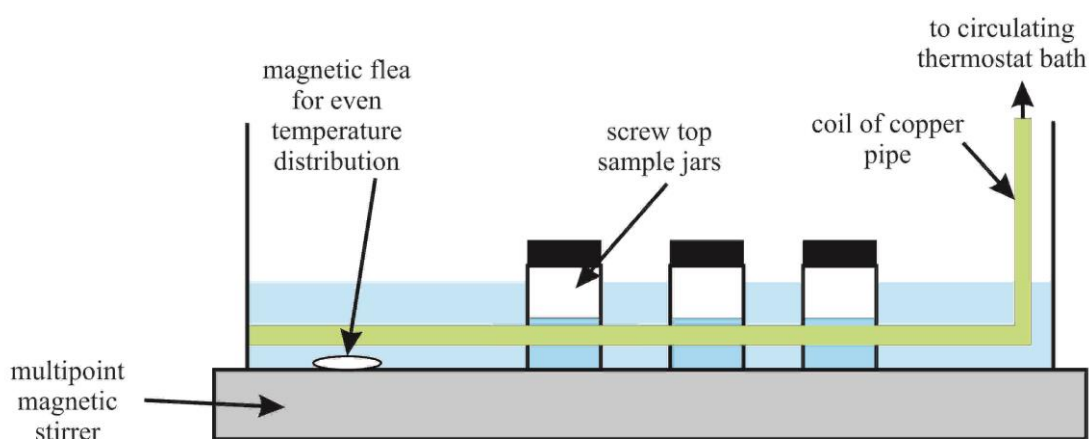
In the work here, a roughened platinum plate from Krüss attached to a Krüss K12 processor tensiometer was used for all measurements.

### 2.2.5 Adsorption isotherms of surfactants from aqueous solution to the calcite-water interface

Adsorption isotherms for surfactants adsorbing from solution to the calcite interface were determined by the solution depletion method. A known volume and concentration of the surfactant solution is added to a known weight of the calcite and left to equilibrate. The calcite is removed (and the adsorbed surfactant with it), and the concentration of surfactant left in the solution determined. Using a mass balance assumption, the amount adsorbed can be determined as a function of the non-adsorbed solution concentration.

In this work 20 ml of the surfactant solution and varying weights of calcium carbonate powder were added to a 60 ml glass jar with screw-top lid and a magnetic flea in the jar. The pH was measured with a Jenway 3510 pH meter (and adjusted using aqueous solutions of HCl and NaOH where needed). The jars were placed in a water-filled glass tank by a coiled copper tube attached to a Grant LTD 6G thermostat bath (Figure 2.9). The glass tank was placed on top of a Variomag Poly 15 multipoint magnetic stirrer and the samples stirred at 400 r.p.m. Repeat measurements were carried out at different time intervals (between 6 to 48 hours) to ensure equilibrium was attained.

**Figure 2.9.** Set-up for adsorption isotherm equilibration.



If the surfactant concentration was to be determined using the Epton titration the entire sample was transferred to a 50 ml centrifuge tube and placed in a Baird & Tatlock Mk IV Auto Bench Centrifuge and centrifuged at ~ 6000 r.p.m. for 10 minutes to

separate the calcite particles from the solution and the supernatant analysed using the technique described in 2.2.1.1.

If the surfactant concentration was to be determined using UV-vis spectrometry some of the sample was transferred to a 1.5 ml centrifuge tube, and centrifuged at 14k r.p.m for 4 minutes. The supernatant was then either diluted or added directly to a cuvette and the concentration determined using the technique described in section 2.2.1.2.

The weight of calcium carbonate to be used was adjusted such that the amount of surfactant in the supernatant was 20-80 % of the initial concentration so as to minimise the uncertainty.

#### *2.2.6 Partition coefficients of surfactants between water and oil phases*

Partition coefficients were also determined using a solution-depletion method. A known concentration of the surfactant was made up in the aqueous phase and 30 ml added to a 60 ml glass jar (as with the adsorption isotherms) along with a magnetic flea. The oil phase was carefully added on top of the water phase (a further 30 ml). This ensures that the head-space volume in the glass jar is small enough so that the change in volume of volatile oil phase due to evaporation can be assumed to be negligible. Samples were placed in the same equilibration set-up as shown in section 2.2.5 and stirred at a speed sufficiently slow to avoid emulsification. After equilibrium was reached, a sample of the aqueous phase was analysed using either the titration or UV-vis spectrometry. As with the adsorption isotherms, repeat measurements were carried out at different time intervals (between 1 and 14 days) to ensure equilibrium was attained.

#### *2.2.7 Determination of microemulsion phase inversion*

To determine which type of microemulsion a set combination of surfactant, water, oil and salt would make, microemulsion phase tubes were prepared to visualise where the transitions between the Winsor systems occur. This was done by making up solutions of the surfactant with concentrations in excess of the  $c_{\mu c}$  in water at varying salt concentrations, adding with the oil in a 1:1 volume ratio in a sealed test tube and inverting the sample several times to promote mixing. The tubes were left at 25 °C until the

thermodynamically unstable emulsions that were formed had separated enough in order to be able to see the number and volumes of the thermodynamically stable phases present at equilibrium.

### 2.2.8 *Calcite-packed column experiments*

The experimental setup used to investigate the flow properties and oil removal for columns packed with calcite powder is shown in Figures 2.10 and 2.11. The column was a modular semi-preparative HPLC stainless steel cylindrical column (Kinesis, UK) with an internal diameter of 10 mm and an internal length of 50 mm fitted with PEEK connectors for flow tubing. The following procedure was used to pack the column with calcite powder. One end of the column was first sealed with a frit (mean pore diameter 2  $\mu\text{m}$ , thickness 1 mm supplied by Kinesis) and an end connector. The calcite powder was then added in small aliquots and a metal rod and hammer used to pack the powder down between aliquots. When full of powder, the second frit was added and the assembly sealed with the second end connector. It is worth noting that the pore diameter of the frits is much larger than the mean pore size within the packed columns. The frits contribute only a small fraction of the overall hydrodynamic resistance of the filled column. The column was weighed before and after filling to determine the mass (and hence volume fraction) of powder in the packed column volume.

Two types of flow experiment were performed with the packed columns. In the first type, used to determine the flow properties of the packed columns, pure water or a pure oil was flowed through the column initially containing only powder to displace air. Using measurements of the mass before and after liquid filling, it was checked that the final volume fraction of trapped air was less than 0.01. The volumetric flow rate was set using the HPLC (Jasco PU-1580 or PU-980 Intelligent HPLC Pump) or syringe pump (WPI model sp100i) and the pressure drop between the pump and the column exit was monitored.

The second type of experiment was used to determine the amount of oil displaced by flowing an aqueous solution into a packed column with oil-filled interstices. The packed column interstices were filled with an oil using a syringe pump with a volumetric flow rate of 8.3  $\mu\text{l min}^{-1}$ . Approximately 5 pore volumes of the oil were pumped to fill the

column.) Again, the column was weighed before and after the oil filling to determine the mass of the oil initially in the packed column and to check that the column contained virtually no trapped air. The column is then attached to an HPLC pump and the aqueous surfactant solution pumped at a set flow,  $Q$  (most experiments were at a  $Q = 5 \mu\text{l min}^{-1}$ ) and the total pressure drop monitored. The amount of oil removed from the column was determined at appropriate time intervals by stopping the pump and removing then weighing the column. Since the density of the oil is lower than the density of the aqueous surfactant solution, the mass of the column increases slightly as the oil is displaced from the column and the measured masses can be used to derive the percent of the original oil in place recovered (%oil recovery). Solution densities required for this calculation were measured using a DMA 35N density meter.

Section 2.2.8.1 discusses the reproducibility and errors associated with this technique, and section 2.2.8.2 discusses the reliability of the pressure sensor 2 readings.

**Figure 2.10** Schematic of the packed calcite powder column flood setup.

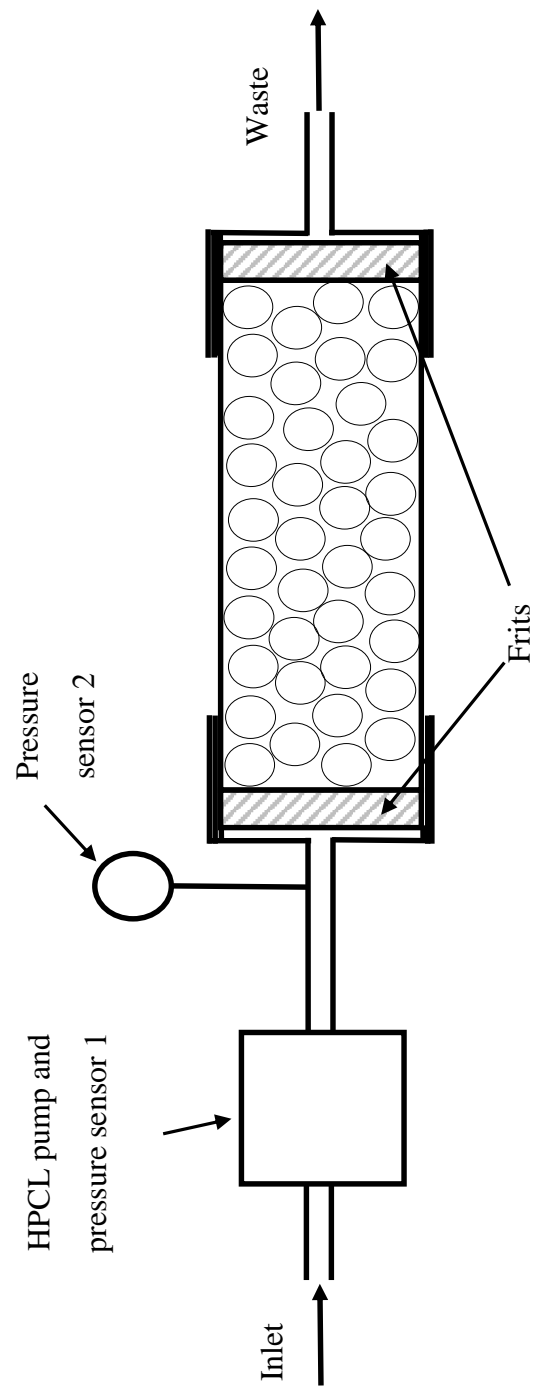


**Figure 2.11** Photograph of the column flood setup.



### 2.2.8.1 *Reproducibility of oil recovery floods*

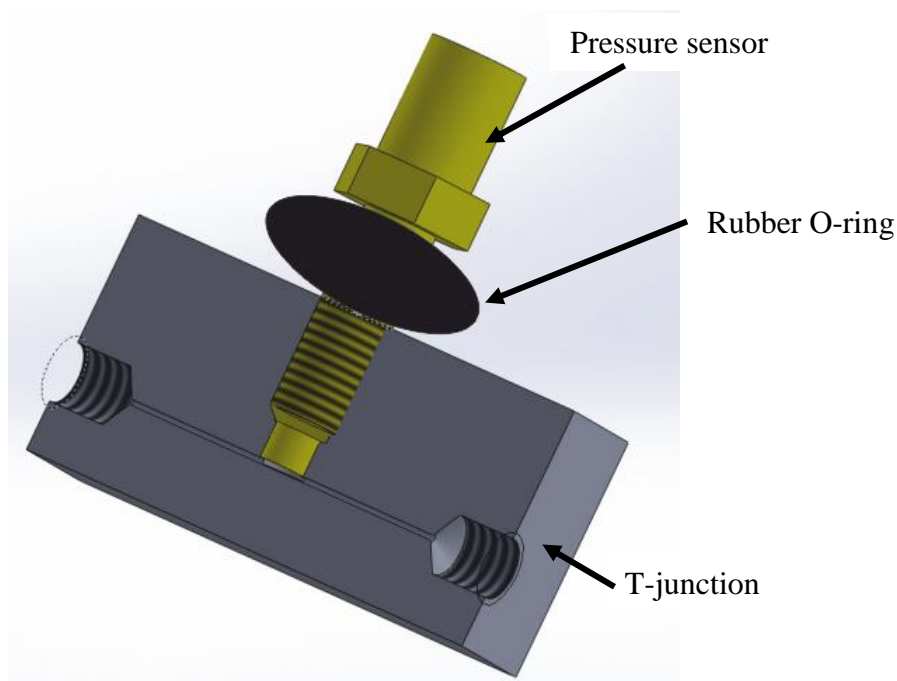
Causes for errors in the column flood oil recovery experiments may come from multiple sources. However, the two main sources of error are the possible introduction of air in to the system (lowering the weight of the column) and from the drying of the connections prior to weighing. The systematic error for this process was determined by packing a column with FC10 calcite, filling it with water (in the same way as it is usually filled with oil before an oil displacement flood), and then continuing to pump water through and stopping the pump and weighing the column using the same process that would be used in oil recovery floods. From these repeated measurements, the estimated uncertainty in an individual column mass measurement is  $\pm 4$  mg. In the case of an FC10 packed column with interstices filled with decane (or heptane), the difference in mass of the column filled with decane and filled with water is approximately 400 mg, this uncertainty in the individual mass measurements corresponds to an uncertainty in the final value of %oil recovered of  $\pm 2\%$ . In the case where toluene is used in place of decane, the difference in the mass of the column filled with toluene and filled with water is only approximately 200 mg (half that of the decane filled column), and as such the error in the %oil recovered is double that of the error for decane recovery. Where plots are made for the difference in %oil recovery between 1 and 4 pore volumes the errors will be double the usual error.

As will be seen in later chapters, at lower surfactant concentrations repeat measurements of the oil recovery do lie within these error boundaries. However, at higher concentrations the errors are greater and reasons will be discussed alongside data in later chapters.

### 2.2.8.2 *Testing the pressure sensor*

The schematic of the column flood set-up shown in Figure 2.10 shows that two pressure sensors were used. The first pressure sensor, labelled as ‘pressure sensor 1’, is inbuilt in to the HPLC pump and has a pressure range of 0.0 - 50.0 MPa and the pressure can only be recorded by looking at the screen and manually noting the pressure reading. Thus, if any effects of the Laplace pressure (generally in the range of 0.0– 0.3 MPa, see Chapter 3 section 3.2.2) on the driving pressure were to be observed, an alternative pressure sensor was needed with: (i) a lower pressure range, (ii) a higher accuracy and (iii) data logging capability to allow many measurements to be taken over time without manual input. These specifications were achieved with an XP5 miniature pressure sensor manufactured by Measurement Specialties™, which was connected to a Pico Technology ADC-20 precision data logger via a terminal board. The sensor has a flush diaphragm and a 10-32 thread, allowing it to be attached inline to an HPLC flow system using a modified t-junction connector such that there is no dead volume, theoretically providing fast response times (Figure 2.12).

**Figure 2.12** Cross section schematic of the set-up for ‘pressure sensor 2’.



The XP5 sensor is a Wheatstone-bridge based strain-gauge pressure sensor which can be purchased in gauge (pressure relative to ambient pressure), absolute (pressure relative to a vacuum) and sealed (pressure relative to a fixed pressure) configurations. In the work carried out here a gauge-type configuration was used that measures the pressure difference from ambient, i.e. the pressure difference between inside and outside of the T-junction in the set-up in Figure 2.12. As the ambient pressure is the same directly outside the T-junction as it is at the end of the waste pipe, the pressure drop is discussed as the pressure drop between the pressure sensor and the waste outlet from the column. In standard configuration, it requires a 10 V power supply, which in this work was provided by a moderated power supply (built in-house) which supplied a steady voltage of  $9.735 \pm 0.002$ . When connected to the ADC-20 data logger, the output voltage of the pressure sensor can be recorded at variable time intervals over variable overall time scales. In most experiments the baseline voltage was determined by recording the output of the sensor when it was in place in the t-junction with only air present in the channel. The differential voltage is then calculated by taking the baseline reading as 0 mV, and all other readings as relative to that. The differential voltage could then be converted to pressure in MPa by using the equation of the straight line when pressure is plotted vs. differential voltage using the calibration data given by the manufacture (full scale output, FSO, of the sensor in mV is 81.31 mV, corresponding to a pressure of 0.5171 MPa).

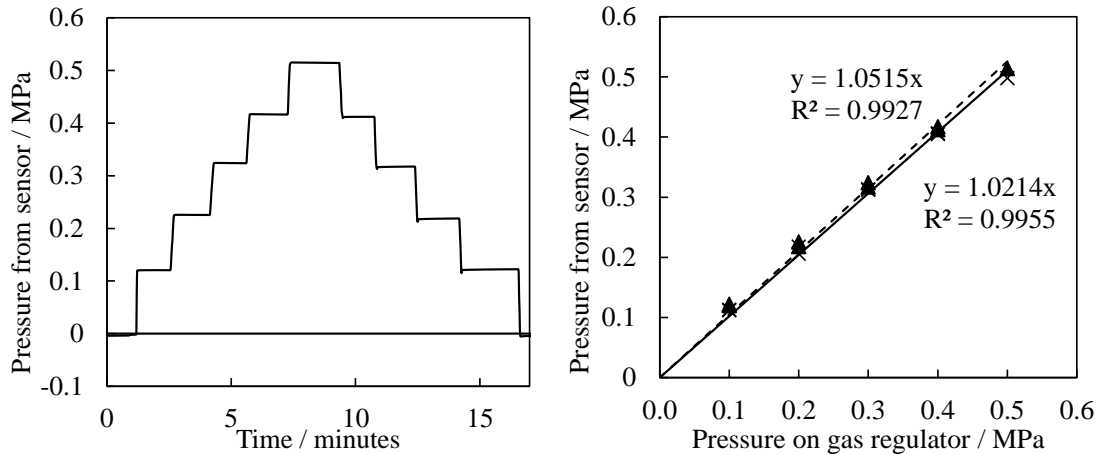
The pressure plots obtained using this set-up for oil recovery floods (shown in Appendix D) often display some interesting characteristics. In order to ensure that no wrong interperetations were made from un-reliable data, a few experiments were carried out to check that the pressure sensing set-up produces reliable results. Three experiments were conducted to: (i) check the calibration of the sensor using gas pressure, (ii) measure the pressure drop across the column with single phase liquid flow, and (iii) test if the sensor can measure negative pressure drops.

#### 2.2.8.2.1 Testing the calibration of the pressure sensor

To test the calibration of the pressure sensor the T-junction was connected to two different gas cylinders (one oxygen, one argon), both with gas pressure regulators fitted, and a stopper attached to the other end of the T-junction. The data logger was set to record every second, and the pressure on the gas pressure regulator altered at set-time intervals. Although the type of gas shouldn't make a difference to the measured pressure, the comparison between the two different pressure regulators increase the reliability of the results. The left plot of Figure 2.13 shows the pressure plot obtained when using the oxygen cylinder. Each plateau of the 'steps' corresponds to where the regulator was left at a constant value. The initial plateau is the baseline reading from attaching the T-junction to the gas cylinder with the cylinder valve closed, and the final plateau where the stopper was removed from the T-junction and the cylinder valve close. Each vertical section of the 'steps' corresponds to where the pressure on the regulator was increased or decreased by 0.1 MPa (when the pressure was decreased the release valve was opened carefully to release the excess gas). The time response between altering the pressure on the regulator and the sensor recording a change, on this time scale, is instantaneous.

The right plot of Figure 2.13 shows the pressure reading from the sensor at the plateaus of the 'steps', for both the oxygen and argon cylinders, against the pressure read from the gas pressure regulator. If both the regulator and the pressure sensor were perfectly calibrated and there was no experimental error, the gradient of the straight line should be unity. The pressures measured with the sensor attached to the oxygen cylinder are within 2 % of this, and when attached to the argon within 5 %. These results show that, by using the pressure sensor in the same configuration in which it would be used for oil recovery experiments, the measurement of gas pressure produces reliable data. There is no reason to expect this to be different for the measurement of liquid pressures.

**Figure 2.13.** Left plot: Pressure measured by the XP5 sensor when connected to an oxygen gas cylinder and the pressure varied as described in the text. Right plot: Pressure measured by the XP5 sensor compared to the pressure on the pressure regulator. The crosses and the solid line are the pressures from the oxygen cylinder and the triangles and the dashed line from the argon cylinder.



#### 2.2.8.2.2 Pressure drop across the column with single phase flow through an FC10 packed column

An interesting trend that is often observed on the pressure plots from the oil displacement floods is, what appears to be, rhythmic spikes and dips in the pressure. To see if this was due to some effect coming from the oil being displaced by the water, or another phenomenon, the pressure drop for single phase flow of water through the column (all pores filled with water and water being pumped through the column) was monitored at different flow rates. Figure 2.14 shows the pressure data as a function of time, and table 2.5 shows the flow rates used and the times at which the flow rates were altered. Two main trends are observed from this plot. Firstly, the magnitude of the spikes and dips in the pressure readings increases with increasing flow rate, and secondly, the time between the spikes and dips decreases with increasing flow rate. Figure 2.15 plots the time between the pressure spikes vs. flow rate. The data fits an exponential equation with a high accuracy, adding to the conclusion that the spikes and dips are rhythmic and not random. These correlations indicate that the source of the spikes and dips come from the HPLC pump and not any other effect from the two-phase flow systems encountered in oil recovery floods. Another indication of this is that the spikes and dips are not seen

when the syringe pump is used instead of the HPLC pump. Although the Jasco PU-1580 and PU-980 pumps are dual piston and thought to be ‘pulse free’ this data shows that, on the pressure scales that are being used throughout this work the flow is not ‘pulse free’. This is something that will be kept in mind when interpreting the oil recovery plots discussed in later chapters.

**Figure 2.14** Continuous monitoring of pressure drop (between pressure sensor 2 and column exit) as the flow rate of water being pumped through an FC10 packed column is changed according to the table 2.5.

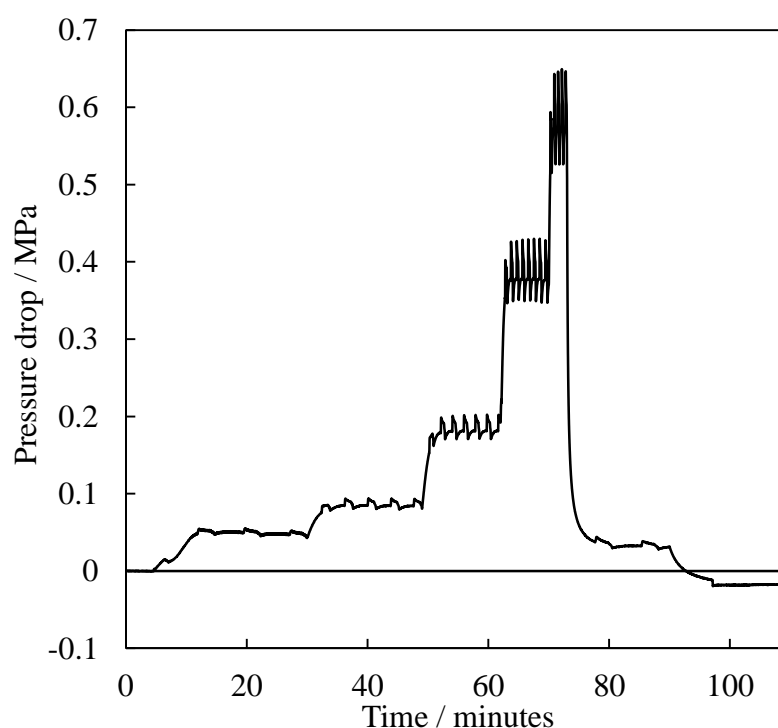
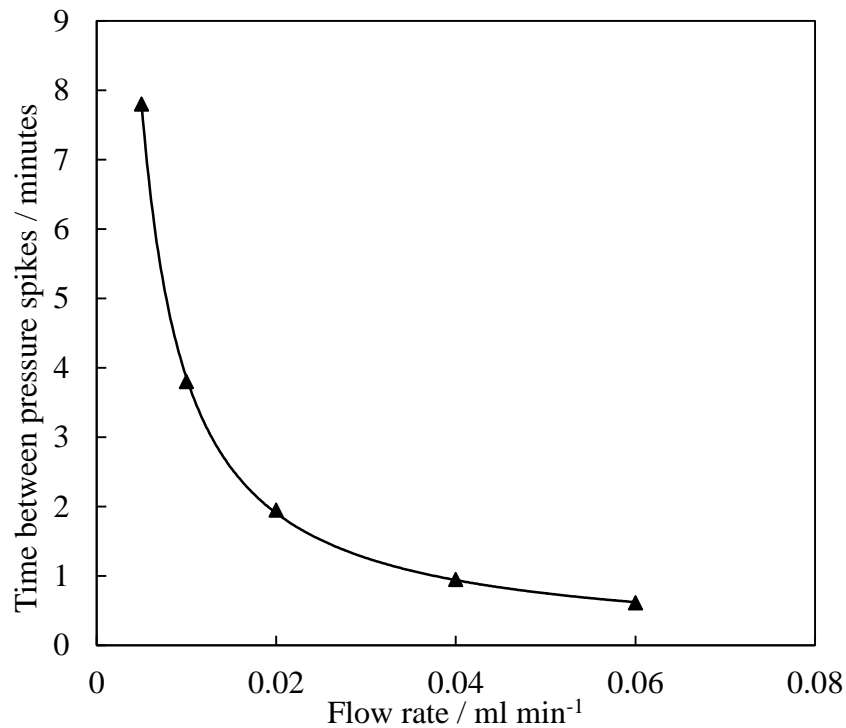


**Table 2.5** The times and flow rates used for obtaining the the pressure data shown in Figure 2.14.

Time / minutes:seconds	Flow rate / ml min <sup>-1</sup>
0 – 4:45	0.000
4:45 – 30:00	0.005
30:00 – 49:00	0.01
49:00 – 62:00	0.02
62:00 – 70:00	0.04
70:00 – 73:00	0.06
73:00 – 90:00	0.005
90:00 – 97:00	Pump off
97:00 – 108:00	Tube disconnected from column

**Figure 2.15** Time between the pressure spikes seen in Figure 2.14 vs. flow rate.

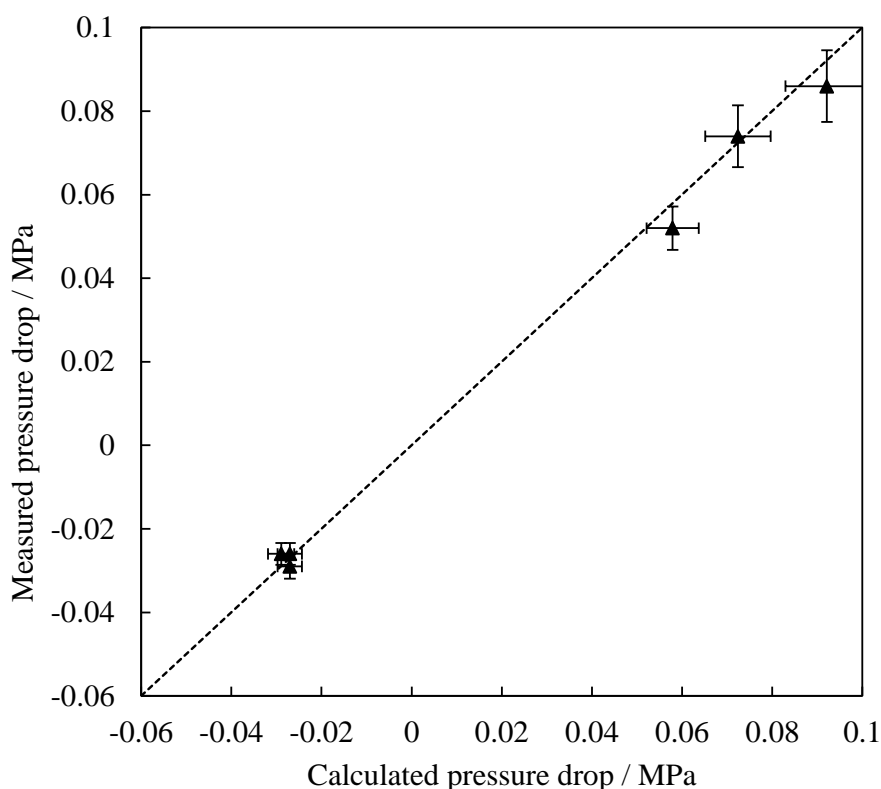


### 2.2.8.2.3 Measurement of negative pressure drops

The specifications of the pressure sensor do not state anything about the ability of the sensor to measure negative pressure drops. As there is a possibility for negative pressure drops to be encountered during the oil displacement floods due to negative Laplace pressures, it was necessary to determine if the pressure sensor would pick these up. This was done by attaching the T-junction, with the stopper on one end, to a 10 ml syringe filled with 5 ml of air (the same configuration as used in testing the calibration with the gas cylinder). Using a syringe pump with the ability to inject and withdraw it was possible to determine if the pressure sensor could measure negative pressure drops. Figure 3.10 shows the measured pressure drop between the inside of the t-junction connected to the syringe and ambient pressure outside the syringe vs. the pressure drop calculated from the change in the volume within the syringe (assuming there is no leaking of gas in to or out of the syringe). All of the positive and the negative measured pressures are the same as the calculated pressures within an error of approximately 10%. As it is known from section 2.2.8.2.1 that the calibration of the sensor is correct (at least for positive pressures), it might be expected that the values should agree within a smaller

percentage. However, the calculated pressure from the change in volume only took in to account the volume within the main syringe body, and not the volume in the connections to and within the t-junction. There may also have been some leaking of gas from the system. The key finding is that sensor does have the ability to measure negative pressure drops, at least down to a pressure of approximately -0.025 MPa within the same error as the positive pressure measured in the same experiment. Tests were not conducted at lower pressure drops to prevent possible damage to the sensor.

**Figure 2.16** Measured pressure drop between the inside of the t-junction attached to an air filled syringe and ambient pressure vs. the pressure calculated from the change in volume of the syringe. The diagonal dotted line indicates the case of perfect agreement.



#### 2.2.8.2.4 Conclusions of pressure sensor testing

The pressure sensor set-up was shown to produce reliable results for both positive and negative pressures. Using this set-up, fluctuations in the pressure drop were seen when using the HPLC pump to pump water through a water filled column. These fluctuations were found to be rhythmic and only associated with the HPLC pump (and not syringe pumps), and thus are probably due to the pumping action of the pistons in the pump. It was also found that the sensor can measure negative pressures to at least -0.025 MPa.

### 2.2.9. *Other techniques*

#### 2.2.9.1. Scanning electron micrographs (SEM)

SEM micrographs of the calcite powders were obtained using a Zeiss EVO60 electron microscope. Samples were sputter coated with a 2 nm thick Au/Pd (Au 82%, Pd 18%) film prior to imaging. SEM images were analysed to estimate the mean particle diameters using Image J software (USA, 1.46r edn.).

#### 2.2.9.2. Nitrogen adsorption isotherms and analysis

Nitrogen adsorption isotherms onto the calcite powders at the boiling temperature of liquid nitrogen were measured using a Micromeritics TriStar 3000 instrument. The data was analysed using the procedures described by Brunauer, Emmett and Teller and by Barrett, Joyner and Halenda for determining the specific surface area and the porosity of the calcite respectively<sup>10,11</sup>.

#### 2.2.9.3. X-ray diffraction patterns and analysis

Powder x-ray diffraction patterns for the three ground calcium carbonate powders were determined using a PANalytical Empyrean powder X-ray diffractometer without any pre-treatment of the samples. For determining the powder x-ray diffraction patterns of the calcite crystal one of the crystals was ground up by hand using a pestle and mortar.

### 2.3 References

1. *CRC Handbook of Chemistry and Physics*, CRC Press/Taylor and Francis, Boca Raton, 89th edn., 2008.
2. Iglauer, S., Wu, Y., Shuler, P., Tang, Y., Goddard III, W.A., New surfactant classes for enhanced oil recovery and their tertiary oil recovery potential, *J. Pet. Sci. Eng.*, **2010**, *71*, 23.
3. Reid, V.W., Longman, G. F. and Heinerth, E., Determination of anionic-active detergents by two-phase titration, *Tenside*, **1967**, *4*, 292.
4. du Nouÿ, L, A new apparatus for measuring surface tension, *J. Gen. Physiol.*, **1919**, *1*, 4.
5. Zuidema, H. and Waters, G., Ring Method for Determination of Interfacial Tension, *Ind. Eng. Chem. Anal. Ed.*, **1941**, *13*, 312.
6. Harkins, W.D., and Jordan, H.F., A Method for the Determination of Surface and Interfacial Tension from the Maximum Pull on a Ring, *J. Am. Chem. Soc.*, **1930**, *52*, 1751.
7. Huh, C., and Mason, S.G., A rigorous theory of ring tensiometry, *Colloid Polym. Sci.*, **1975**, *253*, 566.
8. Vonnegut. B., Rotating Bubble Method for the Determination of Surface and Interfacial Tensions, *Rev. Sci. Instrum.*, **1942**, *13*, 6.
9. Jordan, D.O., Lane, J.E., A thermodynamic discussion of the use of a vertical-plate balance for the measurement of surface tension, *Aust. J. Chem.*, **1964**, *17*, 7.
10. Brunauer, S., Emmett, P.H., and Teller, E., Adsorption of Gases in Multimolecular Layers, *J. Am. Chem. Soc.*, **1938**, *60*, 309.
11. Barrett, E.P., Joyner, L.G., and Halenda, P.P., The determination of pore volume and area distributions in porous substances. I. Computations from nitrogen isotherms, *J. Am. Chem. Soc.*, **1951**, *73*, 373.

## CHAPTER 3

### CHARACTERISATION OF THE CALCITE PACKED COLUMNS

#### 3.1 Introduction

As discussed in Chapter 1, many of the studies determining the oil recovery performance of surfactant solutions are often carried out using rock core samples cut from the outcrop rocks near oil containing reservoirs and using crude oil as the phase to be displaced. Although many techniques are used to characterise the morphology of the rock cores and the flow properties (mainly permeability) are routinely determined and complicated long washing and pre-treatments are carried out<sup>1-6</sup>, there are many parameters which may or may not be sufficiently controlled for a model study of oil recovery. As the aims of the work here is to attempt to understand, in detail, how aqueous surfactant solutions displace oil from a porous system, a reproducible and pure experimental model system is needed. As such, the model system that was chosen to represent an oil reservoir in the work here was a column packed full of calcium carbonate calcite particles (from now on these particles will be referred to as calcite particles) with the interstices between the particles filled with a pure oil.

The use of a pure system not only greatly simplifies the complexities of a real system (though it will still have complications of its own), it also eliminates the need for long complicated washing and ageing procedures, allowing for more results to be obtained in on much shorter time scale. Though the idea of using all pure components for an oil recovery study is not strictly a new one, it is not often seen where all of the components of a model system are characterised in detail, as is the aim of this work.

In order to be able to develop an in-depth understanding of the oil recovery, it is necessary to characterise the model system in as much detail as possible. The results discussed within this chapter aim to show, (i) the porosity of and the flow properties of the packed columns with a discussion of the permeability and pore sizes and (ii) the effect of flow rate and gravity on the displacement of an oil from the column in terms of the capillary number and bond number often seen in oil field literature.

## 3.2 Porosity, permeability and pore sizes within the packed columns

### 3.2.1 Porosity

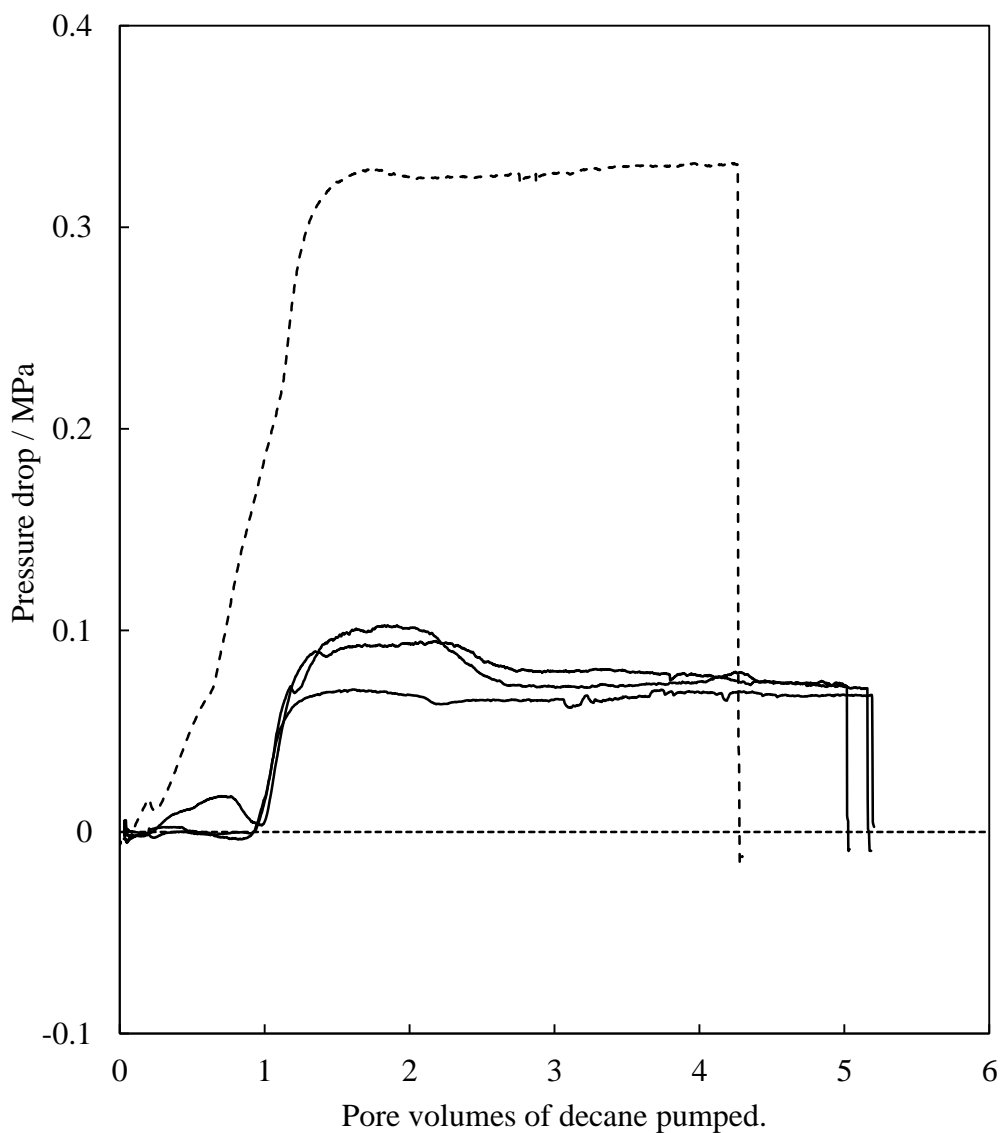
As described in Chapter 2, the three calcite powders all consist of polydisperse, low axial ratio and irregularly shaped particles. The BET measurements show the particles have a porosity of 0.04-0.08 with internal pore diameters ranging from 26 to 110 nm. This porosity will be referred to as microporosity ( $\phi_{\mu}$ ). In packed columns of the calcite powders, the total porosity ( $\phi_{\text{pore}}$ ) is determined from the weight difference between an empty and a packed column and are 0.34 for FC200, 0.40 for FC30 and 0.45 for FC10. These porosity values are equal to  $\phi_{\mu}$  plus the interstitial porosity,  $\phi_i$ , which comes from the pore space external to the packed particles. The porosity determined from the weight and density of the calcite is the same as the porosity determined from the weight and density of decane in the column after an oil flood ( $0.45 \pm 0.01$  for the FC10 calcite), indicating that there is no trapped air within the column, i.e. the oil fills up both the micropores of the particles, and the interstitial pores between the particles. When flooding with aqueous surfactant solutions it is likely that the aqueous solutions will preferentially flow through the interstitial pores (as they have a lower resistance to flow as they are larger). This is related to the idea of flow-bypassing discussed in Chapter 1. To simplify discussions, it is assumed that the oil recovery is only occurring from the interstitial pores. Discussions about porosity of the columns relate to the total porosity.

### 3.2.2 Permeability

The flow properties of packed columns of the calcite particles of different sizes were investigated by flowing pure liquids through the packed columns at a set volumetric flow rate and recording the pressure drop,  $\Delta P$ , between either pressure sensor 1 or 2 and the packed column exit, as discussed in Chapter 2. Figure 3.1 shows the variation of pressure drop between pressure sensor 2 and exit to air, as decane is pumped at two different constant volumetric flow rates into an FC10 packed column initially filled with air. For the faster flow rate of  $0.042 \text{ ml min}^{-1}$ , when the volume of decane pumped is less than the pore volume, the pressure drop increases, almost linearly, as the more permeable air is displaced from the column by the less permeable decane (hence lowering the permeability and increasing the pressure drop need for flow to occur). When no more air is being displaced the pressure drop required to maintain the volumetric flow rate is constant (approximately 0.33 MPa for decane at  $0.042 \text{ ml min}^{-1}$  with FC10).

At the slower flow rate of  $0.0083 \text{ ml min}^{-1}$  a very different trend is observed in the development of  $\Delta P$  with filling of the column by decane. At the start of the fill,  $\Delta P$  starts to increase only after 1 pore volume (pv) of flow, in contrast to the immediate growth of  $\Delta P$  at the higher  $Q$ . Between 1 and 1.5 pv,  $\Delta P$  increases to a plateau of 0.068 MPa. A possible explanation for this behaviour may lie in the relationship between the Laplace pressure and the pressure drop needed to maintain the set-flow rate when the pores are filled with the decane. Using the contact angle measured through a drop of decane on calcite under air ( $0^\circ$ ), the decane-air interfacial tension ( $23.4 \text{ mN m}^{-1}$ ) and the pore size (discussed in section 3.2.3), the calculated Laplace pressure across the decane-air interface in the channels between the calcite particles ( $\Delta P_{\text{chan}}$ ) is calculated to be -0.29 MPa (section 3.2.3). A negative sign indicates that the Laplace pressure will aid the ingress of decane into the air-filled calcite packed column. The total pressure drop across the packed bed needed for the decane to flow at the set flow rate when all the pores are filled with decane,  $\Delta P_{\text{flow}}$ , is taken to be the pressure at the plateau (0.068 MPa). The precise relationship between the Laplace pressure drop across the oil-water interface and the driving pressure drop across the column is not fully understood. However, the results in Figure 3.1 appear to show that when the driving pressure drop needed to flow decane through the column (when the pores are filled with decane),  $\Delta P_{\text{flow}}$ , is of a similar magnitude to the Laplace pressure, the  $\Delta P$  needed to pump the decane through (before all air is displaced) is lowered. Once all of the air has been displaced and there is no longer a Laplace pressure due to the decane-air interface having disappeared, the driving pressure suddenly increases.

**Figure 3.1** Variation of pressure drop (between pressure sensor 2 and column exit) with volume of decane pumped using syringe pump at  $0.0083 \text{ ml min}^{-1}$  (solid lines) and  $0.042 \text{ ml min}^{-1}$  (dashed line) into an FC10 packed column with pore volume fraction 0.45, with the pores initially containing air. (Oil-air tension =  $23.4 \text{ mN m}^{-1}$ , contact angle through decane =  $0^\circ$ ,  $\Delta P_{\text{chan}} = -0.29 \text{ MPa}$ , and  $\Delta P_{\text{flow}} = 0.068 \text{ MPa}$ ). Pore volumes = volume pumped / volume of pores.

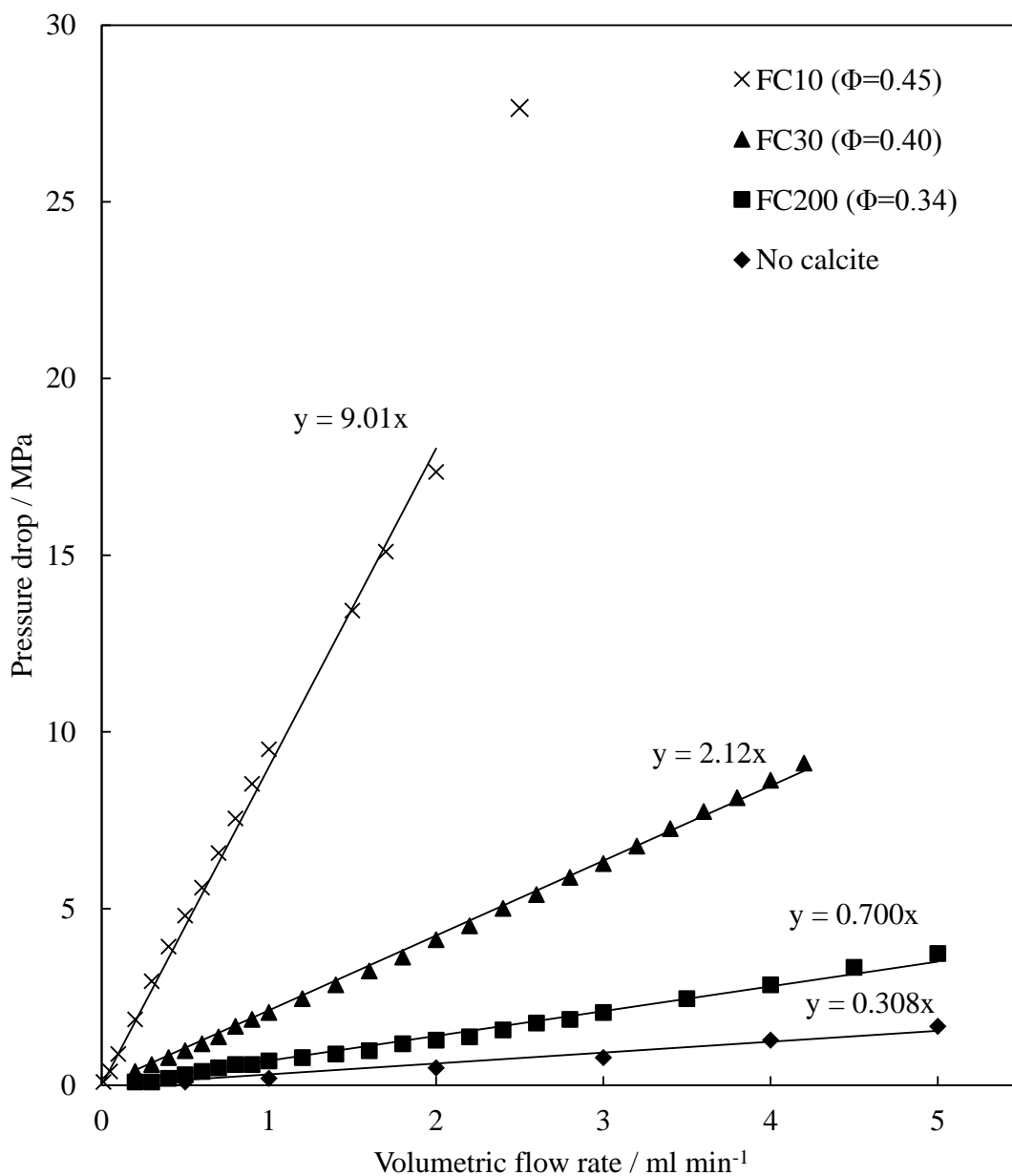


For packed columns filled with water, Figure 3.2 shows that the measured pressure drop is proportional to the volumetric water flow rate for packed columns containing the three calcite powders of different mean particle size and for a column containing no powder but including the frits shown in Figure 2.10 in Chapter 2. These plots demonstrate that Darcy's Law (equation 3.1) is obeyed for the different calcite powders at flow rates yielding pressure drops up to approximately 18 MPa.

The permeability coefficients increase in the order "empty" column ( $40 \times 10^{-15} \text{ m}^2 = 36 \text{ mD}$ ) > FC200 ( $20 \times 10^{-15} \text{ m}^2 = 21 \text{ mD}$ ) > FC30 ( $5.4 \times 10^{-15} \text{ m}^2 = 5.5 \text{ mD}$ ) > FC10 ( $1.2 \times 10^{-15} \text{ m}^2 = 1.2 \text{ mD}$ ), where the viscosity of the water was taken to be  $1 \text{ mPa s}$ .<sup>7</sup> The permeability value for the "empty" column includes the frits but the values quoted for the packed powders do not (i.e. all experiments include the frits, but the driving pressure for the column containing no calcite is subtracted from the driving pressure when the columns are filled with a calcite powder, and the subsequent pressure used for calculating the permeability coefficient for the calcite packed bed alone). This behaviour is expected since the volume fractions of the interstices between the packed calcite particles (the packed column pores) are similar for the different calcite powders but the average packed column pore sizes, and hence the permeabilities, are expected to decrease with decreasing calcite particle size<sup>8-9</sup>. The permeability coefficients calculated using the pressures at the plateaus in Figure 3.1 for decane pumped through an FC10 packed column are the same as those calculated from Figure 3.2 within the experimental error.

For the FC10 packed column, deviation from Darcy's Law is observed for volumetric flow rates greater than approximately  $2 \text{ ml min}^{-1}$  which require a pressure drop  $>18 \text{ MPa}$ . The observed deviation (that pressure drops greater than predicted by Darcy's Law are required at high pressure drops) is consistent with the hypothesis that high pressure drops of  $>18 \text{ MPa}$  cause an increase in the packing density of the calcite powder in the column. Consistent with this idea, it was seen that the FC10 packed column contained some empty space when the column was opened and examined following pumping at a pressure drop of  $27 \text{ MPa}$  (corresponding to the highest data point of the FC10 plot in Figure 3.2). In principle, an alternative explanation for this deviation could be a transition from laminar to turbulent flow at the high pressures. However, the maximum value of Reynolds number (calculated using equation 1.1 in Chapter 1) in all systems tested is approximately  $10^{-6}$  and hence conclude that the deviation is due to packing changes at high pressures.

**Figure 3.2** Variation of pressure drop (between pressure sensor 1 and column exit) with volumetric flow rate for water pumped through packed columns containing either zero calcite, FC10, FC30 or FC200 at 20 °C.



### 3.2.3 Pore size

The data shown in Figure 3.2 can be used to estimate the mean packed column pore sizes for the calcite powders of different mean sizes. As seen in Figure 3.2, liquid flow in the packed columns follows Darcy's law which can be written as:

$$\Delta P = \frac{Q\mu L}{AK_D} \quad (3.1)$$

where  $K_D$  is the permeability coefficient,  $\Delta P$  is the pressure drop across the packed column,  $Q$  is the volumetric flow rate,  $\mu$  is the fluids dynamic viscosity,  $L$  is the packed column length in the direction of the fluid flow and  $A$  is the overall packed column cross-sectional area. The permeability coefficient  $K_D$  of a packed column is expected to depend on the porosity, the average pore diameter and factors dependent on the detailed geometry of the pore network such as tortuosity and inter-connectivity. The results of pressure drop versus volumetric flow rate in Figure 3.2 can be used to estimate an average effective pore radius based on a hypothetical porous system which is hydrodynamically equivalent to the actual pore network present in a packed column. We consider a hypothetical system consisting of a packed column containing a volume fraction  $\phi_{\text{pores}}$  of uniform, cylindrical pores of radius  $r_{\text{pore}}$  aligned parallel to the flow direction<sup>10</sup>. The number of pores ( $n_{\text{pores}}$ ) in the packed column is:

$$n_{\text{pores}} = \frac{\phi_{\text{pore}} A}{\pi r_{\text{pore}}^2} \quad (3.2)$$

Assuming the fluid flow through the cylindrical pores is laminar which in this work it is (section 3.2.2), the Hagen-Poiseuille equation yields the volumetric flow rate  $Q$  as:

$$Q = \frac{n_{\text{pores}} \Delta P \pi r_{\text{pore}}^4}{8\mu L} \quad (3.3)$$

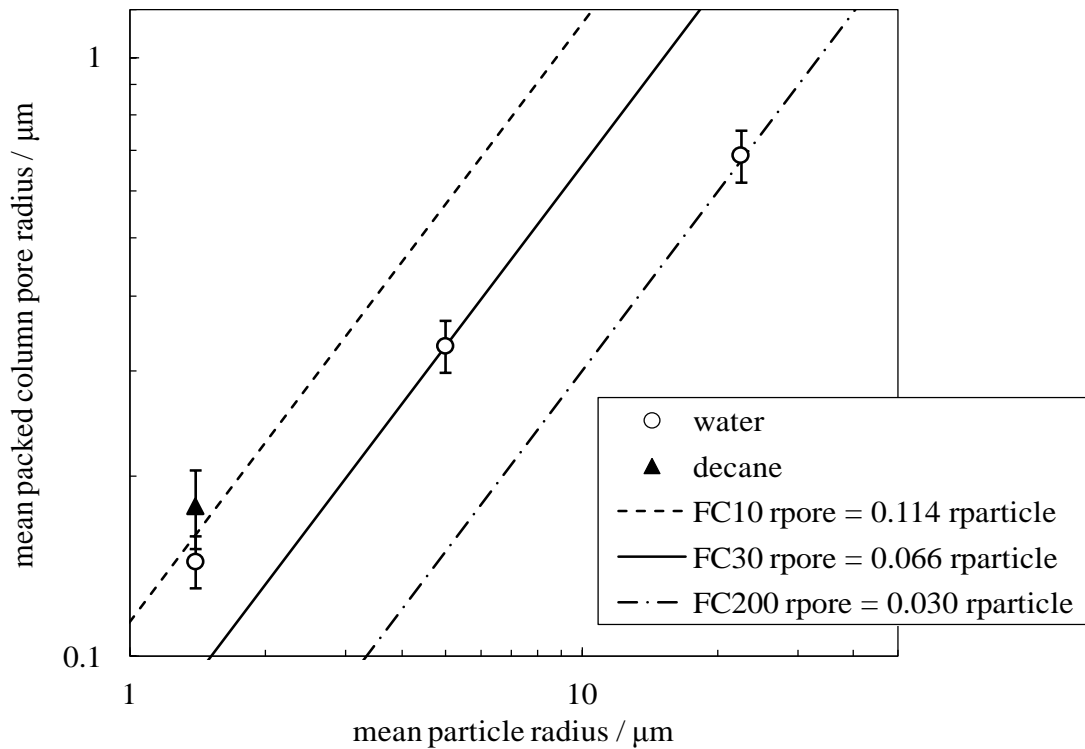
Substituting for  $n_{\text{pores}}$  in equation 3.3 yields the final expression for the value of the average effective (i.e. hydrodynamically equivalent) pore radius  $r_{\text{pore}}$  in terms of the measured values of  $\Delta P$  as a function of  $Q$  (equation 3.4).

$$r_{\text{pore}} = \sqrt{\frac{8Q\mu L}{\phi_{\text{pore}} A \Delta P}} \quad (3.4)$$

Using the data of Figure 3.2, the pressure drop across the packed column  $\Delta P$  was obtained from the measured pressure drop by subtracting the corresponding pressure drop across the flow system and column containing no calcium carbonate powder. Equation 3.4 was then used to derive the values of  $r_{\text{pore}}$  for the three calcite powders which are 0.16  $\mu\text{m}$ , 0.33  $\mu\text{m}$  and 0.69  $\mu\text{m}$  for FC10, FC30 and FC200 respectively.

Computer simulations of the pore size distributions in random close packed, monodisperse, hard spheres for pore volume fractions in the range 0.3 to 0.4 show (i) that the mean pore radius  $r'_{\text{pore}}$  (based on the average radius of a particle which will insert at different points in the pore space) scales with the particle radius according to  $r'_{\text{pore}} = k r_{\text{particle}}$ , and (ii) that the scaling coefficient  $k$  increases with increasing pore volume fraction (mean  $r'_{\text{pore}} \approx 0.14 \times r_{\text{particle}}$  for  $\phi_{\text{pore}} = 0.3$  and mean  $r'_{\text{pore}} \approx 0.24 \times r_{\text{particle}}$  for  $\phi_{\text{pore}} = 0.4$ )<sup>11</sup>. If it is assumed that the mean (hydrodynamically-equivalent) pore radius  $r_{\text{pore}}$  of the calcite powder packed columns scales linearly with  $r_{\text{particle}}$  despite their polydispersity and irregular shape (i.e.  $r_{\text{pore}} = k r_{\text{particle}}$ ), it is expected that the results for the different powders will show different values of the scaling coefficient  $k$  because of the different values of  $\phi_{\text{pore}}$ . As seen in Figure 3.3, the scaling coefficients estimated for the calcite powders range from 0.114 for  $\phi_{\text{pore}} = 0.45$  to 0.030 for  $\phi_{\text{pore}} = 0.34$ , i.e. the packed calcite powders give mean pore radii which are approximately 4 fold smaller than monodisperse, spherical particles of the same radius which are randomly close packed at the same pore volume fraction. Two factors are likely to contribute to this difference. Firstly, the mean value of  $r'_{\text{pore}}$  in the computer simulations (based on the average size of particle which can be inserted into different points in the pore space) is not directly equivalent to the mean  $r_{\text{pore}}$  for the calcite powders which is based on a hydrodynamically equivalent pore radius). Secondly, the calcite particles are polydisperse which seems likely to lead to a reduced mean pore radius relative to the monodisperse hard spheres used in the computer simulations (as smaller particles fill in the gaps between the bigger particles).

**Figure 3.3** Variation of packed column average effective pore radius ( $r_{\text{pore}}$ , derived as described in section 3.2.3) with the mean radius of the calcite particles packed in the column ( $r_{\text{particle}}$ ). For FC10, both water and decane flow measurements were used to determine  $r_{\text{pore}}$ . The diagonal lines correspond to the linear scaling relationships:  $r_{\text{pore}} = 0.114 r_{\text{particle}}$  (upper line for FC10 with  $r_{\text{particle}} = 1.4 \mu\text{m}$  and  $\phi_{\text{pore}} = 0.45$ ),  $r_{\text{pore}} = 0.066 r_{\text{particle}}$  (middle line for FC30 with  $r_{\text{particle}} = 5.0 \mu\text{m}$  and  $\phi_{\text{pore}} = 0.40$ ) and  $r_{\text{pore}} = 0.030 r_{\text{particle}}$  ( $r_{\text{pore}} = 0.030 r_{\text{particle}}$  (lower line for FC200 with  $r_{\text{particle}} = 23 \mu\text{m}$  and  $\phi_{\text{pore}} = 0.34$ ).



The columns were packed manually and it is assumed that the particle distribution is random. A consistent procedure was developed, and the experimentally determined variation in  $\phi_{\text{pore}}$  was approximately  $0.01 \phi_{\text{pore}}$ . While the overall porosity value is consistent, the pore size distribution within the column and between each new packed column is not known and this uncertainty will be kept in mind when interpreting the oil recovery plots in later chapters.

### 3.2.4 Comparison of experimental model conditions to field conditions

Table 3.1 compares the porosity, permeability and pore sizes of the experimental model system with some examples of rock cores used in other surfactant flood experiments. In the majority of studies commercial rock cores are cut from the outcrop rock rather than from the actual reservoir rock as the former is more easily available, and significantly less expensive and not subject to commercial confidentiality. These rock cores are taken to be representative of at least parts of the actual reservoir. Both the porosity and permeability of the experimental model system used here are within range of the rock core values used in the references shown. Pore sizes within rock cores can vary greatly from submicron to the mm scale. Some pores will be from the natural porosity of the rock, and some from the fractures in the rocks.

**Table 3.1** Comparison between the experimental model system used in this work with some examples of field conditions.

Parameter	Experimental model conditions	Field conditions
Porosity	FC10 – 0.45 FC30 – 0.40 FC200 – 0.34	0.27 – 0.30 (non-fractured core) (ref 12) 0.15 (reservoir carbonate) (ref 13)
Permeability	FC10 – 1.2 mD FC30 – 5.5 mD FC200 – 21 mD	2-4 mD (ref 12) 32.7 mD (ref 13)
Pore sizes ( $r_{\text{pore}}$ )	FC10 – 0.16 $\mu\text{m}$ FC30 – 0.33 $\mu\text{m}$ FC200 – 0.69 $\mu\text{m}$	From submicron to mm (refs 14-15)

In order to simplify any comparisons between the multiple systems investigated throughout this work, all of the experiments throughout the rest of this thesis use the FC10 calcite, unless otherwise stated.

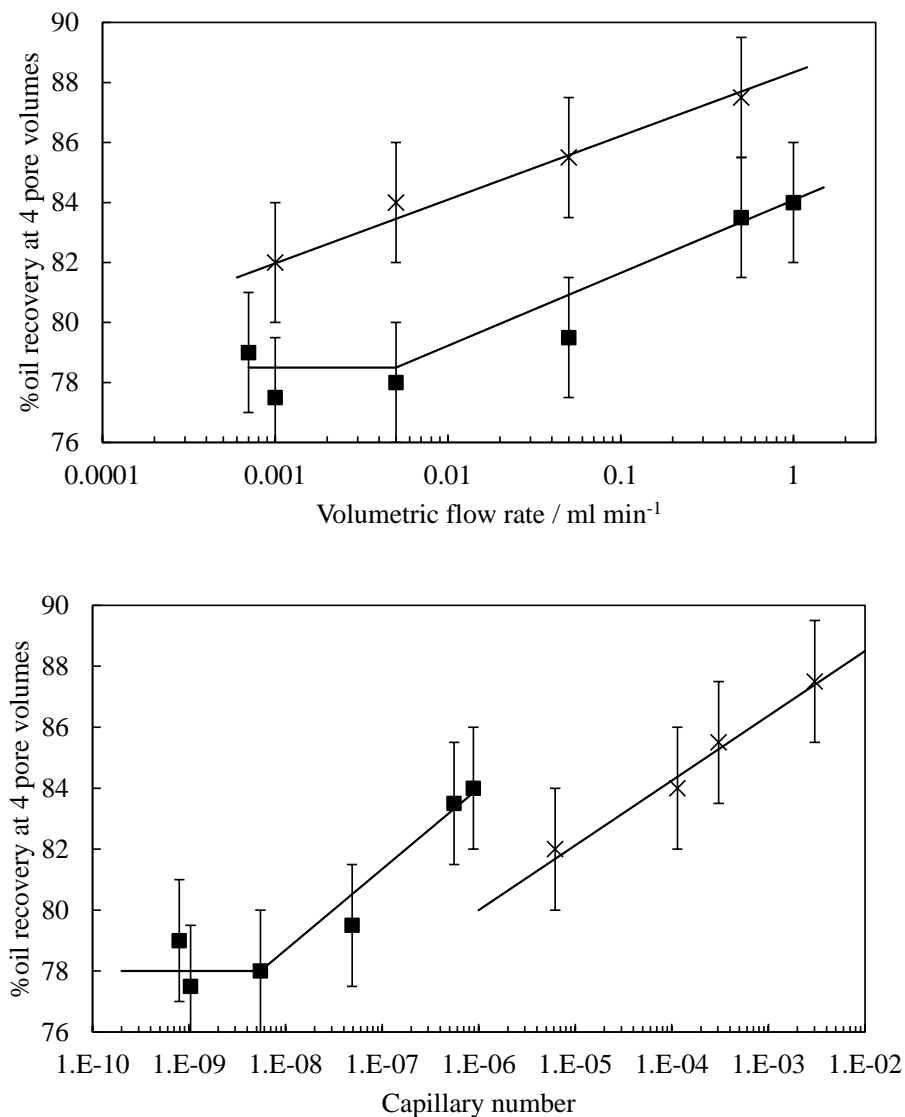
### 3.3 Effect of flow rate and gravity on oil recovery – capillary and bond numbers

As described in the experimental section, most oil removal experiments were made by pumping aqueous solution at a fixed flow rate of  $5 \mu\text{l min}^{-1}$  into the packed columns. This volumetric flow rate corresponds to an average linear velocity of the pumped fluid through the column  $u$  (equal to  $Q/\Phi_{\text{pore}}A$ ) of approximately  $2.5 \times 10^{-6} \text{ m s}^{-1}$  (equal to 0.7 feet per day), similar to actual field conditions<sup>16</sup>. The interplay of pumped fluid velocity (determining viscous forces) and pore-scale capillary effects on the oil mobilisation is normally discussed in terms of the capillary number  $Ca$  which is the ratio of viscous and capillary forces acting on a fluid element. It is expected that, when  $Ca$  is  $<1$ , flow is dominated by capillary effects and oil is trapped in the porous network. Oil is released when  $Ca > 1$  and the flow is dominated by viscous effects. However, as discussed in ref 17, the correct estimation of  $Ca$  for multiphase flow in a porous network has been a long-standing controversy because of the difficulty of estimating the viscous and capillary forces over identical and correct length scales. In the EOR field,  $Ca$  is commonly defined as  $u\mu/\gamma_{\text{oil-water}}$ , for which the velocity  $u$  is an average value over a macroscopic length scale. According to this definition of  $Ca$ , oil mobilisation under typical field conditions occurs for  $Ca$  values greater than about  $10^{-5}$  to  $10^{-7}$ , much less than the expected threshold value of  $Ca$  equal to unity. In addition, the threshold value of  $Ca$  depends on the morphology of the porous network, its wettability and its oil and water content in ways which are not completely understood. Hence, although  $Ca$  provides some useful correlations to interpret the variation of oil recovery with fluid velocity, viscosity and oil-water tension, there are severe difficulties in using it for quantitative predictions.

Qualitatively, it is expected that the amount of oil recovery (after injection of  $>1$  pore volume) should be independent of pumped fluid flow rate when  $Ca$  is very low and to increase with flow rate at high values of  $Ca$ . As seen in Figure 3.5, the oil recovery using pure water is independent of flow rate below  $0.005 \text{ ml min}^{-1}$ . This corresponds to a threshold value of  $Ca$  of approximately  $6 \times 10^{-9}$  ( $\gamma_{\text{oil-water}}$  is  $42.5 \text{ mN m}^{-1}$ ). When surfactant solution is used, the plot shows no flow rate independent region between  $0.001$  and  $0.5 \text{ ml min}^{-1}$  since  $\gamma_{\text{oil-water}}$  is  $0.0078 \text{ mN m}^{-1}$  (as discussed in Chapter 4), giving  $Ca$  values in the much higher range of  $5 \times 10^{-6}$  to  $3 \times 10^{-3}$ . Overall, it can be seen that for a constant imposed flow rate of  $0.005 \text{ ml min}^{-1}$  as used for the majority of oil recovery experiments, systems with higher interfacial tensions (typically experienced when surfactant concentration  $< c_{\text{uc}}$ ) lie within the low  $Ca$  regime in which oil trapping is

expected. Systems with low to ultra-low interfacial tensions (often occurring when surfactant concentration  $\geq$   $c_{uc}$ ) lie within the high Ca regime for which oil drop break-off and mobilisation is expected.

**Figure 3.5** Upper plot: Variation of %oil recovery after 4 pore volumes versus flow rate for water (filled squares) and 10 mM AOT, 75 mM NaCl and 10 mM Na<sub>2</sub> CO<sub>3</sub> (crosses) pumped into an FC10 packed column initially containing decane. The lower plot shows the same oil recovery data plotted versus capillary number.



The bond number for all systems were found to be less than  $3 \times 10^{-4}$ . Thus, the effect of gravity is presumed to be minimal. This was confirmed by carrying out displacement floods with the column held both horizontal and vertically, with no difference found between the oil recovery at each orientation.

### 3.4 Conclusions

The properties of columns packed with polydisperse, low axial ratio and irregularly shaped calcite particles of three different mean sizes have been determined, with particular focus on the porosity, permeability and pore sizes. It was found that with an increase in mean particle size, the porosity decreases slightly, the permeability increases and the pore sizes increase. When compared with computer simulations of randomly close packed monodisperse hard spheres with the same radius and same volume fraction, the calcite packed columns give mean pore volumes which are approximately 4 fold smaller. The properties (porosity, permeability and pore sizes) of the experimental model system were found to be similar to some examples of field conditions.

For high oil-water interfacial tension displacement floods a transition from flow rate independent, to flow rate dependent oil recovery was found with increasing flow rate. This transition was found to be at a capillary number of approximately  $6 \times 10^{-9}$ . When a flow rate of  $5 \mu\text{l min}^{-1}$  is used, high oil-water interfacial tension floods are in the low capillary number regime ( $< 6 \times 10^{-9}$ ), whereas low/ultra-low oil-water interfacial tension floods lie in the high capillary number regime ( $> 6 \times 10^{-9}$ ). Hence, a transition between the two regimes is expected with increasing surfactant concentration, as will be seen in later chapters. The Bond number was calculated to be less than  $3 \times 10^{-4}$ , and there was no difference found between oil recovery floods carried out with the column in different orientations, thus the effect of gravity on oil recovery was concluded to be negligible.

### 3.5 References

1. Standnes, D.C., Austad, T., Wettability alteration in chalk 1. Preparation of core material and oil properties, *J. Petroleum. Sci. Eng.*, **2000**, 28, 111.
2. Standnes, D.C.; Austad, T. Wettability alteration in chalk. 2. Mechanism for wettability alteration from oil-wet to water-wet using surfactants. *J. Petroleum Sci. Eng.*, **2000**, 28, 123.
3. Standnes, D.C.; Austad, T. Wettability alteration in carbonates. Low-cost ammonium surfactants based on bio-derivatives from the coconut palm as active chemicals to change the wettability from oil-wet to water-wet conditions. *Colloids Surfaces A*, **2003**, 218, 161.
4. Al-Sulaimani, H.; Al-Wahaibi, Y.; Al-Bahry, S.; Elshafie, A.; Al-Benani, A. Residual-oil recovery through injection of biosurfactant, chemical surfactant and mixtures of both under reservoir temperatures: induced-wettability and interfacial-tension effects. *SPE Reservoir Eval. Eng.*, **2012**, 15, 210.
5. Stoll, W.M.; al Shureqi, H.; Finol, J.; Al-Harthy, S.A.A.; Oyemade, S.; de Kruijf, A.; van Wunnik, J.; Arkesteijn, F.; Bouwmeester, R.; Faber, M.J. Alkaline/surfactant/polymer flood: from the laboratory to the field. *Soc. Petroleum Eng. J.*, **2011**, 14, 702
6. Babadagli, T., Al-Bemani, A., Boukadi, F., Al-Maamari, R., A laboratory feasibility study of dilute surfactant injection for the Yibal field, Oman, *J. Petroleum Sci. Eng.*, **2005**, 48, 37.
7. *CRC Handbook of Chemistry and Physics*, CRC Press/Taylor and Francis, Boca Raton, 89th edn., 2008.
8. Kozeny, J., Ueber kapillare Leitung des Wassers im Boden, *Wien. Akad. Wiss.*, **1927**, 136, 271.
9. Carman, P.C., Fluid flow through granular beds, *Trans. Instn. Chem. Engrs.*, **1937**, 15, S32.

10. Fletcher, P.D.I.; Haswell, S.J.; He, P.; Kelly, S.M.; Mansfield, A., Permeability of silica monoliths containing micro- and nano-pores. *J. Porous Mater.*, **2011**, *18*, 501.
11. Baranau, V., Hlushkou, D., Khirevich, S. and Tallarek, U., Pore-size entropy of random hard-sphere packings, *Soft Matter*, **2013**, *9*, 3361.
12. Babadagli, T., Evaluation of the critical parameters in oil recovery from fractured chalks by surfactant injection, *J. Pet. Sci. Eng.*, **2006**, *54*, 43.
13. Blunt, M.J., Bijeljic, B., Dong, H., Gharbi, O., Iglauer, S., Mostaghimi, P., Paluszny, A. and Pentland, C., Pore-scale imaging and modelling, *Adv. Water Resour.*, **2013**, *51*, 197.
14. Bera, B., Mitra, S.K., Vick, D., Understanding the micro structure of Berea Sandstone by the simultaneous use of micro-computed tomography (micro-CT) and focussed ion beam-scanning electron microscopy (FIB-SEM), *Micron*, **2011**, *42*, 412.
15. Bera, B., Gunda, N.S.K., Mitra, S.K., Vick, D., Characterization of nanometer-scale porosity in reservoir carbonate rock by focussed ion beam-scanning electron microscopy, *Microsc. Microanal.*, **2012**, *18*, 171.
16. Morrow, N.R., Mason, G., Recovery of oil by spontaneous imbibition. *Curr. Opin. Colloid Interface Sci.*, **2001**, *6*, 321.
17. Armstrong, R.T., Georgiadis, A., Ott, H., Klemin, D., Berg, S., Critical capillary number: desaturation studied with fast X-ray computed microtomography. *Geophys. Res. Lett.*, 2014, **41**, 55.

## CHAPTER 4

# MODELLING DECANE REMOVAL FROM A CALCITE PACKED COLUMN USING AQUEOUS SOLUTIONS OF THE ANIONIC SURFACTANT AOT

### 4.1 Introduction

Chapter 3 discusses how the calcite packed columns were characterised in detail and compared to field conditions. The next steps required to improve understanding of how flooding with aqueous solutions of surfactant can increase oil recovery are to characterise in detail a) the phase behaviour of aqueous solutions of the surfactant and b) the effects of surfactant concentration on the parameters which define the Laplace pressure, one of the main causes for oil becoming trapped in oil reservoirs (other effects such as flow bypassing of oil filled regions due to heterogeneous permeability can also be important but are not studied here). This characterisation requires determining: the effects of surfactant concentration on the adsorption at the three interfaces of the experimental model system (the water-calcite, water-oil and oil-calcite interfaces); how this adsorption alters the interfacial tensions of the three interfaces; and how this in turn alters the three phase contact angle. Further, it is necessary to determine other physicochemical properties such as the critical aggregation concentrations and the equilibrium phases of aqueous solutions containing surfactant both in the presence of and absence of oil. These parameters are then used to understand the oil recovery behaviour when a calcite packed column filled with decane (Chapter 3) is flooded at a constant flow rate with an aqueous solution. In practical terms, it is easier for a liquid-liquid interface to measure the change in tension and calculate the adsorbed amount but for a solid-liquid interface to measure the adsorption and calculate the change in tension.

This chapter discusses, firstly, the characterisation of a system consisting of water-decane-calcite-AOT with three different salt concentrations, in terms of the equilibrium microemulsion behaviour, aqueous phase behaviour, adsorption at the water-calcite interface, changes in the water-decane interfacial tension and the change in the three-phase contact angle as a function of AOT concentration. As it has previously been shown that the partitioning of AOT from water to alkanes is negligible, there is no measurement of the adsorption at and the subsequent change in the decane-calcite tension, as with no

partitioning of the AOT to the decane there can be no adsorption at the decane-calcite interface<sup>1</sup>. Following the experimental results, it will be shown how the contact angles and interfacial tensions can be derived from considerations of the initial surface energies of the three components and adsorption of the AOT.

Following the discussions of this characterisation, it will be shown how the %oil recovery from the packed column varies with surfactant concentration (for one of the salt concentrations, the two remaining salt concentrations will be discussed at the end of the chapter). Prior to interpretation of the %oil recovery results, it is important to note that theoretical interpretations of all the characterisation data relate to the equilibrium free (non-adsorbed) surfactant concentration. For the measurements of the interfacial tensions and contact angles, the surface area to volume ratio (calcite surface area to volume of aqueous phase) is low and thus the extent of surfactant depletion due to adsorption at the calcite-water interface is negligible, hence the initial surfactant concentration ( $[\text{surf}]_{\text{init}}$ ) is approximately equal to the free surfactant concentration ( $[\text{surf}]_{\text{free}}$ ). For the adsorption isotherm measurements, the surface area to volume ratio is high and thus the extent of surfactant loss due to depletion is no longer negligible and  $[\text{surf}]_{\text{init}}$  is not approximately equal to  $[\text{surf}]_{\text{free}}$ , however the  $[\text{surf}]_{\text{free}}$  is determined experimentally. The surface area to volume ratio for %oil recovery experiments is also high, and there is no experimental determination of the  $[\text{surf}]_{\text{free}}$ , hence, a model is derived to show how surfactant adsorption measurements can be used to estimate the concentration of free surfactant present within the packed columns during flooding, and hence allow direct comparison between characterisation results and %oil recovery results.

Finally, a second two-part model is derived to show how, based on the hypothesis that the residual oil is trapped in the form of liquid bridges between contacting calcite particles, the measured %oil recovery variation with surfactant concentration can be understood and predicted for concentrations of surfactant both below and above the  $c_{\text{MC}}$  in terms of the characterisation results, such as the calcite-water-oil contact angle and the water-decane interfacial tensions. Model predictions are compared with the experimental data for all three salt concentrations used.

## 4.2 Microemulsion phase inversion and aqueous phase composition in the presence and absence of decane

Before determining the effects of the surfactant concentration on adsorption at the water-calcite and the water-decane interfaces and the subsequent changes in the interfacial tensions and three-phase contact angle, it is useful to determine the type of microemulsions expected to be formed when the water phase containing a concentration of surfactant in excess of the  $c_{\mu c}$  is contacted with the oil, and to understand the behaviour of the surfactant in the aqueous phase without the presence of the oil.

The phase behaviour of AOT solutions in the presence of oils has been well characterised in the literature. Aveyard et al. have shown that for a system consisting of AOT-water-heptane-NaCl at 25 °C, when the concentration of AOT is below the  $c_{\mu c}$ , the partitioning of AOT monomers into the heptane for systems containing 17.1 to 102.7 mM NaCl is negligible<sup>1</sup>. They also show that with an NaCl concentration of 17.1 mM, when the AOT concentration is raised above the  $c_{\mu c}$  all of the AOT still remains in the water phase, thus indicating the formation of an oil-in-water microemulsion (as the aggregates into which the heptane solubilises are formed in the water). For systems containing 51.3 and 102.7 mM NaCl, they see that when the AOT concentration is raised to above the  $c_{\mu c}$ , the concentration in the aqueous phase remains constant, indicating that the excess AOT forms aggregates in either a separate middle phase or in the oil phase, indicating the formation of either a bicontinuous or a water-in-oil microemulsion.

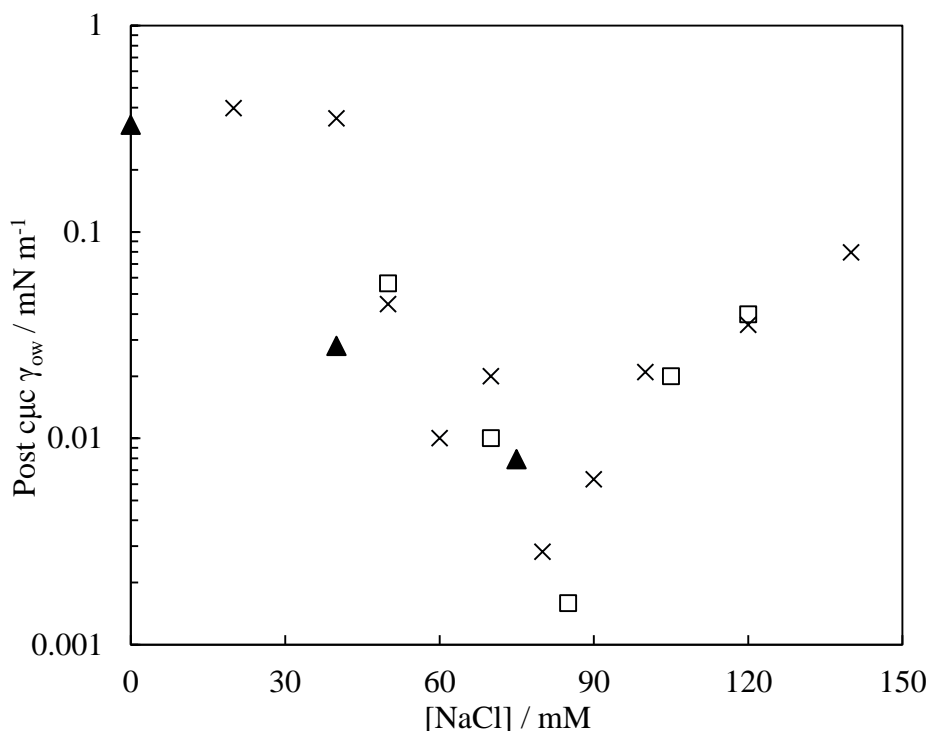
Binks has taken the same AOT-water-heptane-NaCl system at 25 °C (as above) with a greater range of NaCl concentrations and determined both the points of microemulsion and emulsion phase inversion<sup>2</sup>. They found that between 0 and 25 mM NaCl and with an AOT concentration  $>c_{\mu c}$ , a WI system is formed, which when homogenised forms an oil in water emulsion. At an NaCl concentration of 50 mM and AOT concentration  $>c_{\mu c}$ , a WIII system is formed: they found it difficult to determine which emulsion type was formed on homogenisation of these systems. Between NaCl concentrations of 100 and 140 mM NaCl and AOT concentrations  $>c_{\mu c}$ , a WII system was formed, which when homogenised formed a water-in-oil emulsion.

It is well established that as a water-oil-surfactant system goes through microemulsion phase inversion, the water-oil interfacial tension reaches a minimum. Aveyard et al. have shown how the chain length of n-alkanes affects the salt concentration at which this

minimum in the water-oil interfacial tension occurs and how low the tension drops too<sup>3</sup>. They show that with an increase in chain length, the salt concentration at which the minimum occurs increases. Thus, when comparing the current work (which uses decane) to refs 1-2 (which use heptane), the salt concentrations at which microemulsion phase inversion will occur is expected to be higher.

Both Aveyard et al.<sup>4</sup> and Binks<sup>5</sup> have determined the variation of the decane-water interfacial tension for an AOT-water-decane-NaCl system, as a function of NaCl concentration at 25 °C with AOT concentrations in excess of the  $c_{\mu c}$ . Figure 4.1 shows the tension data from those studies (minimum at approximately 85 mM NaCl) and includes the data from this work (from section 4.4.2, filled triangles). The small differences between the data for this current work and the work by Aveyard et al. and Binks probably comes the presence of  $\text{Na}_2\text{CO}_3$  (which is not included in the salinity concentration as the degree of dissociation was not determined). Even so, the general trends are seen to be observed.

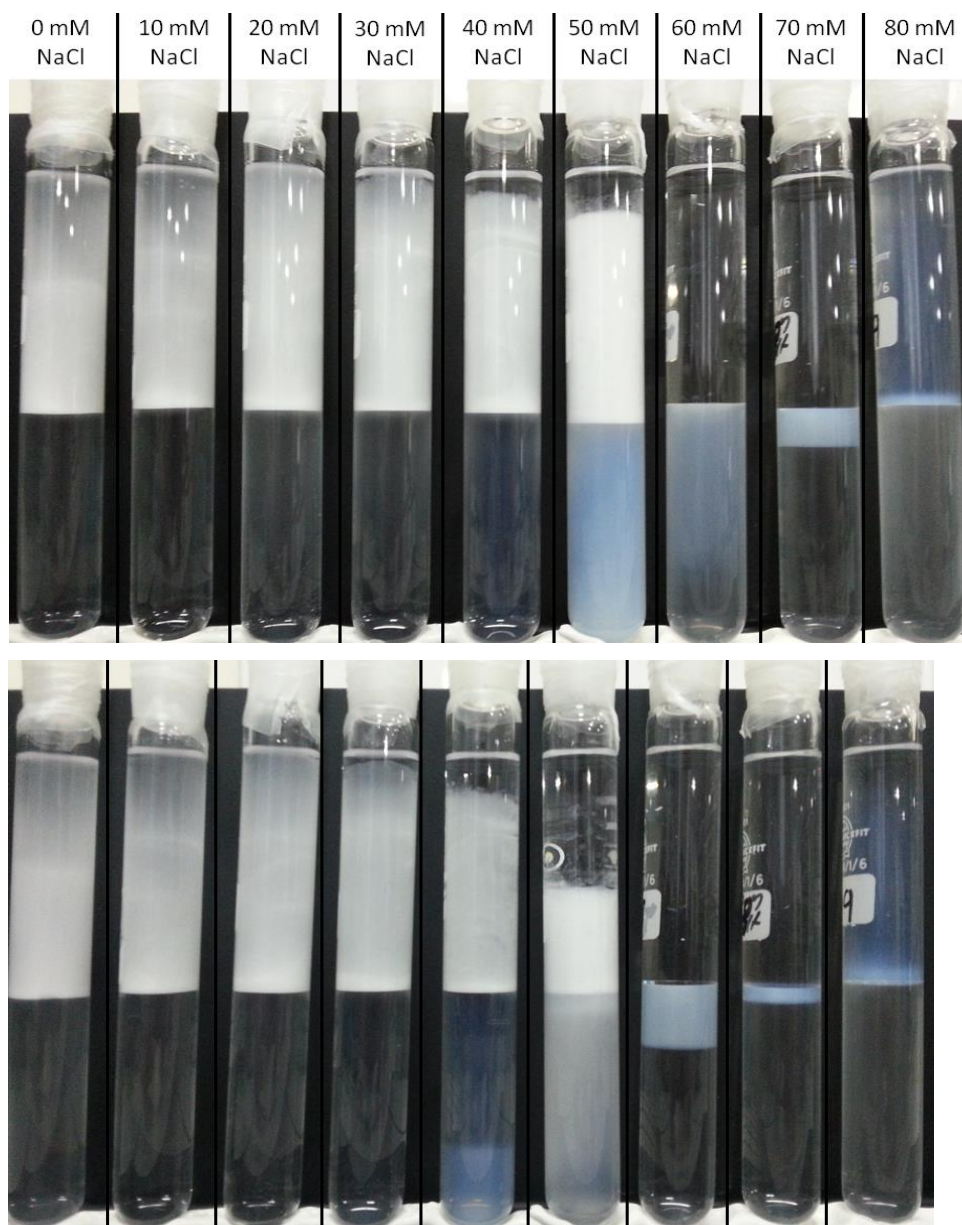
**Figure 4.1** Water-decane interfacial tensions for systems containing AOT in excess of the  $c_{\mu c}$  at 25 °C as a function of NaCl concentration. The crosses refer to data from ref 4, the squares from ref 5 and the triangles from this current work.



For the early work of Binks, for a system consisting of AOT-water-decane-NaCl at 25 °C and AOT concentration  $> c_{\mu c}$ , between [NaCl] 0 and approximately 60 mM a WI system is formed, between approximately 60 mM and approximately 90 mM NaCl a WIII system is formed, and above approximately 90 mM a WII system is formed.

Figure 4.2 shows tubes containing a 1:1 volume ratio of water:decane with the water containing concentrations of AOT  $> c_{\mu c}$ , 10 mM Na<sub>2</sub>CO<sub>3</sub> and varying concentrations of NaCl. The tubes were inverted and left to equilibrate as described in Chapter 2. Between NaCl concentrations of 0 to 40 mM, the decane phase (upper phase) contains some un-resolved emulsion (the breakdown of which increases between 15 and 40 hours of equilibration in some cases), and the water phase has a slight blue colour particularly at higher salt concentrations and after 40 hours of equilibration (indicative of a microemulsion). With an NaCl concentration of 50 mM both phases appear to contain some un-resolved emulsion. Between NaCl concentrations of 60 and 70 mM, a clear third middle phase is observed (particularly after 40 hours of equilibration), indicative of a WIII system. At 80 mM NaCl, the decane appears to contain some un-resolved emulsion even after 40 hours of equilibration, however, a denser blueish region in the middle can be seen, presumably indicating a WIII system (consistent with references 1-5). For the concentrations of NaCl used here (0 to 80 mM), no clear WII system was observed, consistent with ref. 5, where a WII system was reported to occur at [NaCl]  $\geq$  90 mM.

**Figure 4.2** Microemulsion phase tubes of water and decane in a 1:1 volume ratio with 5 mM AOT and 10 mM  $\text{Na}_2\text{CO}_3$  plus the concentrations of NaCl shown (all concentrations in the water phase). The top photo is after 15 hours equilibration and the bottom photo after 40 hours equilibration at 25 °C.



It is important to note that, as in the case of surfactant EOR flooding generally, the aqueous AOT solutions used in the particle packed column experiments are not pre-equilibrated with the decane phase (though some research has been carried out with pre-formed microemulsion flooding<sup>6</sup>). Aqueous solutions containing the salt concentrations shown and AOT concentrations above a critical aggregation concentration ( $c_{ac}$ ) (with values generally similar to the aqueous phase  $c_{\mu c}$ ) prior to equilibration with decane form a turbid aqueous dispersion of lamellar phase, probably in the form of multilamellar, “onion-like” vesicles<sup>7-8</sup>. On equilibration with decane, these mixtures form the microemulsion systems discussed above.

The majority of oil recovery floods throughout this work were carried out with the aqueous phases that were not pre-equilibrated with the oil. However, some experiments were carried out with aqueous solutions that were pre-equilibrated with the oil (in order to remove the lamellar phases). In the systems discussed in this Chapter, no difference was seen between the two types of flood (probably due to the effect of solubilisation being much less than the effect of emulsification, see section 4.5.3.4).

All further experiments were carried out using three different salt concentrations, giving two different Winsor systems upon equilibration of the water phase with excess decane (and a large difference in post  $c_{\mu c}$  decane-water interfacial tension). The salt concentrations which were used for the following experiments and the Winsor systems they form are shown in Table 4.1.

**Table 4.1** The salt concentrations and corresponding Winsor system types formed upon equilibration of the aqueous phase containing a concentration of AOT  $>c_{\mu c}$  with excess decane at 25 °C for the three systems characterised in detail in the following work. All systems also contain 10 mM Na<sub>2</sub>CO<sub>3</sub> in the aqueous phase.

<b>[NaCl] /mM</b>	<b>Winsor system type</b>
0	I
40	I
75	III

### 4.3 Effect of AOT concentration on adsorption to the calcite-water interface, and the altering of the decane-water interfacial tension and calcite-decane-water contact angle

#### 4.3.1 Adsorption of AOT to the calcite-water interface

Figure 4.3 shows the adsorption isotherms for AOT from aqueous solutions to the calcite-water interface. In order to minimise the effect of degradation a lower pH of  $9.3 \pm 0.3$  was used (lower than the unadjusted pH of the solutions). Some measurements were made at pH 10.8 and found to differ only for the measurements with lower AOT concentrations. The difference was found to be due to the extent of degradation (determined by extrapolation of the data in Appendix A). Qualitatively, the adsorption of AOT monomers is weak until just below the critical *aggregation* concentration of the AOT (expected to be similar to the critical *microemulsion* concentrations listed in Table 4.3 for the different systems). Above this point there is a highly co-operative adsorption to form adsorbed films with surface concentrations of around 2 molecules  $\text{nm}^{-2}$ .

In order to understand this trend, it is necessary to know the charge at the calcite-water interface. The iso-electric point (the pH at which the calcite-water interface has no net charge) of the calcite-water interface has been discussed in the literature for decades<sup>9-16</sup>. The main issue appears to stem from the multiple equilibria pathways that can be present in a calcite-water system, and how these equilibria can be affected by parameters such as the partial pressure of  $\text{CO}_2$ . Further complications in the system used here comes from the use of  $\text{Na}_2\text{CO}_3$  and the contribution this can make to the equilibria pathways already present. An approximate isoelectric point value from the literature is pH 9.5, which is within the range of pH values used here (9.0 to 10.8). Hence, the charge on the calcite is likely to be close to zero, though, if any surface charge was to be expected it would most likely be negative due to the presence of  $\text{Na}_2\text{CO}_3$  as a result of specific adsorption by carbonate<sup>16</sup>. Hence, the driving force for AOT adsorption is not likely to include strong electrostatic interaction but is likely to be dominated by hydrophobic interactions (also likely if the surface is negatively charged as the negatively charged heads are not likely to adsorb). Hence, the system shows a highly co-operative adsorption at AOT concentrations similar to the relevant *cac* as the surfactants form aggregates on the surface of the calcite<sup>17</sup>.

Following trials with several different theoretical adsorption isotherms<sup>18-20</sup>, the plots of Figure 4.3 were found to fit best to a Langmuir-type isotherm modified to take account of cooperative (and anti-cooperative) adsorption through the parameter  $\beta$  (equation 4.1)<sup>18</sup>.

$$[\text{surf}]_{\text{free}} = \frac{(\Gamma/\Gamma_{\text{max}})}{(1 - (\Gamma/\Gamma_{\text{max}})) \cdot K_L \cdot e^{-\beta\Gamma/\Gamma_{\text{max}}}} \quad (4.1)$$

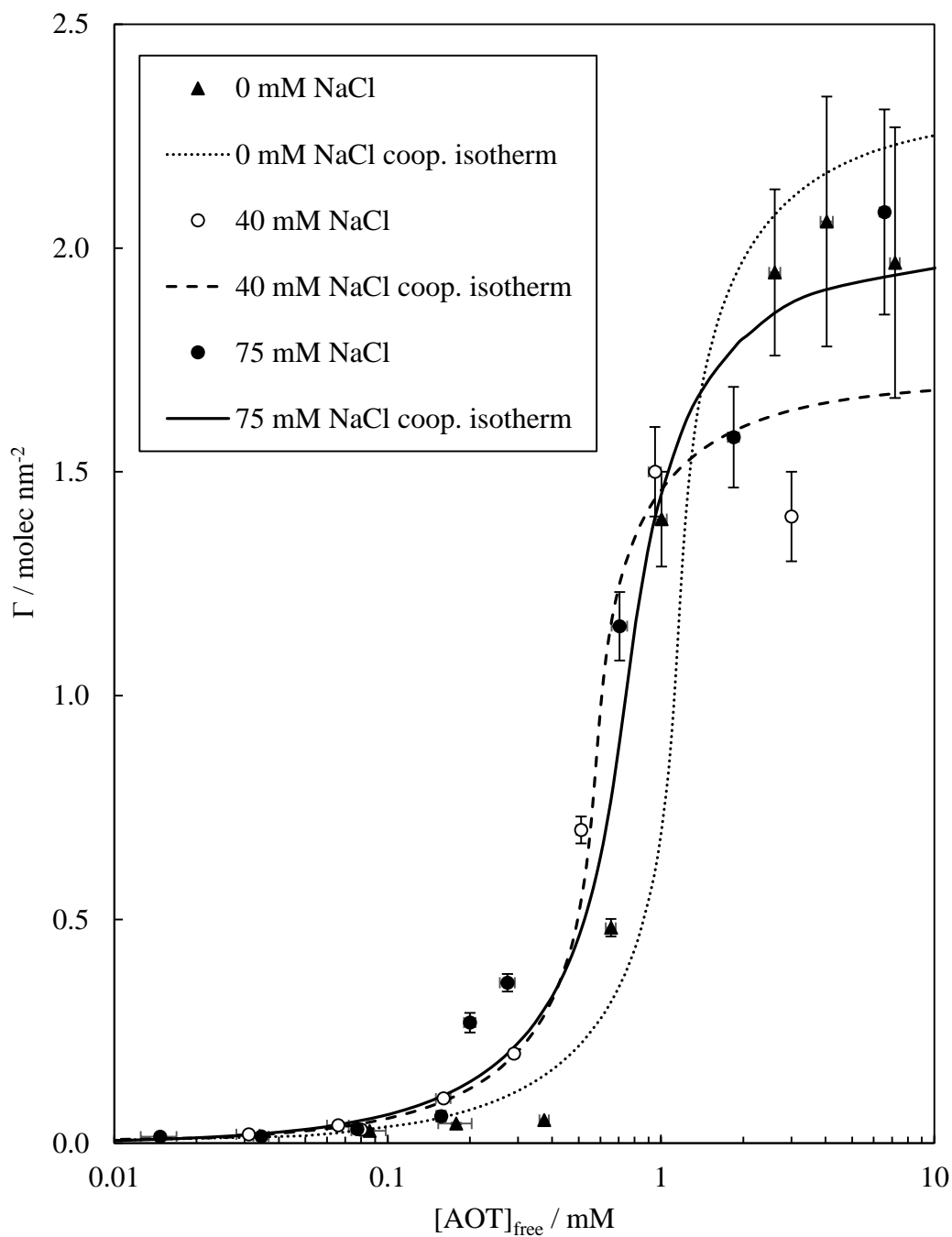
where  $[\text{surf}]_{\text{free}}$  is the equilibrium concentration of non-adsorbed surfactant,  $\Gamma$  is the surface concentration of adsorbed surfactant,  $\Gamma_{\text{max}}$  is the maximum surface concentration,  $K$  is a constant reflecting the strength of adsorption and  $\beta$  is the cooperativity parameter. When  $\beta$  is equal to zero, the isotherm reduces to the Langmuir isotherm;  $\beta > 0$  corresponds to anti-co-operative adsorption and  $\beta < 0$  corresponds to co-operative adsorption.

The fitting parameters for the system with the different salt concentrations are shown in Table 4.2. The fitting parameters are similar for all three systems, with the main variation being in the  $K$  parameter due to the different cac values (from  $K = 0.15 \text{ mM}^{-1}$  for the system containing 0 mM NaCl, to  $K = 0.35 \text{ mM}^{-1}$  for the system containing 75 mM NaCl). The adsorption isotherms of Figure 4.3 are similar to those seen in a previous study of AOT adsorption on calcite<sup>21</sup>.

**Table 4.2** Fitting parameters for fitting the Langmuir type adsorption isotherm (equation 4.1) to the experimental data for AOT from water containing 10 mM  $\text{Na}_2\text{CO}_3$  to the calcite-water interface at different  $[\text{NaCl}]$  (Figure 4.3).

$[\text{NaCl}] / \text{mM}$	$\Gamma_{\text{max}} / \text{molecules nm}^{-2}$	$K / \text{mM}^{-1}$	$\beta$
0	2.3	0.15	-3.5
40	2.0	0.30	-3.5
75	2.2	0.35	-3.5

**Figure 4.3** Adsorption isotherms for the adsorption of AOT to the calcite-aqueous solution interface from aqueous solutions at pH  $9.3 \pm 0.3$  and containing 10 mM  $\text{Na}_2\text{CO}_3$  plus the NaCl concentrations indicated at 25.0 °C. The curved lines show the best fits to the cooperative isotherm (equation 4.1) with the parameters given in table 4.2.



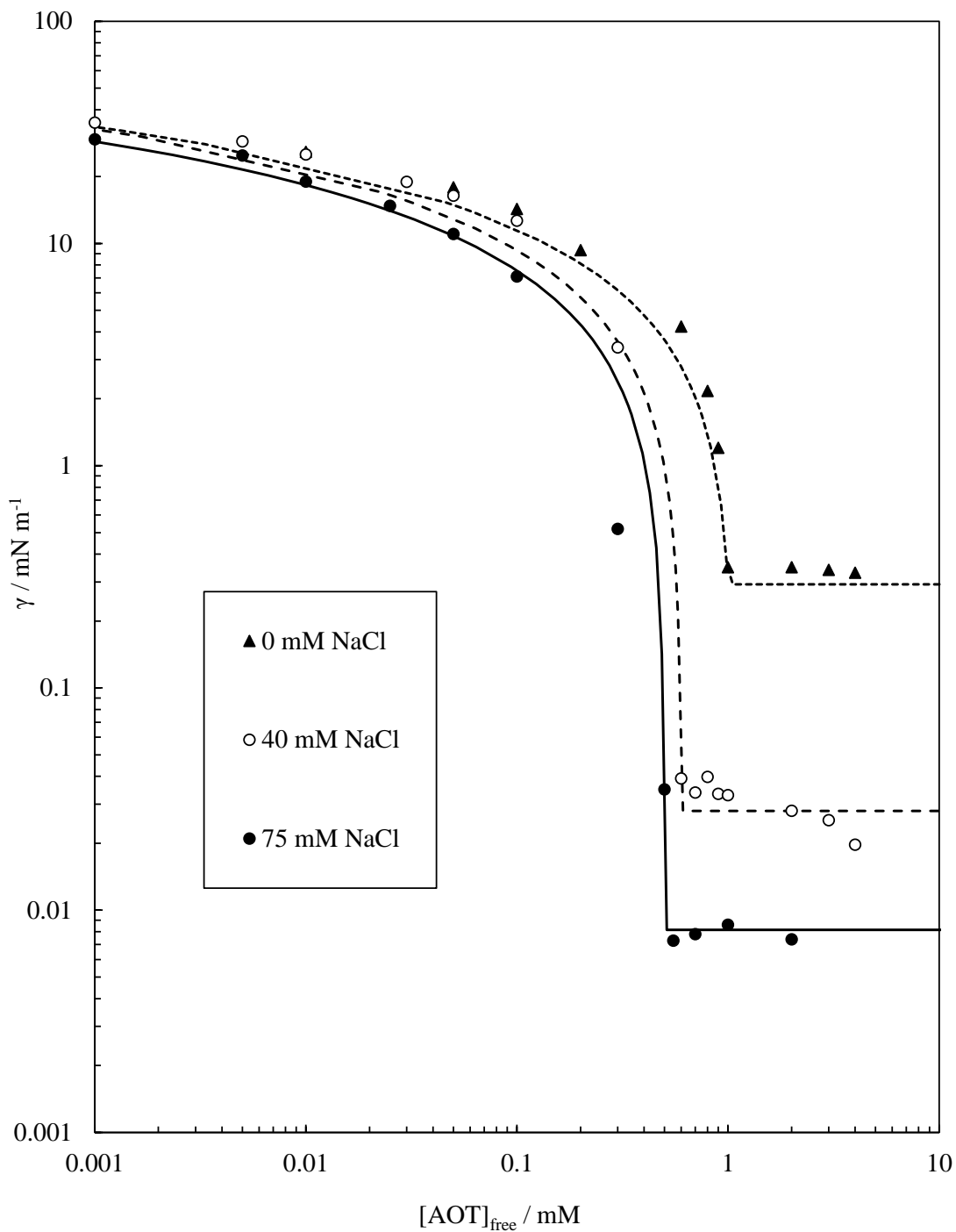
#### 4.3.2 Effect of AOT concentration on the decane-water interfacial tension

Figure 4.4 shows the variation of the decane-water tension with AOT concentration for the three different salt concentrations used (all containing 10 mM Na<sub>2</sub>CO<sub>3</sub> + NaCl indicated). Due to adsorption of AOT monomers at the water-decane interface, the tension decreases from 42.5 mN m<sup>-1</sup> (in the absence of AOT) to a value independent of AOT concentration at the c<sub>μc</sub>. Above the c<sub>μc</sub> the tension is constant as the AOT in excess of the c<sub>μc</sub> forms microemulsion aggregates which do not adsorb at the water-decane interface. As summarised in Table 4.3, the c<sub>μc</sub> and the post-c<sub>μc</sub> interfacial tensions depend on the salt concentration. The post-c<sub>μc</sub> interfacial tension values are in good agreement with both Aveyard et. al.<sup>4</sup> and with Binks<sup>5</sup>. The trend for decreasing interfacial tension with increasing salt is consistent with the change from a Winsor I to a Winsor III system as discussed in section 4.2.

**Table 4.3** A summary of the equilibrium Winsor type behaviour, the post-c<sub>μc</sub> water-decane tension and the aqueous phase c<sub>μc</sub> for the three salt concentrations investigated.

[NaCl] /mM	Winsor system type	Post-c <sub>μc</sub> water-decane interfacial tension /mN m <sup>-1</sup>	Aqueous phase c <sub>μc</sub> (with decane) /mM
0	I	0.33	1.0
40	I	0.028	0.60
75	III	0.0079	0.50

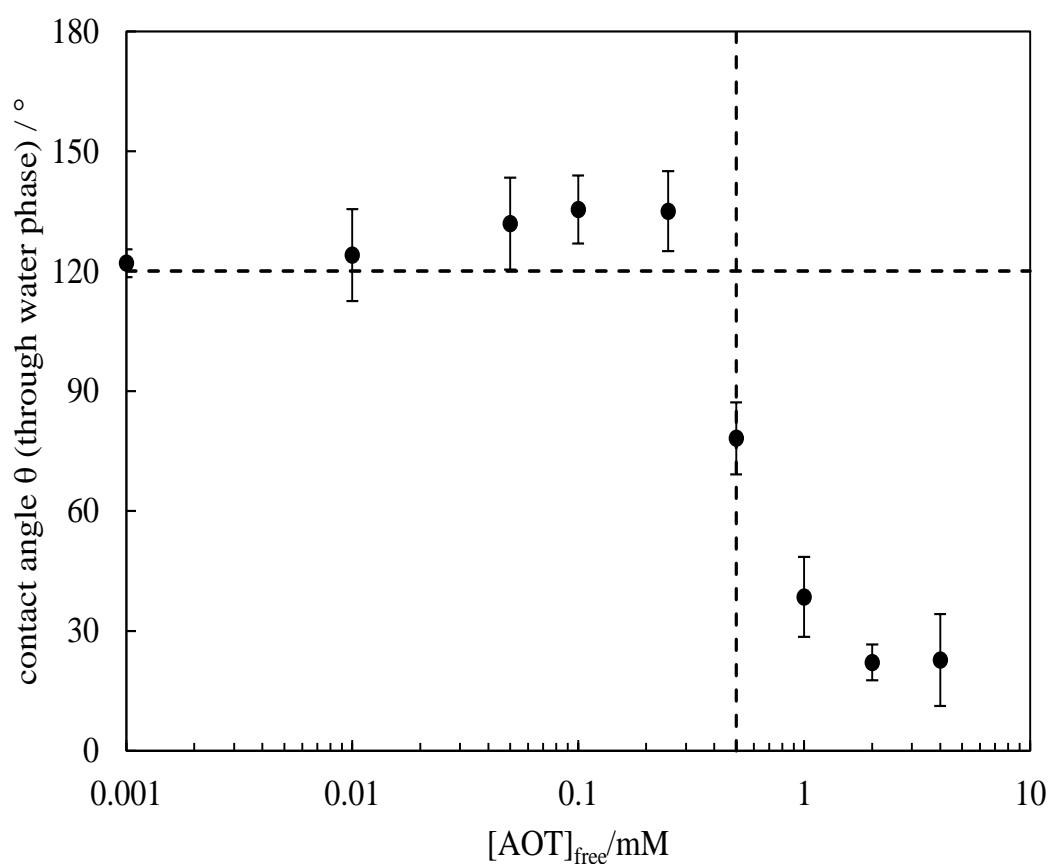
**Figure 4.4** Variation of decane-water tension with aqueous AOT concentration at 25.0°C for solutions containing 10 mM Na<sub>2</sub>CO<sub>3</sub> plus the NaCl concentrations indicated. The lines show the best-fits calculated as described in the text (section 4.3.4).



### 4.3.3 Effect of AOT concentration on the water-calcite-decane contact angle

For the 75 mM NaCl system, the decane-water-calcite contact angle (measured through the water) is  $120 \pm 10^\circ$  in the absence of AOT. As seen in Figure 4.5, the contact angle increases slightly with increasing [AOT], decreases sharply around the  $c_{\mu c}$  and finally decreases slightly further before reaching a high [AOT] plateau value of approximately  $20^\circ$ . The contact angle behaviour of the systems containing 0 and 40 mM NaCl (not shown) is qualitatively similar (differing only in the position of the sudden drop due to the different  $c_{\mu c}$  values); therefore, for clarity, the following discussions focus on the 75 mM NaCl system. The significance and cause of the slight increase and sudden decrease in the contact angle is discussed in the following section.

**Figure 4.5** Variation of decane-water-calcite contact angle (measured through the aqueous phase) with aqueous AOT concentration for solutions containing 75 mM NaCl and 10 mM  $\text{Na}_2\text{CO}_3$  at 25 °C. The vertical dashed line indicates the  $c_{\mu c}$  and the horizontal dashed line shows the contact angle in the absence of added AOT.



#### 4.3.4 Modelling the effect of AOT adsorption on the interfacial tensions and three phase contact angle

The equilibrium calcite-water-decane contact angle is determined by the relative magnitudes of the calcite-water, decane-water and calcite-decane interfacial tensions. The three interfacial tensions in the absence of AOT can be estimated using considerations of the polar and dispersion force contributions to the excess surface energies (surface tensions) of each component. The interfacial surface energy of any substance x against air ( $\gamma_{x\text{-air}}$ ) can be expressed as the sum of the components arising from the polar and dispersion forces ( $\gamma^p$  and  $\gamma^d$  respectively) as shown in equation 4.2<sup>22-28</sup>.

$$\gamma_{x\text{-air}} = \gamma_{x\text{-air}}^p + \gamma_{x\text{-air}}^d \quad (4.2)$$

Values of  $\gamma^p$  and  $\gamma^d$  derived from tension and contact angles and other methods are available in the literature. Values ( $\gamma^p$  and  $\gamma^d$  respectively) are 50.4 and 21.5 mJ m<sup>-2</sup> for water<sup>22</sup>, 0 and 23.8 mJ m<sup>-2</sup> for decane<sup>22</sup> and 10.2 and 22.9 mJ m<sup>-2</sup> for calcite<sup>23</sup>. It should be noted that the values quoted for calcite depend strongly on the thermal pre-treatment and state of hydration of the calcite surface<sup>23,29-32</sup>. The values used here correspond to water-saturated calcite since this is most likely to correspond to the calcite powders in the packed column flooding experiments. If the surface energies of two components x and y against air are known, the x-y interfacial energy can be calculated using<sup>22</sup>:

$$\gamma_{x-y} = \gamma_{x\text{-air}} + \gamma_{y\text{-air}} - 2\sqrt{\gamma_{x\text{-air}}^p \gamma_{y\text{-air}}^p} - 2\sqrt{\gamma_{x\text{-air}}^d \gamma_{y\text{-air}}^d} \quad (4.3)$$

Using equation 4.3 and the surface energy components noted above, the three interfacial tensions in the absence of surfactant were calculated;  $\gamma_{\text{decane-water},0} = 50.5$ ,  $\gamma_{\text{calcite-water},0} = 15.3$  and  $\gamma_{\text{decane-calcite},0} = 10.2$  mN m<sup>-1</sup>. From the three interfacial tensions, the water-calcite-decane contact angle  $\theta$  (through the water) is given by Young's equation.

$$\cos\theta = \frac{\gamma_{\text{calcite-decane}} - \gamma_{\text{calcite-water}}}{\gamma_{\text{water-decane}}} \quad (4.4)$$

which yields a value of 96° for pure water, slightly lower than but comparable with the value of 120±10° measured for water containing 10 mM Na<sub>2</sub>CO<sub>3</sub> and 75 mM NaCl.

In order to calculate the variation of contact angle with surfactant concentration, the variation of the three interfacial tensions with surfactant concentration must be estimated. The decane-water tension as a function of AOT concentration is measured directly. As mentioned in the introduction to this chapter, it is known that AOT monomers do not partition to a measureable extent from aqueous solution containing NaCl to alkane solvents and hence it is assumed here that  $\gamma_{\text{decane-calcite}}$  remains equal to its value in the absence of AOT  $\gamma_{\text{decane-calcite},0}$  for all AOT concentrations<sup>1</sup>. For the calcite-water interface, the tension as a function of AOT concentration is obtained by integration of the measured adsorption isotherm according to the Gibbs adsorption equation<sup>33</sup>. The isotherm given in equation 4.1 is not readily integrated so, the simpler Langmuir isotherm is used instead, in combination with the Gibbs adsorption equation. The starting point is replacing  $\Gamma$  in the Gibbs adsorption equation (Chapter 1 equation 1.9) with the Langmuir isotherm equation (Chapter 1 equation 1.8) to give equation 4.5.

$$\Gamma = \frac{\Gamma_{\text{max}} K[\text{surf}]_{\text{free}}}{1 + K[\text{surf}]_{\text{free}}} = - \frac{1}{kT} \frac{d\gamma}{d \ln[\text{surf}]_{\text{free}}} \quad (4.5)$$

Rearrangement of equation 4.5 leads to equation 4.6, followed by integration to give equation 4.7.

$$\left( \frac{-kT\Gamma_{\text{max}} K[\text{surf}]_{\text{free}}}{1 + K[\text{surf}]_{\text{free}}} \right) d[\text{surf}]_{\text{free}} = d\gamma \quad (4.6)$$

$$-kT\Gamma_{\text{max}} K \frac{1}{K} \ln(1 + K[\text{surf}]_{\text{free}}) = \gamma + \text{COI} \quad (4.7)$$

where COI is the constant of integration. At  $[\text{surf}]_{\text{free}} = 0$ ,  $\gamma = \gamma_0$ , hence  $0 = \gamma_0 + \text{COI}$ , and  $\text{COI} = -\gamma_0$ . Hence equation 4.8 becomes apparent.

$$\gamma = \gamma_0 - kT\Gamma_{\text{max}} \ln(1 + K[\text{surf}]_{\text{free}}) \quad (4.8)$$

Equation 4.8 then allows the modelling of the change in interfacial tensions by fitting the equation to the experimental data using the Langmuir isotherm parameters. Hence, adsorption isotherms can be backed out from interfacial tension experimental data, and interfacial tensions backed out from adsorption isotherm experimental data. Although the Langmuir isotherm is not the best fit to the adsorption data for calcite-water adsorption at low concentrations, it still captures where most of the adsorption occurs at

the higher concentrations. As it is at the point of higher adsorption where the tension changes the most, the fitting manages to capture the change in tension with enough precision for the current study.

Figure 4.6 shows the three interfacial tensions estimated as described above and the corresponding variation of derived contact angle  $\theta$  with AOT concentration and comparison with the measured angles. The adsorption and corresponding interfacial tensions for the water-decane interface are calculated only for AOT monomers (where above the  $c_{\mu c}$  the concentration remains constant) as it was shown in section 4.3.2 that the aggregates do not adsorb. The Langmuir parameters were varied to obtain the best fit to the experimental interfacial tension results. For the calculation of the adsorption and subsequent change in the interfacial tension at the calcite-water interface the total AOT concentration is used (including aggregates) as the experimental data shows that there is some adsorption above the  $c_{ac}$  (due to aggregates forming on the surface). The Langmuir parameters were varied to obtain the best fit to the experimental adsorption data. As mentioned, the adsorption and subsequent change in the decane-calcite interfacial tension was not considered as it was reported that AOT does not partition to alkanes to a measurable extent<sup>1</sup>. The final fitting parameters and complete set of graphs can be seen in Appendix C.

Despite the large uncertainty in the surface energy components of calcite and the use of the Langmuir isotherm which is not an ideal fit to the experimental calcite-water adsorption data, the calculated plot correctly predicts the slight increase in contact angle as [AOT] approaches the  $c_{\mu c}$  (due to the decrease in the decane-water interfacial tension) and the sharp decrease in  $\theta$  at [AOT]  $\approx c_{\mu c}$  (due to the calcite-water tension dropping below the calcite-decane tension in the presence of an ultralow decane-water tension). For [AOT]  $> c_{\mu c}$ , the calculations predict that  $\theta = 0^\circ$  whereas the measured values are in the range 40-20°.

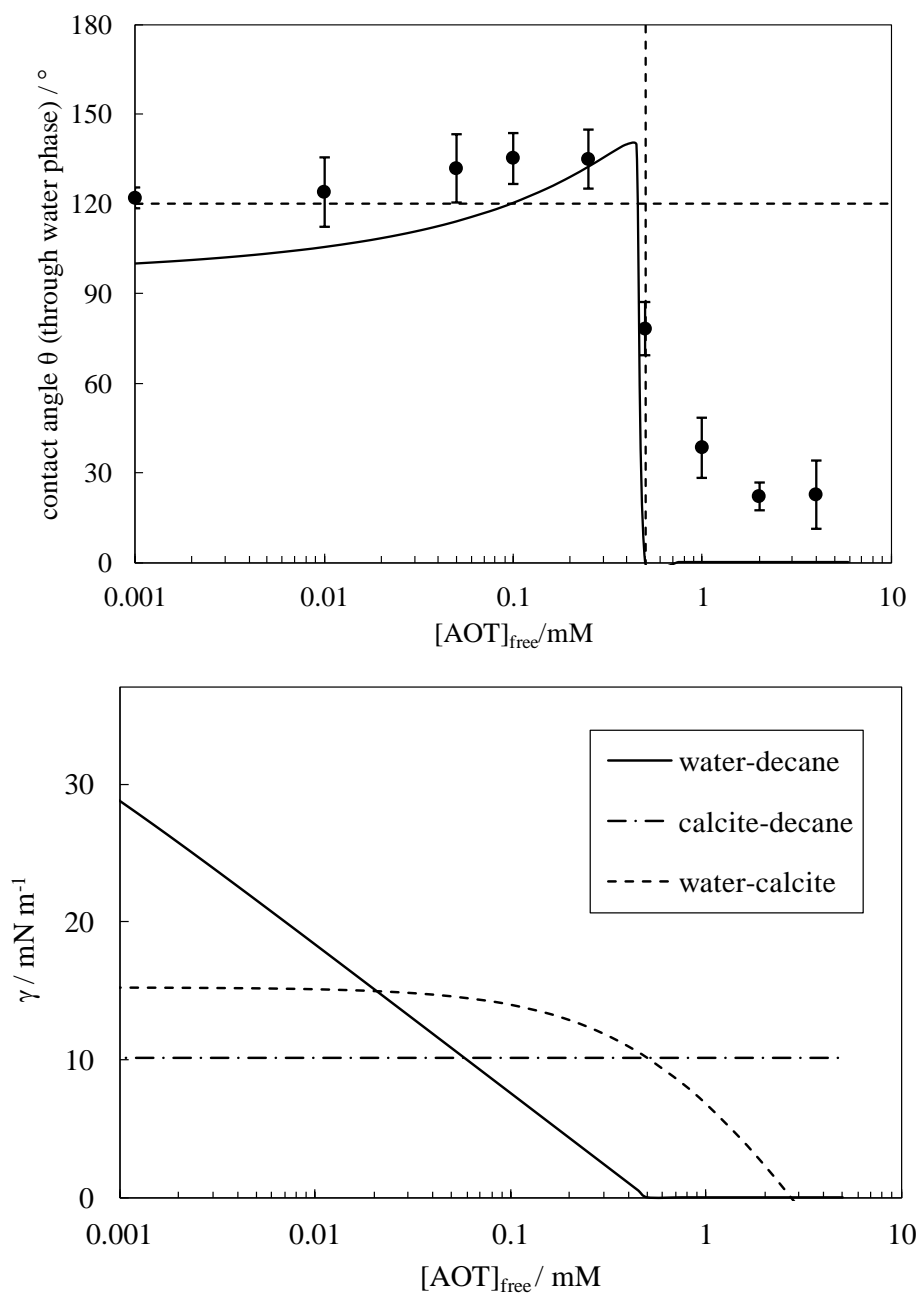
There are multiple possibilities as to why this difference occurs. It has been well discussed as to whether a true equilibrium contact angle is ever achieved, in which case the contact angles above the  $c_{\mu c}$  may not actually be the true equilibrium values, and thus will not match up with the contact angles predicted with the use of Young's equation (which assumes true equilibrium)<sup>34</sup>. Another complication is that the formation of a thin film of the oil on the calcite surface, or reorientation of molecules (oil or surfactant) at

the calcite surface, meaning that the actual interfacial tension between the calcite-water or calcite-oil is between the water or oil and the thin film or reoriented molecules, as opposed to the water and the calcite.<sup>35</sup>

Another possible reason for this discrepancy could be that the assumption of no AOT adsorption from decane to the decane-calcite interface (based on the observed lack of partitioning of AOT from aqueous NaCl solution to alkanes<sup>1</sup>) may not be valid in the presence of calcium carbonate. Leaching of calcium ions from the calcite might produce  $\text{Ca}(\text{AOT})_2$  species that may partition to decane and adsorb at the decane-calcite interface. Such partitioning and adsorption could potentially decrease  $\gamma_{\text{decane-calcite}}$  and increase  $\theta$  at high [AOT].

Additional considerations of how surfactants can affect contact angles relevant to EOR, e.g. solid surface roughness and surfactant mixture effects are described in refs. 36-37.

**Figure 4.6** Upper plot: Variation of decane-water-calcite advanced static contact angle (measured through the aqueous phase) tension with aqueous AOT concentration for solutions containing 75 mM NaCl and 10 mM Na<sub>2</sub>CO<sub>3</sub> at 25 °C. The vertical dashed line indicates the  $c_{\mu c}$ . The horizontal dashed lined shows the contact angle in the absence of added AOT. The solid line shows the calculated contact angle from the water-decane (measured), water-calcite (derived from the measured adsorption isotherm) and decane-calcite (invariant with [AOT]) tensions shown in the lower plot. The tensions are modelled with equation 4.8, the fitting parameters can be found in Appendix C.



#### 4.3.5 Overview of systems to be used for oil recovery experiments

An overview of the key parameters for the three characterised systems that were used for the oil recovery experiments in the following sections are summarised in table 4.4. The three systems produce two different equilibrium Winsor systems, three different values of the  $c_{\mu c}$ , vastly different post- $c_{\mu c}$  water-decane interfacial tensions and very similar three-phase contact angle behaviour. The vast differences in the post- $c_{\mu c}$  water-decane interfacial tensions should produce some differences in the oil recovery performances of each system.

**Table 4.4** An overview of all the properties determined for each water-decane-calcite-AOT system containing the three different salt concentrations plus 10 mM  $\text{Na}_2\text{CO}_3$  at 25 °C and between a pH of 9.0 to 10.8.

[NaCl] / mM	0	40	75
<b>Aqueous phase <math>c_{\mu c}</math> / mM</b>	1.0	0.60	0.50
<b>Winsor system type formed with 1:1 aqueous phase:decane</b>	I	I	III
<b>Post <math>c_{\mu c}</math> water-decane interfacial tension / <math>\text{mN m}^{-1}</math></b>	0.33	0.028	0.0079
<b>Measured calcite-water-decane <math>\theta</math> through water in absence of AOT (<math>\pm 15</math>) / °</b>	123	126	120
<b>Measured calcite-water-decane <math>\theta</math> through water post <math>c_{\mu c}</math> (<math>\pm 15</math>) / °</b>	37	31	22

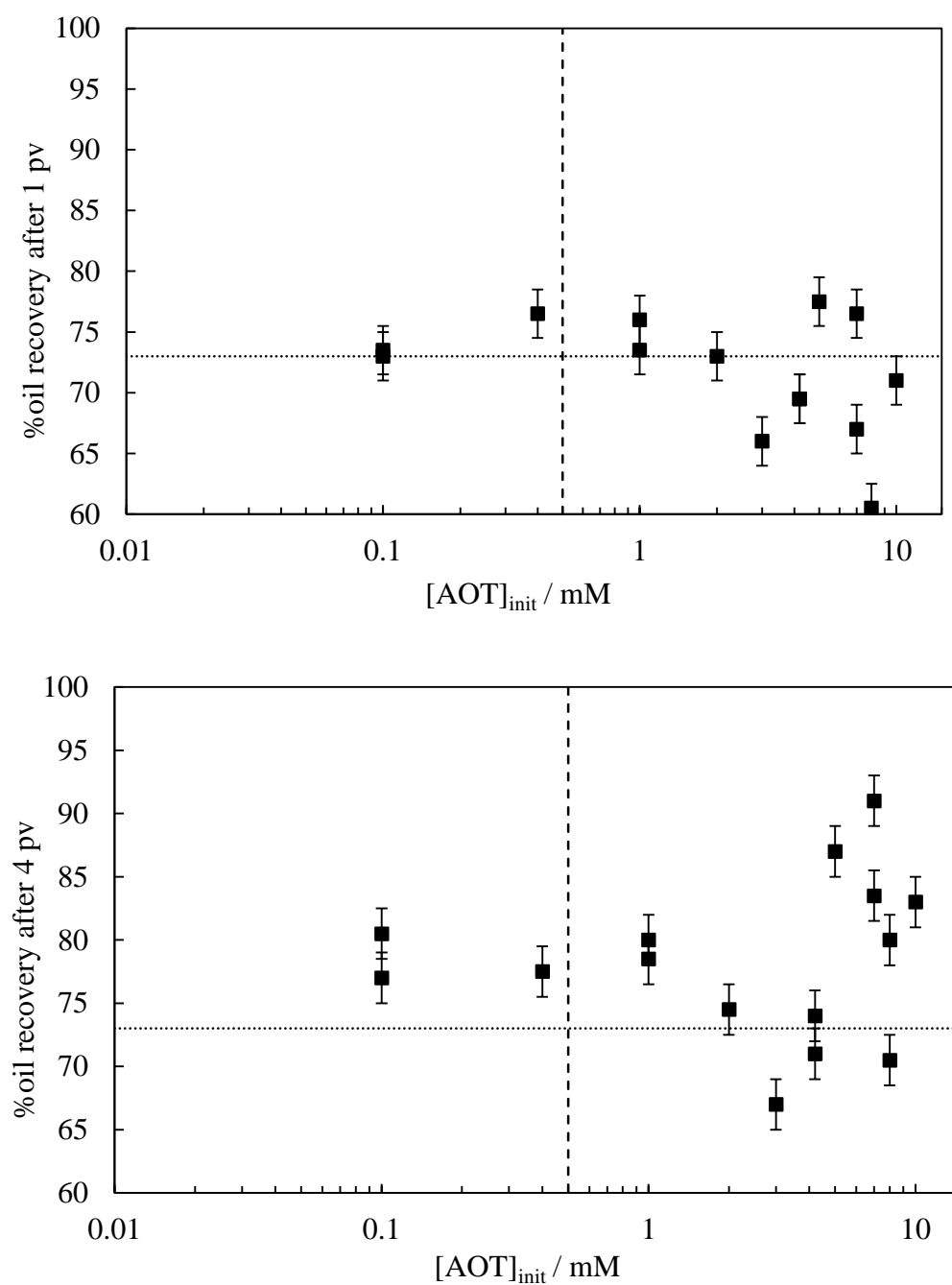
## 4.4 Decane removal from calcite packed columns

### 4.4.1 *Experimental results and the need for a model*

Figure 4.7 shows the experimental results for flooding aqueous solutions of AOT containing 75 mM NaCl and 10 mM Na<sub>2</sub>CO<sub>3</sub> through an FC10 packed column with interstices filled with decane at a flow rate of 5  $\mu\text{l min}^{-1}$  and at 25 °C. Both after 1 pore volume and 4 pore volumes of flooding, up to and even some time after the c<sub>μc</sub> there is no significant change in oil recovery. This observation is initially surprising, as although there is no definitive consensus in the literature on how the oil-water interfacial tension and three-phase contact angle effect oil recovery, some change at the c<sub>μc</sub> where both of these parameters change dramatically might be expected, particularly as in this case where the contact angle changes from above to below 90° resulting in a change in the sign of the Laplace pressure. At approximately 1 mM (twice the c<sub>μc</sub>) the oil recovery starts to drop to a minimum at approximately 3 mM, followed by a sudden increase. Again, this is surprising, as above the c<sub>μc</sub> where all of these changes occur, the contact angle and oil-water interfacial tension (and adsorption at the interfaces) remains constant, and by association, so does the Laplace pressure. Thus, if the remaining oil is trapped in some way by the Laplace, then something is clearly occurring which means that the surfactant concentration pumped in to the column is not directly related to the surfactant concentration seen in Figures 4.3-4.6 (as discussed briefly in the introduction of this chapter). Thus, in order to interpret the oil recovery plots in Figure 4.7, two models will be derived. The first to correct the concentrations to be equivalent to the concentrations in Figures 4.3-4.6 (section 4.5.2), and the second two-part model used to model the % oil recovery at the different oil-water interfacial tensions and three-phase contact angles encountered (section 4.5.3).

The difference in oil recovery between the two plots in Figure 4.7 will be discussed in section 4.4.3. In order to simplify discussions, all further oil recovery plots discussed will be for the oil recovery after 4 pore volumes of aqueous flooding.

**Figure 4.7** Oil recovery as a function of initial concentration of AOT pumped in to an FC10 packed column with interstices filled with decane for the system containing 75 mM NaCl and 10 mM Na<sub>2</sub>CO<sub>3</sub> at a flow rate of 5 μl min<sup>-1</sup> after 1 pore volume (top) and 4 pore volumes (bottom). The vertical dashed line is the c<sub>μc</sub> and the horizontal dotted line the oil recovery with no surfactant present (and only the salt)



#### 4.4.2 *Derivation of model to calculate concentration of free (non-adsorbed) surfactant in particle packed columns*

As mentioned in section 4.1, the problem that occurs when attempting to interpret the oil recovery data in terms of the adsorption, interfacial tension and contact angle data, is due to the large surface area to volume ratio. Adsorption then leads to a large difference between the initial surfactant concentration pumped in to the column ( $[\text{surf}]_{\text{init}}$ ) and the concentration of non-adsorbed, or free surfactant in the bulk of the water ( $[\text{surf}]_{\text{free}}$ ). As it is  $[\text{surf}]_{\text{free}}$  which is relevant for the adsorption, interfacial tension and contact angle experiments, it is necessary to calculate the  $[\text{surf}]_{\text{free}}$  from the  $[\text{surf}]_{\text{init}}$ . To do this a model was developed, based on a mass balance assumption, initially only considering the surfactant depleted due to adsorption at the calcite-water interface (excluding adsorption at the oil-water interface). The assumptions of the model are as follows;

1. The initial surfactant concentration,  $[\text{surf}]_{\text{init}}$ , is equal to the concentration of surfactant that is adsorbed,  $[\text{surf}]_{\text{adsorbed}}$ , plus the concentration of surfactant that is free,  $[\text{surf}]_{\text{free}}$ .
2. The adsorption of surfactant to the calcite-water interface reaches its equilibrium value.
3. The adsorbed amount of surfactant,  $\Gamma$ , remains constant with consecutive pore volumes of the surfactant solution flooded through the column.

The first assumption is likely to be true in most cases. The most relevant case in which it may not hold is that of if the surfactant is degrading. By extrapolation of the data in Appendix A, the amount of AOT degradation predicted in these floods is not likely to cause a large deviation from this assumption within the error of the experiment. The second assumption is quite probable given the large surface area to volume ratio allowing for the AOT to come in to contact with the calcite surface, thus minimising rate limiting steps such as diffusion through the water from slowing the adsorption process down. Finally, the last assumption of a constant  $\Gamma$  value, whilst it may be an over simplification, within the error of the experiment it seems likely that it will hold true. For a dynamic system such as the one in question here, some simplifications like this have to be made in order for an analytical solution to be developed without the need for long computations and repetitive algorithms. A second simplification made to allow for the analytical derivation is that the model will calculate the overall moles free (and hence  $[\text{surf}]_{\text{free}}$ ) between the start of the column up to and including the waste. This

simplification does not then take in to account any concentration gradients that may occur across the column<sup>38</sup>. It also means that the increase in  $[\text{surf}]_{\text{free}}$  with the number of pore volumes pumped may differ a little from that predicted as discussed later. Once again, this simplification allows for a much simpler model to be developed which should be able to provide a reasonable explanation for experimental results within the error of the experiment.

The derivation begins with defining the total number moles of surfactant in the system (equation 4.9) followed by the moles of this that are adsorbed (equation 4.10) and non-adsorbed (or free) (equation 4.11).

$$\text{Total Moles} = n\phi_{\text{pore}} V_{\text{total}} [\text{surf}]_{\text{init}} \quad (4.9)$$

$$\text{Moles Adsorbed} = (1 - \phi_{\text{pore}}) V_{\text{total}} f A_{\text{particle}} \rho \frac{\Gamma}{N_{\text{AV}}} \quad (4.10)$$

$$\text{Moles non-adsorbed} = V_{\text{total}} \left( n\phi_{\text{pore}} [\text{surf}]_{\text{init}} - (1 - \phi_{\text{pore}}) V_{\text{total}} f A_{\text{particle}} \rho \frac{\Gamma}{N_{\text{AV}}} \right) \quad (4.11)$$

where  $n$  is the number of pore volumes pumped,  $\phi_{\text{pore}}$  the volume fraction of interstitial pores (between particles) in the column,  $V_{\text{total}}$  the total internal volume of the column,  $f$  the fraction of the particle surface accessible to the water,  $A_{\text{particle}}$  the specific surface area of the particles (the surface area per unit mass),  $\rho$  the density of the particles, and  $N_{\text{AV}}$  Avogadro's number. Using equation 4.10 for the moles adsorbed (and hence, by conversion,  $[\text{surf}]_{\text{adsorbed}}$ ) and the mass balance assumption (equation 4.12), equation 4.13 is derived, where the numerator of the fraction calculates the sum of the moles free and moles adsorbed and the denominator simply converts this to concentration.

$$[\text{surf}]_{\text{init}} = [\text{surf}]_{\text{free}} + [\text{surf}]_{\text{adsorbed}} \quad (4.12)$$

$$[\text{surf}]_{\text{init}} = \frac{\left( n\phi_{\text{pore}} [\text{surf}]_{\text{free}} + (1 - \phi_{\text{pore}}) f A_{\text{particle}} \rho \frac{\Gamma}{N_{\text{AV}}} \right)}{n\phi_{\text{pore}}} \quad (4.13)$$

The relationship between  $[\text{surf}]_{\text{free}}$  and adsorbed surface concentration  $\Gamma$  is given by the adsorption isotherm (equation 4.1),  $A_{\text{particle}}$  and  $\phi_{\text{pore}}$  are separately measured (Chapter 2 and 3), the calcite density is  $2.71 \text{ g cm}^{-3}$  and so the only unknown parameter is  $f$ . The model described in section 4.4.3 enables the estimation of  $f$  which depends on the fraction of oil remaining in the column. For the range of %oil recovery values

measured here,  $f$  is estimated to be in the range 0.3 – 0.6. In order to simplify the calculations, a mean value of  $f = 0.4$  was used in all cases (unless otherwise stated) to convert the values of  $[\text{surf}]_{\text{init}}$  to  $[\text{surf}]_{\text{free}}$  on the plots of % oil recovery versus surfactant concentration. Due to the errors which may arise from this more simplistic approach, it was deemed not necessary to take in to account the adsorption at the oil-water interface as the accuracy of the model is not great enough to enable clear differentiation between the relative interfacial areas of all the interfaces.

This scale transformation enables the values of % oil recovery to be linked directly with the corresponding values of interfacial tensions, contact angles and critical aggregation concentrations. In addition, the difference ( $[\text{surf}]_{\text{init}} - [\text{surf}]_{\text{free}}$ ) provides a measure of the “wasted” surfactant which is retained by the packed column and is therefore likely to provide an important input into the assessment of the economic viability of the oil recovery process.

Figure 4.8 shows the relationship between  $[\text{AOT}]_{\text{free}}$  and  $[\text{AOT}]_{\text{init}}$  for flooding of the AOT solutions containing 75 mM NaCl through an FC10 packed column. At low concentrations, the relationship is linear where the adsorption corresponds to the small linear increase in the adsorption isotherms in Figure 4.3. When the sudden increase in adsorption occurs at the cac (0.50 mM  $[\text{AOT}]_{\text{free}}$ ), although there is an increase in  $[\text{AOT}]_{\text{init}}$ , there is little increase in  $[\text{AOT}]_{\text{free}}$ . As the adsorption approaches the plateau value, the  $[\text{AOT}]_{\text{free}}$  starts to increase again. At very high concentrations, as the adsorbed amount remains the same and the  $[\text{AOT}]_{\text{free}}$  increases, the effect of the adsorption decreases.

By taking the ratio between  $[\text{AOT}]_{\text{init}}$  and  $[\text{AOT}]_{\text{free}}$ , a more quantitative view of how much surfactant is depleted by adsorption at the calcite-water interface can be determined. For instance, in the case of 1 pore volume having been pumped through the column, in the region of a linear increase in adsorption with surfactant concentration it is seen that the  $[\text{AOT}]_{\text{free}}$  is approximately 12 times less than the  $[\text{AOT}]_{\text{init}}$ , indicating a significant loss of surfactant. The value rises to a maximum of 28 at the peak of the adsorption. Using these two values, the concentration of surfactant solution that needs to be pumped in to the column in order for the  $[\text{AOT}]_{\text{free}}$  to be equal to the  $c_{\mu c}$ , 0.50 mM, is between 6.6 to 15.4 mM.

When 4 pore volumes are pumped through, the  $[AOT]_{init}$  needed for a certain  $[AOT]_{free}$  decreases, almost linearly, across the full concentration range (with the exception of the very high concentrations), by a factor of approximately 3.4. The reason this factor is not 4 (as might be expected due to 4 times the amount of solution being pumped through) is due to the constant  $\Gamma$  value assumed in the derivation of the model. As the adsorbed amount stays the same, after 1 pore volume has been pumped through, all of the following pore volumes contribute solely to the  $[AOT]_{free}$  and not the  $[AOT]_{adsorbed}$ . In reality the system is in dynamic equilibrium and an increase in  $\Gamma$  is expected as the  $[AOT]_{free}$  increases if the initial  $\Gamma \leq \Gamma_{max}$ . However, as discussed, in order to simplify this analytical model, the expected adsorption increase has been noted but not included in the calculations. The results of the model still provide a convincing rationale behind the experimental oil recovery data expressed in the form of Figure 4.9.

The increase in surfactant concentration in the effluent with increasing pore volumes of solution pumped through porous media has been seen experimentally in various different studies, such as those in refs 39-41.

**Figure 4.8** Relationship between the initial concentration of AOT ( $[AOT]_{init}$ ) in solution with 75 mM NaCl and 10 mM  $Na_2CO_3$  pumped in to an FC10 packed column with a fraction of the surface available to the water of 0.4 and the corresponding concentration of surfactant ‘free’ after some has been depleted by adsorption to the calcite-water interface ( $[AOT]_{free}$ ) at different pore volumes of the solutions being pumped through. The diagonal dashed line shows the case of no adsorption.

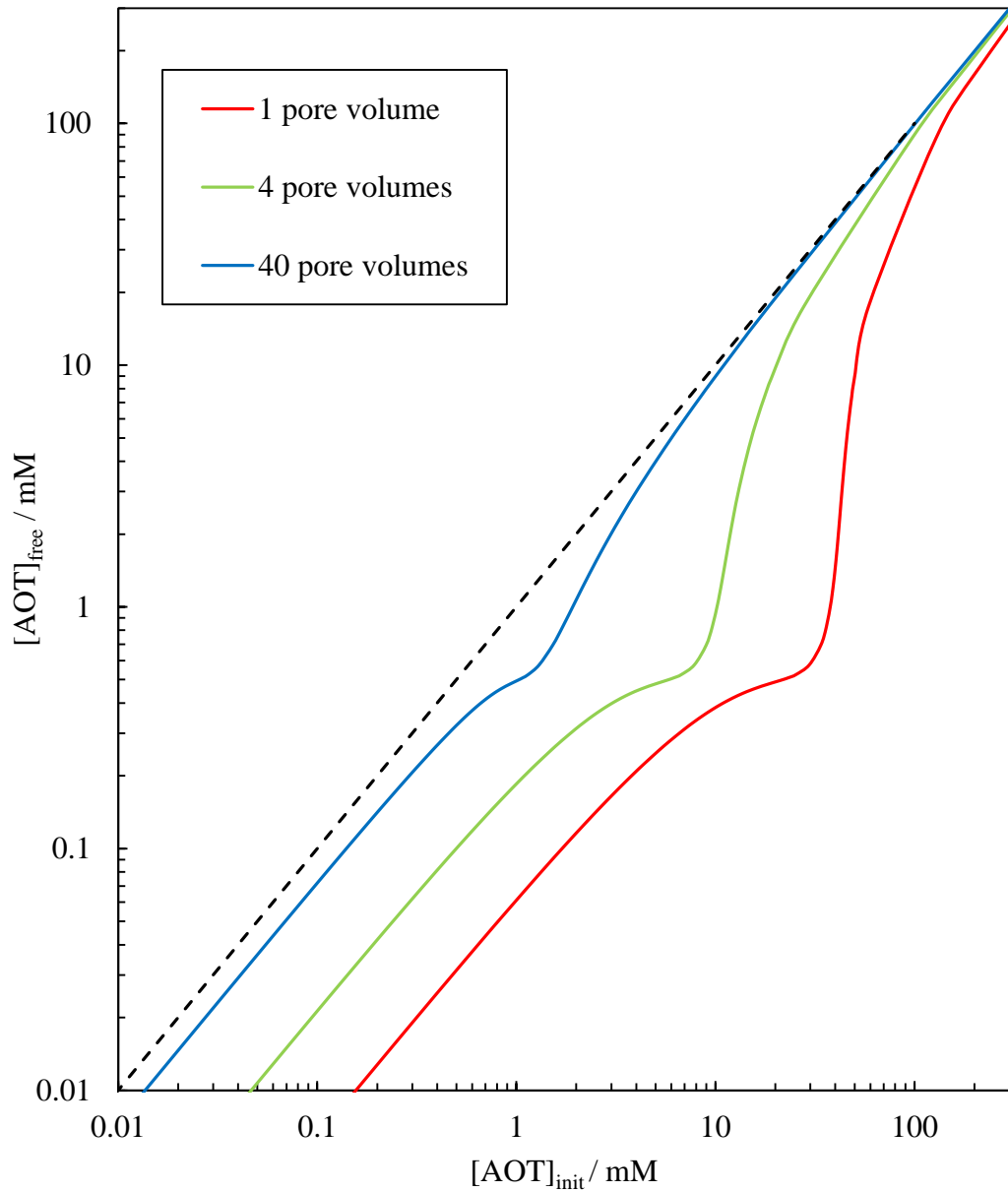
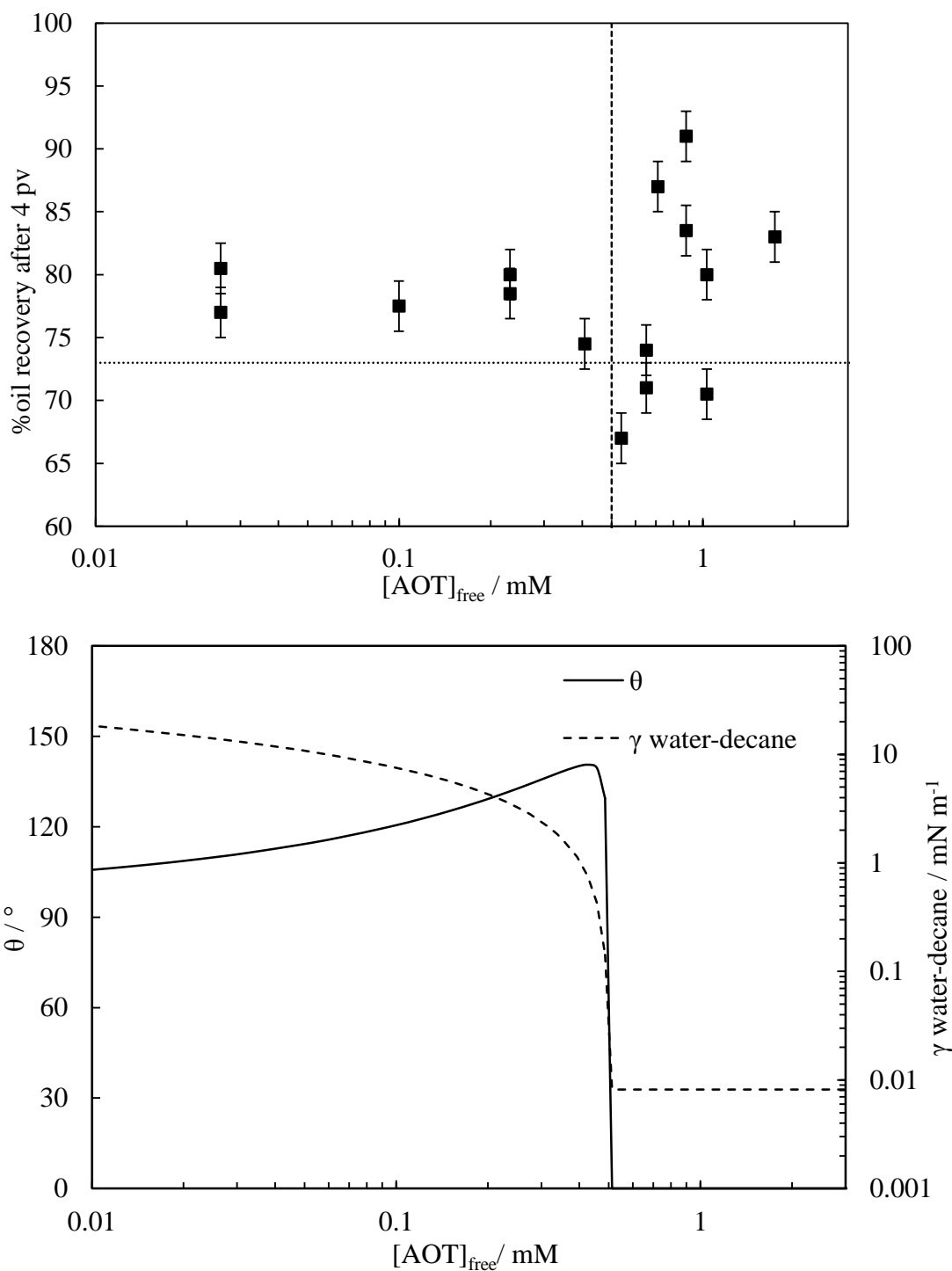


Figure 4.9 now allows for a direct comparison between the change in the oil-water interfacial tension and contact angles and the % oil recovery as all measurements refer to the concentration of free surfactant. Below the  $c_{\mu c}$  where there is no significant change in the oil-water interfacial tension or contact angle, there is also no significant change in the oil recovery. As the  $c_{\mu c}$  is approached and the contact angle and the oil-water interfacial tensions drop, the oil recovery also drops. The sudden increase in oil recovery comes after the  $c_{\mu c}$  where both the oil-water tension and the contact angle remain constant. As described in Chapter 3, the % oil recovery is determined at low flow rate conditions such that capillary forces dominate over viscous forces, at least for systems with higher oil-water interfacial tensions. For surfactant concentrations below the critical aggregation concentration, the surfactant potentially affects the % oil recovery only because of the changes in the contact angle and the value of the oil-water interfacial tension. Above the critical aggregation concentration (when the concentration of non-adsorbed, non-aggregated surfactant, contact angle and oil-water tension all remain constant), the surfactant aggregates present can additionally remove oil by solubilisation and emulsification, which would presumably have an increased effect with an increase in surfactant concentration, as seen in Figure 4.9. As detailed in section 4.4.3, both these mechanisms are invoked to model the measured plots of %oil recovery as a function of surfactant concentration.

**Figure 4.9** %oil recovery (after 4 pore volumes) as a function of AOT free concentration for the system containing 75 mM NaCl (top). This figure has the same y-axis %oil recovery data as Figure 4.6, though the x-axis concentrations have been converted to  $[AOT]_{\text{free}}$  as described in the text, allowing comparison with the contact angle and interfacial tension data (bottom, same data as Figure 4.5). Again, the vertical dashed line is the  $c_{\text{mc}}$  and the horizontal dotted line the oil recovery with no surfactant present (and only the salt).



#### 4.4.3 *Two-part model to calculate effect of interfacial tension, contact angle and solubilisation on %oil recovered*

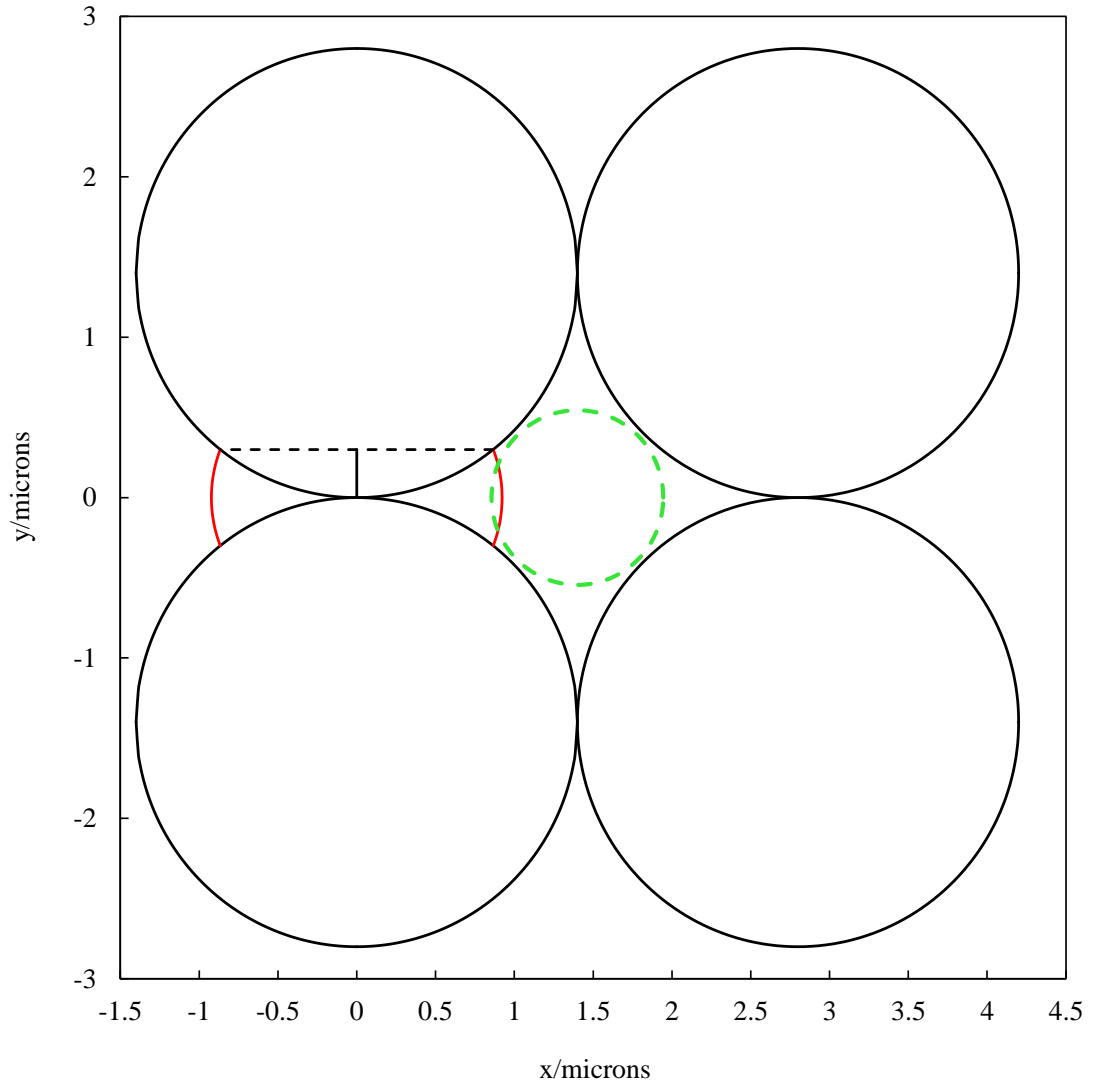
##### 4.4.3.1 *Principles of the model for oil recovery with $[surf] < c_{uc}$*

The equations and implementation of the first part of the model make little sense without an understanding of the principles behind the model. Hence, initially these principles will be discussed. As the majority of the equations are not essential to understanding the theory of the oil recovery and the effect of the interfacial tension and contact angles on the recovery, they are not included in the main body of this text. If the reader is interested, a walk through the main equations is in Appendix B, and the spreadsheet set-up for the calculations is in the ESI on the CD at the front of this thesis (file title, “Liquid bridge calculations spreadsheet.xlsx”).

As a starting point, it will be considered how the % oil recovery is affected by contact angle  $\theta$  and oil-water tension  $\gamma$  when the surfactant concentration is below the  $c_{uc}$ . In order to (greatly) simplify the calculations, the packed particle bed is taken to consist of monodisperse spheres packed in a cubic arrangement as shown in Figure 4.10. This type of cubic packing was selected because the volume fraction of interstitial space (denoted as  $\phi_{pore}$ ) is equal to  $(1 - \pi/6) = 0.48$  and is close to the value of  $\phi_{pore} = 0.45$  measured for the randomly packed FC10 calcium carbonate particles used here. The proposal for how the oil is trapped is that, following flooding by aqueous surfactant solution, the oil remaining in the particle packed column is trapped in the form of liquid bridges between contacting particles<sup>42-46</sup>, as shown in Figure 4.10. Although not strictly the same, this type of trapping could be considered to be a form of flow bypassing, where the displacing phase passes through the middle of the pore, but not the narrowest part of the pore where the bridge is left behind.

For the calculations, the profile of the liquid bridge is approximated as a circular arc. The profiles, volumes and surface areas for a set of liquid bridges which all have a constant value of contact angle  $\theta$  but different values of the parameter  $h_p$  defined in Figure 4.10 are calculated using EXCEL (see Appendix B). For each bridge of different  $h_p$  value, the known geometry of the bridge's curved oil-water interface and the value of the oil-water tension enables the calculation of the Laplace pressure difference across the oil-water interface  $\Delta P_{bridge}$ . A positive value of  $\Delta P_{bridge}$  indicates that the pressure inside the bridge is higher than outside the bridge.

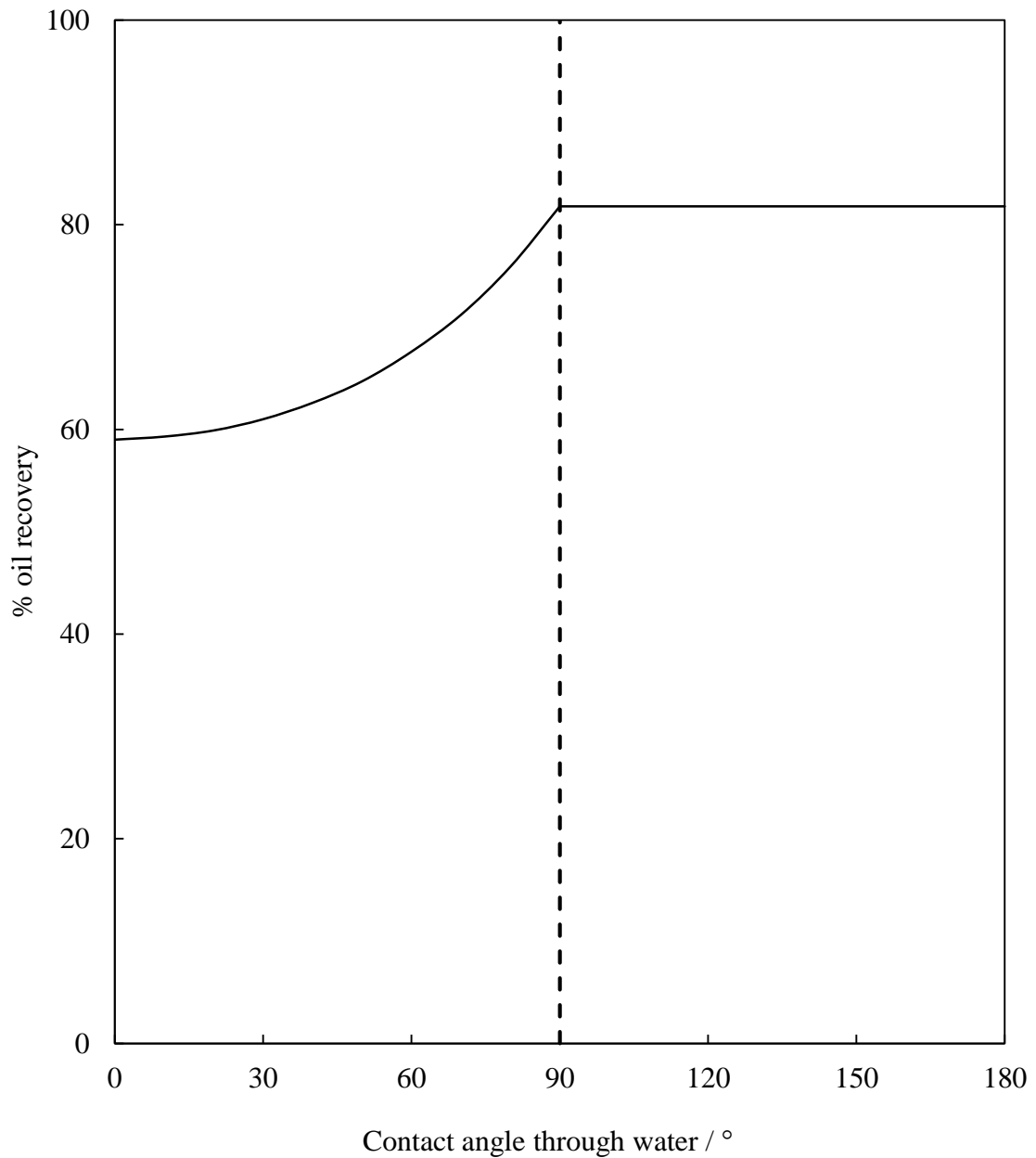
**Figure 4.10** Cubic packing of calcite spheres showing the cross sectional profile of a liquid oil bridge (red), the distance  $h$  (vertical solid black line) and the circular profile of a water phase flow channel (green dashed line). Note that only a single oil liquid bridge is shown here; each particle-particle contact point is assumed to have an identical liquid bridge. The configuration shown here is calculated for calcite-water-oil contact angle  $\theta$  (measured through the water) equal to  $107^\circ$ , particle radius =  $1.4 \mu\text{m}$  and  $h_p = 0.3 \mu\text{m}$ .



The next step is to consider which factors determine the size of the oil bridge which is stranded as aqueous surfactant solution is pumped through the initially oil-filled packed bed. It will be assumed that the water flows through the particle interstices indicated by the green dashed circle in Figure 4.10. The size of this flow channel depends on the size of the residual oil liquid bridges. The average, effective radius of these flow channels (denoted as  $r_{\text{chan}}$ ) is estimated as the radius of the circle which has an area equal to the area of the particle interstice minus the areas of the four liquid bridges in contact with it. It will also be assumed that  $r_{\text{chan}}$  cannot exceed the radius of the circle circumscribed by the particles ( $= r_{\text{chan,max}}$ ). Thus, by setting the value of  $h$  for the liquid bridges, it is then possible to calculate  $r_{\text{chan}}$  for a set value of liquid bridge size. In order to achieve flow through  $r_{\text{chan}}$ , the driving pressure must exceed the maximum Laplace pressure difference which occurs when a hemi-spherical “bulge” of aqueous phase into the oil-filled interstice occurs. This maximum Laplace pressure  $\Delta P_{\text{chan}} = 2\gamma_{\text{ow}}/r_{\text{chan}}$ , and is also known as the capillary entry pressure. For fixed contact angle  $\theta$  and oil-water tension  $\gamma_{\text{ow}}$ , the system can “choose” whether to bulge and breakthrough through small pores and leave large liquid bridges (thereby giving a low % oil recovery) or to bulge and create large flow channels and leave small liquid bridges.

Here it is postulated that the size of the trapped liquid bridges and corresponding value of the flow channel size  $r_{\text{chan}}$  is determined by the condition that  $\Delta P_{\text{bridge}} = \Delta P_{\text{chan}}$  (for  $r_{\text{chan}} < r_{\text{chan,max}}$ ) or that  $r_{\text{chan}} = r_{\text{chan,max}}$ . The resulting estimation of %oil recovery is found to depend only on the contact angle  $\theta$  and is independent of the decane-water interfacial tension. This being the case, a universal graph can be plotted (Figure 4.11) for all systems with concentrations of surfactant  $< c_{\text{uc}}$  on the effect of contact angle on %oil recovery (in the case of flow rate corresponding to low Ca, i.e. capillary forces dominate). There is a rise from 58 %oil recovery with a  $0^\circ$  contact angle through the water to 82 % with a contact angle of  $90^\circ$  or greater. The limiting oil recovery at 82 % is due to the  $r_{\text{chan-max}}$  having been reached. This trend is very similar to that seen by Zhao et al.<sup>47</sup>

**Figure 4.11** The predicted %oil recovery for flooding aqueous solutions through a cubic packed arrangement of monodisperse hard spheres in a low flow rate regime corresponding to capillary forces dominating. The %oil recovery is calculated as described in the text. The vertical dashed line indicates the transition from the condition of  $r_{chan}$  being determined by  $\Delta P_{bridge} = \Delta P_{chan}$  to the condition that  $r_{chan}$  is determined by  $r_{chan} = r_{chan,max}$  (to the left of the line the former condition, to the right the latter).



#### 4.4.3.2 Additional oil recovery when $[surf] > cac$

The theory outlined above enables the estimation of % oil recovery due to the effect of the added surfactant on the contact angle  $\theta$ . For surfactant concentrations in excess of the  $c_{\mu c}$ , two additional factors arise. Firstly, the additional surfactant is present in the form of aggregates which can also remove trapped oil by solubilisation. To estimate this contribution, we assume that each mole of aggregated surfactant solubilises  $R_{sol}$  moles of decane, where  $R_{sol}$  is the equilibrium solubilisation molar ratio equal to  $[\text{solubilised decane}]/([\text{AOT}] - c_{\mu c})$ . Based on this assumption, the %oil recovered by solubilisation using  $n$  pore volumes of aqueous phase is given by

$$\% \text{oil}_{sol} = n MV_{\text{decane}} R_{sol} ([\text{AOT}] - c_{\mu c}) 100 \quad (4.13)$$

where  $MV_{\text{decane}}$  is the molar volume of decane. The total %oil recovery is equal to the sum of the contributions from the contact angle effect and from the solubilisation. Secondly, as discussed above, when the surfactant concentration is increased to  $>c_{\mu c}$ , the oil-water tension reaches a very low value which causes the capillary number to change from the low capillary number regime to the high regime. In this regime, viscous forces dominate over capillary forces which leads to the breakup and mobilisation of trapped oil. This process is similar to emulsification in which the newly formed emulsion drops require adsorption of surfactant to be stabilised. In order that the oil-water tension does not increase, only surfactant in excess of the  $c_{\mu c}$  is likely to adsorb to the newly formed emulsion drops. Hence, the amount of oil mobilisation by breakup and mobilisation (emulsification) is likely to be proportional to  $([\text{AOT}] - c_{\mu c})$ . It is assumed here that  $R_{em}$  moles of decane is emulsified per mole of aggregated AOT in excess of the  $c_{\mu c}$ . The %oil recovered by solubilisation plus emulsification using  $n$  pore volumes of aqueous phase is then given by

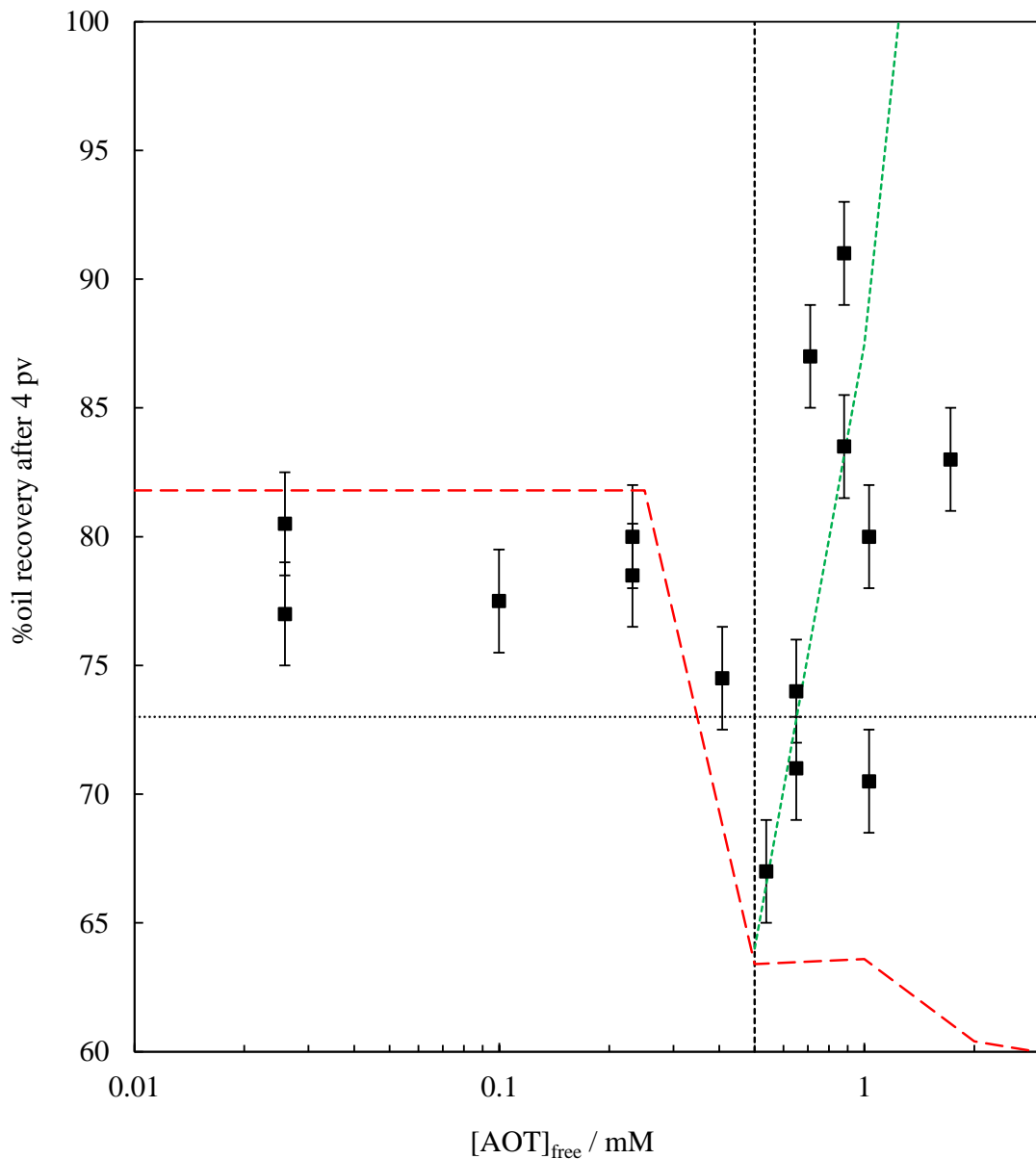
$$\% \text{oil}_{sol+em} = n MV_{\text{decane}} (R_{sol} + R_{em}) ([\text{AOT}] - c_{\mu c}) 100 \quad (4.14)$$

where the parameters  $R_{sol}$  and  $R_{em}$  are input as a single parameter as there is no easy way to distinguish between the two processes (other than the limitations of  $R_{sol}$  as described later).

#### 4.4.3.3 *Comparison of experimental results to the derived model*

Figure 4.12 compares the measured variation of %oil recovery as a function of the  $AOT_{\text{free}}$  concentration for the system containing 75 mM NaCl and 10 mM  $Na_2CO_3$  with the model calculations. The model calculations for the oil recovery resulting from contact angle changes alone correctly predict the unchanging recovery at low concentrations and the decrease in recovery as the  $c_{\mu c}$  is approached due to the contact angle decreasing. The increase in oil recovery above the  $c_{\mu c}$  is reasonably well represented by equation 4.14 with a value of  $(R_{\text{sol}} + R_{\text{em}})$  equal to 600 moles of decane per mole of aggregated AOT. The maximum equilibrium solubilisation ratio of decane by AOT under these conditions ( $R_{\text{sol}}$ ) is approximately 10 (by extrapolation of the data from ref. 48). Hence, for the system of Figure 4.12 with an ultralow value of the post- $c_{\mu c}$  oil-water interfacial tension equal to  $0.0079 \text{ mN m}^{-1}$ , the bulk of the post- $c_{\mu c}$  increase in oil recovery occurs by breakup and mobilisation (emulsification) of the trapped oil as a result of the high capillary number. It is worth noting that the uncertainties in the %oil recovery values for  $[AOT] > c_{\mu c}$  are larger than the uncertainty of  $\pm 2\%$  estimated from repeatability measurements of the mass of packed column (see Experimental). This greater irreproducibility observed above the  $c_{\mu c}$  may be due to slight variations in the calcite particle packing from run to run having a large effect on the %oil recovery due to solubilisation and emulsification (but not on the oil recovery resulting only from contact angle changes for  $[AOT] < c_{\mu c}$ ).

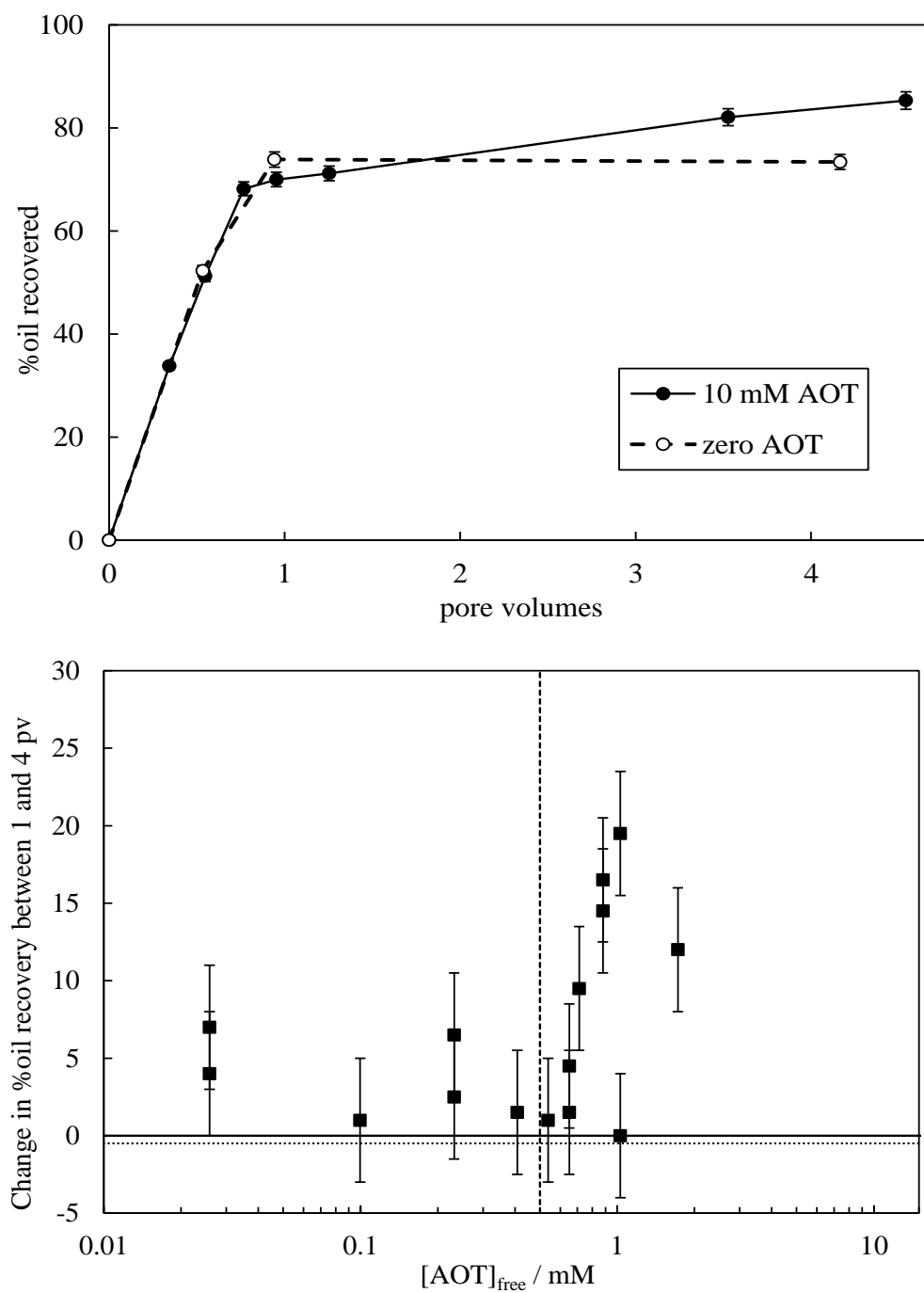
**Figure 4.12** Variation of %oil recovered after 4 pore volumes as a function of the non-adsorbed (free) AOT concentration for solutions containing 75 mM NaCl and 10 mM Na<sub>2</sub>CO<sub>3</sub> at 25 °C. The vertical black dashed line shows the  $c_{\mu c}$  and the horizontal black dotted line indicates the %oil recovered in the absence of AOT. The red dashed line shows the predicted %oil recovered from the contact angle alone mechanism, and the green dotted line the %oil recovered from the contact angle and the solubilisation/emulsification mechanisms combined, both calculated using the model described in the text.



As mentioned previously, the %oil recovery plots are interpreted after 4 pore volumes as resulting from surfactant-induced contact angle changes plus solubilisation and emulsification for AOT concentrations above the  $c_{\mu c}$ . For systems containing AOT concentration  $\leq c_{\mu c}$ , the %oil recovery resulting from contact angle changes should be complete following the injection of approximately 1 pore volume whereas the contribution from solubilisation and emulsification (for AOT concentrations  $> c_{\mu c}$ ) should continue to increase with the number of pore volumes injected. The top graph in Figure 4.13 compares plots of %oil recovery versus pores volumes injected for systems above and below the  $c_{\mu c}$  (representative of the general trends observed). Below the  $c_{\mu c}$ , when oil recovery occurs only by contact angle change, the oil recovered remains constant after 1 pore volume. Above the  $c_{\mu c}$ , where oil recovery occurs by both contact angle change and solubilisation plus emulsification, the recovery continues to rise after 1 pore volume.

Though not all of the oil recovery plots are as clear as those shown in Figure 4.13, when the difference in oil recovery between 1 and 4 pore volume is plotted vs. the free concentration of surfactant (Figure 4.13, bottom), a clear trend is observed. Consistent with the model proposed here, the difference in recovery is only significant for AOT concentrations in excess of the  $c_{\mu c}$ .

**Figure 4.13** Top: Variation of %oil recovery with number of pore volumes pumped for  $0.005 \text{ ml min}^{-1}$  of aqueous solutions containing  $75 \text{ mM NaCl}$  and  $10 \text{ mM Na}_2\text{CO}_3$  into an FC10 packed column with pore volume fraction 0.45 initially containing decane at  $25 \text{ }^\circ\text{C}$ . Plots for  $10 \text{ mM AOT}$  and zero AOT are compared. Bottom: Variation of the change in %oil recovery between 1 and 4 pore volumes versus  $[\text{AOT}]_{\text{free}}$  (free at 4 pv). The vertical dashed line indicates the  $c_{\text{mc}}$  of AOT under these conditions, and the horizontal dotted line the case with no surfactant present.



Figures 4.14 and 4.15 show the %oil recovery (experimental and theoretical) and the difference in %oil recovery between 1 and 4 pv for the AOT systems containing 0 and 40 mM NaCl respectively. As mentioned previously, the contact angle and interfacial tension behaviour of these systems and the system containing 75 mM NaCl are qualitatively similar, with the only differences being the lowness of the post-c<sub>µc</sub> water-decane interfacial tension, the c<sub>µc</sub> concentration and the Winsor system (both are WI, whereas the 75 mM NaCl system is a WIII, summarised in table 4.4). Thus, the only expected difference is the point at which the %oil recovery starts to drop (due to drop in contact angle at the c<sub>µc</sub>) and the value of the (R<sub>sol</sub> + R<sub>em</sub>) parameter in the post-c<sub>µc</sub> oil recovery modelling (a higher post c<sub>µc</sub> γ<sub>ow</sub> is likely to mean less emulsification).

The change in oil recovery between 1 and 4 pore volumes for both systems show a very similar trend to that of the system containing 75 mM NaCl, increasing the confidence in the idea of the post-c<sub>µc</sub> oil recovery by solubilisation and emulsification (plus that from the θ). Further to this, the solubilisation plus emulsification ratios which reasonably represent the post-c<sub>µc</sub> oil recovery are 45 for the system containing 0 mM NaCl (Figure 4.14) and 200 for the system containing 40 mM NaCl (Figure 4.15). Thus, there is an increase in the solubilisation plus emulsification ratio from 45 to 600 as the post-c<sub>µc</sub> tension drops from 0.33 to 0.0079 mN m<sup>-1</sup> (between NaCl concentrations of 0 to 75 mM NaCl).

The oil recovery with no surfactant for both salt concentrations is 75 ± 2 %. The oil recovery with [AOT]<sub>free</sub> < c<sub>µc</sub> (just before the contact angles drop below 90 ° are very close to that of the case with no surfactant. This is expected as the contact angle with no surfactant and with [AOT] < c<sub>µc</sub> is above 90 ° so the oil recovery is limited by the r<sub>chan</sub> = r<sub>chan-max</sub> parameter. Although the calculated and measured oil recoveries with [AOT]<sub>free</sub> below the c<sub>µc</sub> do not quite match up, the trends of both are similar.

**Figure 4.14** Top: Variation of %oil recovered after 4 pore volumes as a function of the non-adsorbed (free) AOT concentration for solutions containing 0 mM NaCl and 10 mM Na<sub>2</sub>CO<sub>3</sub>. The red dashed line shows the %oil recovered from the contact angle alone mechanism, and the green dotted line the %oil recovered from the contact angle and the solubilisation/emulsification mechanisms combined, both calculated using the model described in the text. Bottom: Variation of the change in %oil recovery between 1 and 4 pore volumes versus [AOT]<sub>free</sub> (free at 4 pv) under the same conditions as the top plot. Note the error bars are double the 2 % as the points are the difference between two measurements. For both plots, The vertical black dashed lines shows the c<sub>μc</sub> and the horizontal black dashed line indicates the data in the absence of AOT.

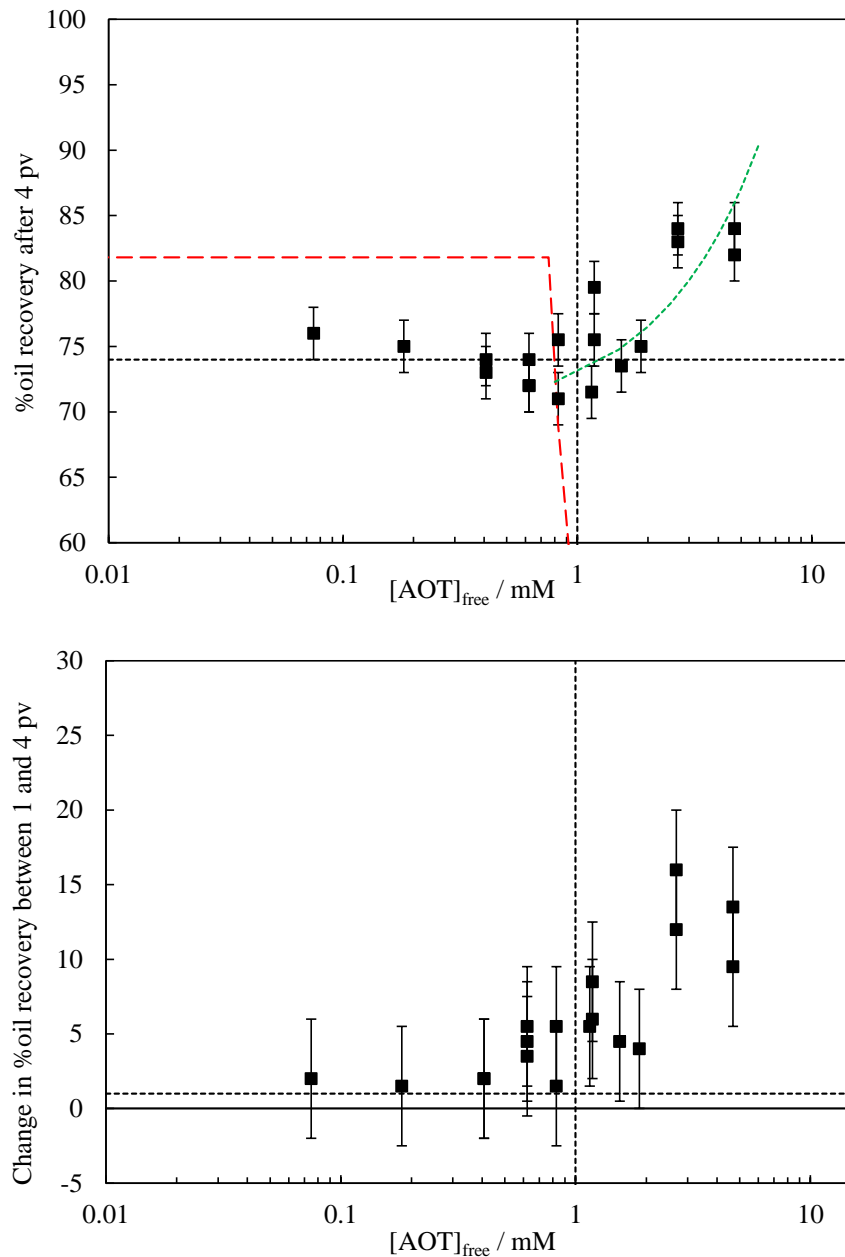
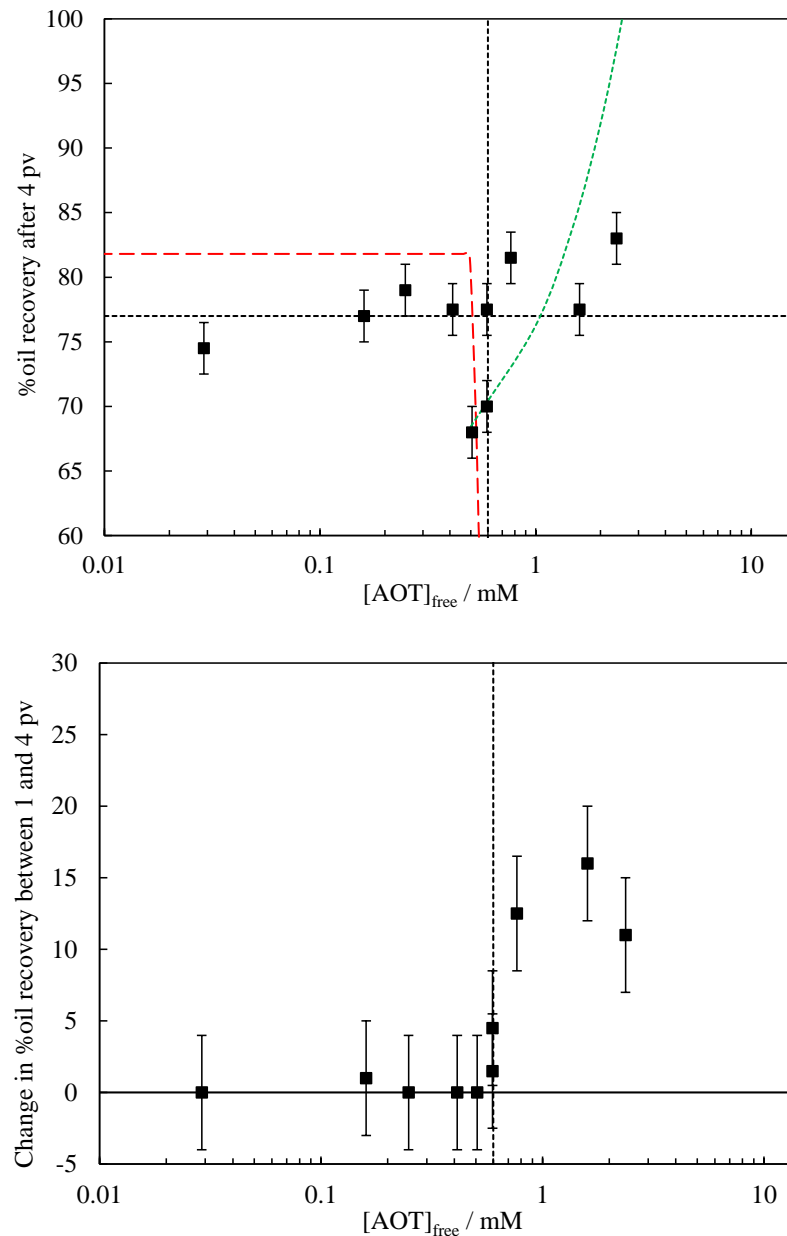
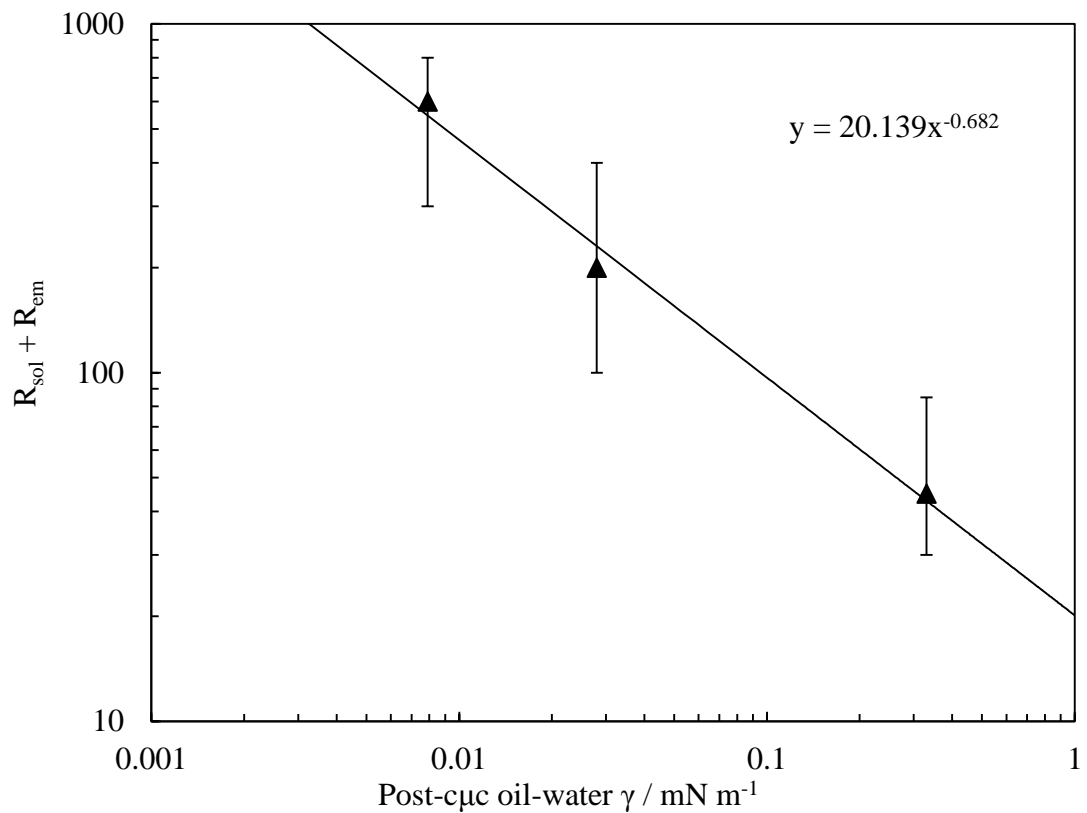


**Figure 4.15** Top: Variation of %oil recovered after 4 pore volumes as a function of the non-adsorbed (free) AOT concentration for solutions containing 40 mM NaCl and 10 mM Na<sub>2</sub>CO<sub>3</sub>. The red dashed line shows the %oil recovered from the contact angle alone mechanism, and the green dotted line the %oil recovered from the contact angle and the solubilisation/emulsification mechanisms combined, both calculated using the model described in the text. Bottom: Variation of the change in %oil recovery between 1 and 4 pore volumes versus [AOT]<sub>free</sub> (free at 4 pv) under the same conditions as the top plot. Note the error bars are double the 2 % as the points are the difference between two measurements. For both plots, The vertical black dashed lines shows the c<sub>μc</sub> and the horizontal black dashed line indicates the data in the absence of AOT.



The value of  $R_{sol} + R_{em}$  is plot vs. post-cµc interfacial tension in Figure 4.16. It shows that the data can be fitted to a power-law relationship. If the relationship is general, it would enable the prediction of the post-cµc oil recovery for any surfactant system. This approach will be applied to the other surfactant systems studied in Chapter 5. The error bars are calculated as the values above and below the average fitting of the green lines in Figures 4.12, 4.14 and 4.15 which cause the line to go through the highest and lowest points of the post-cµc oil recovery.

**Figure 4.16** A plot of the values of the  $R_{sol} + R_{em}$  parameters in figures 4.12, 4.14 and 4.15 vs. the respective post-cµc oil-water interfacial tensions. The solid straight line is the fit to a power function curve.



## 4.5 Conclusions

The effect of NaCl concentration on the microemulsion phase inversion of systems consisting of aqueous solutions of AOT containing 10 mM Na<sub>2</sub>CO<sub>3</sub> with an equal volume of decane was determined. Systems with 0, 40 and 75 mM NaCl, giving WI, WI and WIII phase behaviour respectively, were selected for study. The calcite-water adsorption, water-decane interfacial tensions and the calcite-water-decane contact angles as a function of AOT concentrations were determined for each system. The calcite-water adsorption for all three systems was qualitatively similar, with low adsorption up to the cac, whereafter strong cooperative adsorption was observed up to a plateau of approximately 2 molecules nm<sup>-2</sup>. The reason for this was deemed to be due to surface charge on the calcite likely being close to neutral (or slightly negative) leading to no strong (or slightly repulsive) electrostatic forces between the surfactant head and the calcite surface, hence the adsorption mechanism was proposed to be through hydrophobic interactions between surfactant molecules forming aggregates on the surface of the calcite. The water-decane interfacial tensions as a function of AOT concentration for all three systems show the same trend of starting at approximately 45 mN m<sup>-1</sup> and dropping to a value independent of the AOT concentration above c<sub>µc</sub> as aggregates are formed which no longer adsorb at the water-decane interface.

The adsorption and subsequent change in interfacial tensions were successfully modelled using a combination of the Langmuir isotherm and the Gibbs adsorption equation and the subsequent tensions used to model the three phase contact angle as a function of AOT concentration. The calcite-water-decane three-phase contact angle (advanced static, measured through the water) starts at approximately 110° in the absence of AOT, rising to approximately 150° with increasing AOT concentration due to the decrease in the water-decane tension and a calcite-water tension higher than the calcite-decane tension. At the c<sub>µc</sub> where the water-decane interfacial tension reaches a minimum (value of which depends on the salt concentration), and the calcite-water tension drops below that of the calcite-decane, the contact angle is predicted to fall to 0°. However, the measured contact angles drop to approximately 40° at the c<sub>µc</sub>, with a further decrease to a plateau at 20° with increasing AOT concentration. Possible reasons for this difference were discussed.

A model has been derived to enable the calculation of the free surfactant concentration within a particle packed column from the initial concentration of surfactant pumped in to the column as a function of pore volumes pumped, when the adsorption isotherm of the surfactant to the particle surfaces is known. The model allows for the direct comparison between the interfacial tension, contact angle and the %oil recovery as all refer to the free surfactant concentration, i.e. the model takes account of the surfactant depletion from solution by adsorption at the calcite-water interface.

A second two-part model has been derived which enables the modelling of the %oil recovered when flooding aqueous solutions of surfactant based on the assumption that the remaining oil is trapped as liquid bridges between the particles in the packed column. The first part of the model determines the %oil recovered when the surfactant concentration is below the  $c_{\mu c}$  (and the flow rate slow enough such that the oil recovery is determined only by the interfacial forces) as a function of oil-water interfacial tension and the three phase contact angle. It was found that the oil recovery is determined solely by the three-phase contact angle and is not effected by the oil-water interfacial tension, and that an increasing contact angle (through the water) increases the oil recovery from 58 % at  $0^\circ$  to a limiting value from  $90-180^\circ$  of 82 %. The second part of the model determines the extra oil recovered when the surfactant concentration is above the  $c_{\mu c}$  from solubilisation and emulsification mechanisms (where emulsification is thought to be similar to the oil breakup and mobilisation due to an increase in the capillary number from a decrease in the oil-water interfacial tension). It was found that a decrease in the post- $c_{\mu c}$  interfacial tension lead to an increase in the post- $c_{\mu c}$  oil recovery. Experimental results also showed that there was no significant increase in oil recovery between 1 and 4 pv when the surfactant concentration was below the  $c_{\mu c}$ . When above the  $c_{\mu c}$  there was a noticeable difference in recovery with increasing pv. This was expected as the oil recovery below the  $c_{\mu c}$  (determined by contact angle alone) should be complete by water breakthrough (between approximately 0.7-0.8 pore volumes) whereas the extra recovery from solubilisation and emulsification would be expected to continue after water breakthrough.

Overall, an experimental model system consisting of AOT-water-decane-calcite was characterised in terms of calcite-water adsorption, water-decane interfacial tensions and calcite-water-decane three-phase contact angles as a function of AOT concentration for three different aqueous phase salt concentrations (0, 40 and 75 mM NaCl, all with 10

mM Na<sub>2</sub>CO<sub>3</sub> present). The characterised systems were used to displace decane from an calcite packed column, and the resulting oil recovery related to the water-decane interfacial tensions and the three-phase contact angle through the use of two models (both derived here).

#### 4.6 References

1. Aveyard, R.; Binks, B.P.; Clark, S.; Mead, J. Interfacial tension minima in oil-water-surfactant systems Behaviour of alkane-aqueous NaCl systems containing Aerosol OT. *J. Chem. Soc. Faraday Trans. 1*, **1986**, 82, 125.
2. Binks, B.P., Emulsion type below and above the CMC in AOT microemulsion systems, *Colloids & Surfaces A*, **1993**, 71, 167.
3. Aveyard, R.; Binks, B.P.; Clark, S.; Mead, J. Interfacial tension minima in oil-water-surfactant systems Effects of alkane chain length and presence of n-alkanols in systems containing Aerosol-OT, *J. Chem. Soc. Faraday Trans. 1*, **1986**, 82, 1755.
4. Aveyard, R., Binks, B.P., Clark, S., Fletcher, P.D.I., Lyle, I.G., Displacement of oil by aqueous surfactant solutions from capillaries sealed at one end, *Colloids & Surfaces A*, **1996**, 113, 295.
5. Binks, B.P., Ph.D. Thesis, University of Hull, 1985.
6. Jeirani, Z., Jan, B.M., Ali, B.S., See. C.H., Saphanuchart, W., Pre-prepared microemulsion flooding in enhanced oil recovery: a review, *J. Pet. Sci. Technol.*, **2014**, 32, 180.
7. Skouri, M.; Marignan, J.; May, R. X-ray and neutron-scattering study of the lamellar and L<sub>3</sub> phases of the system aerosol-OT-water: effect of NaCl and decane. *Colloid & Polymer Sci.*, **1991**, 269, 929.
8. Balinov, B.; Olsson, U.; Soderman, O. Structural similarities between the L<sub>3</sub> and bicontinuous cubic phases in the AOT-brine system. *J. Phys. Chem.*, **1991**, 95, 5931.
9. Somasundaran, P.; Agar, G.E. The zero point of charge of calcite. *J. Colloid Interface Sci.*, **1967**, 24, 433.
10. Smallwood, P.V. Some aspects of the surface chemistry of calcite and aragonite. Part 1: an electrokinetic study. *Colloid & Polymer Sci.*, **1977**, 255, 881.
11. Thompson, D.W; Pownall, P.G. Surface electrical properties of calcite. *J. Colloid Interface Sci.*, **1989**, 131, 74.

12. Moulin, P.; Roques, H. Zeta potential measurement of calcium carbonate. *J. Colloid Interface Sci.*, **2003**, *261*, 115.
13. Eriksson, R.; Merta, J.; Rosenholm, J.B. The calcite/water interface I. Surface charge in indifferent electrolyte media and the influence of low-molecular-weight polyelectrolyte. *J. Colloid Interface Sci.*, **2007**, *313*, 184.
14. Eriksson, R.; Merta, J.; Rosenholm, J.B. The calcite/water interface II. Effect of added lattice ions on the charge properties and adsorption of sodium polyacrylate. *J. Colloid Interface Sci.*, **2008**, *326*, 396.
15. Sondi, I.; Biscan, J.; Vdovic, N.; Skapin, S.D. The electrokinetic properties of carbonates in aqueous media revisited. *Colloids & Surfaces A*, **2009**, *342*, 84.
16. Heberling, F.; Trainor, T.P.; Lutzenkirchen, J.; Eng, P.; Denecke, M.A. Bosbach, D. Structure and reactivity of the calcite-water interface. *J. Colloid Interface Sci.*, **2011**, *354*, 843.
17. Paria, S., Khilar, K.C., A review on experimental studies of surfactant adsorption at the hydrophilic solid-water interface, *Adv. Colloid Interface Sci.*, **2004**, *110*, 75.
18. Brunauer, S.; Love, K.S.; Keenan, R.G. Adsorption of nitrogen and the mechanism of ammonia decomposition over iron catalysts. *J. Amer. Chem. Soc.*, **1942**, *64*, 751.
19. Giles, C.H.; Smith, D.; Huitson, A. A general treatment and classification of the solute adsorption isotherm. I. Theoretical. *J. Colloid Interface Sci.*, **1974**, *47*, 755.
20. Foo, K.Y.; Hameed, B.H. Insights into the modelling of adsorption isotherm systems. *Chem. Eng. J.*, **2010**, *156*, 2.
21. Stocker, I.N.; Miller, K.L.; Welbourn, R.J.L.; Clarke, S.M.; Collins, I.R.; Kinane, C.; Gutfreund, P. Adsorption of Aerosol-OT at the calcite/water interface – Comparison of the sodium and calcium salts. *J. Colloid Interface Sci.*, **2014**, *418*, 140.

22. van Oss, C.J. *Interfacial forces in aqueous media*, New York: Marcel Dekker, **1994**.
23. Schoff, C.K. Wettability phenomena and coatings. Chap. 14, pp. 375-395 in Schrader, M.E. Loeb, G. (Eds.) *Modern approach to wettability: theory and applications*. Plenum Press, New York, **1992**.
24. Binks, B.P., Clint, J.H., Solid wettability from surface energy components: relevance to pickering emulsions, *Langmuir*, **2002**, *18*, 1270.
25. Binks, B.P., Dyab, A.K.F., Fletcher, P.D.I., Contact angles in relation to emulsions stabilised solely by silica nanoparticles including systems containing room temperature ionic liquids, *Phys. Chem. Chem. Phys.*, **2007**, *9*, 6391.
26. Fowkes, F.M., Additivity of intermolecular forces at interfaces. I. Determination of the contribution to surface and interfacial tensions of dispersion forces in various liquids, *J. Phys. Chem.*, **1963**, *67*, 2538.
27. Owens, D.K., Wendt, R.C., Estimation of the surface free energy of polymers, *J. Appl. Polym. Sci.*, **1969**, *13*, 1741.
28. Fletcher, P.D.I., Holt, B.L., Controlled Silanization of Silica Nanoparticles to Stabilize Foams, Climbing Films and Liquid Marbles, *Langmuir*, **2011**, *27*, 12869.
29. Okayama, T.; Keller, D.S.; Luner, P. The wetting of calcite surfaces. *J. Adhesion*, **1997**, *63*, 231.
30. Keller, D.S.; Luner, P. Surface energetic of calcium carbonates using inverse gas chromatography. *Colloids & Surfaces A*, **2000**, *161*, 401.
31. Calhoun, A.; Chiang, E. Determination of the surface energetic of surface modified calcium carbonate using inverse gas chromatography. *J. Vinyl & Additive Technol.*, **2006**, *12*, 174.
32. Arsalan, N.; Palayangoda, S.S.; Burnett, D.J., Buiting, J.J.; Nguyen, Q.P. Surface energy characterization of carbonate rocks. *Colloids & Surfaces A*, **2013**, *436*, 139.

33. Lucassen-Reynders, E.H. Contact angles and adsorption on solids. *J. Phys. Chem.*, **1963**, *67*, 969.
34. Tavana, H., Thermodynamic Status of Contact Angles. Chap. 7, pp. 329-422 in Neumann, A.W., David, R., Zuo, Y. (Eds.) *Applied Surface Thermodynamics*, Second Edition, CRC Press, Boca Raton, **2011**.
35. Tavana, H. and Neumann, A.W., Interpretation of Contact Angles. Chap. 8, pp. 423-490 in Neumann, A.W., David, R., Zuo, Y. (Eds.) *Applied Surface Thermodynamics*, Second Edition, CRC Press, Boca Raton, **2011**.
36. Morrow, N.R. The effects of surface roughness on contact angle with special reference to petroleum recovery. *J. Can. Petroleum Technol.*, **1975**, *14*, 42.
37. Somasundaram, P.; Zhang, L. Adsorption of surfactants on minerals for wettability control in improved oil recovery processes. *J. Petroleum Sci. Eng.*, **2006**, *52*, 198.
38. Mannhardt, K., Novosad, J.J., Chromatographic movement of surfactant mixtures in porous media, *Chem. Eng. Sci.*, **1991**, *46*, 75.
39. Gogoi, S.B., Adsorption-desorption of surfactant for enhanced oil recovery, *Transp. Porous Med.*, **2011**, *90*, 589.
40. Liu, Q., Dong, M., Zhou, W., Ayub, M., Zhang, Y.P., Huang, S., Improved oil recovery by adsorption-desorption in chemical flooding, *J. Pet. Sci. Eng.*, **2004**, *43*, 75.
41. Curbelo, F.D.S., Garnica, A.I.C., Neto, E.L.B., Enhanced oil recovery and adsorption of ionic surfactant, *J. Pet. Sci. Technol.*, **2013**, *31*, 663.
42. Haines, W.B. Studies in the physical properties of soils. II A note on the cohesion developed by capillary forces in an ideal soil. *J. Agric. Sci.*, **1925**, *15*, 529.
43. Fisher, R.A. On the capillary forces in an ideal soil; correction of formulae given by W.B. Haines. *J. Agric. Sci.*, **1926**, *16*, 492.

44. Kralchevsky, P.A.; Nagayama, K. Capillary bridges and capillary-bridge forces. In “Particles at fluid interfaces and membranes”, Elsevier, Amsterdam, **2001**, chap. 11, pp. 469.
45. Armstrong, R.T., Porter, M.L., Wildenschild, D., Linking pore-scale interfacial curvature to column-scale capillary pressure, *Adv. Water. Resour.*, **2012**, *46*, 55.
46. Armstrong, R.T., Porter, M.L. and Wildenschild, D., Linking pore-scale interfacial curvature to column-scale capillary pressure, *Adv. Water Resources*, **2012**, 55.
47. Zhao, X., Blunt, M.J., Yao, J., Pore-scale modelling: Effect of wettability on waterflood oil recovery, *J. Pet. Sci. Eng.*, **2010**, *71*, 169.
48. Fletcher, P.D.I. Characterisation of Aerosol OT-stabilised oil-in-water microemulsions using a time-resolved fluorescence method. *J. Chem. Soc. Faraday Trans. 1*, **1987**, *83*, 1493.

## CHAPTER 5

### MODEL VALIDATION USING A CATIONIC AND A NONIONIC SURFACTANT

#### 5.1 Introduction

Chapter 4 discusses the characterisation of a system consisting of water, decane, calcite and AOT with 10 mM Na<sub>2</sub>CO<sub>3</sub> and three different concentrations of NaCl, in terms of the microemulsion phases formed, aqueous phase behaviour, adsorption at the water-calcite interface, change in the water-decane interfacial tensions and the change in the three-phase contact angles as a function of AOT concentration. The three different salt concentrations altered the  $c_{\mu c}$  (and  $c_{ac}$ ) moderately and the post- $c_{\mu c}$  water-decane interfacial tensions considerably. The aqueous surfactant solutions were pumped through the calcite packed columns (the characterisation of which were discussed in Chapter 3) with the interstices between the calcite particles filled with decane. Two models were then derived to enable the interpretation of the %oil recovery as a function of surfactant concentration. The first model to convert  $[\text{surf}]_{\text{init}}$  to  $[\text{surf}]_{\text{free}}$  to allow a direct comparison between the adsorption, interfacial tension and three-phase contact angle characterisation data with the %oil recovery experiments. The second two-part model to enable modelling of the extent of oil recovery both with surfactant concentrations below and above the  $c_{\mu c}$  based on the hypothesis that the oil is trapped as liquid bridges between the particles. The two models enabled an understanding of the %oil recovery as a function of AOT concentration.

To further test the models derived in Chapter 4, it is necessary to see if the predictions and modelling still work for systems which behave differently to the water-decane-calcite-AOT system. Thus, two other three phase systems were chosen which had the potential to behave significantly differently. If the systems behave significantly differently to the AOT containing system discussed in Chapter 4, yet the models still fit the experimental data well, then this increases the confidence that can be had in the predictive capabilities of the models.

The results in this chapter discuss the characterisation of and the oil recovery performance of two different systems, one with a cationic surfactant and one with a nonionic surfactant. The first system consists of water, toluene, calcite and the pure

cationic surfactant C14BDMAC. As the charge of the headgroup is opposite to that of the AOT, the C14BDMAC has the potential to behave significantly differently in the characterisation and oil recovery experiments. The second system consists of water, heptane, calcite and the un-pure commercial (technical grade) nonionic surfactant CW-100S. The use of an un-pure technical grade surfactant will take the current study one step closer to a 'real' system, i.e. a system closer to that which would be encountered at an actual oil field, as pure surfactants are far too expensive to be used in industrial applications. The results for both the above systems are analysed using the two models derived in Chapter 4 and compared to the water-decane-calcite-AOT system.

In an effort to aid the flow of some of the following sections it is first necessary to briefly explain the nature of the equilibration times and the differences between initial and equilibrium measurements for the oil-water interfacial tensions and the water-oil-calcite contact angles. The AOT containing systems in Chapter 4 showed a very quick attainment of equilibrium values for both the interfacial tensions and contact angles (and hence there is no discussion about this aspect in that chapter). The interfacial tension and contact angle measurements for the C14BDMAC containing system were seen to change slowly over time periods of up to a couple of hours, though the difference between the initial and the final values of each measurement were all within a 10 % error. As such, the choice between which values to use had few consequences on the final outcome of the characterisation and modelling of the oil recovery. Even so, a brief discussion is had about some possible causes for this longer equilibration time. As it will be seen in section 5.3.4, the water-oil-calcite contact angles for the system containing the nonionic CW-100S surfactant can change significantly over time. It is for this reason that both the initial and equilibrium interfacial tensions and contact angles are shown in the figures, and a further discussion had about which values might be most relevant to the current research.

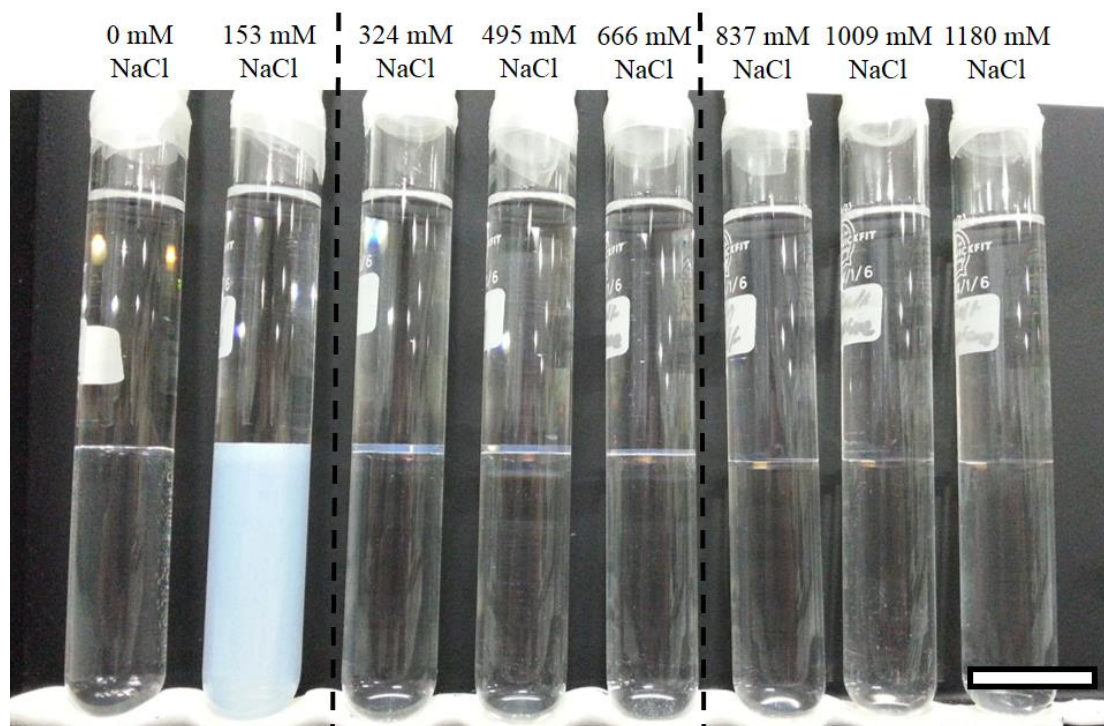
## 5.2 Characterisation of and oil recovery performance of a system consisting of water, toluene, calcite and the cationic surfactant C14BDMAC

### 5.2.1 Microemulsion phase inversion and surfactant partitioning

Alaei *et al.*<sup>1</sup> have shown how brine concentration (where their brine consists of a mixture of monovalent and divalent salts) can cause emulsion phase inversion for a water-toluene system containing C14BDMAC at 25°C. They show that following homogenisation of a 1:1 volume ratio of water:toluene and [C14BDMAC] >  $c_{\mu c}$ , an oil in water emulsion is formed with 0.1 to 1 wt. % of brine, and a water in oil emulsion between 3 to 10 wt.% brine. Thus, with a water-toluene system containing C14BDMAC at 25 °C there is an inversion from an oil-in-water to a water-in-oil emulsion (indicating microemulsion phase inversion too) between brine concentrations of 1 and 3 wt.%.

Figure 5.1 shows tubes containing a 1:1 volume ratio of water:toluene containing concentrations of C14BDMAC in excess of the  $c_{\mu c}$ , 10 mM Na<sub>2</sub>CO<sub>3</sub> and varying concentrations of NaCl. The tubes were inverted and left to equilibrate for 3 days at 25 °C. The vertical dashed black lines indicate the transition from WI to WIII to WII type systems (from left to right), as determined from the number of equilibrium thermodynamically stable phases present. The phase inversion from a WI to WIII system occurs between NaCl concentrations of 153 and 324 mM (approximately 1 - 2 wt.% total salt including Na<sub>2</sub>CO<sub>3</sub>), and the inversion from WIII to WII between NaCl concentrations of 666 and 837 mM (approximately 4 - 5 wt.% total salt including Na<sub>2</sub>CO<sub>3</sub>), in good agreement with the concentrations of brine found to cause emulsion phase inversion by Alaei *et al.*

**Figure 5.1** Microemulsion phase tubes of water and toluene in a 1:1 volume ratio with 5 mM C14BDMAC and 10 mM Na<sub>2</sub>CO<sub>3</sub> plus the concentrations of NaCl shown (all concentrations in the water phase). after 3 days of equilibration at 25 °C. The scale bar represents 20 mm.

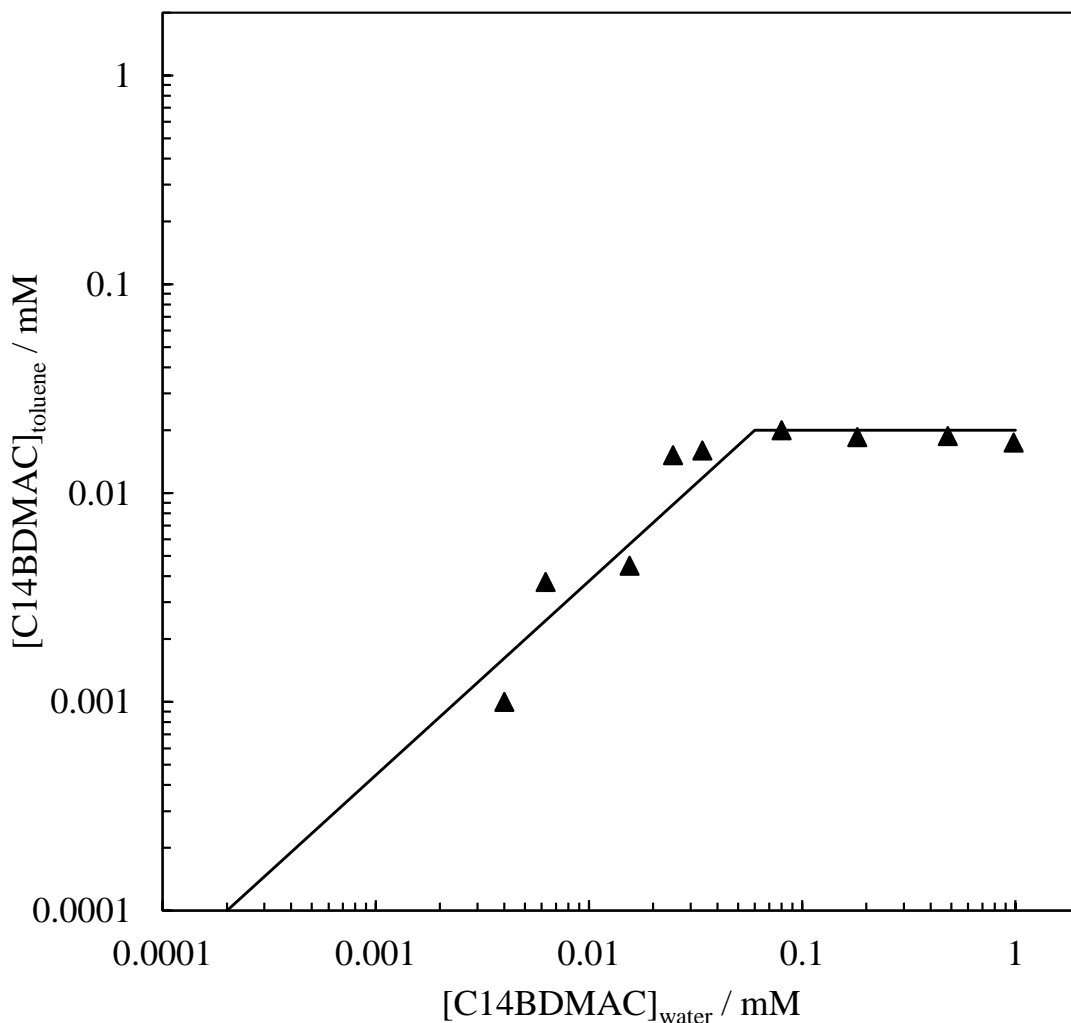


The salt concentration chosen for further characterisation and oil recovery experiments was 150 mM NaCl and 10 mM Na<sub>2</sub>CO<sub>3</sub>.

The partitioning of the C14BDMAC between the water (containing 150 mM NaCl and 10 mM Na<sub>2</sub>CO<sub>3</sub>) and toluene at 25 °C is shown in Figure 5.2. The monomer partition coefficient,  $K_{P-tw}$ , below the  $c_{\mu c}$  is approximately 0.4. The salt concentration used here corresponds to approximately 1 wt.% total salt. The  $K_{P-tw}$  is lower than that reported by Alaei *et al.*<sup>1</sup> for C16BDMAC in 1 wt.% brine and at 40 °C ( $K_{P-tw} = 6.5$ ). This is probably due to the fact that their measurements were for C16BDMAC (which has 2 extra carbons on the tail), likely to have a higher affinity for the oil as the hydrophobic region is larger. Further, the higher temperature may also have an effect. For the current system, above concentrations of approximately 0.06 mM (in the water phase), the concentration of surfactant in the water phase increases whereas the concentration in the toluene remains constant, indicating a Winsor I system. The concentrations of the surfactant in both phases at the breakpoint indicates the  $c_{\mu c}$  of the surfactant in that phase. The  $c_{\mu c}$  determined from the partitioning data (0.06 mM in the water phase) is in very good

agreement with the  $c_{\mu c}$  in the water determined by interfacial tension measurements in section 5.2.4.

**Figure 5.2** Equilibrium concentrations of C14BDMAC in equilibrated water and toluene phases, where the water contains 150 mM NaCl and 10 mM Na<sub>2</sub>CO<sub>3</sub> and at 25 °C. The solid line is a manually fitted trend line.



Partitioning of the surfactant to the oil is another possible cause for the depletion of the  $[\text{surf}]_{\text{free}}$  (along with adsorbing to the calcite-water interface), leading to a further difference between the initial concentration of surfactant pumped in to the column and the concentration of free (non-adsorbed) surfactant. For example, with a  $K_{P-\text{ow}}$  of 1, at complete partition equilibrium with a 1:1 volume ratio of water:oil and concentration of the surfactant below the  $c_{\mu c}$ , the  $[\text{surf}]_{\text{free}}$  is depleted by 50 %. Aveyard *et al.*<sup>2</sup> show that the partitioning of the nonionic surfactant C<sub>12</sub>E<sub>5</sub> between water and heptane at 25 °C is

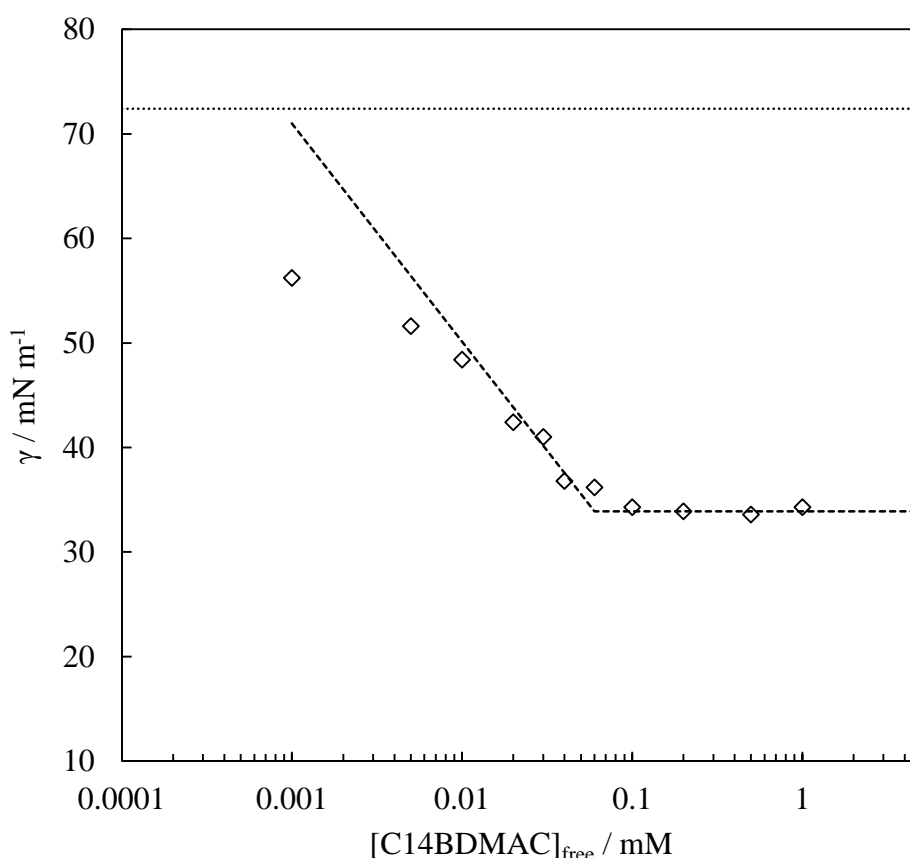
highly in favour of the oil, with a  $K_{P-ow}$  of approximately 300. In this case the loss of surfactant due to partitioning could potentially be quite significant.

As the  $K_{P-ow}$  for the current system is small, and that complete partition equilibrium is unlikely to be obtained, the loss of surfactant due to partitioning of the monomers from the water to the oil was not considered in the converting of the  $[\text{surf}]_{\text{init}}$  to the  $[\text{surf}]_{\text{free}}$ . A further point worth noting is that during the column flood experiments the partitioning of surfactant is not between a 1:1 volume ratio of water:oil as the oil is being displaced, so most of the loss of surfactant due to partitioning is likely to be limited to the partitioning in to the much smaller volume of the oil trapped behind as bridges.

### 5.2.2 *cac* and aqueous phase behaviour of C14BDMAC

Alaei et al.<sup>1</sup> show that, unlike AOT in a water-alkane system with only NaCl as the salt, the  $c_{\mu c}$  of the C16BDMAC in water for a water-toluene system is not approximately equal to the  $cac$  of the C16BDMAC in water for the same brine concentrations. As such, it was necessary to determine the  $cac$  for C14BDMAC in water plus 150 mM NaCl and 10 mM Na<sub>2</sub>CO<sub>3</sub>. This was achieved through measurement of the surface tension of a range of concentrations of the C14BDMAC in the salt solution at 25 °C, and the break point in the tension plot taken to be the  $cac$  (Figure 5.3).

**Figure 5.3** Surface tensions (air-water interfacial tensions) of water containing 150 mM NaCl, 10 mM Na<sub>2</sub>CO<sub>3</sub> and varying concentrations of C14BDMAC at 25 °C. The horizontal dotted line indicates the surface tension with zero surfactant, and the two dashed lines are manually fitted trend lines to indicate the break point.

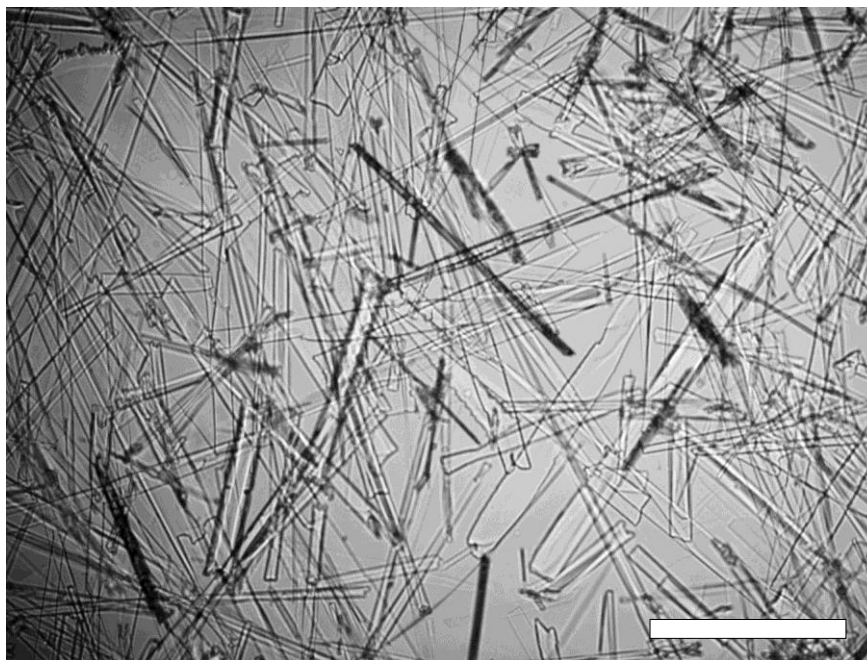


Although there are some errors associated with determining the break point in the tensions, the  $cac$  of C14BDMAC in water containing 150 mM NaCl and 10 mM Na<sub>2</sub>CO<sub>3</sub> at 25 °C is seen to be approximately 0.06 mM, the same as the value of the  $c_{\mu c}$  in water determined from both the partitioning data in Figure 5.2 and the tensions in Figure 5.8,

in disagreement with Alaei et al. Alaei et al. discuss the possibilities for the differences in behaviour of their C16BDMAC-water-toluene system (where  $c_{ac} \neq c_{uc}$ ) to the AOT-water-heptane systems (where  $c_{ac} = c_{uc}$ ) and state that the reason for the differences between the two could be the change from an anionic to a cationic surfactant or from an alkane to an aromatic oil or a combination of both. From the results shown in this current work it seems that a further parameter needs to be considered, that being the presence of divalent ions (present in high concentrations in the work by Alaei *et al.* but not here) For this current work, no further work was carried out to understand the differences.

For freshly made aqueous solutions of C14BDMAC in 150 mM NaCl and 10 mM Na<sub>2</sub>CO<sub>3</sub> (made by diluting individual aqueous stock solutions of each component), it was seen that over time (a few hours), at higher concentrations of C14BDMAC and at room temperature (approximately 22 °C), crystals of precipitated surfactant start to form. A micrograph of the formed crystals from a solution of 5 mM C14BDMAC, 150 mM NaCl and 10 mM Na<sub>2</sub>CO<sub>3</sub> left at room temperature for 12 hours is shown in Figure 5.4.

**Figure 5.4** Optical micrograph of the crystals formed from the precipitation of C14BDMAC from an aqueous solution of 5 mM C14BDMAC, 150 mM NaCl and 10 mM Na<sub>2</sub>CO<sub>3</sub> left at room temperature (approximately 22 °C) for 12 hours. The scale bar represents 500 μm.

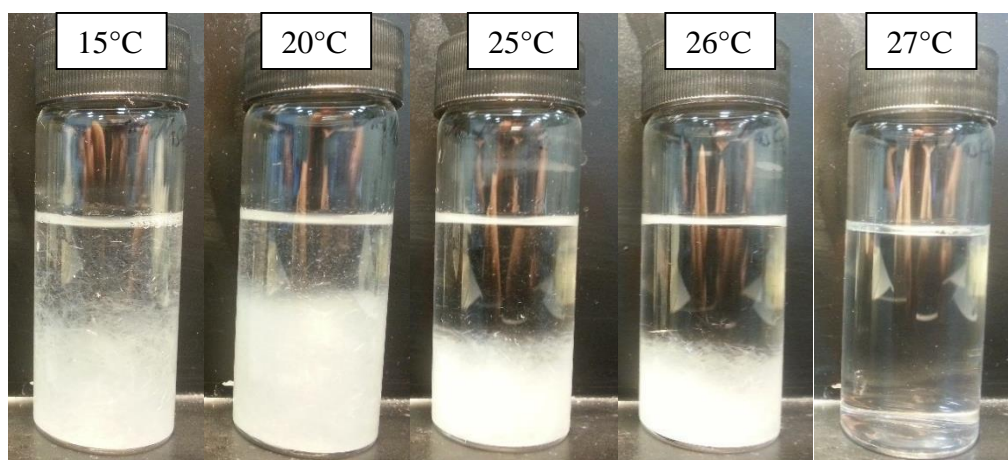


A possible explanation for this precipitation is that room temperature is lower than the Krafft temperature for this system. To determine if this is the case, a sample of 10

mM C14BDMAC in water containing 150 mM NaCl and 10 mM Na<sub>2</sub>CO<sub>3</sub> was held at 15 °C until crystals were well formed (1 hour). The temperature was then raised in appropriate intervals and the sample held at each temperature for 30 minutes. At a temperature of 27 °C all of the crystals were seen to have dissolved (Figure 5.5). These results indicate that the Krafft temperature for this system is approximately 27 °C (as the solubility suddenly increases at this temperature). Hence, below this temperature the C14BDMAC can only dissolve as monomers up to a certain concentration, though the kinetics of the precipitation from the initially supersaturated solutions is complex and may involve equilibria between micelles, monomers and precipitate (and can take a significant amount of time to occur)<sup>3-5</sup>.

Although in the current work a full understanding of this process was not developed, one significant consequence needs to be noted. For aqueous solutions of C14BDMAC, the concentration in the water will only increase up to the solubility (for systems at precipitation equilibrium). The precipitated surfactant is unavailable for solubilising the oil or for adsorbing at the water-oil interface to lower the tension and/or stabilise oil droplets broken off during flooding. Thus, there may not be an increase in oil recovery with increasing surfactant concentration when the total surfactant concentration is above the  $c_{uc}$  as  $[\text{surf}]_{\text{free}}$  is limited by the solubility of the surfactant.

**Figure 5.5** Solutions of 10 mM C14BDMAC in water containing 150 mM NaCl and 10 mM Na<sub>2</sub>CO<sub>3</sub>. The samples were left at 15 °C for 1 hour, then for 30 minutes at all of the other temperatures.



A further observation is that, as the precipitation of the C14BDMAC takes place over a few hours, measurements of the oil-water interfacial tensions and water-oil-calcite

contact angles may be unaffected by the precipitation (as these only take a few minutes to complete). So although low tensions are observed (Figure 5.8), these tensions may not occur during column floods (which take place over approximately 24 hours) as the C14BDMAC has had time to precipitate out before the end of the experiment. This will be taken in to account when interpreting the oil recovery performance of the surfactant solutions.

### 5.2.3 Adsorption of the C14BDMAC to the water-calcite and toluene-calcite interfaces

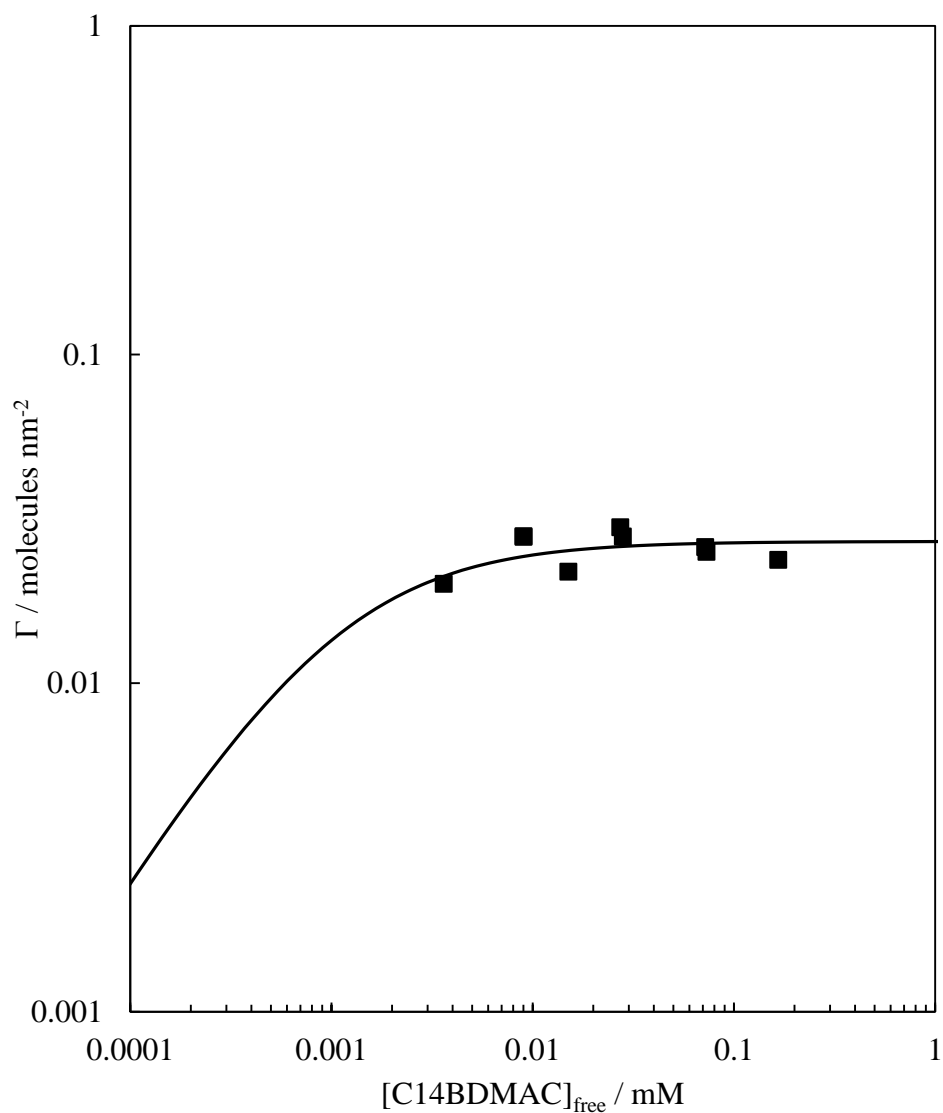
The adsorption of the C14BDMAC to the water-calcite interface at pH 10.8 and 25 °C is shown in Figure 5.6. Unlike the AOT systems where there was a strong cooperative adsorption around the cac, the C14BDMAC shows no strong adsorption across the concentration range studied. As mentioned in Chapter 4, the charge at the calcite-water interface at this pH is likely to be close to neutral. Such a low adsorption of a cationic surfactant may, however, suggest that the calcite is positively charged and thus repels the surfactant. Ma et al.<sup>6</sup> see a similar cooperative adsorption for an anionic surfactant (SDS) and the low adsorption of a cationic surfactant (CPC) on to calcite at pH 10.8 at 25 °C.

Due to the detection limits of the titration technique used, the adsorption of C14BDMAC at lower concentrations than those seen in Figure 5.6 was not possible. Thus, when fitting the Langmuir type (for the  $[\text{surf}]_{\text{free}}$  model) and the Langmuir (for modelling  $\theta$ ) isotherms to the experimental data, there is a large error in the K parameter which controls the fitting at the low concentrations. However, as the adsorption is so low the effect of the surfactant concentration on the calcite-water interfacial tensions is small, and thus large changes in K makes little difference to the end result of modelling the tensions and hence of modelling the three phase contact angles.

The highest concentration of C14BDMAC that will be present in the toluene is 0.02 mM (as seen in Figure 5.2) and as such the adsorption of surfactant from toluene to the toluene-calcite interface only needs to be determined up to this concentration. A concentration this low is near the detection limit of the titration. Further, the presence of toluene in the chloroform causes the accuracy of the titration technique to be significantly reduced (for undetermined reasons). Hence, with the current technique it was not possible to determine if the C14BDMAC adsorbs at the toluene-calcite interface at the concentration range of interest. Ideally had time permitted other techniques could

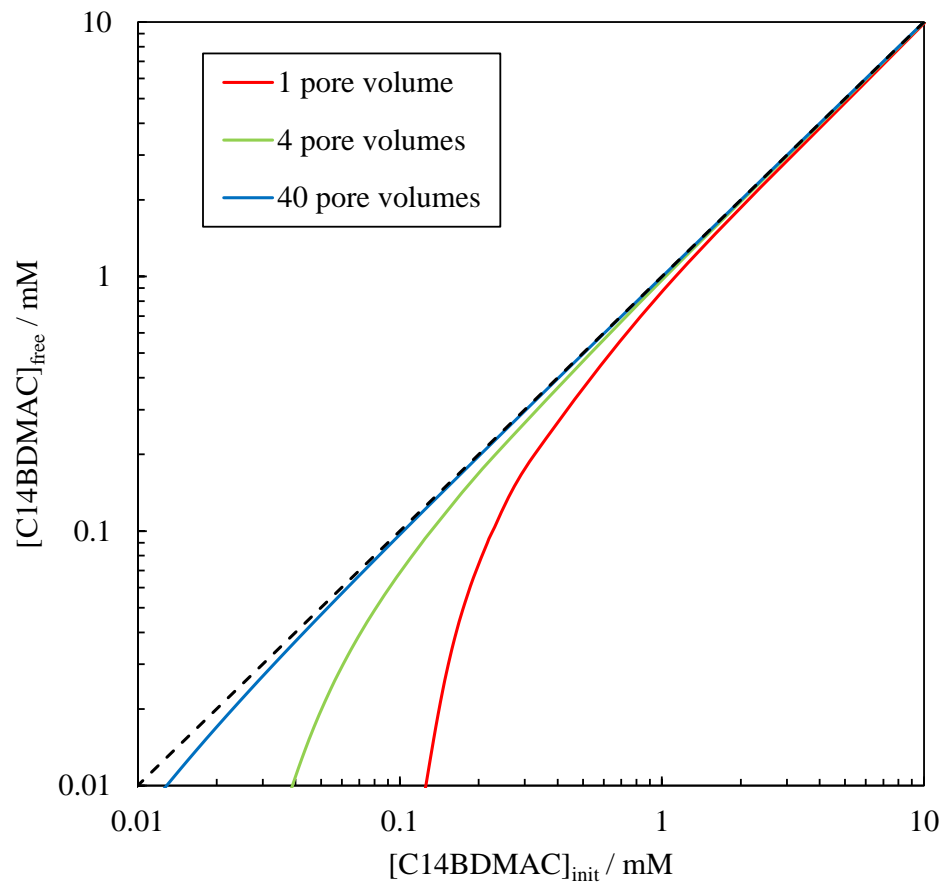
have been used to determine the surfactant concentrations at lower concentrations. As the adsorption to the water-calcite interface is so low, and the fact that adsorption of the surfactant at the toluene-calcite interface would have a negative impact on the modelling of the contact angles, it was assumed that the adsorption of C14BDMAC to the toluene-calcite interface is negligible, and therefore that the toluene-calcite interfacial tension is invariant with [C14BDMAC].

**Figure 5.6** Adsorption isotherm for the adsorption of C14BDMAC to the calcite-aqueous solution interface from aqueous solutions at pH 10.8 and containing 150 mM NaCl and 10 mM Na<sub>2</sub>CO<sub>3</sub> at 25.0 °C and pH 10.8. The curved line shows the fit to the cooperative Langmuir type isotherm (Chapter 4, equation 4.1), with  $\Gamma_{\max} = 0.027$  molecules nm<sup>-2</sup>,  $K = 1000$  mM<sup>-1</sup> and  $\beta = 0$ .



The relationship between  $[C14BDMAC]_{init}$  and  $[C14BDMAC]_{free}$  after pumping aqueous phases of C14BDMAC containing 150 mM NaCl and 10 mM  $Na_2CO_3$  through an FC10 packed column with  $f = 0.4$  is shown in Figure 5.7. Due to the low adsorption the ratio between the free concentration and the initial concentration is much lower than that observed for the AOT systems in Chapter 4 (particularly when  $[C14BDMAC]_{init} \geq 0.1$  mM). The large loss of surfactant predicted at low concentrations has a large error associated with it (as discussed with the fitting of the adsorption isotherm). Due to the lack of an increase in oil recovery (section 5.2.6), it is not readily determined if this model produces reliable results for this system.

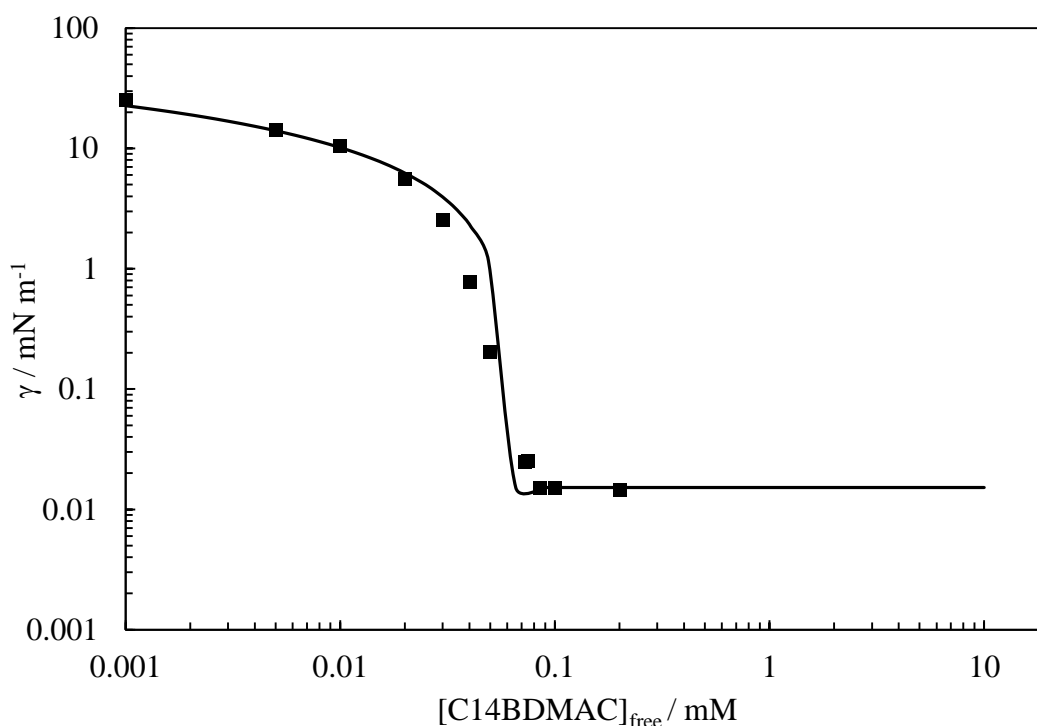
**Figure 5.7** Relationship between the initial concentration of C14BDMAC in solution ( $[C14BDMAC]_{init}$ ) with 150 mM NaCl and 10 mM  $Na_2CO_3$  pumped in to an FC10 packed column with  $f = 0.4$  and the corresponding concentration of surfactant ‘free’ after some has been depleted by adsorption to the calcite-water interface ( $[C14BDMAC]_{free}$ ) at different pore volumes of the solutions pumped through the column. The diagonal dashed line shows the case of no adsorption.



#### 5.2.4 Effect of C14BDMAC concentration on the toluene-water interfacial tensions

Figure 5.8 shows the variation of the toluene-water tension with C14BDMAC concentration ( $[C14BDMAC]_{free}$  refers to the concentration in the water phase). There was a small change in tension with time, though the final values (used in Figure 5.8) were steady after approximately 30 minutes and were within approximately a 5 % error of the initial values. As with the AOT system in Chapter 4, the tension decreases due to adsorption of C14BDMAC monomers from  $30.5 \text{ mN m}^{-1}$  (in the absence of C14BDMAC) to a value independent of C14BDMAC concentration at the  $c_{\mu c}$  ( $0.015 \text{ mN m}^{-1}$ ). The  $c_{\mu c}$  (determined as the break point in the interfacial tension data) is approximately  $0.06 \text{ mM}$ , in good agreement with the value of the  $c_{\mu c}$  determined from the partitioning data in section 5.2.1. The post- $c_{\mu c}$  interfacial tension is similar to the AOT system in Chapter 4 containing  $40 \text{ mM NaCl}$  and  $10 \text{ mM Na}_2\text{CO}_3$ .

**Figure 5.8** Variation of toluene-water tensions with aqueous C14BDMAC concentration at  $25.0 \text{ }^\circ\text{C}$  for solutions containing  $150 \text{ mM NaCl}$  and  $10 \text{ mM Na}_2\text{CO}_3$  (pre or pseudo equilibrated with the toluene) and  $\text{pH } 10.8$ . The line shows the best-fit calculated as described in Chapter 4 section 4.3.4, the fitting parameters are in Appendix C.



### 5.2.5 *Effect of C14BDMAC concentration on the water-calcite-toluene contact angles*

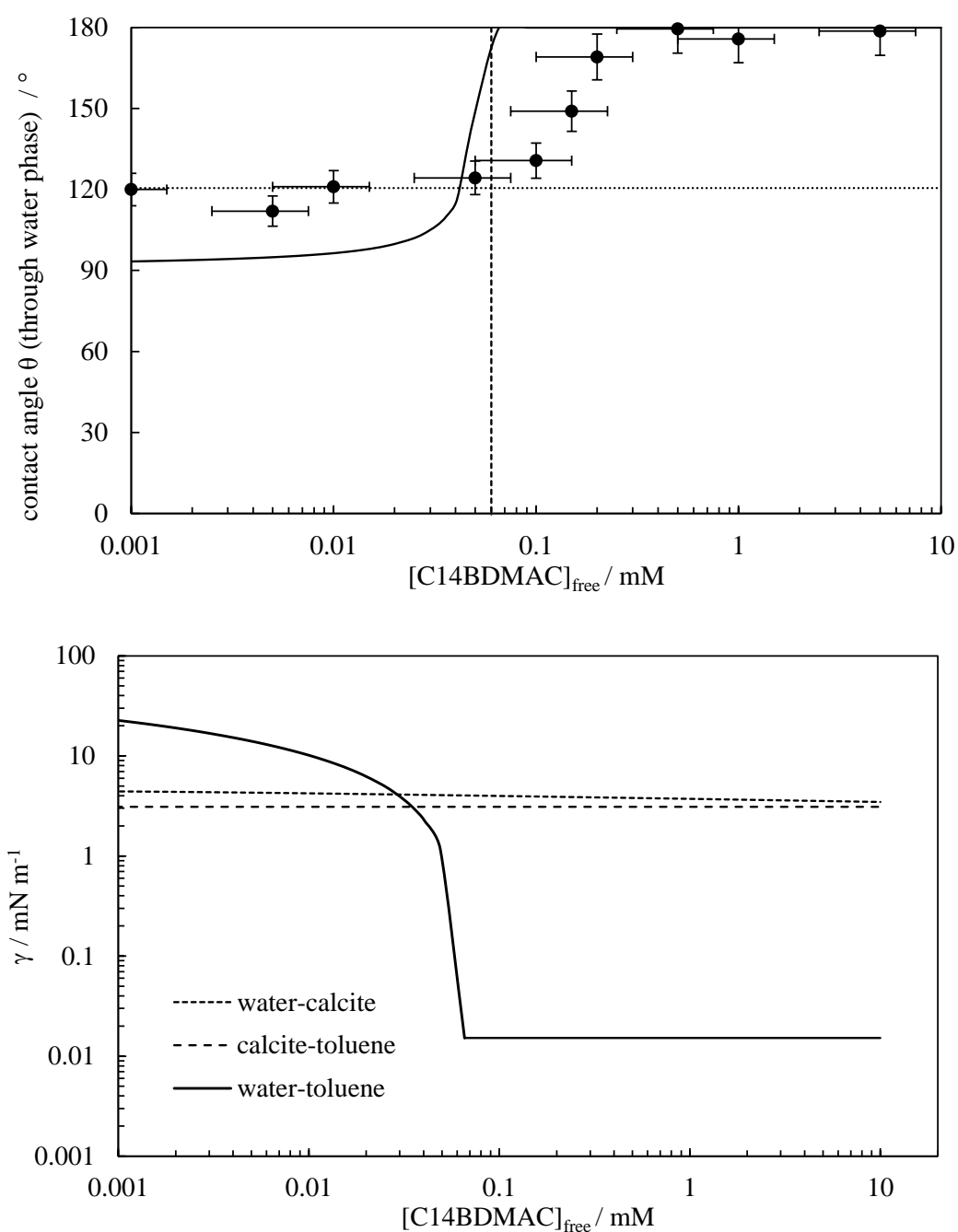
One main difference between measuring the contact angles for the current system and the AOT containing system in Chapter 4 is worth noting. This being that the contact angle of a drop of water placed on the crystal under toluene slowly changes over time to a constant value after approximately 2 hours (longer than tension equilibration). The difference between the initial contact angle and the contact angle after equilibrium is generally only slightly outside of the 10 % error for each individual measurement of the contact angle (interfacial tensions in Figure 5.8 stay the same within an error of approximately 5 %). Possible reasons for the slow change are multiple, such as the equilibrium of the adsorption of the C14BDMAC to the various interfaces. Another likely reason could be due to the partition equilibrium. Although pre or pseudo equilibrated phases are used for most measurements, due to the large volume difference between the drop and the bulk and the relatively large surface area to volume ratio of the drop, the concentration of C14BDMAC within the drop may be quite sensitive to effects related to the non-equilibrium state of the partitioning of the C14BDMAC between the water and the toluene. As such, the change in the contact angle could simply be due to a slow change in the concentration of the C14BDMAC within the drop.

The effect of non-equilibrated partition concentrations can be observed when the concentration in one of the phases is changed and the concentration in the other phase kept constant. When the initial concentration of C14BDMAC in the drop (the water phase) was kept constant at 0.05 mM (approximately the  $c_{\mu c}$ ) and the concentration in the toluene varied from 0 mM to the partition equilibrated concentration of 0.02 mM,  $\theta$  (after equilibration for a few hours) increases from 119 to 124 °. As seen in Figure 5.9, a lower [C14BDMAC] in the drop corresponds to a lower initial  $\theta$ . When the [C14BDMAC] in the toluene is lower than the expected partition equilibrated concentration, it may be expected that the surfactant will partition out of the drop and in to the bulk of the toluene, resulting in a lower [C14BDMAC] in the drop. As discussed, when the equilibrium contact angle of a system with [C14BDMAC] in the toluene lower than the expected partition equilibrium, the contact angle is lower than when the partition concentrations are used. This is in good agreement with the idea that the C14BDMAC partitions out of the drop resulting in a lower concentration in the drop, and hence a lower contact angle.

Due to this possible partition equilibrium effect, all of the contact angles to be modelled as a function of surfactant concentration (Figure 5.9) were taken to be the initial contact angles (as [C14BDMAC] within the drop is known as none has partitioned in to the oil). As mentioned in section 5.2.4, the equilibrium interfacial tensions were used. In this case the volumes of each phase were similar and there is a lower surface area to volume ratio for both phases, thus the effect of the loss of surfactant due to partitioning is likely to be minimised. It is worth re-stating that the difference between the initial and the equilibrium contact angles is only just outside of the estimated 10 % error for each individual measurement, and the initial and equilibrium tensions are within a 5 % error, thus the choice of which type of value to be used in the modelling (equilibrium or initial) is not likely to have a significant effect on the final results.

As with the AOT containing system in Chapter 4, below the  $c_{\mu c}$  there is a small increase in contact angle with an increase in the surfactant concentration (as the oil-water tension drops). However, in a distinct contrast to the AOT containing systems the post- $c_{\mu c}$  contact angle jumps to  $180^{\circ}$ , as opposed to dropping to  $0^{\circ}$ . This is caused by the ultra-low oil-water interfacial tension when the calcite-water tension is higher than the calcite-oil due to the low amount of adsorption of C14BDMAC to the calcite-water interface. This distinct difference is useful when testing the validity of the models, as if the models still fit the data for this system it increases the reliability and confidence that can be had in the predictive capabilities of the models for future systems.

**Figure 5.9** Upper plot: Variation of toluene-water-calcite advanced initial contact angle (measured through the aqueous phase) with aqueous C14BDMAC concentration for solutions containing 150 mM NaCl and 10 mM Na<sub>2</sub>CO<sub>3</sub> at 25 °C and pH 10.8. The vertical dashed line indicates the  $c_{\mu c}$ . The horizontal dashed line shows the contact angles in the absence of added C14BDMAC. The solid line shows the calculated contact angle from the water-toluene (measured), water-calcite (derived from the measured adsorption isotherm) and toluene-calcite (assumed invariant with [C14BDMAC]) tensions shown in the lower plot. The tensions are modelled with equation 4.8, the fitting parameters can be found in Appendix C.



In order for the calculated contact angles to come close to matching the experimental data the value of the calcite-water tension in the absence of C14BDMAC has to be made lower than that calculated from the surface energy components of the pure water and calcite (calculated  $\gamma_{0\text{-calcite-water}} = 15.3 \text{ mN m}^{-1}$ ,  $\gamma_{0\text{-calcite-water}}$  used in Figure 5.9 =  $4.5 \text{ mN m}^{-1}$ ). With a higher value of  $\gamma_{0\text{-calcite-water}}$  the step up of the contact angle to  $180^\circ$  occurs at approximately  $0.01 \text{ mM [C14BDMAC]}_{\text{free}}$ , a much lower concentration than that which is observed experimentally. A justification for doing this is that the water surface energy components are taken from the literature values of pure water. Here however, the water contains  $150 \text{ mM NaCl}$  and  $10 \text{ mM Na}_2\text{CO}_3$ . Although the effect of salt concentration on an air-water interfacial tension is often to increase the tension, here it may be expected to lower it between the water and the calcite as the salt ions may adsorb at the ionic surface of the calcite, and hence lower the tension.

To further justify this change it needs to be determined if the model can still fit the contact angles determined for the AOT systems in Chapter 4 if the initial calcite-water tension is lowered (as these systems also contain salt concentrations  $\leq$  half the salt concentration for the current system). It turns out that lowering  $\gamma_{0\text{-calcite-water}}$  for the AOT system containing  $75 \text{ mM NaCl}$  (half way between zero and that used in current system) to  $10 \text{ mN m}^{-1}$  causes the fit to not match the data as well as when the literature value is used. This is due to the fact that lowering the water-calcite tension to  $10 \text{ mN m}^{-1}$  causes it to become lower than the calcite-decane tension without any surfactant present ( $10.3 \text{ mN m}^{-1}$ ). However, due to the delicate balance between the three interfacial tensions and the large uncertainties in the surface energy components, it is not un-reasonable to continue using the adjusted  $\gamma_{0\text{-calcite-water}}$  for the current system alone in order to obtain a better modelling, and leave it unchanged for the other systems. Small changes in the other tensions (particularly the calcite-oil tensions) can cause the model to match the data with a range of calcite-water tensions. As discussed in Chapter 4, as well as the uncertainties in the surface energy components, there are also other factors to consider in the variation between theory and experimental results, such as non-equilibrium contact angles and surface roughness etc.

The surface energy components of toluene, ( $\gamma^p = 2.3 \text{ mJ m}^{-2}$  and  $\gamma^d = 28.5 \text{ mJ m}^{-2}$ ), were taken from reference 7.

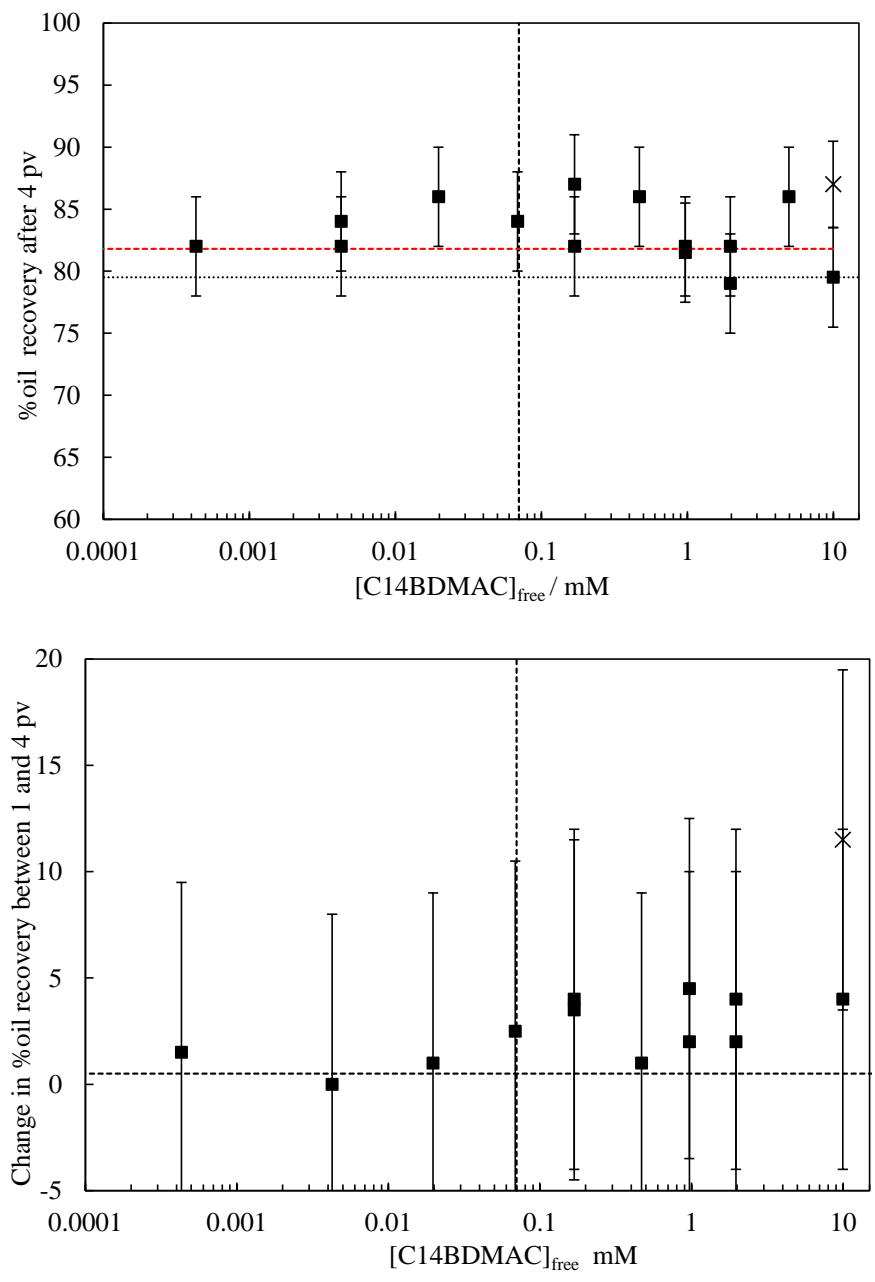
Overall, it can be seen that when the lower  $\gamma_{0\text{-calcite-water}}$  is used for the modelling, the theory is close to matching the experimental data. It catches the small increase in contact angle up to a  $[\text{C14BDMAC}]_{\text{free}}$  in the water of approximately 0.06 mM (the c $\mu$ c) and the sudden rise to 180 °. In this case, the experimental data does match the predicted post-c $\mu$ c contact angle (whereas the AOT systems did not), though the sudden jump up occurs at slightly higher concentrations than those predicted from the theory.

### 5.2.6 Toluene removal from a calcite packed column using aqueous solutions of C14BDMAC: experimental results and comparison to the model

Figure 5.10 compares the oil recovery performance of the C14BDMAC in aqueous solutions of 150 mM NaCl and 10 mM Na<sub>2</sub>CO<sub>3</sub> at 25 °C with the model calculations. As the contact angles at all surfactant concentrations are above 90 ° the %oil recovery is limited by the  $r_{\text{chan}} = r_{\text{chan,max}}$  condition. Hence, the %oil recovery for all surfactant concentrations is predicted to be 82 % by the contact angle alone mechanism. As mentioned in section 5.2.2, due to the precipitation of the C14BDMAC from the solutions (as a consequence of the system being below the Krafft point), above the solubility limit (which is presumed to be some concentration below the cac) there is no further increase in  $[\text{C14BDMAC}]_{\text{free}}$  with increasing overall concentration of C14BDMAC. Due to this there is not expected to be any increase in %oil recovery above the  $c_{\mu\text{c}}$ , and therefore no ‘extra’ oil recovery by the solubilisation/emulsification mechanisms. Hence the oil recovery for all surfactant concentrations should remain constant at 82 %. Further to this, the difference in oil recovery between 1 and 4 pore volumes is expected to remain negligible for all surfactant concentrations. The first trend, of a constant %oil recovery value of 82 % is seen clearly in the top graph of Figure 5.10, and the second trend of a negligible difference in oil recovery between 1 and 4 pore volumes is seen in the bottom graph of Figure 5.10 (despite the large error bars which are due to the small density difference between the toluene and the water phases).

To alleviate the problems of surfactant precipitation in this system, column floods can be carried out at higher temperatures. As 10 mM C14BDMAC was seen to fully dissolve at 27 °C, the temperature is not needed to be raised much to prevent precipitation (so the  $\Gamma$ ,  $\gamma$  and  $\theta$  values should remain similar). A preliminary flooding experiment was carried out with 10 mM C14BDMAC (and 150 mM NaCl and 10 mM Na<sub>2</sub>CO<sub>3</sub>) at 30 °C (to ensure the temperature does not drop below the Krafft temperature), the results of which are shown as the ‘x’ data points in both graphs of Figure 5.10. For the same concentration of  $[\text{C14BDMAC}]_{\text{init}}$  (10 mM), when the temperature is raised from 25 °C to 30 °C the %oil recovery after 4 pv increases from 80 to 87 % and the difference in oil recovery between 1 and 4 pv increases from 4 to 12 %. The difference appears to be reasonably significant between these two data points, though more floods at 30 °C need to be carried out to further confirm this trend and to enable the fitting of the  $r_{\text{sol}}+r_{\text{em}}$  part of the model to the flooding data.

**Figure 5.10** Top: Variation of %oil recovered after 4 pv as a function of the non-adsorbed (free) C14BDMAC concentration in the water for solutions containing 150 mM NaCl and 10 mM Na<sub>2</sub>CO<sub>3</sub> at 25 °C and pH 10.8. The red dashed line shows the %oil recovered from the contact angle alone mechanism calculated using the model described in the Chapter 4. Bottom: Variation of the change in %oil recovery between 1 and 4 pv versus [C14BDMAC]<sub>free</sub> (free at 4 pv) under the same conditions as the top plot. For both plots, The vertical black dashed lines shows the c<sub>μc</sub> and the horizontal black dashed line indicates the data in the absence of C14BDMAC. The ‘x’ data points are for the column flood at 30 °C.



### **5.3 Characterisation of and oil recovery performance of a system consisting of water, heptane, calcite and the commercial nonionic surfactant CW-100S**

Both the AOT and the C14BDMAC surfactants are > 98 % pure and are therefore usually used only in research applications as products this pure are far too expensive to use in large scale industrial processes. The surfactant discussed in this section (CW-100S) is a commercial grade surfactant with a distribution of chain lengths and some of the starting product from which the surfactant is made (diethanolamine) still present. It may be due to this impure nature of the surfactant that many of the trends in the results are not quite as clear as has been observed for the previous two surfactants. Some possible reasons for the differences are discussed, though in some situations a full understanding of why the differences occur is not easily determined without further work. To avoid losing sight of the main aim of this chapter (the further testing of the models derived in Chapter 4), some of the unusual phenomena exhibited by this system are not discussed in a significant amount of detail.

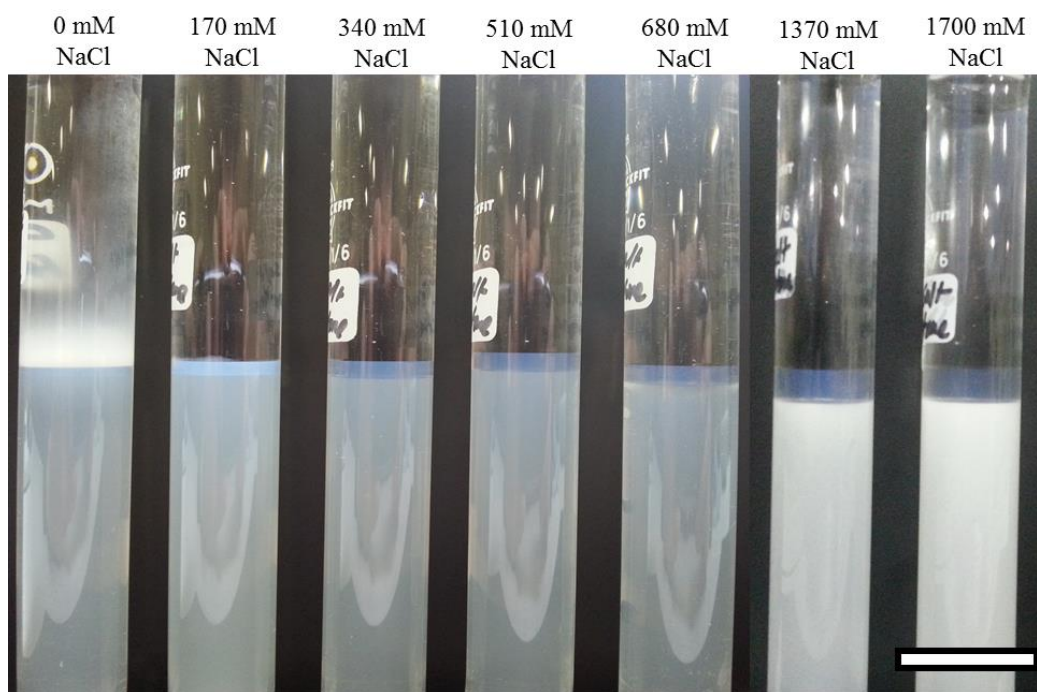
Although it is very common for varying forms of the nonionic surfactant CW-100S to be used in shampoos and a variety of other cosmetic products<sup>8</sup> as well as being used in some oil recovery research<sup>9-10</sup>, it is hard to find any in depth studies on its surface science properties. Thus, unlike the AOT and C14BDMAC, there is little literature to directly compare the trends observed here to, though comparisons too similar systems is still possible.

#### *5.3.1 Aqueous phase behaviour, microemulsion phase inversion, surfactant partitioning and the cac*

Aqueous solutions of CW-100S are clear at low concentrations and become very cloudy at higher concentrations (starting approximately at the cac). This could potentially be, as with the AOT solutions, due to the formation of liquid crystal phases. The study by Cho<sup>9</sup> shows that CW-100S increases the viscosity of water, and that the addition of NaCl can increase the viscosity further. They explain that their results are the consequence of the ‘salting out’ of the surfactant. This ‘salting out’ could be in the form of liquid crystal precipitation. However, without further experiments it is not possible to form a definitive conclusion about the existence of liquid crystals. It is worth noting that the cloudiness did not significantly disappear with a decrease in temperature, so the cloudiness is unlikely to be due the cloud point of the surfactant system.

Figure 5.11 shows tubes containing a 1:1 volume ratio of water:heptane containing concentrations of CW-100S in excess of the  $c_{\mu c}$  and varying concentrations of NaCl which were inverted and left to equilibrate for 2 days at 25 °C. The cloudiness in the water phases (the bottom phase) is mainly from the surfactant in the aqueous phase (and not un-resolved emulsions). The tube containing 0 mM NaCl is the only case in which only two distinct phases are observed. All the other tubes containing NaCl concentrations between 170 and 1700 mM show a distinct middle phase, probably indicating a Winsor III type system. The salt concentration chosen for further characterisation and oil recovery experiments was 0 mM NaCl.

**Figure 5.11** Microemulsion phase tubes of water and heptane in a 1:1 volume ratio with 25 mM CW-100S plus the concentrations of NaCl shown (all concentrations with respect to the water phase). after 2 days of equilibration at 25 °C. The scale bar represents 20 mm.



The partitioning of the CW-100S between the pure water and heptane at 25 °C is shown in Figure 5.12. The monomer partition coefficient,  $K_{Pow}$ , below the  $c_{\mu c}$  is approximately 0.85. This is much lower than the partitioning of the  $C_{12}E_5$  nonionic surfactant investigated by Aveyard *et al.*<sup>2</sup> discussed earlier in this chapter ( $K_{Pow} = 300$ ), though it is over twice that of the  $K_{Pow}$  of the  $C_{14}BDMAC$  between toluene and water from this work (section 5.2.1).

Above concentrations of approximately 0.16 mM (in the water phase), the concentration of surfactant in the water phase increases, whereas the concentration in the heptane remains constant, indicating a Winsor I system (in agreement with the microemulsion phase tubes). The  $c_{\mu c}$  in water determined from the breakpoint in the partitioning data (approximately 0.16 mM) is within the range of the  $c_{\mu c}$  in the water determined by interfacial tension measurements in section 5.3.3 (0.12 - 0.70 mM).

**Figure 5.12** Equilibrium concentrations of CW-100S in equilibrated water and heptane phases (no salt) at 25 °C. The solid line is a manually fitted trend line

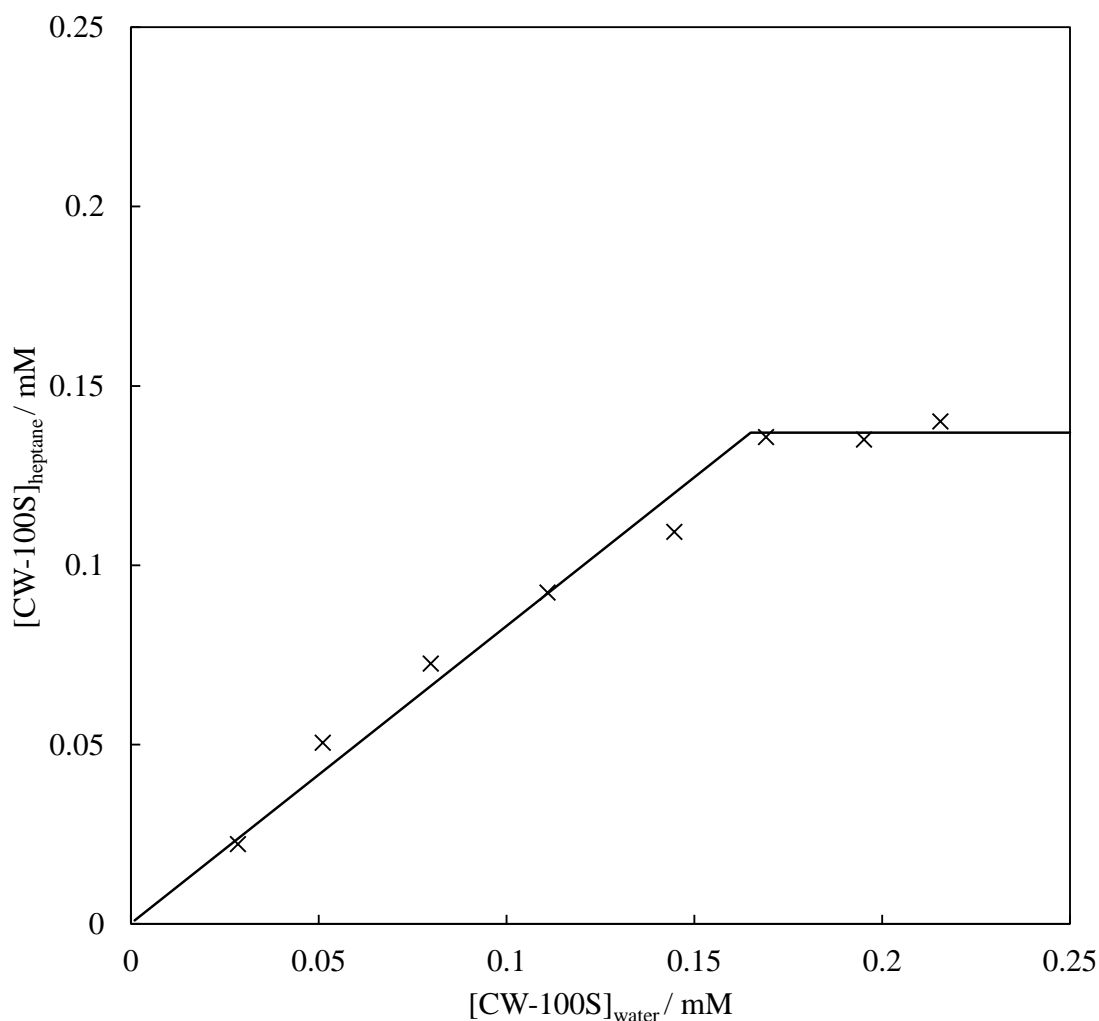
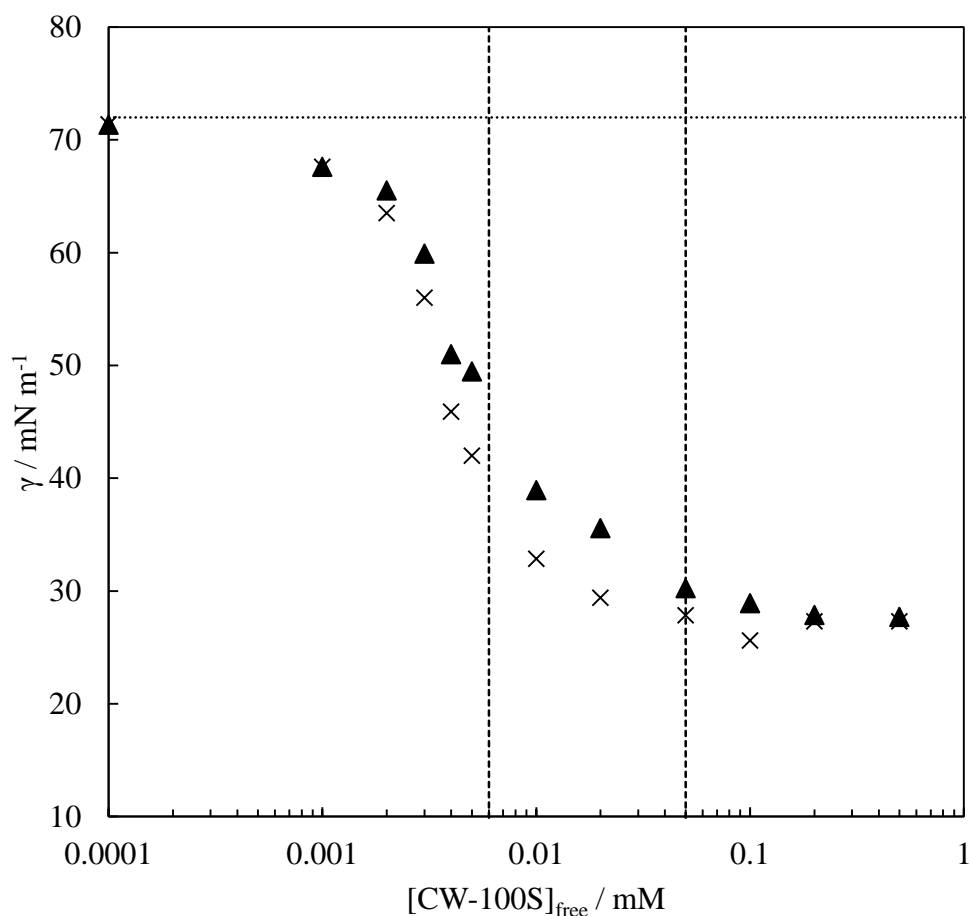


Figure 5.13 shows the variation of the air-water surface tension with [CW-100S]. Two trends need to be noted. Firstly, the surface tensions only approached a steady value after approximately an hour (both initial and equilibrium values are shown), and secondly, the surfactant does not behave as ideally as both the AOT and the C14BDMAC. Instead of the gradient becoming progressively steeper up to the

breakpoint to a horizontal trend (as expected from the Gibbs adsorption equation), the gradient becomes steeper, then shallower, followed by a horizontal trend. Although this trend is not expected for pure surfactants, it is a common trend seen for commercial (or technical) grade nonionic surfactants<sup>11</sup>. Some studies have been carried out to attempt to understand the effects of impurities in producing such trends<sup>12</sup>, though here no further interpretation is made.

**Figure 5.13** Surface tensions (air-water interfacial tensions) of water containing varying concentrations of CW-100S at 25 °C, the triangles are the initial tensions and the crosses the equilibrium tensions. The horizontal dotted line indicates the surface tension with zero surfactant, and the two vertical dashed lines indicate the range of concentrations the cac may be within.



As no clear single value for the cac is easily obtained, it is easier to quote the cac as a range of concentrations, which in this case is 0.006 - 0.05 mM CW-100S. This cac range is a significant amount lower than the water-heptane c<sub>1c</sub> determined both from the partitioning (Figure 5.12) and the interfacial tension measurements (Figure 5.16), which is in the range 0.12 - 0.70 mM.

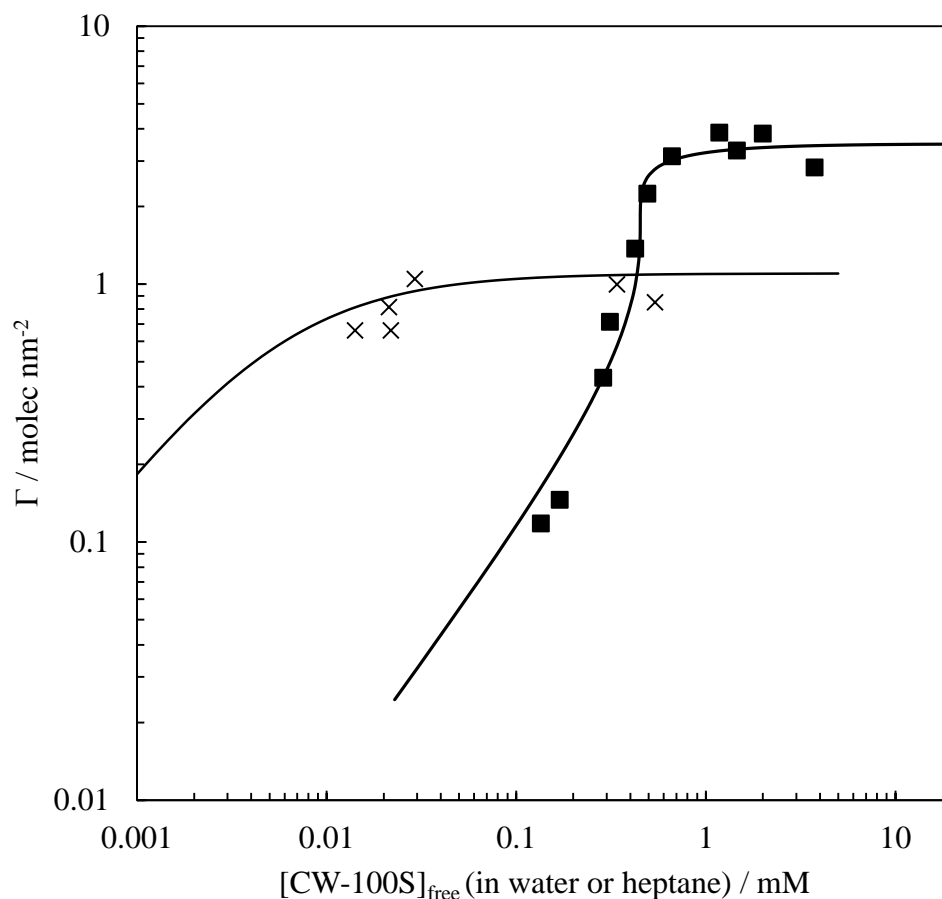
### 5.3.2 Adsorption of the CW-100S to the water-calcite and heptane-calcite interfaces

Figure 5.14 shows the adsorption of the CW-100S to the water-calcite and the heptane-calcite interfaces at 25 °C. The adsorption to the water-calcite interface is very similar to that seen by the AOT in Chapter 4. However, most of the adsorption occurs at concentrations approximately 10 times higher than the  $c_{ac}$  determined by surface tension measurements. The adsorption is even more cooperative in nature than the AOT ( $\beta = -4$  for CW-100S,  $\beta = -3.5$  for AOT) and the  $\Gamma_{max}$  is higher (3.5 molecules  $nm^{-2}$  for CW-100S, approximately 2.2 molecules  $nm^{-2}$  for AOT). Without further work it is not possible to fully understand why the cooperative adsorption occurs at concentrations much higher than the  $c_{ac}$  determined by surface tension measurements. Interestingly, the point at which most of the adsorption occurs is similar to the  $c_{\mu c}$  in water for a water-heptane system, which is in the range 0.12 - 0.70 mM.

The adsorption to the heptane-calcite interface appears to be much less cooperative (as much as can be seen from the data), with higher adsorption at lower concentrations and a  $\Gamma_{max}$  approximately half that of the adsorption at the water-calcite interface. Again, the detection limit of the technique did not allow for the determination of the adsorption at lower concentrations than those shown). All of the fitting parameters can be seen in Table 5.2.

Kuno et al.<sup>13-16</sup> have investigated the adsorption of the nonionic surfactant polyoxyethylene nonylphenol,  $C_9PhE_x$  (with  $x = 1-10$ ), on to polar and non-polar surfaces from polar and non-polar solvents. The results from their studies which are of most interest here are how the adsorption of the surfactant to calcium carbonate changes with different solvents. They see that when the difference in polarity is large (calcium carbonate and cyclohexane), the adsorption is non-cooperative, i.e. Langmuir-type adsorption, and corresponds to an ordered monolayer of the surfactant at the interface. When the polarity difference is similar (water and calcium carbonate), the adsorption isotherms indicate multilayer adsorption. These observations can also be said of the data in Figure 5.14. The area per surfactant at  $\Gamma_{max}$  for the CW-100S adsorption at both the water-calcite and heptane-calcite interfaces (0.28 and 0.91 molecules  $nm^{-2}$  respectively) are very similar to the adsorption of the  $C_9PhE_6$  to the water-calcium carbonate and cyclohexane-calcium carbonate interfaces (0.21 and 0.93 molecules  $nm^{-2}$  respectively)<sup>16</sup>.

**Figure 5.14** Adsorption isotherms for the adsorption of CW-100S to the water-calcite (squares) and the heptane-calcite (crosses) interfaces at 25.0 °C and pH 9.5 ± 0.5. The curved lines show the fits to the cooperative Langmuir type isotherm (Chapter 4, equation 4.1), with fitting parameters shown in Table 5.2.

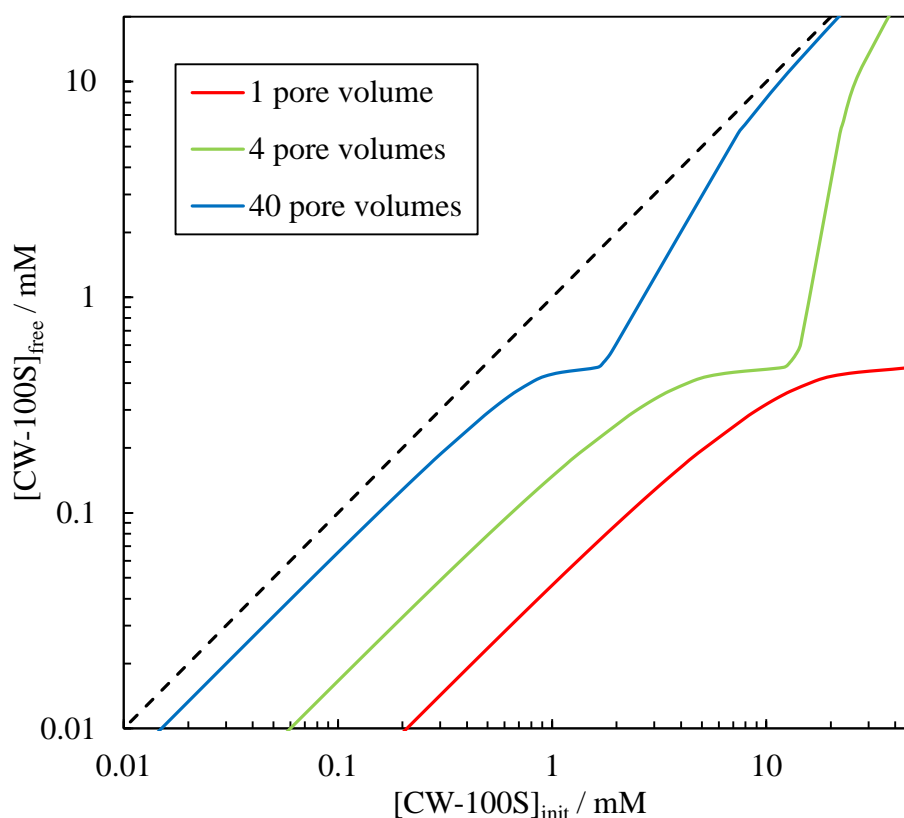


**Table 5.2** Fitting parameters for the Langmuir type isotherms in Figure 5.14, and the area per surfactant adsorbed at  $\Gamma_{\max}$ . Note that the  $K$  for the heptane-calcite adsorption has a large error due to limited data at low concentrations.

Interface	$\Gamma_{\max}$ / molecules $\text{nm}^{-2}$	Area per surfactant at $\Gamma_{\max}$ / $\text{nm}^2 \text{ molecules}^{-1}$	$\beta$	$K$ / $\text{mM}^{-1}$
water-calcite	3.5	0.28	-4.0	0.3
heptane-calcite	1.1	0.91	0.0	200

The relationship between  $[\text{CW-100S}]_{\text{init}}$  and  $[\text{CW-100S}]_{\text{free}}$  after pumping aqueous phases of CW-100S through an FC10 packed column with  $f = 0.4$  is shown in Figure 5.15. In order to keep the model simple, the heptane-calcite adsorption is not considered. The relationship is very similar to that for the AOT containing systems in Chapter 4. The main difference is that the maximum amount lost (corresponding to the peak of the adsorption isotherm) is higher than that seen for the AOT, as the  $\Gamma_{\text{max}}$  is 3.5 molecules  $\text{nm}^{-2}$ , whereas for the AOT it was approximately 2.2 molecules  $\text{nm}^{-2}$ .

**Figure 5.15** Relationship between the initial concentration of CW-100S in solution ( $[\text{CW-100S}]_{\text{init}}$ ) pumped in to an FC10 packed column with  $f = 0.4$  and the corresponding concentration of surfactant ‘free’ after some has been depleted by adsorption to the calcite-water interface ( $[\text{CW-100S}]_{\text{free}}$ ) at different pore volumes of the solutions pumped through the column. The diagonal dashed line shows the case of no adsorption

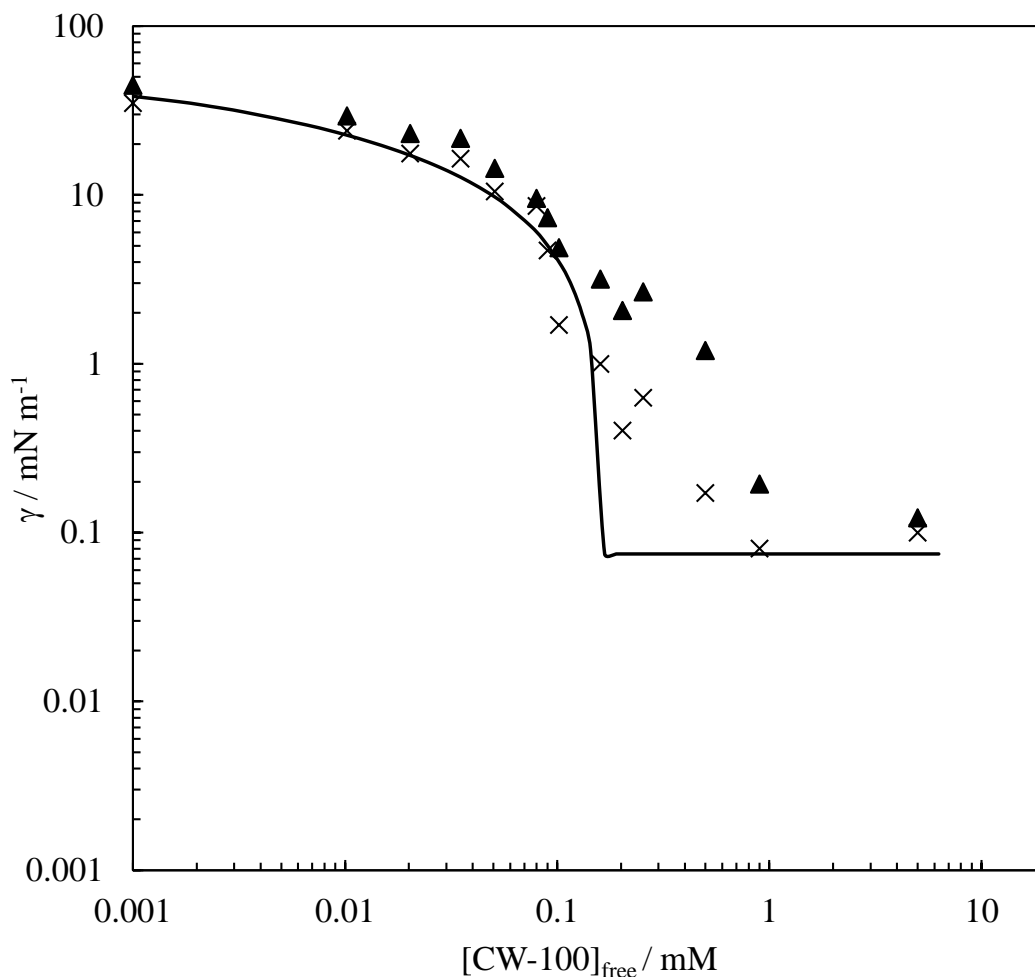


### 5.3.3 *Effect of CW-100S concentration on the heptane-water interfacial tensions*

Figure 5.16 shows the variation of the heptane-water interfacial tension with CW-100S concentration ( $[CW-100S]_{\text{free}}$  refers to the concentration in the water phase). As mentioned in the introduction to this chapter, both the initial and equilibrated tensions are shown to aid the discussions of the change in the water-heptane-calcite contact angles in section 5.3.4. The tensions follow a similar trend to the surface tensions in Figure 5.13, where the gradient becomes progressively steeper, then shallower, followed by a levelling off to a horizontal plateau. The first aggregates may be forming at the point at which the gradient becomes shallower, followed by complete aggregation at the break point to horizontal<sup>12</sup>. It is for this reason that the modelling of the tension is made to follow the first steep gradient down to a plateau.

When interfacial tensions take a longer time to equilibrate the equilibration time is often limited by the diffusion of the surfactant from the bulk of the phase to the interface<sup>17</sup>. It may be expected, then, that the difference between the initial and the equilibrium tensions would be greatest at lowest concentrations. This trend however is not observed in Figure 5.16. The greatest difference between initial and equilibrium tensions is seen for the ‘in-between’ concentrations. Thus, the equilibration of the tensions may be more complex than just diffusion controlled rates. As the greatest difference between the initial and equilibrium tension occurs around and just after the point where aggregates are first formed, the slow equilibration could be as a consequence of the complex equilibria between the aggregation and adsorption of the varying chain lengths of the surfactant present. To determine if this is the case, further work would need to be carried out where the ratio of the different chain lengths present could be controlled.

**Figure 5.16** Variation of heptane-water tensions with aqueous CW-100S concentration at 25.0°C in pure water (pre or pseudo equilibrated with the toluene). The curved line shows the best-fit calculated as described in Chapter 4 section 4.3.4. The triangles are the initial tensions and the crosses the equilibrium tensions.



The  $c_{\mu c}$ , taken to be the point at which the gradient changes from a steep to a shallow gradient (where initial aggregates are expected to be formed), is approximately 0.16  $\text{mM}$  in the water, and the post- $c_{\mu c}$  oil-water tension is approximately 0.08  $\text{mN m}^{-1}$ . This post- $c_{\mu c}$  oil-water tension is in the midrange of all the post- $c_{\mu c}$  tensions encountered within this work.

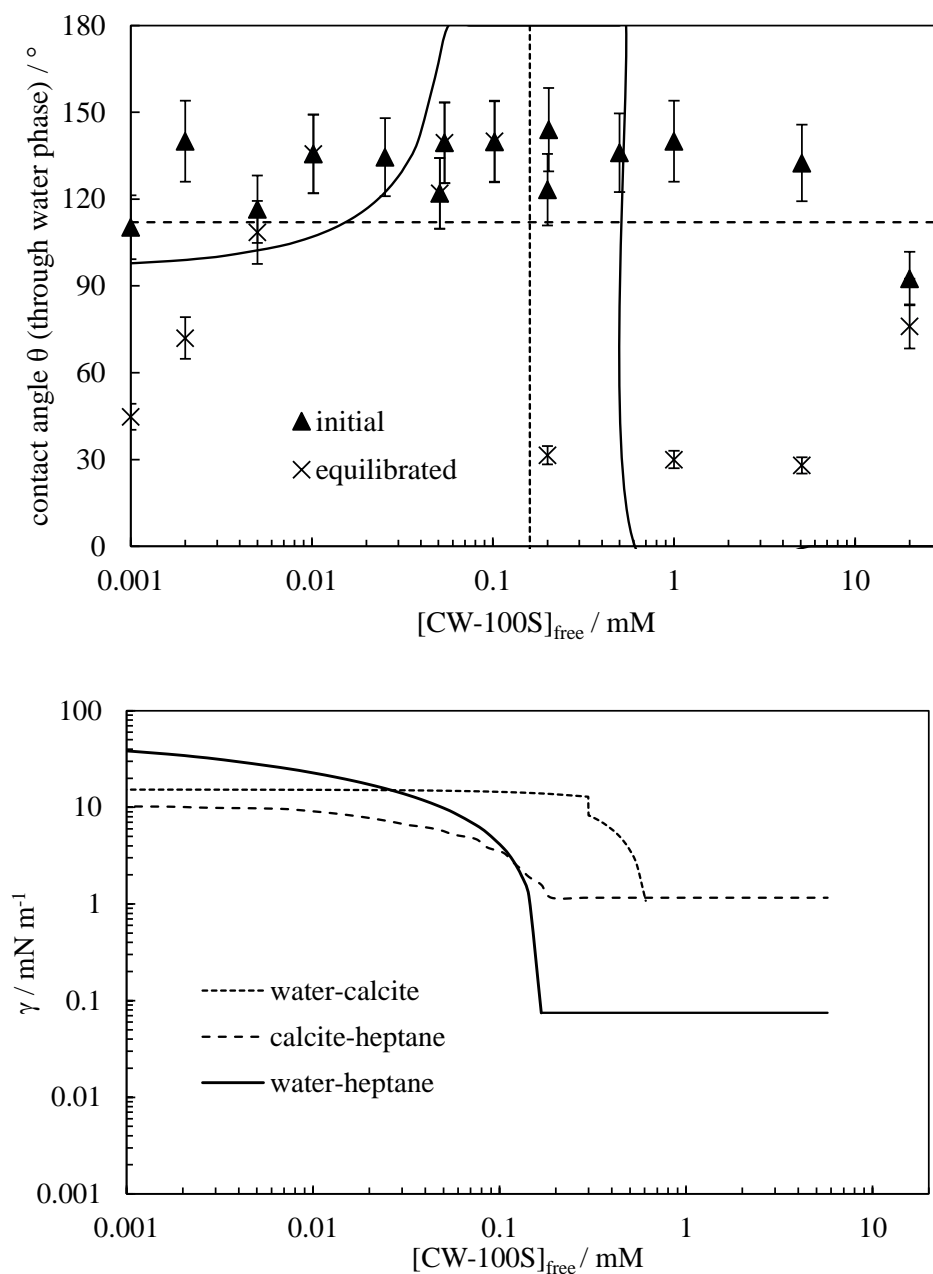
#### 5.3.4 Effect of CW-100S concentration on the water-calcite-heptane contact angles

As discussed in Chapter 4, the change in the calcite-water and calcite-oil interfacial tensions can be approximated from the adsorption data using the combined Gibbs adsorption equation and the Langmuir isotherm. Although the Langmuir isotherm did not provide the best fit to the experimental data for the adsorption of AOT to the calcite-water interface, it still captured the point at which most of the adsorption occurred and hence provided a good approximation for the change in the interfacial tensions. Here, however, as the adsorption of the CW-100S to the calcite-water interface is even more cooperative in nature than the AOT, the Langmuir isotherm does not suitably match the experimental data. As the Langmuir type isotherm (Chapter 4, equation 4.1) is not easily integrated, it was necessary to find a suitable replacement equation to model the adsorption which can also be combined with the Gibbs adsorption equation and integrated. Despite multiple attempts, such an isotherm was not found. It was therefore decided upon to use multiple straight line equations for the different sections of the isotherm and ‘stitch’ together the results (utilising the IF function in EXCEL). The final equation resulting from the combination, rearrangement and integration of the straight line equation ( $\Gamma = m [\text{surf}]_{\text{free}} + c$ ) and the Gibbs adsorption equation is shown in equation 5.1.

$$\gamma = \gamma_0 - \left( [\text{surf}]_{\text{free}} kT(m+c) \right) \quad (5.1)$$

where  $m$  is the gradient of the line and  $c$  the y-intercept. This results in three different straight line sections being fitted to the water-calcite adsorption data, one for the low concentration adsorption, the second for the cooperative ‘step’ and the final for the plateau at  $\Gamma_{\text{max}}$ . This approach is only used for the water-calcite adsorption and tension changes, the heptane-calcite and heptane-water adsorption and tension changes were modelled using the Langmuir isotherm as with the AOT and C14BDMAC systems. The calculated tensions and corresponding measured and calculated contact angles are shown in Figure 5.17. The calcite-heptane tensions are plotted vs. the aqueous phase concentration, though the tensions are calculated from the corresponding concentrations which would be present in the heptane phase at each individual concentration in the water phase. The surface energy components for the heptane ( $\gamma^p = 0 \text{ mJ m}^{-2}$  and  $\gamma^d = 20.1 \text{ mJ m}^{-2}$ ) were taken from reference 7.

**Figure 5.17** Upper plot: Variation of the heptane-water-calcite advanced initial and equilibrium contact angles (measured through the aqueous phase) with aqueous CW-100S concentration in pure water at 25 °C. The vertical dashed line indicates the  $c_{\mu c}$ . The horizontal dashed line shows the contact angle in the absence of added CW-100S. The solid line shows the calculated contact angle from the water-toluene (measured), water-calcite and toluene-calcite tensions (both derived from the measured adsorption isotherms) shown in the lower plot. The ‘kink’ in the water-calcite tension is an artefact from the fitting together of the three lines of best fit (described in the text). The tensions in the lower plot were calculated with equation 4.8, the fitting parameters are in Appendix C.



There are a number of interesting trends which can be observed in Figure 5.17. Firstly, the initial contact angles stay approximately the same within the error across the whole concentration range and are  $130 \pm 20^\circ$ , similar to the contact angle in the absence of surfactant. Unlike both the AOT and the C14BDMAC containing systems, the equilibrium contact angles for this CW-100S containing system can vary dramatically from the initial angles. The time for the equilibrium values to be established can also vary to a large extent (even for repeats of the same concentrations). An unusual trend sometimes observed is that the change from high contact angle to the contact angle at equilibrium can occur in a rapid motion after the drop has been left on the surface for up to approximately an hour. Other times the change can occur quickly over the first few minutes in which the drop was placed on the surface, and still other times the change can be gradual over the course of a few hours.

The large change in contact angle is much larger than that exhibited by the C14BDMAC containing system discussed in the first half of this chapter, for which the change was thought to be due to partition equilibrium effects. It is not possible to cause the modelled contact angles to match the experimental results, in particular the low angles at low concentrations of surfactant followed by the steep rise in  $\theta$ . The effect of using different concentrations of CW-100S in the heptane phase than that predicted from the partition coefficient is similar to that observed for the C14BDMAC containing system (using lower concentrations in the oil than that calculated from the partitioning causes the contact angle to be similar to those observed for lower concentrations of surfactant in the water). The adsorption isotherms and water-heptane interfacial tension measurements produce reasonably reliable results, so it is interesting that the contact angle measurements behave so erratically.

A final observation for the measurement of these contact angles is that, if the water drop is placed on the calcite under air followed by careful addition of the heptane (the reverse to the usual technique), the contact angles with concentrations of CW-100S in the aqueous phases of 0.002 to 0.2 mM were all  $40 \pm 20^\circ$ . Thus, a further possible reason for the large change in the contact angles seen in Figure 5.17 could be due to the presence of a thin film of the heptane which either drains away (giving rise to the smooth changes from initial to equilibrium contact angles) or is suddenly ruptured (giving rise to the sudden change in contact angle). Following the removal of the thin heptane film the water phase would then be in contact with the calcite and thus produce contact angles

similar to when water is placed on the calcite before the heptane is added (in which case there cannot be a heptane film). However, unless further experiments were carried out this is purely speculative. Further, this explanation does not account for the large difference between the measured angles and those predicted from the interfacial tensions.

### 5.3.5 Heptane removal from a calcite packed column using aqueous solutions of CW-100S: experimental results and comparison to the model

Figure 5.18 compares the oil recovery performance of the CW-100S aqueous solutions at 25 °C with the model calculations. As the equilibrium time for the measurement of the contact angles was so erratic, it is not easy to determine which angles (initial or equilibrium) might be expected to be encountered during the column floods. Hence the predicted oil recovery for both types of contact angle is shown. With  $[\text{CW-100S}]_{\text{free}}$  below the  $c_{\mu c}$  the experimental oil recovery is seen to fluctuate between approximately 70 and 80 %, which could be due to the multiple variations of contact angles which may be present within the column. To avoid over interpretations being made from the erratic data, no further observations will be made for the oil recovery with  $[\text{CW-100S}]_{\text{free}}$  below the  $c_{\mu c}$ . The increase in oil recovery due to the solubilisation/emulsification is seen to occur at the  $c_{\mu c}$ , indicating that the conversion from  $[\text{surf}]_{\text{init}}$  to  $[\text{surf}]_{\text{free}}$  using the first model produces reliable results despite not taking in to account the surfactant partitioning and adsorption at the heptane-calcite interface.

The oil recovery from the contact angle plus the solubilisation/emulsification mechanisms above the  $c_{\mu c}$  is reasonably well represented with a value of the  $R_{\text{sol}}+R_{\text{em}}$  parameter of 150 (with post- $c_{\mu c}$  water-heptane interfacial tension =  $0.08 \text{ mN m}^{-1}$ ). When this is plotted on the graph of  $R_{\text{sol}}+R_{\text{em}}$  vs. post- $c_{\mu c}$  interfacial tension along with the data from the AOT containing system (Figure 5.19), the data for both systems follow the same trend line. This increases the confidence in the post- $c_{\mu c}$  oil recovery prediction as being universal for all surfactant systems (if the surfactant remains dissolved and does not precipitate out, as with the C14BDMAC).

**Figure 5.18** Top: Variation of %oil recovered after 4 pv as a function of the non-adsorbed (free) CW-100S concentration in the water at 25 °C. The red dashed line shows the %oil recovered from the contact angle alone mechanism for initial contact angles, the purple dashed line for equilibrium contact angles and the green dotted line the %oil recovered from the equilibrium contact angle and the solubilisation/emulsification mechanisms combined, all calculated using the model described in the Chapter 4 Bottom: Variation of the change in %oil recovery between 1 and 4 pv versus  $[CW-100S]_{free}$  (free at 4 pv) under the same conditions as the top plot. For both plots, The vertical black dashed lines shows the  $c_{\mu c}$  and the horizontal black dashed line indicates the data in the absence of CW-100S.

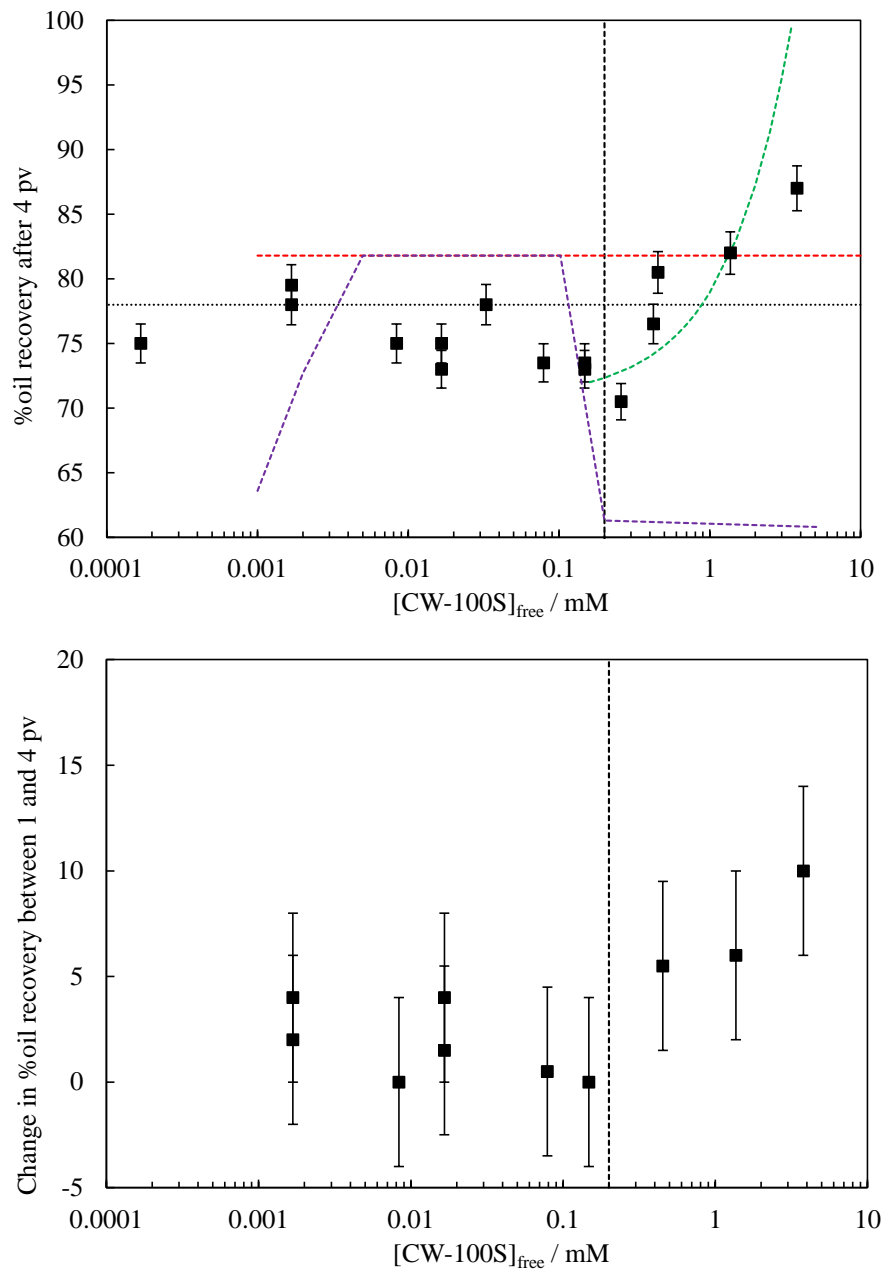
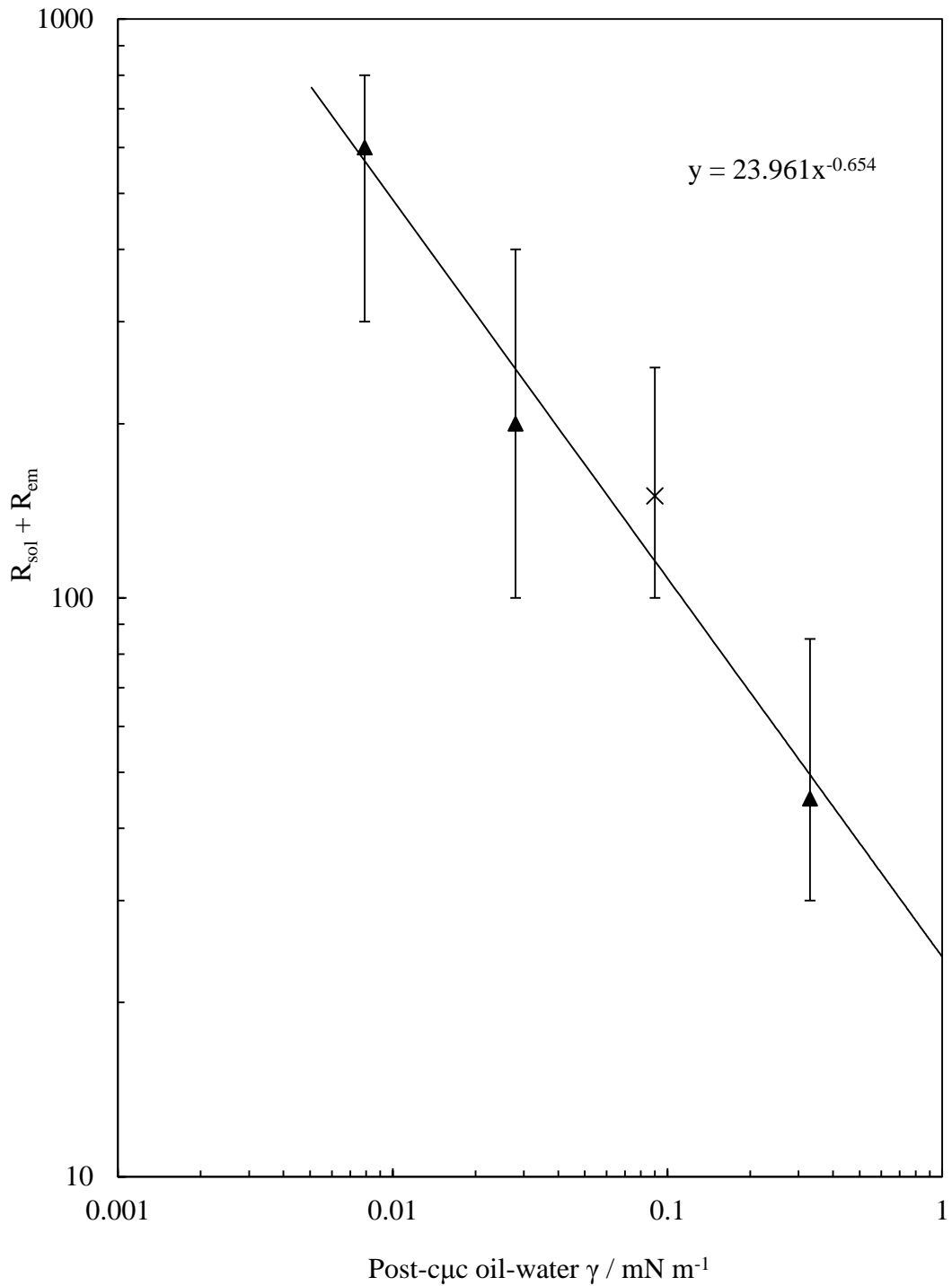


**Figure 5.19**  $R_{sol} + R_{em}$  parameters in figures 4.12, 4.14 and 4.15 from Chapter 4 and from Figure 5.19 in this chapter vs. the respective post-cmc oil-water interfacial tensions. The solid straight line is the fit to a power function curve. The triangles are the data from the AOT systems in Chapter 4 and the cross from the CW-100S system in the current chapter.



## 5.4 Conclusions

With the aim of further testing the models derived in Chapter 4 using two systems which behaved differently to the AOT containing systems, two separate three-phase systems were characterised and the oil recovery performance measured. The two systems investigated consisted of; i) water, toluene, calcite and the pure cationic surfactant C14BDMAC, and ii) water, heptane, calcite and the un-pure commercial (technical grade) nonionic surfactant CW-100S. Both systems formed a Winsor I system upon equilibration of the components with a  $[\text{surf}] \geq \text{cmc}$ . The following conclusions focus on the significant differences between the two systems discussed in this chapter and the AOT systems in Chapter 4 and how the differences have affected the oil recovery performance and the modelling thereof.

There were three main differences between the behaviour of the system consisting of water, toluene, calcite and the pure cationic surfactant C14BDMAC and the AOT containing systems in Chapter 4. The first being that the adsorption of the C14BDMAC to the calcite-water interface was seen to be much lower, with a  $\Gamma_{\text{max}}$  of 0.027 molecules  $\text{nm}^{-2}$ , as opposed to the 2.2 molecules  $\text{nm}^{-2}$  observed for the AOT containing systems. The consequence of this on the contact angles is the second main difference, that being that the post-cmc contact angles were 180 °, as opposed to the 0 ° (predicted) for the AOT containing systems. Finally, as 25 °C was below the Krafft temperature for the C14BDMAC in water containing 150 mM NaCl and 10 mM  $\text{Na}_2\text{CO}_3$ , the surfactant precipitated out of the solutions over the period of a few hours.

There were two main consequences of these differences on the oil recovery, those being: i) due to the contact angle at all concentrations being above 90 °, the oil recovery was limited by the  $r_{\text{chan}} = r_{\text{chan,max}}$  condition, and ii) there was no extra oil recovery with concentrations of surfactant above the cmc as the surfactant precipitates out (and was no longer available for adsorbing at the toluene-water interface). Hence, the % oil recovery was calculated to remain constant at 82 % and for there to be no difference in oil recovery between 1 and 4 pore volumes across the whole concentration range (and no value for  $r_{\text{sol}+\text{rem}}$ ). These two trends were both observed experimentally and modelled successfully. Initial experiments for oil recovery at 30 °C (to prevent precipitation of surfactant) had promising results in that the oil recovery above the cmc increased.

The system consisting of water, heptane, calcite and the un-pure nonionic surfactant, CW-100S had similar behaviour to the AOT containing systems in terms of the post-c<sub>μc</sub> contact angles, aqueous phase behaviour and the water-calcite adsorption. There were a number of differences observed too. The first difference being that the calcite-water adsorption was slightly more cooperative in nature ( $\beta = 4.0$ , opposed to  $\beta = 3.5$  for AOT systems), and the  $\Gamma_{\max}$  was higher (3.5 molecules nm<sup>-2</sup>, opposed to 2.2 molecules nm<sup>-2</sup> for the AOT systems). A second difference was that the surfactant does partition in to the oil, and does also adsorb at the oil-water interface (in a non-cooperative Langmuir type adsorption). The measurement of the heptane-water interfacial tensions as a function of surfactant concentration produced a plot that is often observed for technical grade nonionic surfactants, where the gradient becomes progressively steeper, followed by a region of a shallower gradient, followed by a levelling off to a plateau. The contact angles at some concentrations showed significant differences between the initial and the equilibrium measurements. Further to this, the contact angle equilibrium times were very erratic in nature and were seen to vary from minutes to hours for some repeats of the same concentrations.

The consequence of the erratic behaviour of the contact angles meant that the modelling of the oil recovery was carried out using both the initial and the equilibrium contact angles. The experimental data for the %oil recovery was seen to fluctuate between 70 and 80 % for concentrations of surfactant below the c<sub>μc</sub>, which may have been due to the multiple possibilities of the contact angles that could be encountered during a column flood. The post-c<sub>μc</sub> oil recovery results from the contact angle plus the emulsification/solubilisation ratio was well modelled using a value of 150 for the  $R_{\text{sol}}+R_{\text{em}}$  parameter (for a post c<sub>μc</sub> oil water interfacial tension of 0.08 mN m<sup>-1</sup>). This value followed the same trend line as the AOT systems when  $R_{\text{sol}}+R_{\text{em}}$  was plotted against the post-c<sub>μc</sub> oil-water interfacial tensions, thus increasing the confidence in the predictive capabilities of the model.

Overall, taking in to account factors which may affect the assumptions of the models (such as surfactant precipitation as a consequence of being below the Krafft point), both models derived in Chapter 4 provide a good match to the experimental data obtained using both the cationic and nonionic surfactant systems.

## 5.5 References

1. Alaei, P., Binks, B.P., Fletcher, P.D.I., Salama, I.E., Horsup, D.I., Surfactant Properties of Alkylbenzyltrimethylammonium Chloride Oilfield Corrosion Inhibitors, *Corrosion*, NACE 2013, paper 2158, 1.
2. Aveyard, R., Binks, B.P., Clark, S., and Fletcher P.D.I., Effects of Temperature on the Partitioning and Adsorption of C<sub>12</sub>E<sub>5</sub> in Heptane-Water mixtures, *J. Chem. Soc. Faraday Trans.*, **1990**, *86*, 3111.
3. Rodriguez, C.H., Lowery, L.H., Scamehorn, J.F., Harwell, J.H., Kinetics of Precipitation of Surfactants. I. Anionic Surfactants with Calcium and with Cationic Surfactants, *J. Surfactants. Deterg.*, **2001**, *4*, 1.
4. Rodriguez, C.H., Scamehorn, J.F., Kinetics of Precipitation of Surfactants. II. Anionic Surfactant Mixtures, *J. Surfactants. Deterg.*, **2001**, *4*, 15.
5. Rodriguez, C.H., Yuan, W-L., Scamehorn, J.F., O'Rear, E.A., Kinetics of Precipitation of Surfactants. III. Atomic Force Microscopy of Precipitate Crystals, *J. Surfactants. Deterg.*, **2002**, *5*, 269.
6. Ma, K., Cui, L., Dong, Y., Wang, T., Da, C., Hirasaki, G.J., Biswal, S.L., Adsorption of cationic and anionic surfactants on natural and synthetic carbonate materials, *J. Colloid Interface Sci.*, **2013**, *408*, 164.
7. van Oss, C.J. *Interfacial forces in aqueous media*, New York: Marcel Dekker, **1994**.
8. Fiume, M.M., Heldreth, B., Bergfeld, W.F., Belsito, D.V., Hill, R.A., Klaassen, C.D., Liebler, D.C., Marks, J.G., Shank, R.C., Slaga, T.J., Snyder, P.W., Andersen, F.A., Safety Assessment of Diethanolamides as Used in Cosmetics, *Int. J. Toxicology*, **2013**, *32*, 36S.
9. Cho, W.G., Rheological Behaviour of Surfactant Mixtures by Varying the Concentration of Polyols, *J. Korean Oil Chem. Soc.*, **2009**, *26*, 422.
10. Iglauer, S., Wu, Y., Shuler, P., Tang, Y., Goddard III, W.A., New surfactant classes for enhanced oil recovery and their tertiary oil recovery potential, *J. Pet. Sci. Eng.*, **2010**, *71*, 23.

11. Lin, S-Y., Lin, Y-Y., Chen, E-M., Hsu, C-T. and Kwan, C-C., A Study of the Equilibrium Surface tension and the Critical Micelle Concentration of Mixed Surfactant Solutions, *Langmuir*, **1999**, *15*, 4370.
12. Clint, J.H., Micellization of mixed nonionic surface active agents, *J. Chem. Soc., Faraday Trans. 1*, **1975**, *71*, 1327.
13. Kuno, H. and Abe, R., The adsorption of polyoxyethylated nonylphenol on calcium carbonate in aqueous solution, *Kolloid-Z*, **1961**, *177*, 40.
14. Abe, R, Kuno, H., The adsorption of polyoxyethylated nonylphenol on carbon black in aqueous solution, *Kolloid-Z*, **1962**, *181*, 70.
15. Kuno, H., Abe, R. and Tahara, S., The Adsorption of Polyoxyethylated Nonylphenol in Cyclohexane Solution, *Kolloid-Z*, **1964**, *198*, 77.
16. Rybinski, W. and Schwuger, M.J., Adsorption and Wetting. Chap. 2., pp. 45-108 in Schick, M.J. (Eds.) *Nonionic Surfactants Physical Chemistry*, Marcel Dekker, Inc., New York, **1987**.
17. Binks, B.P., Fletcher, P.D.I., Paunov, V.N., Segal, D., Equilibrium and Dynamic Adsorption of C12E5 at the Air-Water Surface Investigated Using Ellipsometry and Tensiometry, *Langmuir*, **2000**, *16*, 8926.

## CHAPTER 6

### SUMMARY OF CONCLUSIONS, FUTURE WORK AND PRELIMINARY EXPERIMENTS

#### 6.1 Summary of conclusions

In Chapter 3 the flow properties of a column packed with three different sized calcite particle powders were characterised in some detail. The porosities, permeability's and pore sizes were found to be similar to some examples of reservoir outcrop rock. For a column packed with the smallest particle size (FC10,  $r_{\text{particle}} = 1.4 \mu\text{m}$ ) the porosity,  $\phi_{\text{pore}} = 0.45$ , the permeability 1.2 mD and the pore size,  $r_{\text{pore}} = 0.16 \mu\text{m}$ . This system was used for the majority of experiments throughout this work. When the oil was displaced by an aqueous phase the capillary number (Ca) at which oil break-off and mobilisation occurred was approximately  $6 \times 10^{-9}$ . Oil recovery floods with low [surf] were in the low Ca regime, and floods with high [surf] in the high Ca regime. Gravity did not appear to have a significant effect on oil recovery.

The surface chemistry properties of three different surfactants were characterised in detail for systems consisting of water, an oil, calcite, varying salt concentrations and the surfactant at 25 °C. Table 6.1 summarises the systems investigated along with the main surface chemistry properties determined. Both AOT (anionic) and C14BDMAC (cationic) were pure surfactants, and the CW-100S (nonionic) an un-pure technical grade commercial surfactant. Both the AOT and CW-100S had similar cooperative adsorption to the calcite-water interface, indicating formation of a multilayer. Due to this relatively high adsorption the equilibrium post-cyc water-calcite-oil contact angle fell to approximately 30 ° (from tension data this was predicted to be 0 °). Both systems also formed cloudy water phases at higher concentrations (higher than approximately the cac). For the AOT systems this was known to be due to the formation of lamellar liquid crystal phases, also assumed to be the case for the CW-100S. The CW-100S showed erratic behaviour when measuring the contact angles, this was for undetermined reasons. The C14BDMAC had very weak adsorption at the calcite-water interface. This led to a post-cyc contact angle of 180 °. Further, the surfactant precipitated out of solution at higher concentrations. This was determined to be as a consequence of 25 ° being below the Krafft temperature of the system (determined to be approximately 27 °C).

**Table 6.1** Summary of the main parameters for all water-oil-calcite systems investigated. All systems were investigated at 25 °C.

Surfactant	AOT	AOT	AOT	C14BDMAC	CW-100S
Oil	decane	decane	decane	toluene	heptane
[NaCl] / mM	0	40	75	150	0
[Na <sub>2</sub> CO <sub>3</sub> ] / mM	10	10	10	10	0
Aqueous phase $c_{\mu c}$ / mM	1.0	0.60	0.50	0.06	0.17
Equilibrium Winsor system	I	I	III	I	I
Post- $c_{\mu c}$ $\gamma_{\text{water-oil}}$ / mN m <sup>-1</sup>	0.33	0.028	0.0079	0.015	0.080
Three-phase $\theta$ (thru' water, no surfactant) / °	123	126	120	121	112
Three-phase $\theta$ (thru' water, post $c_{\mu c}$ ) / °	37	31	22	180	140-30 (non-eqlbm to eqlbm)
$\Gamma_{\text{max}}$ water-calcite / molecules nm <sup>-2</sup>	2.3	2.0	2.2	0.027	3.5
Monomer partition coefficient / $K_{P-ow}$	0	0	0	0.40	0.85

Two models were derived to enable modelling of the oil recovery performance of the aqueous surfactant solutions being pumped through the powder packed columns with interstices filled with the oil. The first model to enable the concentration of free surfactant,  $[\text{surf}]_{\text{free}}$ , present within the packed columns during flooding to be calculated from the initial concentration pumped in,  $[\text{surf}]_{\text{init}}$ . This allowed a direct comparison between characterisation results (which relate to  $[\text{surf}]_{\text{free}}$ ) and %oil recovery results (which relate to  $[\text{surf}]_{\text{init}}$ ). The second two-part model showed how, based on the hypothesis that the residual oil is trapped in the form of liquid bridges between contacting calcite particles, the measured %oil recovery variation with surfactant concentration can be understood and predicted for concentrations of surfactant both below and above the  $c_{\mu c}$  in terms of the characterisation results. The model was implemented by taking the packed bed to consist of monodisperse spheres packed in a cubic arrangement.

The second model worked on the principle of the balancing between the Laplace pressure across the oil-water interface of the bridges, and the Laplace pressure across the oil-water interface of the bulge of water being forced through the interstices between the particles (when the two Laplace pressures become equal, no more oil is recovered). With  $[\text{surf}]_{\text{free}} < c_{\mu c}$ , the oil recovery was found to be determined by the contact angle alone. This allowed for a universal graph to be plotted indicating the oil recovery expected for any given contact angle. This showed a rise from 58 %oil recovery with a  $0^\circ$  contact angle through the water to 82 % with a contact angle of  $90^\circ$  or greater. The limiting oil recovery at 82 % was due to a limiting factor denoted as  $r_{\text{chan}} = r_{\text{chan,max}}$  whereby the effective radius of the flow channels through the particle interstices cannot exceed the radius of the circle circumscribed by the particles. With  $[\text{surf}] > c_{\mu c}$  it was proposed that extra oil could be recovered by both solubilisation and emulsification mechanisms, the modelling of which was implemented using the  $R_{\text{sol}}+R_{\text{em}}$  parameter (the ratio of solubilised and emulsified oil to the concentration of surfactant  $> c_{\mu c}$ ).

The predicted oil recovery for the AOT containing systems matched, with reasonable precision, much of the experimental data. The trend of little change in oil recovery (due to the limit  $r_{\text{chan}} = r_{\text{chan,max}}$ ) with  $[\text{AOT}] < c_{\mu c}$ , followed by a decrease in oil recovery with a decrease in contact angle at  $[\text{AOT}] \approx c_{\mu c}$ , and an increase with  $[\text{AOT}] > c_{\mu c}$  due to solubilisation + emulsification was seen both experimentally and modelled successfully. The post- $c_{\mu c}$  oil recovery was seen to be dependent on the oil-water interfacial tension, and was found to be dominated by emulsification. With a decrease

in the post- $c_{\mu c}$  oil-water interfacial tension there was an increase in the post- $c_{\mu c}$  oil recovery. A plot of  $R_{sol}+R_{em}$  vs. post- $c_{\mu c}$  oil-water interfacial tension for the three salt concentrations investigated was seen to obey a power-law relationship.

The system containing C14BDMAC had a predicted oil recovery of 82 % across the full concentration range investigated. This was due to the contact angle never dropping below 90 °, and that the concentration in the water did not increase to above the  $c_{\mu c}$  due to the temperature being below the Krafft temperature of the system. This trend was observed both experimentally and modelled successfully. Initial experiments were conducted at 30 °C (above the Krafft temperature) so that the surfactant concentration can exceed the  $c_{\mu c}$ . This produced promising results in increasing the oil recovery with  $[surf] > c_{\mu c}$ .

As the system containing CW-100S had very erratic contact angle data the modelling of the oil recovery was not quite as simple. The oil recovery with  $[surf] < c_{\mu c}$  was seen to vary between 70 and 80 %, possibly due to contact angle variation. The value of the  $R_{sol}+R_{em}$  parameter used to model the post- $c_{\mu c}$  rise in oil recovery and the post- $c_{\mu c}$  oil-water interfacial tension obeyed the same power law relationship as the AOT containing system.

Overall, through the use of pure model systems for which many of the surface chemistry properties were known, it was shown how knowledge of the adsorption isotherm enables the estimation of the concentration of non-adsorbed surfactant in the packed column experiments which, in turn, allows detailed analysis of the %oil recovery variation with surfactant concentration in terms of the measured contact angles, the  $c_{\mu c}$  and the post- $c_{\mu c}$  oil-water interfacial tension. For surfactant concentrations  $< c_{\mu c}$ , the %oil recovery is determined by the contact angle. Above the  $c_{\mu c}$ , additional oil is recovered by a solubilisation plus emulsification mechanism.

## 6.2 Future work and preliminary experiments

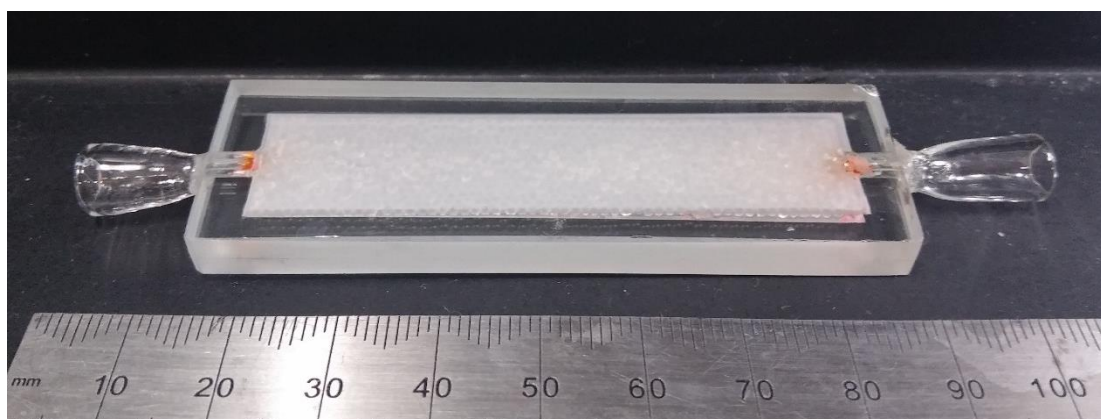
### 6.2.1 Future work

There are two-significant scopes for future work. Firstly, the visualisation of the oil recovery to see if liquid bridges between touching particles can be observed. Secondly, as the oil recovery depends on the balancing of the Laplace pressures across the bridges and across the interface of the bulge being forced through the interstices, if the bulge pressure could be increased this may lead to further oil recovery. One way this could be achieved is through foam flooding as this would lead to an air-water interface at the bulge which typically has a higher tension than an oil-water interface, thus leading to a higher Laplace pressure across the bulge. The following two sections present some preliminary results for these two scopes for future work.

### 6.2.2 Visualisation of the oil recovery using a glass-bead micromodel

With the aim of visualising oil bridges between particles left behind following an aqueous phase flood, three glass columns were produced with varying internal dimensions. Figure 6.1 shows one such column.

**Figure 6.1** Example of glass columns used for oil recovery visualisation (with glass beads inside chamber). The end connectors are hand-made luer fittings.

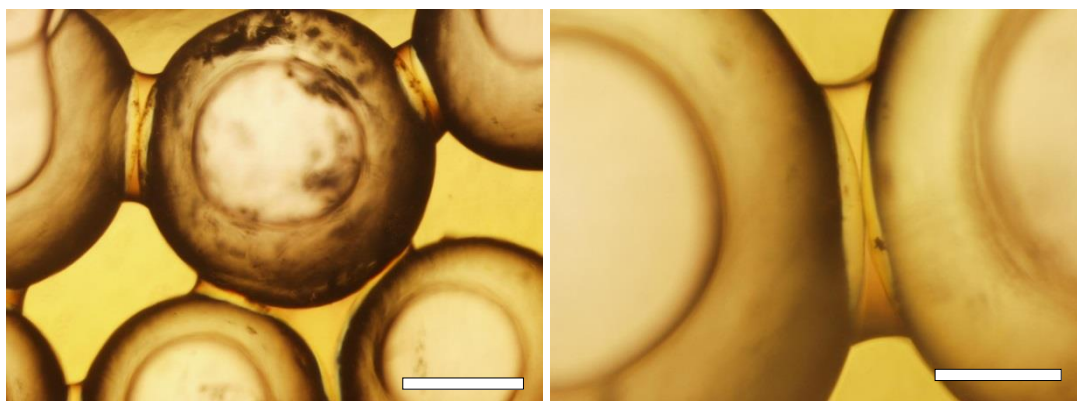


The columns were packed with soda lime glass beads (SiLibeads Type P, Sigmund Lindner) of diameter 1.0-1.3 mm. In order to minimise the scattering of light from the multiple glass-liquid interfaces present it was necessary to adjust the refractive index of each phase to closely match that of the glass (1.5284). The oil used was toluene (RI = 1.496), to which benzyl bromide (RI = 1.575) was added to adjust the RI to 1.519. An

80 wt.% sucrose solution was used as the displacing phase (as sucrose increases the RI of water from 1.330 to 1.444 at this concentration). It was thought that, to enable clear identification between the phases present, each phase may need to be stained with a fluorescent dye which is solely miscible with one phase. The toluene was stained with Sudan Red, and the water with fluorescein. It was later found that the best images were obtained with standard optical microscopy.

Figure 6.2 shows optical micrographs of the liquid bridges left behind following the displacement of a toluene solution containing benzyl bromide (3:1 volume ratio) with an 80 wt.% aqueous solution of sucrose at a flow rate of  $5 \mu\text{l min}^{-1}$ .

**Figure 6.2** Optical micrographs of the oil (toluene) bridges left behind between glass beads within the column shown in Figure 6.1 following flooding with the aqueous phase (as described in the text). The scale bar on the left micrograph represents  $500 \mu\text{m}$  and the scale bar on the right micrograph represents  $200 \mu\text{m}$ .



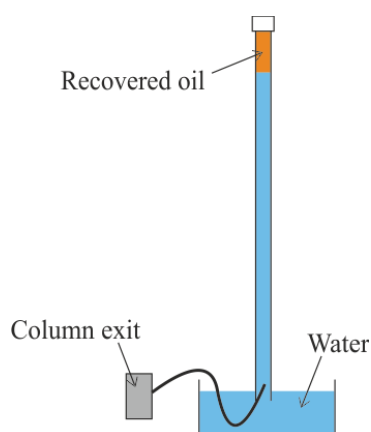
Some bridges appear to only be between two-particles, whereas some appear to form a larger bridge between multiple particles. The contact angle (measured through the water) of the bridges ( $125^\circ$ ) is the same as that determined from the sessile drop of the same aqueous solution under the same toluene solution on soda lime glass ( $121 \pm 10^\circ$ ).

There are multiple possibilities to extend this work further, such as; i) carrying out floods at different known contact angles to see if this effects the shape and size of the bridges left behind, and ii) analysing the micrographs to determine the %oil recovered and seeing if this matches up with the %oil recovered determined from weight measurements. Further, a more in depth analysis of the flow properties of the glass bead packed columns would allow a better comparison between this system and the calcite packed column experiments.

### 6.2.3 Foam flooding

The addition of a third flowing phase (air) in to the calcite packed column means that the oil recovery can no longer be determined through mass measurements. Thus, before determining if foam flooding has the ability to increase oil recovery by increasing the bulge pressure, a new technique was required to measure the oil recovery performance of a displacement flood. The technique developed consisted of a long glass tube (with graduations) initially filled with water, sealed at the top and the bottom placed in a water bath. The tube from the column exit is placed in to the bottom of the glass tube. As oil is recovered, it rises to the top of the glass tube, and displaces the water. The oil recovered can then be determined according to the graduations on the glass tube. This set-up is shown in Figure 6.3.

**Figure 6.3** Oil recovery detector for use with foam flooding experiments. Only water and oil phases are shown.



Some column floods were carried out using only aqueous surfactant solutions (no foaming), and the %oil recovered from both weighing the column and the technique in Figure 6.3 agreed within the 2 % experimental error.

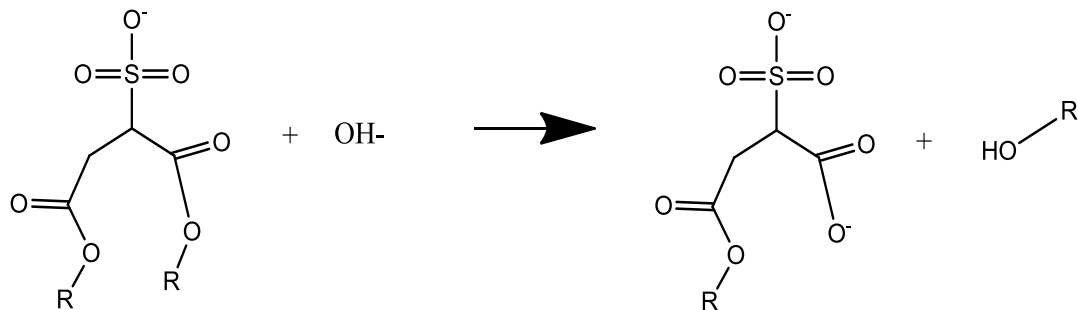
Multiple foam flood techniques were tested, including; i) consecutive injection of the aqueous phase followed by air, ii) simultaneous injection of aqueous phase and air (with the use of a T-junction piece) and iii) injection of pre-made foam. These experiments were carried out using the AOT-water-decane system containing 75 mM NaCl and 10 mM Na<sub>2</sub>CO<sub>3</sub> with [AOT]<sub>free</sub> > c<sub>µc</sub>. No significant repeatable increase in oil recovery was observed. One reason for this could be due to the large destabilisation effect the decane has on the foams. To further test this idea of foam flooding, a system that forms a foam which is stable in the presence of the oil should be investigated.

## APPENDIX A - DEGRADATION OF AOT IN AQUEOUS SOLUTIONS

### A1 Degradation of AOT

There have been a few studies on the degradation of AOT, most of which have been focussed on the degradation in microemulsion systems<sup>1-2</sup>. Little work has been carried out to determine the degradation kinetics of a system consisting only of water-AOT-salt in the presence of OH<sup>-</sup> ions. The proposed system for the degradation of AOT is shown in Figure A1 below. It is thought that in a system with the AOT concentration in excess of the cac, that only the monomers will degrade. This is due to the probability that the OH<sup>-</sup> ions will be repelled by the negative charge of the oxygen in the head group of the AOT. As aggregates of AOT in water consist of the head groups on the outside, the point at which the degradation is proposed to take place (where the alkyl chain is linked to the oxygen of the sulphonate group) is in effect protected by the negatively charged 'shell' of the head groups repelling the OH<sup>-</sup> ions.

**Figure A1** Possible method of the degradation of aqueous AOT under high pH conditions.



where the R group is C<sub>8</sub>H<sub>17</sub>. It is also possible that the second ester link will hydrolyse as well, though for now it will be assumed that only one is hydrolysed. From this mechanism, the rate law of the reaction can be assumed to be as follows:

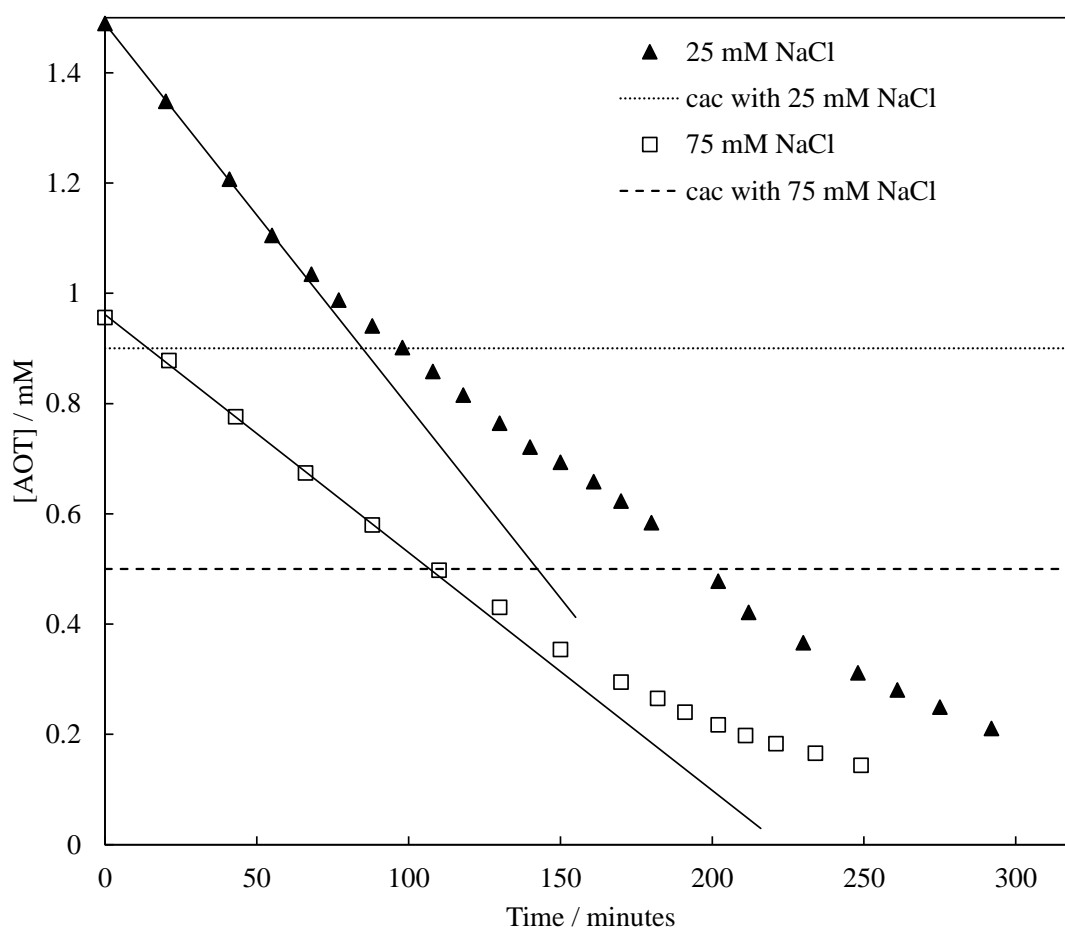
$$\text{rate} = k''[\text{AOT}_{\text{mon}}][\text{OH}^-] \quad (\text{A1})$$

where [AOT<sub>mon</sub>] is the concentration of AOT present as monomers and k'' is the second order rate constant, with units M<sup>-1</sup> s<sup>-1</sup>.

If this is the case, then when a system is buffered and hence the [OH<sup>-</sup>] constant, the rate should only depend on [AOT<sub>mon</sub>] (if [OH<sup>-</sup>] is in excess of the concentration of

[AOT<sub>mon</sub>]). Therefore, when the total concentration of AOT is above the cac, hence [AOT<sub>mon</sub>] is also constant, a pseudo zero order reaction should be observed, thus a plot of concentration vs. time will give a straight line. When the AOT concentration drops below the cac, [AOT<sub>mon</sub>] is no longer constant and a pseudo first order reaction should be observed, and hence the concentration vs. time plot changes to an exponential trend. Due to this phenomenon, salt will appear to have an unusual effect on the kinetics of the reaction due to the effect it has on altering the cac of the surfactant. This effect can be seen in Figure A2 below. The OH<sup>-</sup> ion concentrations for all experiments were calculated using the value of the pK<sub>w</sub> of water at the different temperatures.

**Figure A2** The effect of salt concentration on the degradation of AOT in aqueous solutions containing 10 mM Na<sub>2</sub>CO<sub>3</sub> plus the NaCl concentration shown at 25 °C. The cac of the surfactant in the system containing 25 mM NaCl was approximated to be ~0.9 mM (by extrapolation from ref 3 and comparison with the other systems from this work), and in the system containing 75 mM NaCl it was determined to be 0.50 mM. The average OH<sup>-</sup> concentration for both systems is ~ 5.4 mM for both systems.



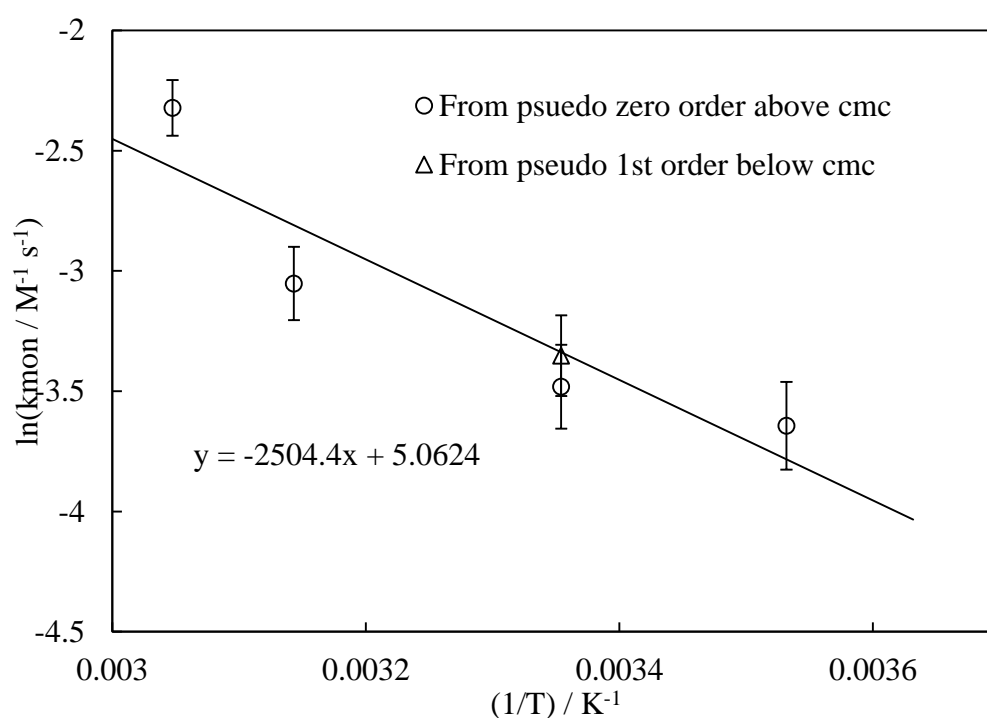
The change in the trend of the graph from straight to exponential when the [AOT] drops below the cac appears to confirm the rate law proposed (equation A1). This being the case, experiments were carried out with the concentration of AOT above the cac at four different temperatures, thus allowing the pseudo zero order rate constants to be determined. From these zero order rate constants, the actual second order rate constant can be determined and plotted on an Arrhenius plot (Figure A3). For comparison purposes, a second order rate constant calculated from a pseudo first order rate constant (from an experiment carried out with [AOT]<sub>total</sub> below the cac) is also plotted. The pseudo first and pseudo zero order rate equations are shown in equations A2 and A3 respectively.

$$\text{rate}' = k'[\text{AOT}_{\text{mon}}] \quad (\text{A2})$$

$$\text{rate} = k \quad (\text{A3})$$

where  $k'$  is the pseudo first order rate constant and is equal to  $k[\text{OH}^-]$  and has units of  $\text{s}^{-1}$  and  $k$  is the pseudo zero order rate constant and is equal to  $k[\text{OH}^-][\text{AOT}]$  and has units of  $\text{M}$ .

**Figure A3** Arrhenius plot for the determination of the activation energy of the degradation of AOT by reaction with hydroxide ions.



Using the linear Arrhenius equation (equation A4) the activation energy was calculated to be  $21 \pm 6 \text{ kJ mol}^{-1}$ .

$$\ln k = \frac{-E_a}{R} \frac{1}{T} + \ln A \quad (\text{A4})$$

where  $E_a$  is the activation energy,  $R$  the universal gas constant,  $T$  the absolute temperature and  $A$  the Arrhenius factor.

Kurz<sup>4</sup> investigated the effects of micellisation on the kinetics for the hydrolysis of monoalkyl sulphates in alkali conditions (whereas AOT is a sulphonate), and reports a similar retardation of the rates when the concentration is above the cac. They also reported an acceleration of the rate with the formation of aggregates when it came to the hydrogen ion catalysed hydrolysis (acidic conditions). This was presumably due to the negative head of the surfactants attracting the  $\text{H}^+$  ions closer to the site of the degradation reaction.

## A2 References

1. Garcia-Rio, L., Hervés, P., Leis, J.R., Mejuto, J.C. and Pérez-Juste, K., Determination of the hydrolysis rate of AOT in AOT-isoctane-water microemulsions using sodium nitroprusside as chemical probe, *J. Phys. Org. Chem.*, **2002**, *15*, 576.
2. Mao, S., Chen, Z., Fan, D., An, X. and Shen, W., Spectrometric study of AOT-hydrolysis reaction in water/AOT/isoctane microemulsions using phenolphthalein as a chemical probe, *J. Phys. Chem. A*, **2012**, *116*, 158.
3. Binks, B.P., Ph.D. Thesis, University of Hull, 1985.
4. Kurz, J.L., Effects of micellization on the kinetics of the hydrolysis of monoalkyl sulfates, *J. Phys. Chem.*, **1962**, *66*, 2239.

## APPENDIX B

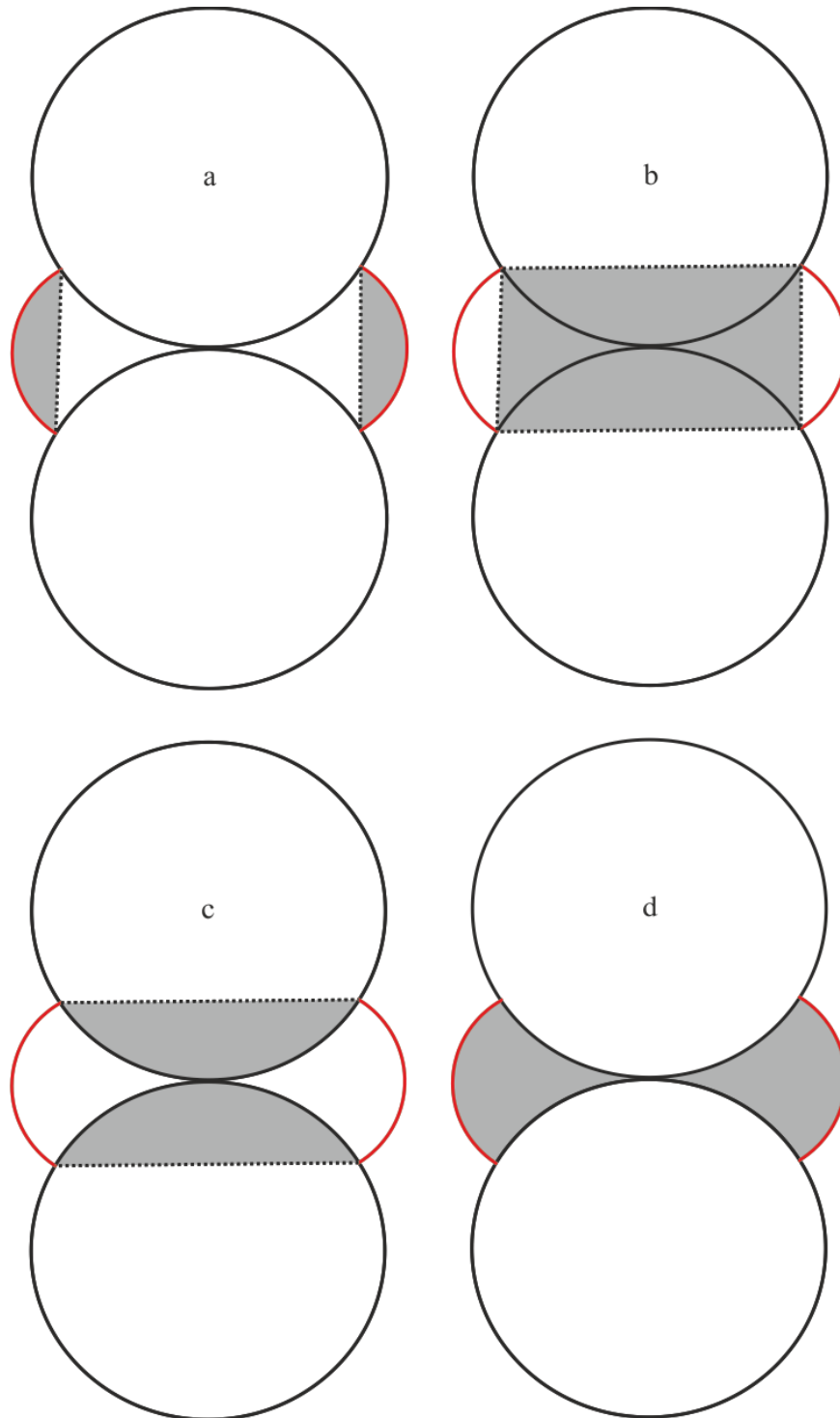
### EQUATIONS FOR THE LIQUID BRIDGE MODEL

#### B1 Introduction

There are three main parts involved in the derivation of the model. Firstly, to be able to calculate the volumes and curvature at the oil water interface of the liquid bridges in a set geometry (set contact angle and bridge height), secondly to calculate the value of  $r_{chan}$  and thirdly to calculate the interfacial areas between the three phases (to enable an estimation of  $f$ , the fraction of particle surface area in contact with water).

In order to be able to calculate the various volumes, curvatures and areas, the bridge region is split in to three different sections (Figure B1). These regions are the bridge arc, shown as the shaded region in (a), the bridge cylinder, shown as the shaded region in (b), and the spherical caps of the particles, shown as the shaded region in (c). The calculations throughout this appendix will relate back to one of the three regions.

**Figure B1** 2D diagrammatic view of the sections within the oil bridge regions for which the volumes are calculated. The black circles represent the spherical particles, the red curves the boundary of the liquid bridges. The grey areas indicate the liquid bridge arc area (a), the bridge cylinder area (b), the particle cap area (c) and the total bridge area (d). The area in d is given by the area in a plus the area in b minus the area in c.



## B2 Pappus Centroid Theorems

Some of the calculations used to determine the areas and corresponding volumes shown in Figure B1, require the use of both the first and second Centroid theorems of Pappus. The centroid of a shape is the average of all the points in the shape, and for an object of uniform mass it is the centre of gravity of the object. Both of Pappus' theorems will be stated here and the subsequent use of them explained in more detail as their use arises.

The first theorem states that the surface area,  $A$ , of a *surface* of revolution generated by the revolution of a curve about an external axis is equal to the arc length,  $L$ , multiplied by the distance,  $d_1$ , travelled by the curves centroid,  $G_1$  (equation B1, Figure B2).

$$A = Ld_1 = 2\pi LG_1 \quad (\text{B1})$$

The second theorem states that the volume,  $V$ , of a *solid* of revolution generated by the revolution of a lamina about an external axis is equal to the area of the lamina,  $A_L$ , multiplied by the distance,  $d_2$ , travelled by the lamina's centroid,  $G_2$  (equation B2, Figure B2).

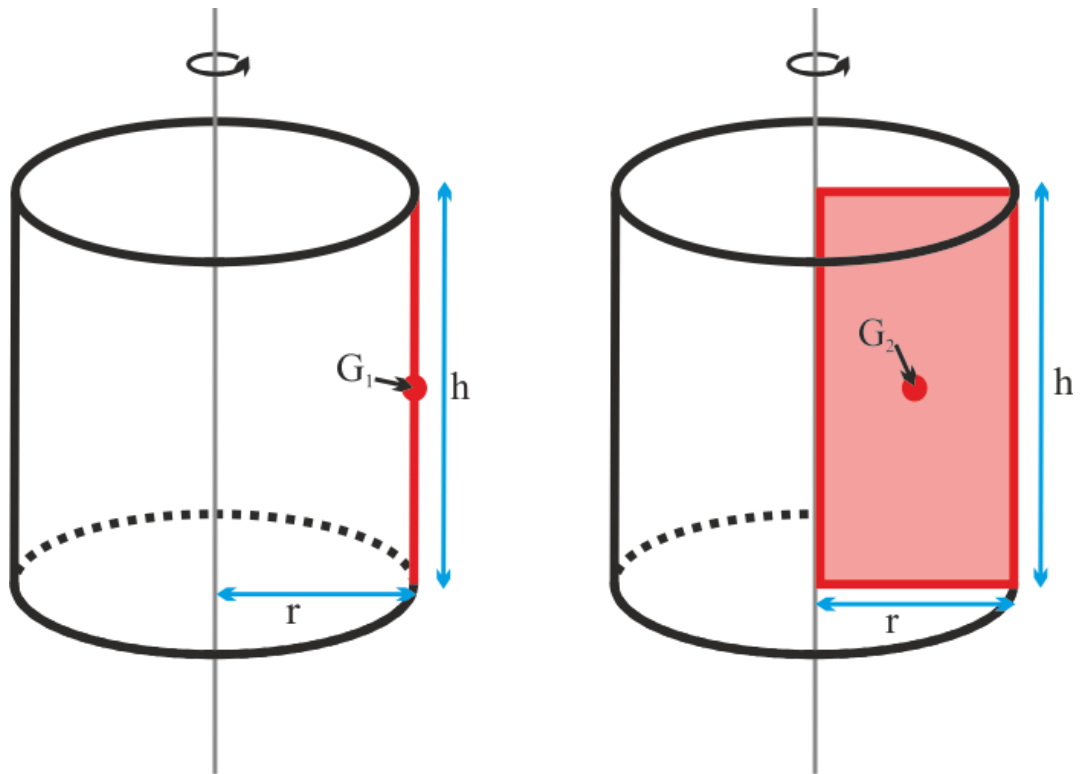
$$V = A_L d_2 = 2\pi A_L G_2 \quad (\text{B2})$$

The parameters  $L$ ,  $G_1$ ,  $A_L$  and  $G_2$  change depending on the nature of the curve (curved, straight, hinged at the axis of rotation etc.), or the shape of the lamina (triangle, rectangle, semicircle etc.), and can often be looked up in tables of pre-calculated values, such as the ones in ref 1. Figure B2 shows an example for the case of a straight line curve parallel to the axis of rotation (left) and of a rectangle parallel to the axis of rotation (right). The subsequent equations for the area of the cylinder formed from the rotation of the straight line around the axis,  $A_{\text{cyl}}$  (from equation B1), and the volume of the cylinder formed from the rotation of the rectangle around the axis,  $V_{\text{cyl}}$  (from equation B2), are equations B3 and B4 respectively.

$$A_{\text{cyl}} = 2\pi hr \quad (\text{B3})$$

$$V_{\text{cyl}} = \pi r^2 h \quad (\text{B4})$$

**Figure B2** Definition of the parameters used in equations B3 and B4 for the area of a surface of revolution generated by the revolution of a straight line curve parallel to the axis of rotation (left, red line = curve) and the volume of the solid of revolution generated by the revolution of a lamina around an external axis (right, red rectangle = lamina).



### B3 Calculating the volumes of the liquid bridges and the Laplace pressure across the oil-water interface of the bridge

All of the parameters used in the equations throughout this section are defined in Figure B3. To make Figure B3 clearer, some parameters are defined as their symbol divided by 2. When seen in equations, the symbols are either used as the symbol alone (e.g.  $z_b$ ), indicating that it is the length or angle shown in Figure B3 multiplied by 2 (e.g.  $2(z_b/2)$ ), or as defined in Figure B3 (e.g.  $z_b/2$ ).

The first volume to be calculated is that of the bridge arc shown as the shaded region in (a) in Figure B1. By approximating the lamina to be rotated around the axis as a segment of a circle, as in Figure B3 (the full circle can be seen in red), where the solid red line is the outline of the segment of the circle being considered for the calculations, the volume of the arc obtained from rotating the circular segment around the axis (down the middle of the particles) can be determined using Pappus second theorem (equation B2). The area of the lamina, the circular segment, is calculated using equation B5, and the centroid of the circular segment using equation B6.

$$A_{b-circseg} = r_b^2 (z_b - \sin(z_b)) / 2 \quad (B5)$$

$$G_{b-circseg} = \left( 4r_b \sin\left(\frac{z_b}{2}\right) \right)^3 / (3(z_b - \sin(z_b))) \quad (B6)$$

Equation B2 can then be used to calculate the volume of the bridge arc,  $V_{b-arc}$ , by substituting  $A_{b-circseg}$  and  $G_{b-circseg}$  in place of  $A_L$  and in place of  $G_2$  (equation B7).

$$V_{b-arc} = 2\pi A_{b-circseg} G_{b-circseg} \quad (B7)$$

The volume of the cylinder shown as the shaded region in (b) in Figure B1) obtained by rotating the rectangular lamina with height  $2h_p$  and length  $A_p/2$  around the axis,  $V_{b-cyl}$ , is determined by equation B8.

$$V_{b-cyl} = \pi \left( \frac{a_p}{2} \right)^2 (2h_p) \quad (B8)$$

Finally, the volume of the ‘caps’ of the particles shown as the shaded region in (c) in Figure B1, can be calculated (by treating them as a spherical cap), using equation B9.

$$V_{p\text{-cap}} = \frac{\pi h_p}{6} \left( 3 \left( \frac{a_p}{2} \right)^2 + h_p^2 \right) \quad (\text{B9})$$

Since the volumes of all three sub sections in Figure B1 are known, the volume of the actual liquid bridge,  $V_{b\text{-total}}$  is calculated using equation B10.

$$V_{b\text{-total}} = V_{b\text{-cyl}} + V_{b\text{-arc}} - 2V_{p\text{-cap}} \quad (\text{B10})$$

where  $V_{p\text{-cap}}$  is multiplied by 2 as there are two particle caps per bridge.

$V_{b\text{-total}}$  is the volume of each individual bridge, so in order to obtain the %oil recovery the volume of all the bridges together needs to be determined. To start, the number of particles per volume for a cubic packed arrangement can be determined by B11.

$$n_p = \left( \frac{1}{2r_p} \right)^3 \quad (\text{B11})$$

Since there are 6 half bridges per particle, the number of bridges per volume can be determined by equation B12.

$$n_b = 3n_p \quad (\text{B12})$$

The total volume fraction of the bridges,  $\phi_{\text{bridges}}$  is then calculated by multiplying the number of bridges per volume,  $n_b$ , by the total volume of each bridge (equation B13).

$$\phi_{\text{bridges}} = n_b V_{b\text{-total}} \quad (\text{B13})$$

Finally, the % oil recovery can be calculated using equation B14 (where  $\phi_{\text{pore}}$  is equivalent to  $\phi_{\text{oil}}$  as all the pores are initially filled with oil).

$$\% \text{oil recovery} = \left( 1 - \frac{\phi_{\text{bridges}}}{\phi_{\text{pore}}} \right) 100 \quad (\text{B14})$$

Thus, using the various equations above, for a set contact angle and value of  $h_p$  (set manually), the volume of the oil left behind as liquid bridges can be calculated, and hence the %oil recovery for set-geometries of the bridges.

The determination of the other parameters, such as the length  $a_p$  and the angle  $z_p$ , can be done using relatively simple geometry. The calculations for these are not discussed

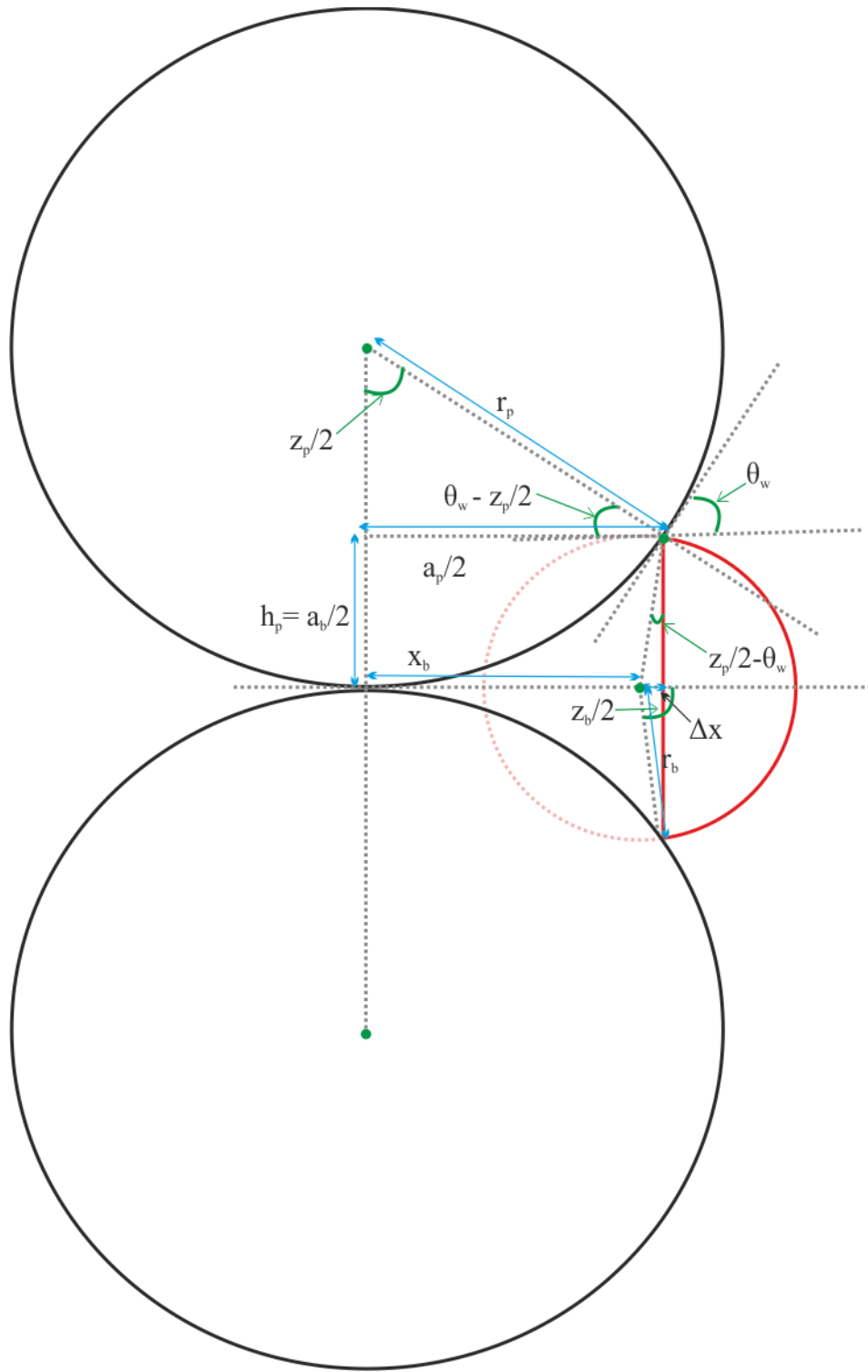
to avoid over complicating this section, however, the EXCEL spreadsheet (“Liquid bridge calculations spreadsheet.xlsx) which calculates all the parameters automatically can be found in the ESI on the CD attached to this thesis..

The Laplace pressure across the oil-water interface of the bridge can be calculated using equation B15 for the Laplace pressure using the principal radii of curvature of the bridge.

$$\Delta P_{\text{bridge}} = \gamma_{\text{ow}} \left( \frac{1}{r_b} + \frac{1}{r_{\text{average}}} \right) \quad (\text{B15})$$

where  $r_{\text{average}}$  is the average distance from the centre-centre axis of the contacting spheres and the outside edge of the bridge.

**Figure B3** Definition of terms used in the calculations for the volumes and areas of the liquid bridges trapped between the cubic packed spherical particles. Some parameters are shown as their value divided by 2 (which simplifies the diagram by removal of unnecessary lines).



#### B4 Calculating $r_{\text{chan}}$ and the Laplace pressure across the interface of the bulge of liquid being pumped through the pore

As discussed in section 4.5.3.1 of Chapter 4,  $r_{\text{chan}}$  is the average effective pore radius through which the aqueous phase flows, leaving the oil behind as bridges.  $r_{\text{chan}}$  is the radius of the circle with area the same as that between the particles (not including the bridges). In Figure B4, this corresponds to the area within the grey lines minus the area contained within two half-bridges (red lines), with both lines bounded by the particle surface. In equation B16 the total area within the grey lines is given by the parts within the brackets before the minus sign. The multiple of 4 outside the brackets is required, as for each interstice, there are four lots of the areas denoted by the grey lines.

$$A_{\text{interstices}} = \left( \left( 1 - \frac{\pi}{4} \right) r_p^2 - 2A_{\text{halfbridge}} \right) 4 \quad (\text{B16})$$

where  $A_{\text{halfbridge}}$  is the area of the half bridges within the grey area.  $A_{\text{halfbridge}}$  is given by adding the answer to equation B5 (area of the circular segment,  $A_{\text{b-circseg}}$ ) to the answer of equation B17 (area of the bridge cylinder minus the area of the particle cap,  $A_{\text{b-cyl-liquid}}$ ) and dividing by two (equation B18).

$$A_{\text{b-cyl-liquid}} = (a_p a_b) - r_p^2 (z_p - \sin z_p) / 4 \quad (\text{B17})$$

$$A_{\text{halfbridge}} = \frac{(A_{\text{b-circarc}} + A_{\text{b-cyl}})}{2} \quad (\text{B18})$$

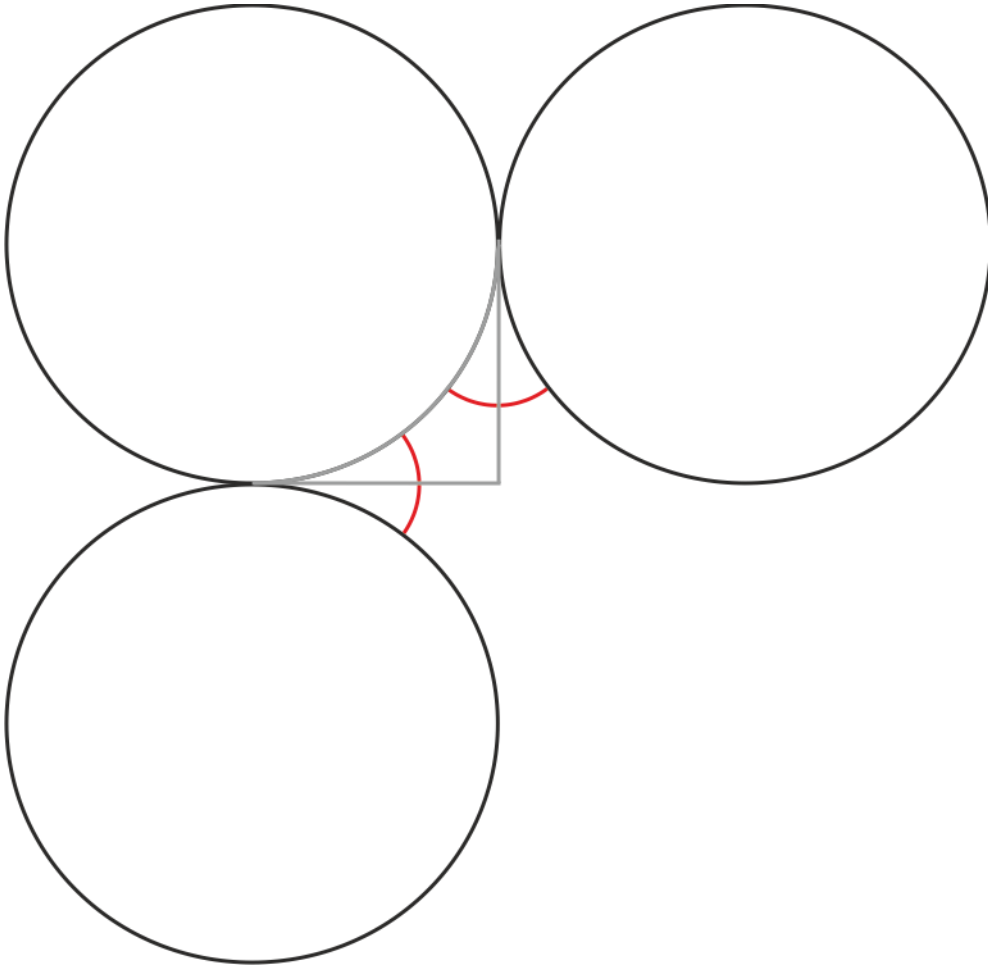
The average effective pore (or channel) radius through which the aqueous phase bulges and flows through is calculated using equation B19.

$$r_{\text{chan}} = \sqrt{\frac{A_{\text{interstices}}}{\pi}} \quad (\text{B19})$$

The Laplace pressure of the bulge is then given by equation B20.

$$\Delta P_{\text{chan}} = \frac{2\gamma_{\text{ow}}}{r_{\text{chan}}} \quad (\text{B20})$$

**Figure B4** Diagram indicating the areas calculated for the determination of  $r_{\text{chan}}$ .



Both  $\Delta P_{\text{bridge}}$  and  $\Delta P_{\text{chan}}$  can be calculated (equations B15 and B20) for a set height,  $h_p$ , and set contact angle,  $\theta_w$ . Hence, by setting a value for the contact angle, the  $h_p$  parameter can be varied until  $\Delta P_{\text{bridge}} = \Delta P_{\text{chan}}$ . The volume, and therefore % oil recovery, from this combination of  $h_p$  and  $\theta_w$  can then be calculated. The final parameter to calculate is the value of  $r_{\text{chan,max}}$ , which is determined using equation B21.

$$r_{\text{chan,max}} = (\sqrt{2} - 1)r_p \quad (\text{B21})$$

## B5 Calculating the interfacial areas between the three phases for an estimation of the parameter $f$

The oil-water interfacial area is calculated using the form of equation B1 for the area of a surface of revolution to give the area of the bridge arc (equation B22). The area of the bridge cylinder,  $A_{b-cyl}$ , is not needed as this is an internal part of the bridge and as such, does not form part of the oil-water interface.

$$A_{ow-bridge} = 2\pi G_{b-circseg} L_{b-circseg} \quad (B22)$$

where  $L_{b-circseg}$  is calculated using equation B23.

$$L_{b-circseg} = r_b Z_b \quad (B23)$$

The oil-water interfacial area per volume ( $A_{ow-vol}$ ) is then determined by multiplying the value from equation B22 by the number of bridges per volume,  $n_b$  (equation B24).

$$A_{ow-vol} = A_{ow-bridge} n_b \quad (B24)$$

The oil-particle interfacial area is equal to the area of the cap of the particle in the bridge region (Figure B4) and is calculated using equation B25.

$$A_{p-cap} = A_{p-o} = 2\pi r_p h_p \quad (B25)$$

The particle-oil interfacial area per volume ( $A_{p-o-vol}$ ) is then determined by multiplying the value from equation B25 by the number of particles per volume,  $n_p$  multiplied by 6 (as there are 6 particle caps per particle) (equation B26).

$$A_{po-vol} = A_{p-cap} n_p 6 \quad (B26)$$

Thus, the water-particle interfacial area per volume ( $A_{pw-vol}$ ) can be calculated by taking the calcite-oil interfacial area per volume from the total particle surface area per volume (equation B27)

$$A_{pw-vol} = A_{p-vol} - A_{po-vol} = (\pi / 2 / r_p) - A_{po-vol} \quad (B27)$$

The fraction of the particle surface area in contact with the aqueous phase,  $f$ , is then easily determined for each liquid bridge geometry.

## **B6**   **References**

1.   Weisstein, E.W., CRC Concise Encyclopaedia of Mathematics, **2002**, Second Edition, RC Press, p 2131

**APPENDIX C - CONTACT ANGLE MODELLING AND [SURF]<sub>FREE</sub> MODEL  
FITTING PARAMETERS AND GRAPHS FOR ALL SYSTEMS  
INVESTIGATED**

**C1 Model fitting parameters and graphs for systems containing water-decane-calcite-AOT**

**Table C1** Model fitting parameters for the system consisting of water-decane-calcite-AOT at the three different salt concentrations. All systems also contain 10 mM Na<sub>2</sub>CO<sub>3</sub>.

[NaCl] / mM	0	40	75
$c\mu c_w (cac_w) / \text{mM}$	1	0.6	0.5
$c\mu c_d (cac_d) / \text{mM}$	0	0	0
<b>Monomer partition coefficient (<math>K_{P-dw}</math>)</b>	0	0	0
<b>Langmuir <math>K_{L-wd}</math> (equation 4.8) / mM<sup>-1</sup></b>	5000	10000	10000
<b>Langmuir <math>\Gamma_{\max wd}</math> (equation 4.8) / molecules nm<sup>-2</sup></b>	1.276	1.259	1.212
<b>Langmuir <math>K_{L-wc}</math> (equation 4.8) / mM<sup>-1</sup></b>	0.64	1.13	1.36
<b>Langmuir <math>\Gamma_{\max wc}</math> (equation 4.8) / molecules nm<sup>-2</sup></b>	2.4	2.4	2.4
<b>Langmuir type <math>K_{L-wc}</math> (equation 4.1) / mM<sup>-1</sup></b>	0.15	0.30	0.35
<b>Langmuir type <math>\Gamma_{\max wc}</math> (equation 4.1) / molecules nm<sup>-2</sup></b>	2.3	2.0	2.2
<b>Langmuir type <math>\beta</math> (equation 4.1)</b>	-3.5	-3.5	-3.5
$\gamma_{0-wd} / \text{mN m}^{-1}$	45.1	45.1	42.5
$\gamma_{0-cd} / \text{mN m}^{-1}$	10.2	10.2	10.2
$\gamma_{0-wc} / \text{mN m}^{-1}$	15.3	15.3	15.3

**Figure C1** Upper plot: Variation of decane-water-calcite advanced static contact angle (measured through the aqueous phase) tension with aqueous AOT concentration for solutions containing  $0 \text{ mM NaCl}$  and  $10 \text{ mM Na}_2\text{CO}_3$  at  $25 \text{ }^\circ\text{C}$ . The vertical dashed line indicates the  $c_{\text{uc}}$ . The horizontal dashed lined shows the contact angle in the absence of added AOT. The solid line shows the calculated contact angle from the water-decane (measured), water-calcite (derived from the measured adsorption isotherm) and decane-calcite (invariant with  $[\text{AOT}]$ ) tensions shown in the lower plot.

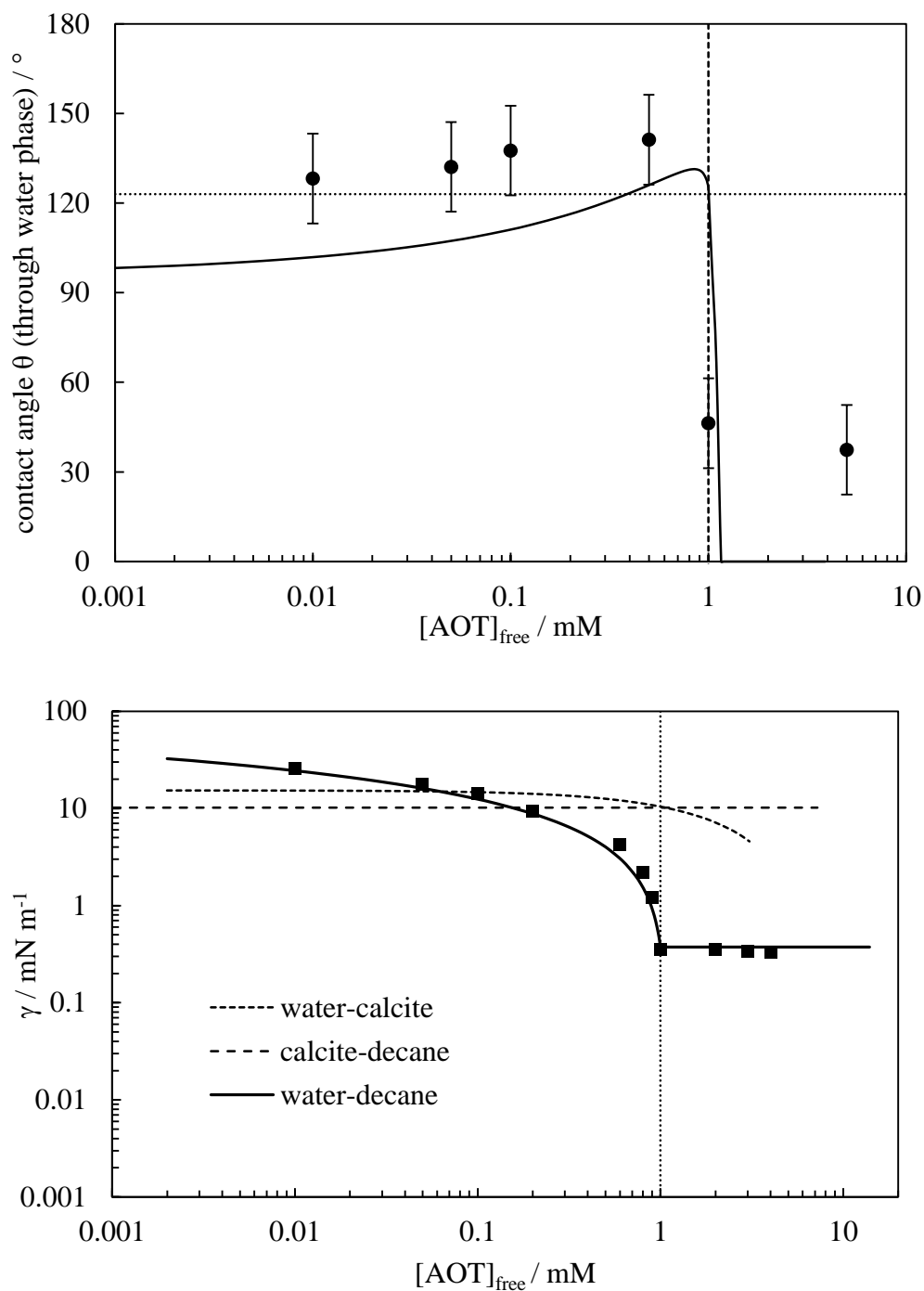


**Figure C2** Variation of the AOT amount of surfactant at the three interfaces. The solid lines show the calculated values for the adsorption at the water-decane (derived from interfacial tension measurements) and water-calcite (measured). The solid line for the adsorption at the decane-calcite interface (invariant with [AOT]) is not seen as the  $\Gamma$  values are all zero. The solid squares show the experimental data for the adsorption at the calcite-water for solutions containing  $0\text{ mM NaCl}$  and  $10\text{ mM Na}_2\text{CO}_3$  interface at  $\text{pH } 9.3 \pm 0.3$  and  $25\text{ }^\circ\text{C}$ .

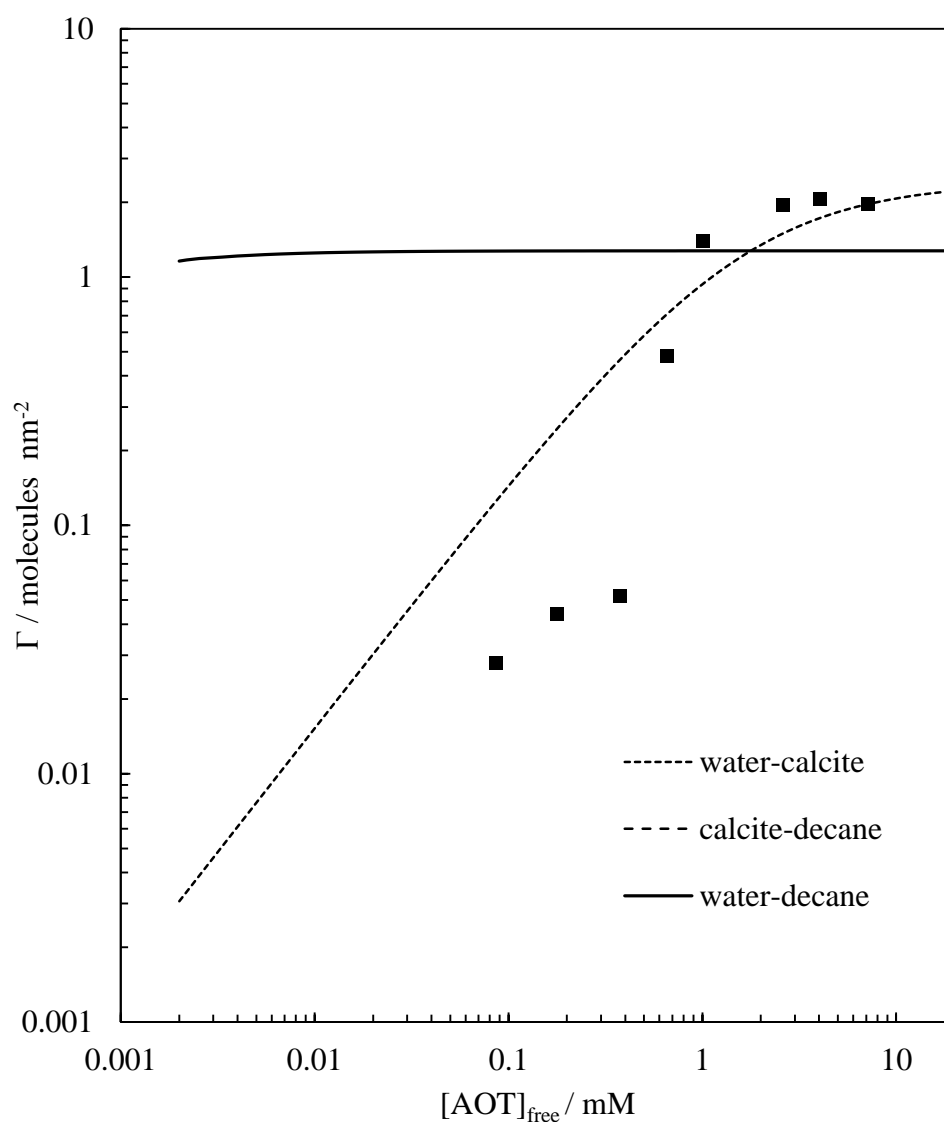


**Figure C3** Upper plot: Variation of decane-water-calcite advanced static contact angle (measured through the aqueous phase) tension with aqueous AOT concentration for solutions containing 40 mM NaCl and 10 mM Na<sub>2</sub>CO<sub>3</sub> at 25 °C. The vertical dashed line indicates the c<sub>μc</sub>. The horizontal dashed lined shows the contact angle in the absence of added AOT. The solid line shows the calculated contact angle from the water-decane (measured), water-calcite (derived from the measured adsorption isotherm) and decane-calcite (invariant with [AOT]) tensions shown in the lower plot.

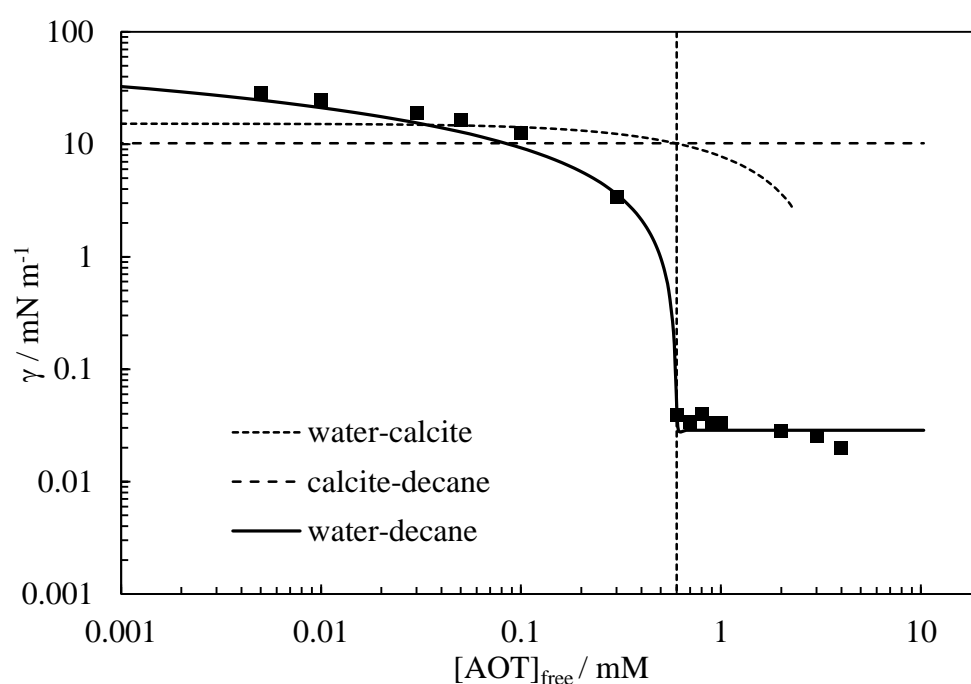
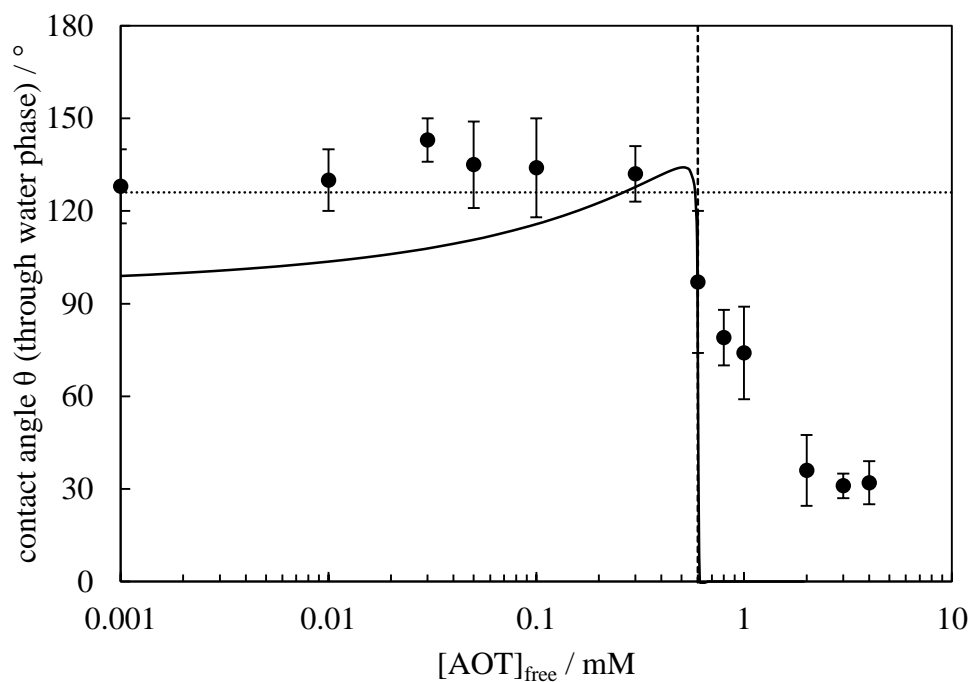


**Figure C4** Variation of the adsorbed amount of AOT at the three interfaces. The solid lines show the calculated values for the adsorption at the water-decane (derived from interfacial tension measurements) and water-calcite (measured). The solid line for the adsorption at the decane-calcite interface (invariant with [AOT]) is not seen as the  $\Gamma$  values are all zero. The solid squares show the experimental data for the adsorption at the calcite-water for solutions containing  $40 \text{ mM NaCl}$  and  $10 \text{ mM Na}_2\text{CO}_3$  interface at  $\text{pH } 9.3 \pm 0.3$  and  $25 \text{ }^\circ\text{C}$ .

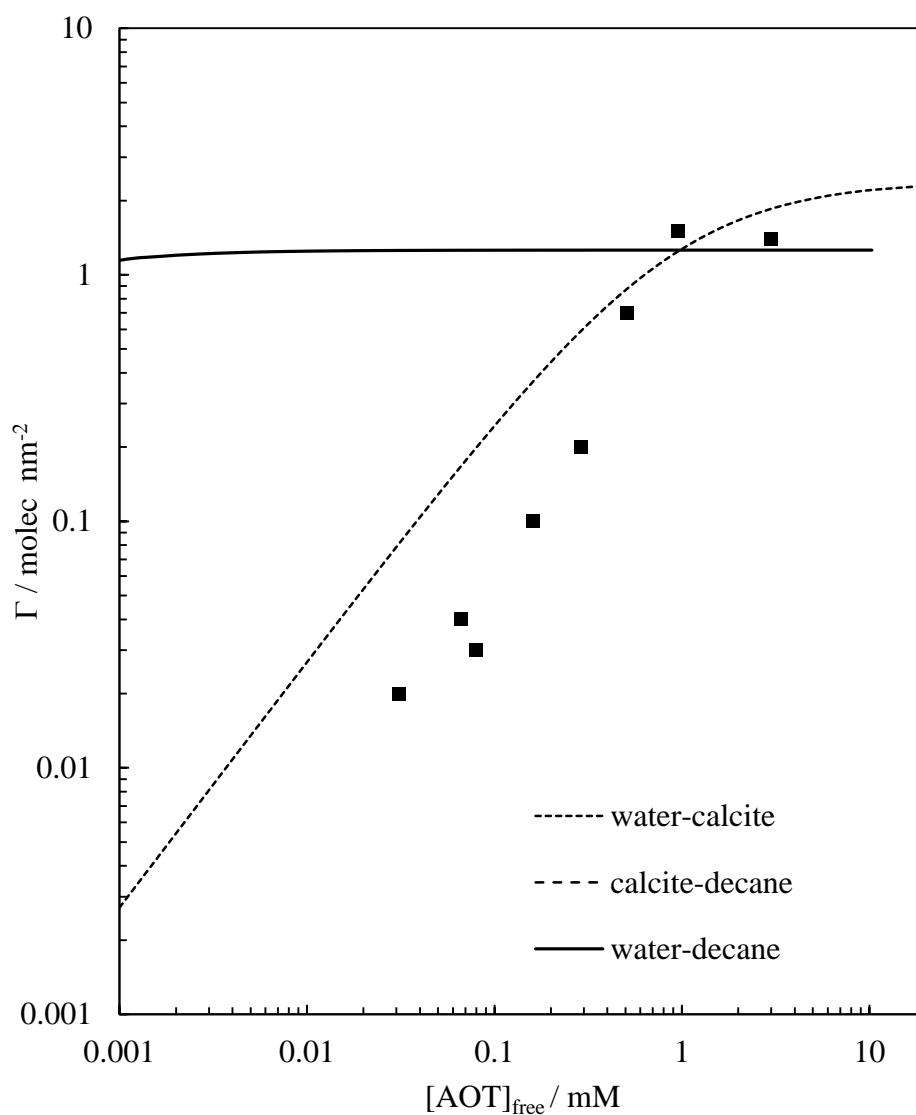


**Figure C5** Upper plot: Variation of decane-water-calcite advanced static contact angle (measured through the aqueous phase) tension with aqueous AOT concentration for solutions containing  $75 \text{ mM NaCl}$  and  $10 \text{ mM Na}_2\text{CO}_3$  at  $25^\circ\text{C}$ . The vertical dashed line indicates the  $c_{\text{uc}}$ . The horizontal dashed lined shows the contact angle in the absence of added AOT. The solid line shows the calculated contact angle from the water-decane (measured), water-calcite (derived from the measured adsorption isotherm) and decane-calcite (invariant with  $[\text{AOT}]$ ) tensions shown in the lower plot.

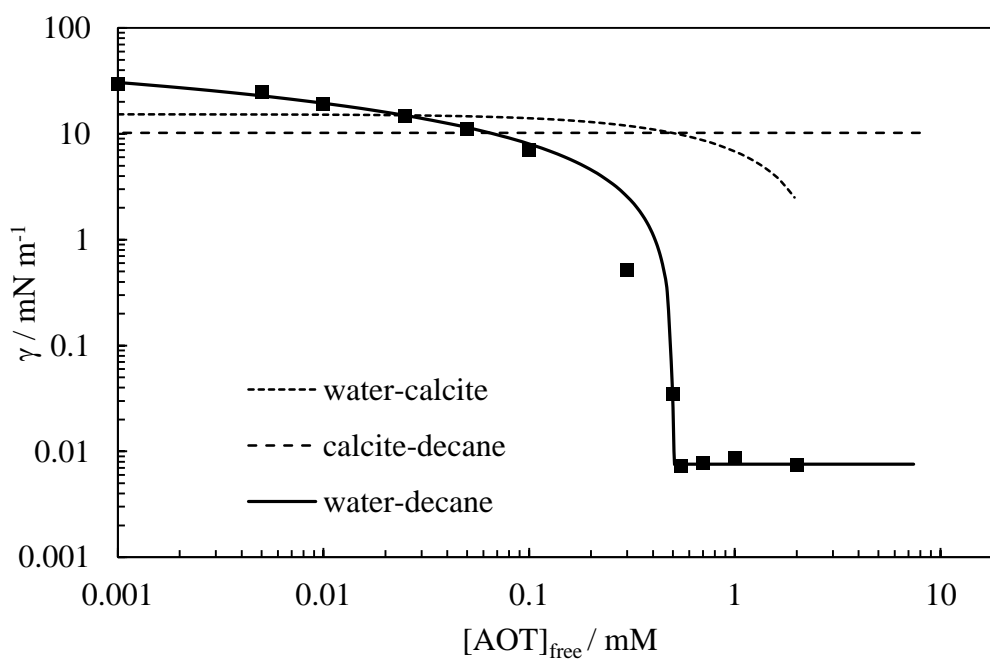
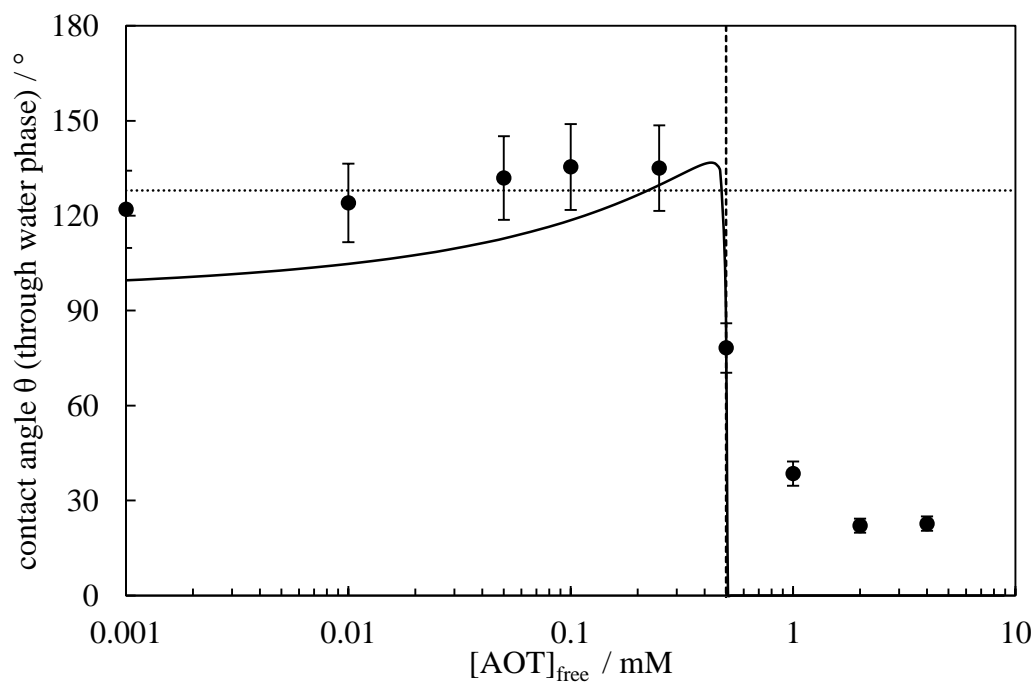
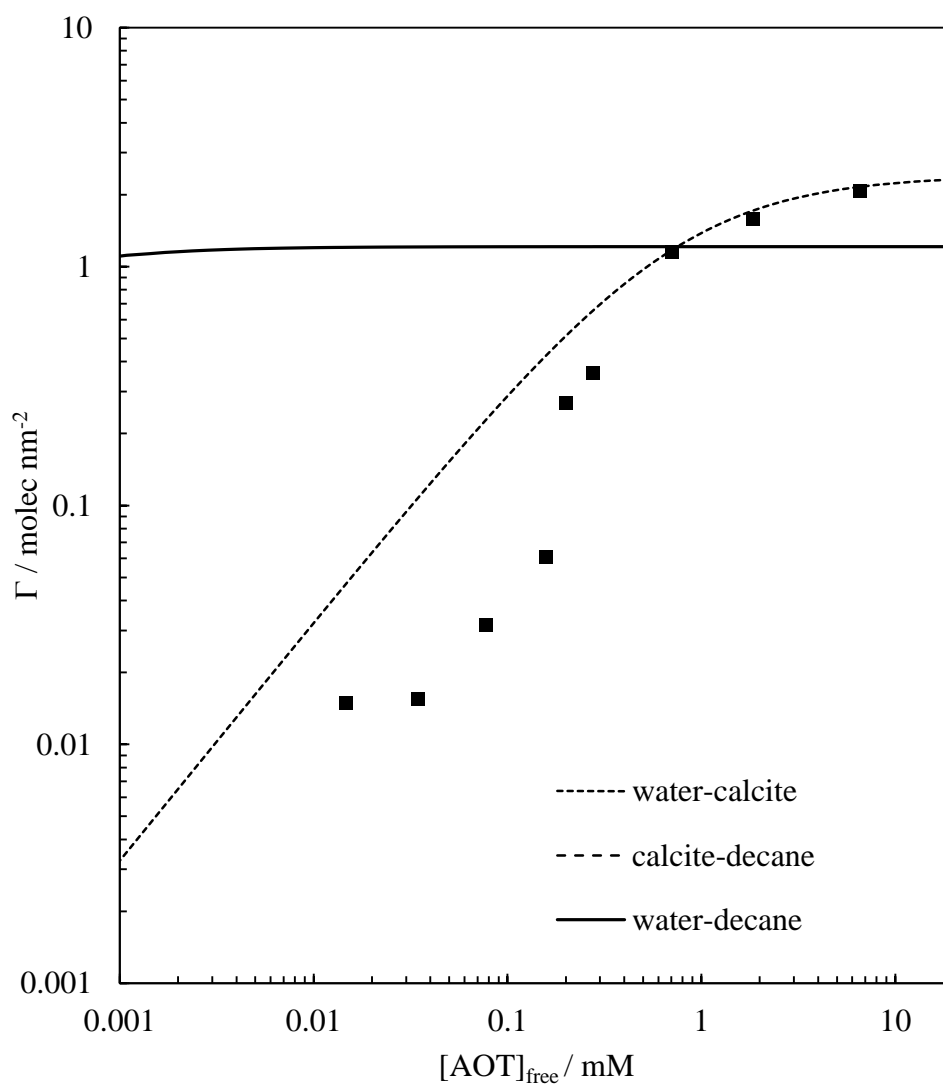


**Figure C6** Variation of the adsorbed amount of AOT at the three interfaces. The solid lines show the calculated values for the adsorption at the water-decane (derived from interfacial tension measurements) and water-calcite (measured). The solid line for the adsorption at the decane-calcite interface (invariant with [AOT]) is not seen as the  $\Gamma$  values are all zero. The solid squares show the experimental data for the adsorption at the calcite-water for solutions containing 75 mM NaCl and 10 mM Na<sub>2</sub>CO<sub>3</sub> interface at pH 9.3 ± 0.3 and 25 °C..



**C2 Model fitting parameters and graphs for systems consisting of water-toluene-calcite-C14BDMAC**

**Table C2** Model fitting parameters for the system consisting of water-toluene-calcite-C14BDMAC. The system also contains 10 mM Na<sub>2</sub>CO<sub>3</sub>.

[NaCl] / mM	150
$c\mu c_w (cac_w) / \text{mM}$	0.06
$c\mu c_t (cac_t) / \text{mM}$	0.02
Monomer partition coefficient ( $K_{P-tw}$ )	0.4
Langmuir $K_{L-wt}$ (equation 4.8) / mM <sup>-1</sup>	7775
Langmuir $\Gamma_{\max wt}$ (equation 4.8) / molecules nm <sup>-2</sup>	1.383
Langmuir $K_{L-wc}$ (equation 4.8) / mM <sup>-1</sup>	1000
Langmuir $\Gamma_{\max wc}$ (equation 4.8) / molecules nm <sup>-2</sup>	0.027
Langmuir <i>type</i> $K_{L-wc}$ (equation 4.1) / mM <sup>-1</sup>	1000
Langmuir <i>type</i> $\Gamma_{\max wc}$ (equation 4.1) / molecules nm <sup>-2</sup>	0.027
Langmuir <i>type</i> $\beta$ (equation 4.1)	0
$\gamma_{0-wt} / \text{mN m}^{-1}$	35
$\gamma_{0-ct} / \text{mN m}^{-1}$	3.1
$\gamma_{0-wc} / \text{mN m}^{-1}$	4.5

**Figure C7** Upper plot: Variation of toluene-water-calcite advanced static contact angle (measured through the aqueous phase) tension with aqueous C14BDMAC concentration for solutions containing 150 mM NaCl and 10 mM Na<sub>2</sub>CO<sub>3</sub> at 25 °C. The vertical dashed line indicates the c<sub>μc</sub>. The horizontal dashed lined shows the contact angle in the absence of added C14BDMAC. The solid line shows the calculated contact angle from the water-toluene (measured), water-calcite (derived from the measured adsorption isotherm) and toluene-calcite (invariant with [C14BDMAC]) tensions shown in the lower plot.

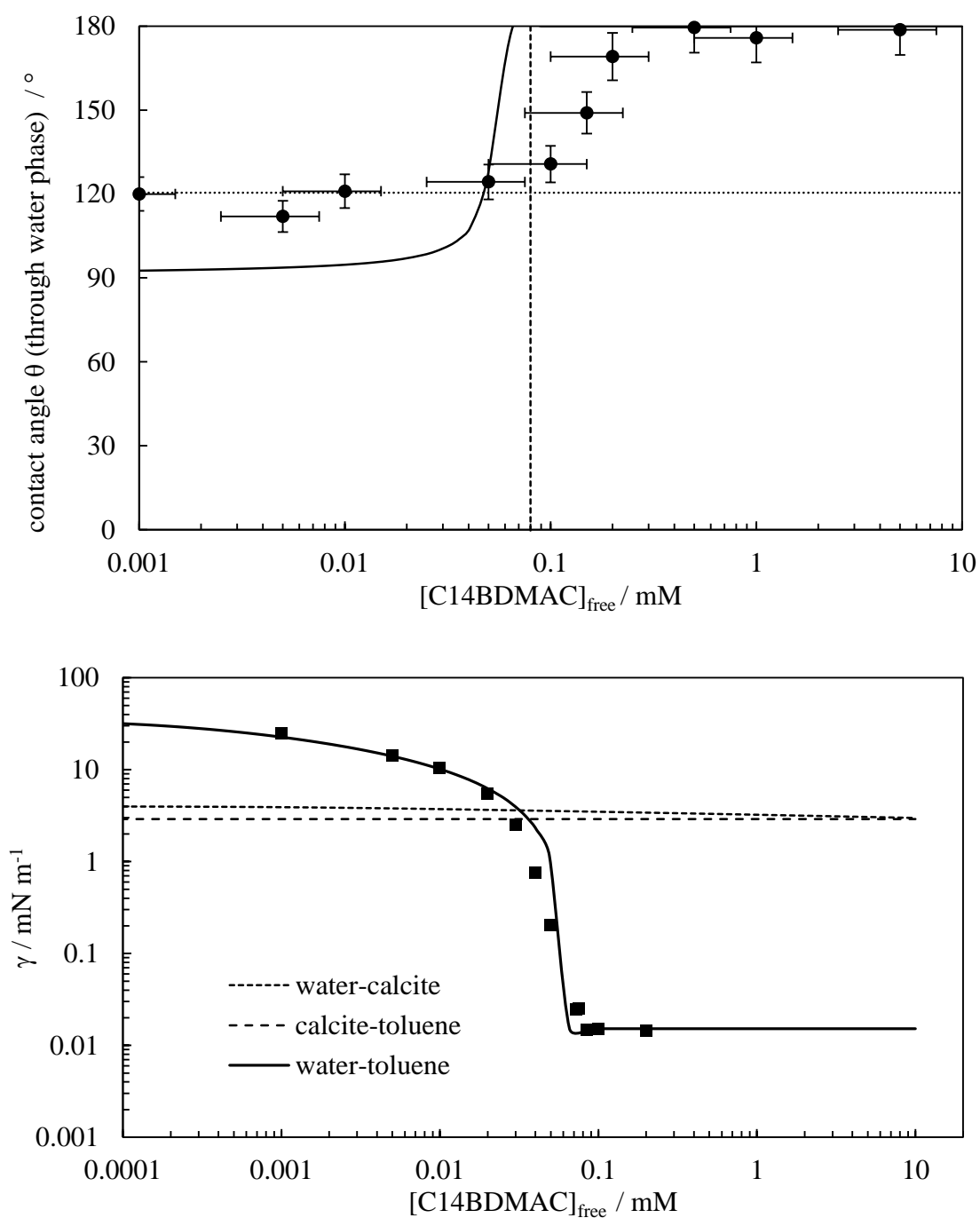
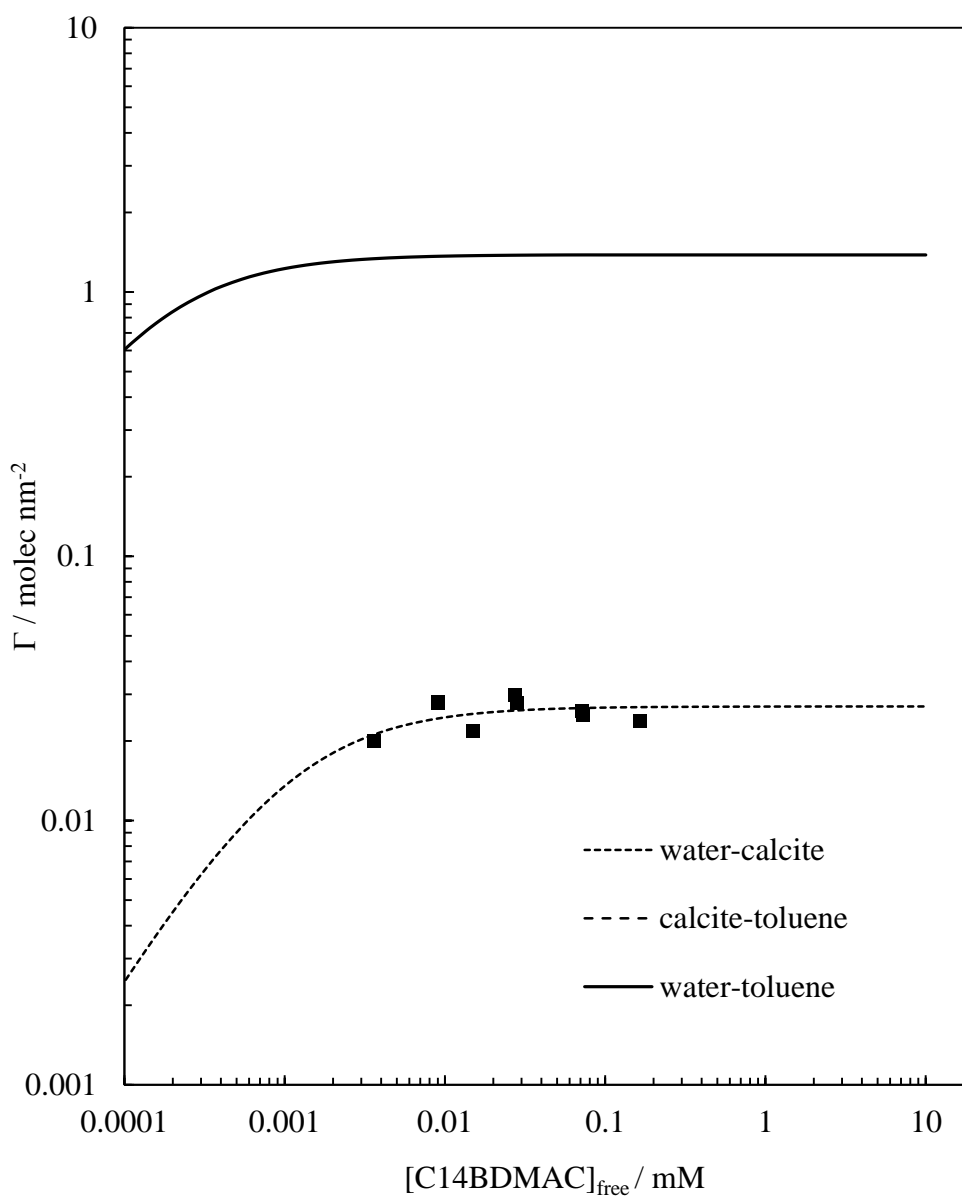


**Figure C8** Variation of the adsorbed amount of C14BDMAC at the three interfaces. The solid lines show the calculated values for the adsorption at the water-toluene (derived from interfacial tension measurements) and water-calcite (measured). The solid line for the adsorption at the toluene-calcite interface (invariant with [C14BDMAC]) is not seen as the  $\Gamma$  values are all zero. The solid squares show the experimental data for the adsorption at the calcite-water for solutions containing *150 mM NaCl and 10 mM Na<sub>2</sub>CO<sub>3</sub>* interface at pH 10.8 and 25 °C..



**C2 Model fitting parameters and graphs for systems consisting of water-heptane-calcite-CW-100S**

**Table C3** Model fitting parameters for the system consisting of water-heptane-calcite-CW-100S. The system contains no Na<sub>2</sub>CO<sub>3</sub>. Where subscripts 1-3 on c and m for straight lines are for the 1<sup>st</sup>, 2<sup>nd</sup> and 3<sup>rd</sup> lines fitted to the adsorption data.

<b>[NaCl] / mM</b>	0
<b><math>c\mu_{cw}</math> (<math>cac_w</math>) / mM</b>	0.165
<b><math>c\mu_{ch}</math> (<math>cac_h</math>) / mM</b>	0.137
<b>Monomer partition coefficient (<math>K_{P-ow}</math>)</b>	0.85
<b>Langmuir <math>K_{L-wh}</math> (equation 4.8) / mM<sup>-1</sup></b>	1810
<b>Langmuir <math>\Gamma_{max\ wh}</math> (equation 4.8) / molecules nm<sup>-2</sup></b>	2.0
<b>Langmuir <math>K_{L-hc}</math> (equation 4.8) / mM<sup>-1</sup></b>	60
<b>Langmuir <math>\Gamma_{max\ hc}</math> (equation 4.8) / molecules nm<sup>-2</sup></b>	1.0
<b><math>m_{1-wc}</math> / molecules nm<sup>-2</sup> mM<sup>-1</sup></b>	2.1547
<b><math>c_{1-wc}</math> / molecules nm<sup>-2</sup></b>	-0.1935
<b><math>m_{2-wc}</math> / molecules nm<sup>-2</sup> mM<sup>-1</sup></b>	7.2846
<b><math>c_{2-wc}</math> / molecules nm<sup>-2</sup></b>	-1.5973
<b><math>m_{3-wc}</math> / molecules nm<sup>-2</sup> mM<sup>-1</sup></b>	0
<b><math>c_{3-wc}</math> / molecules nm<sup>-2</sup></b>	3.4
<b>Langmuir type <math>K_{L-wc}</math> (equation 4.1) / mM<sup>-1</sup></b>	0.3
<b>Langmuir type <math>\Gamma_{max\ wc}</math> (equation 4.1) / molecules nm<sup>-2</sup></b>	3.5
<b>Langmuir type <math>\beta</math> (equation 4.1)</b>	-4.0
<b><math>\gamma_{0-wh}</math> / mN m<sup>-1</sup></b>	47.0
<b><math>\gamma_{0-ch}</math> / mN m<sup>-1</sup></b>	10.3
<b><math>\gamma_{0-wc}</math> / mN m<sup>-1</sup></b>	15.3

**Figure C9** Upper plot: Variation of heptane-water-calcite advanced static contact angle (measured through the aqueous phase) tension with aqueous CW-100S concentration for solutions containing 0 mM NaCl and 0 mM Na<sub>2</sub>CO<sub>3</sub> at 25 °C. The vertical dashed line indicates the c<sub>μc</sub>. The horizontal dashed lined shows the contact angle in the absence of added CW-100S. The solid line shows the calculated contact angle from the water-heptane (measured), water-calcite and heptane-calcite (both derived from the measured adsorption isotherm) tensions shown in the lower plot.

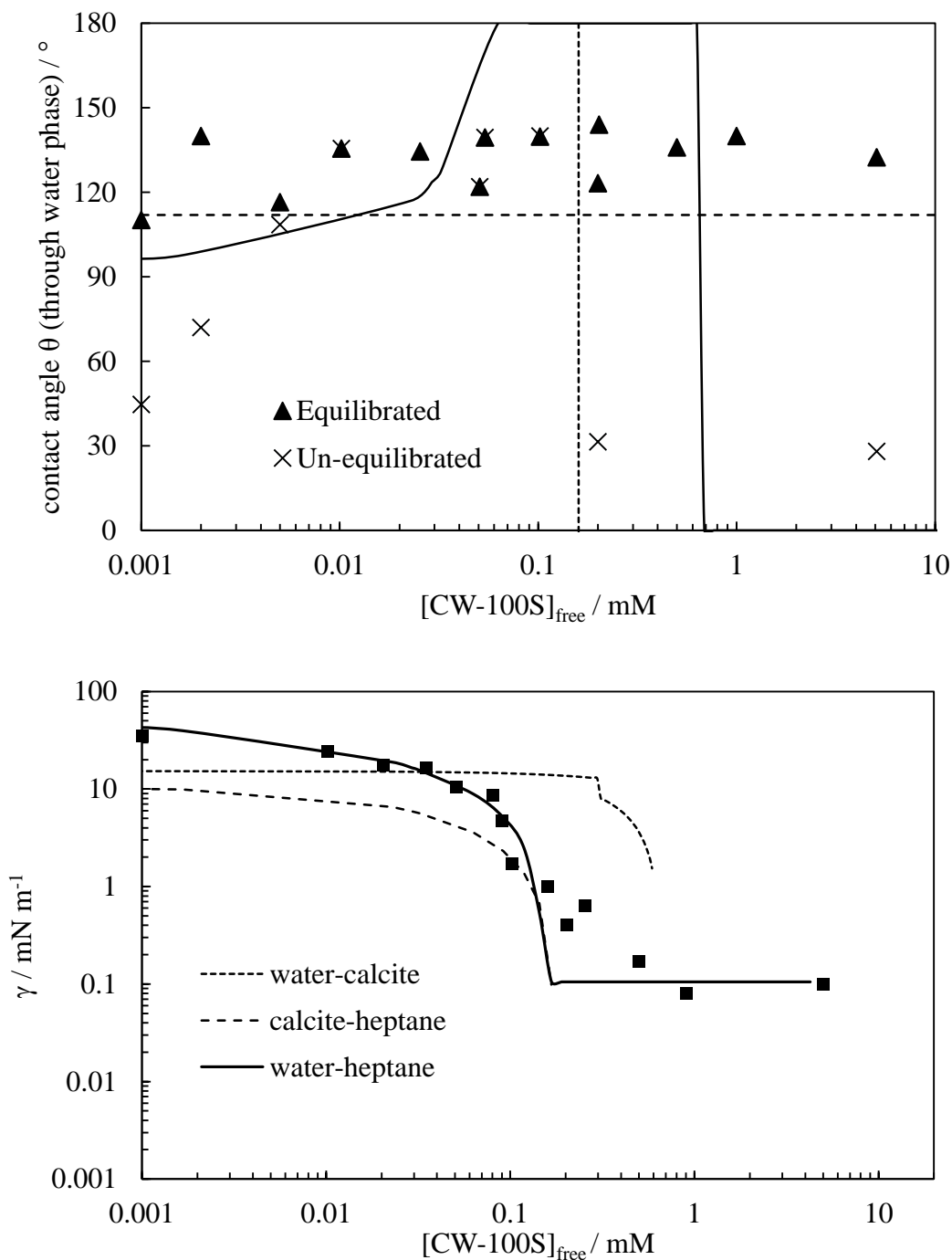
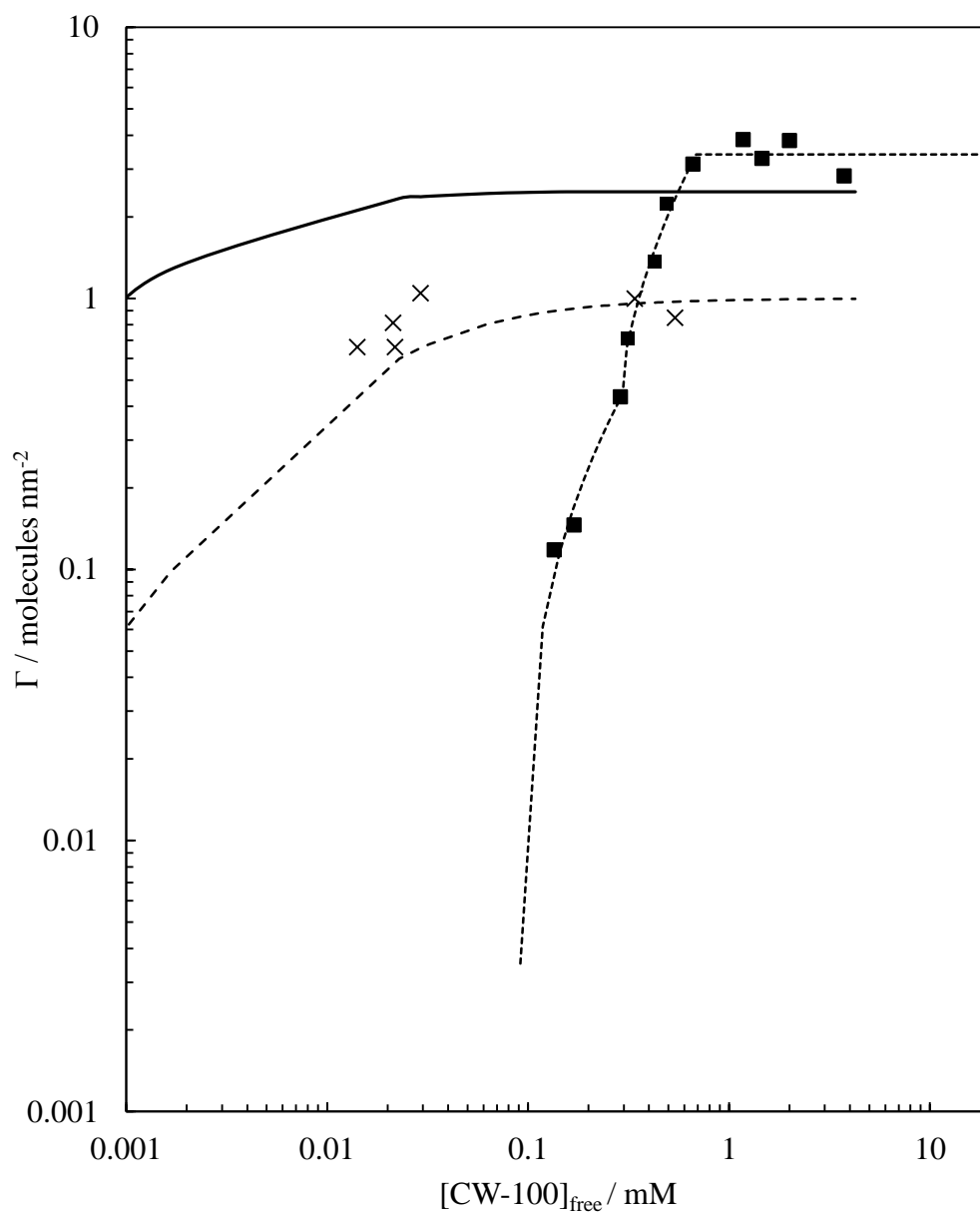


**Figure C10** Variation of the adsorbed amount of C14BDMAC at the three interfaces. The solid lines show the calculated values for the adsorption at the water-heptane (derived from interfacial tension measurements), water-calcite (measured) and heptane-calcite (measured). The solid squares show the experimental data for the adsorption at the calcite-water interface for solutions containing  $0 \text{ mM NaCl}$  and  $0 \text{ mM Na}_2\text{CO}_3$  interface at  $\text{pH } 9.3 \pm 0.3$  and  $25 \text{ }^\circ\text{C}$  and the crosses the experimental data for adsorption at the heptane-calcite interface at  $25 \text{ }^\circ\text{C}$ .



## APPENDIX D

### SUMMARY OF DRIVING PRESSURE PLOTS FOR VARIOUS FLOODS

#### D1 Introduction

Some discussions for some of the various pressure drops measured whilst pumping a liquid through the calcite packed columns have already been discussed (mainly in Chapter 3). Here, an overview of all the types of flooding experiments for which pressure plots were measured will be discussed, as well as comparing and contrasting in which situations the measured pressure plots match up with the pressures expected from theory.

There are three types of flooding experiments for which pressure drops were determined. These are; (i) single phase flow of water being pumped through a calcite packed column with interstices filled with water, (ii) two-phase flow of oil displacing air from the interstices of a calcite packed column, and (iii) two-phase flow of aqueous phase displacing the oil from the interstices of a calcite packed column. The pressure plots for both the first and second type of flooding experiments (single phase flow of water, and two-phase flow of oil displacing air) have been discussed in some detail in Chapter 3, so here only a brief recap is made with a little further discussion and some extra results. No discussion has been had on the pressure plots for the third type of flooding experiments (aqueous phase displacing oils), hence here there will be a full discussion of such plots. For each of the types of flooding experiment to be discussed, a brief discussion of the trends that may be expected to be observed will be had, following by a description of the experimental results and how they do or don't match up with the trends expected from theory.

It is noted that the pressure drops for most two-phase flow systems show varying extents of irreproducibility. This makes it harder to determine any definitive explanations for the variations in the pressure. Even so, some attempts at interpreting the pressure plots is made, though the reader should keep in mind that the interpretations carry a degree of speculation as further work needs to be done to enable a clearer understanding of the processes involved in determining the driving pressure.

## **D2 Single phase flow of water through calcite packed columns**

### *D2.1 Expectations from theory*

As discussed in the Introduction (Chapter 1), single phase flow is a much more simple situation to consider than two-phase flow. The first thing to be considered for a single phase system is whether the flow is laminar or turbulent. Once this is determined, if the flow is determined to be laminar, then the pressure drops as a function of flow rate are expected to be a straight line in accordance with Darcy's law.

### *D2.2 Comparison of experimental results to theory*

As discussed in Chapter 3, the pressure drop as a function of the flow rate for the flow of water through a column packed with all three particle sizes of the calcite powder follow Darcy's law up to pressure drop of 18 MPa. For the flow rates which required pressure drops greater than this, a deviation from Darcy's law was observed. This observed deviation was found to be due to the fact that pressure drops of  $>27$  MPa cause an increase in the packing density of the calcite powder in the column.

### **D3 Two-phase flow of oil displacing air from calcite packed columns**

#### *D3.1 Expectations from theory*

The exact relationship between the pressure drop across the local oil-water interface and the driving pressure across the column is not fully understood. However, there are three main situations which may be expected to be encountered when one fluid is being displaced by another in a porous medium such as the one being studied here. The case in which a negative Laplace pressure is aiding the flooding and will lower the driving pressure needed for flow to occur ( $\theta < 90^\circ$  through water), the case in which a positive Laplace pressure is hindering the flooding and will raise the driving pressure needed for flow to occur ( $\theta > 90^\circ$  through water), and finally where  $\theta = 90^\circ$ , where there is no Laplace pressure to either help or hinder the flooding.

#### *D3.2 Comparison of experimental results to theory*

The plots for decane displacing air in Chapter 3 at the slow flow rate did appear to show some signs of the Laplace pressure aiding the flow and lowering the pressure required to pump the oil at that flow rate (shown by the 0 MPa pressure drop across the column up to oil breakthrough). A negative pressure drop may have been expected to be have been observed as the Laplace pressure acts to ‘pull in’ the aqueous phase, though this was not seen. If there was no imposed flow rate and the water was flowing as a soul consequence of the Laplace pressure, then a negative pressure drop is more likely to have been recorded, however, in this case the column is being continually provided with a source of water by the HPLC pump, and as such this may have affected the value of the negative pressure. Interestingly, at the faster flow rate where the pressure drop required to flow the decane through the column was much higher than the predicted Laplace pressure, there was no signs of the Laplace pressure aiding the flow. All of these trends were observed for when both toluene and heptane were used to displace the air.

*n.b. The relative permeability of a fluid is the ratio of the permeability of that fluid through a porous medium containing a certain saturation of another immiscible fluid to the permeability of that fluid through the same porous medium with no other fluid present (the absolute permeability, i.e. the single phase permeability from Darcy’s law). Since the presence of another fluid in the porous medium decreases the effective porosity, the relative permeability of a fluid is usually  $< 1$ .*

## **D4 Two-phase flow of aqueous phase displacing oil from calcite packed columns**

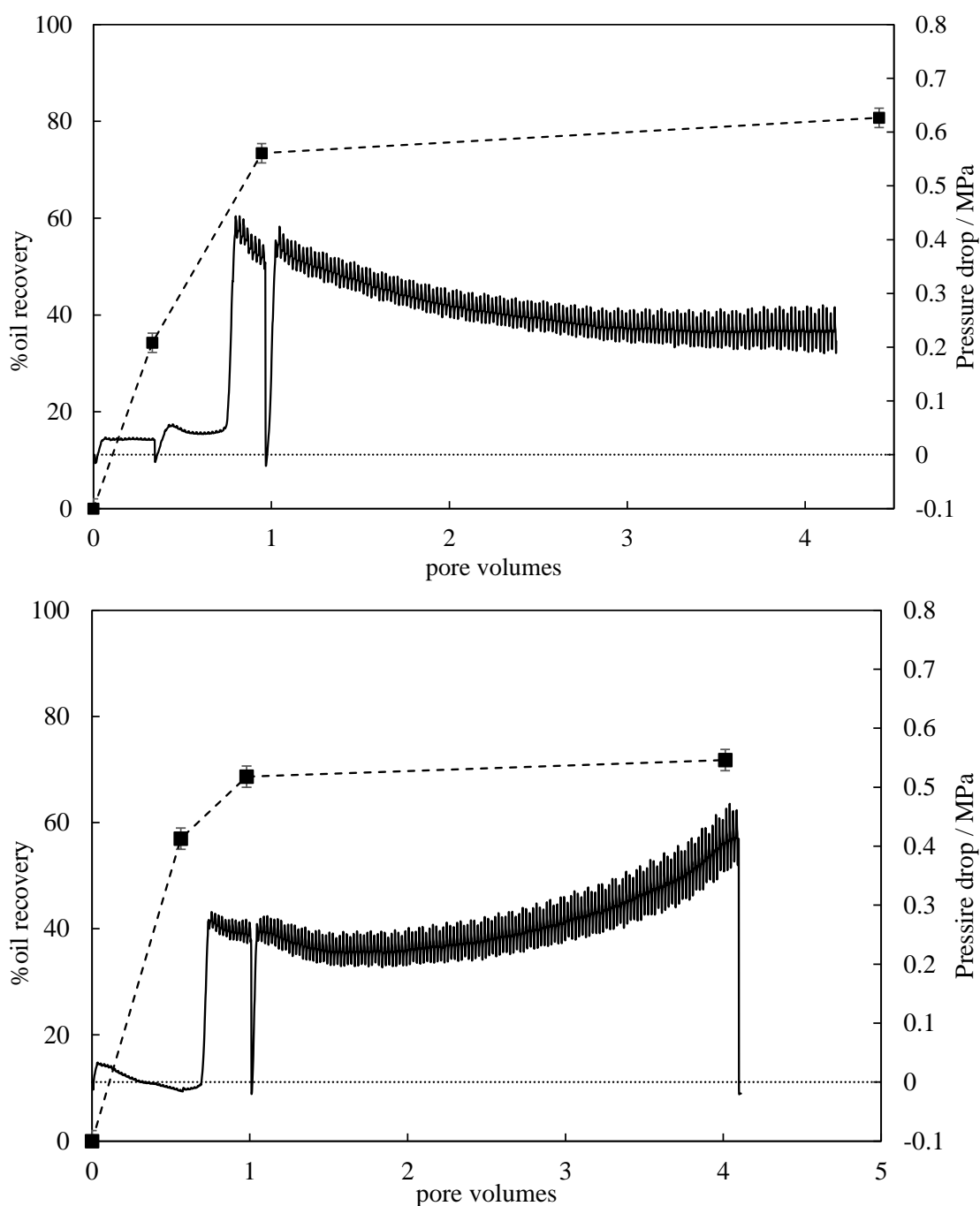
### *D4.1 Expectations from theory*

The theory for the effect of the Laplace pressure on the driving pressure for the two-phase flow of aqueous phases displacing oil from the calcite packed columns is very similar to that of the oil displacing the air. The main difference is due to the large change in the relative viscosities between the two-phases. With a significantly smaller viscosity difference between aqueous phase and oil than that for oil and air, the likelihood for oil remaining trapped instead of being forced out by the displacement phase is much greater. This being the case, after displacement phase breakthrough, the driving pressure is likely to be higher than expected due to relative permeability effects.

### *D4.2 Comparison of experimental results to theory*

Figure D1 shows the pressure plots (and %oil recovery) for the pressure drop between pressure sensor 2 and the waste for pumping either aqueous solutions of 0.1 mM AOT, 75 mM NaCl and 10 mM Na<sub>2</sub>CO<sub>3</sub> (top) or 2 mM AOT, 0 mM NaCl and 10 mM Na<sub>2</sub>CO<sub>3</sub> (bottom) in to an FC10 packed column with interstices initially filled with decane. Both aqueous phases have [AOT]<sub>free</sub> concentrations below the c<sub>uc</sub> at the pore volumes discussed (0-4), and as such, despite the differences in salt concentrations, will both have a similar contact angle (between approximately 110 - 150°) and similar decane-water interfacial tensions (between approximately 10 - 40 mN m<sup>-1</sup>). There will also be no solubilisation or emulsification, and hence the oil removal should be determined by the contact angle alone. With the similarities between the two systems, it would be expected that the pressure plots would be very similar, particularly as the Laplace pressure across the water-decane interfaces will be of a similar value and both will be positive as the contact angle is >90°. While there are some similarities between the two plots, there are also some stark differences.

**Figure D1** Top: Variation of pressure drop (between pressure sensor 2 and column exit)(solid line) and oil recovery (solid squares and dashed line) with pore volumes of water containing 0.1 mM AOT, 75 mM NaCl and 10 mM Na<sub>2</sub>CO<sub>3</sub>, pumped at 0.005 ml min<sup>-1</sup> into an FC10 packed column with pore volume fraction 0.45 initially containing decane. Bottom: Same as top graph, only with 2 mM AOT, 0 mM NaCl and 10 mM Na<sub>2</sub>CO<sub>3</sub> in the water. Both systems correspond to [AOT]<sub>free</sub> < c<sub>μc</sub> and hence are within regime in which the contact angle alone determines the %oil recovered. ( $\Delta P_{\text{chan}} = \sim 0.13$  MPa and  $\Delta P_{\text{flow}} = \sim 0.044$  MPa.)



The plots in Figures D1 do not appear to show a systematic or clear repeatable trend between 0 pore volumes and water break through, and the trends after water breakthrough are significantly different. Though there are still some useful discussions which may be had about the trends observed.

Both plots in Figure D1 start at -0.010 MPa, which could be due to a number of reasons, though one possibility is that the setting of the baseline for the pressure reading is analogous and could be chosen to be any number of readings, such as air, aqueous phase or decane in the T-junction with or without the T-junction attached to the column. In all experiments it was chosen to be with the T-junction filled with the aqueous phase and not attached to the column. Whether this produces a reasonable value for the baseline was not determined, however, the differences between the baselines, particularly with a liquid filled T-junction, is likely to be small and not contribute significantly to the overall pressure plots. The fact that the majority of pressure plots show the very same starting point indicates that it is due to the baseline determination.

After the start at -0.010 MPa, both plots rise to 0.030 MPa (approximately 10 times lower than the Laplace pressures expected for high interfacial tension systems), when the top plot plateaus, and the bottom plot slowly decreases to a little below the starting pressure. As mentioned previously, both systems have very similar contact angles and interfacial tensions, and as such would be expected to have similar pressure plots. However, the pressure plots for all the systems investigated through this work all have a similar irreproducibility between repeat and similar runs up to the point of water breakthrough (approximately 0.7-0.8 pore volumes). The only trend that all of the pressure plots have in common is the sudden jump in pressure at water breakthrough. The pressures to which the jump goes to is generally between 0.2-0.4 MPa, approximately 10 times higher than the corresponding pressure drop needed to pump pure water through an FC10 packed column with water filled interstices (0.045 MPa) (Figure 3.2, Chapter 3). This jump is likely to be caused by the change from a system in which both the oil and water are flowing, to a system in which the oil is stationary (residual oil saturation) and the water is flowing. Such a large jump may not have been expected as the 20-30 % of the oil trapped is likely trapped in the least accessible places, and hence where there is less water flow even when only water is present. However, as the sudden increase is consistently at the point of water breakthrough, it seems plausible to suggest that it is due to some relative permeability effects.

After the point of the sudden jump up in the driving pressure, both graphs in Figure D1 show opposite trends. In the top graph, the driving pressure slowly drops down to a plateau value at approximately 3 pore volumes. Interestingly, the oil recovery also slowly increases between 1 and 4 pore volumes. An increase in oil recovery correspondingly means that more pore space becomes available for the water to flow through, hence a lower pressure is required to pump the water through at the set flow rate. The slight increase in oil recovery after water breakthrough is not expected for this system as the concentration is below the  $c_{uc}$ , though as this is a complicated porous system ideality is not always achieved (as seen in the difference in oil recovery between 1 and 4 pore volumes for all three systems). Thus, although some progressive oil recovery is observed, it seems likely that oil saturation (where no more oil is removed) will occur slightly after water break through (allowing for the non-ideality). As seen in the top plot of Figure D1, the pressure reaches a plateau after approximately 2 pore volumes, presumably at the point of oil saturation. Most of the pressure plots for floods below the  $c_{uc}$  show a similar trend to this one (for other salt concentrations with this surfactant, for the other surfactant systems and for the oils displacing air).

The trend seen in the bottom graph of Figure D1 where the pressure slowly increases between 1 and 4 pore volumes is not readily explained in terms of relative permeability changes, as the oil recovery remains constant (within the error) between 1 and 4 pore volumes, and for the pressure required to increase oil would have to be put back in the column. As this trend occurs much less often than the trend in the top graph, it seems reasonable to treat this trend as an anomaly. One possible reason could be that as this is a dynamic system, and the packing of the particles is random and hence have some moving room, that a shift in some of the particles to block some of the pores would lead to an increase in the driving pressure required to pump the aqueous phase.

A final observation of the plots in Figure D1 is that after the sudden jump in driving pressure at water breakthrough, the rhythmic fluctuations in the pressure readings, as discussed in the experimental, suddenly become a lot more prominent and more so than the fluctuations seen when water is pumped through at the same flow rate when all the interstices are filled with water. As the fluctuations are a consequence of the dual piston pumping motion of the HPLC pump, and the pumping motions are controlled by the pump in such a way as to produce a steady flow rate (with variable pressure), little interpretation is possible as to why the fluctuations increase at water breakthrough unless

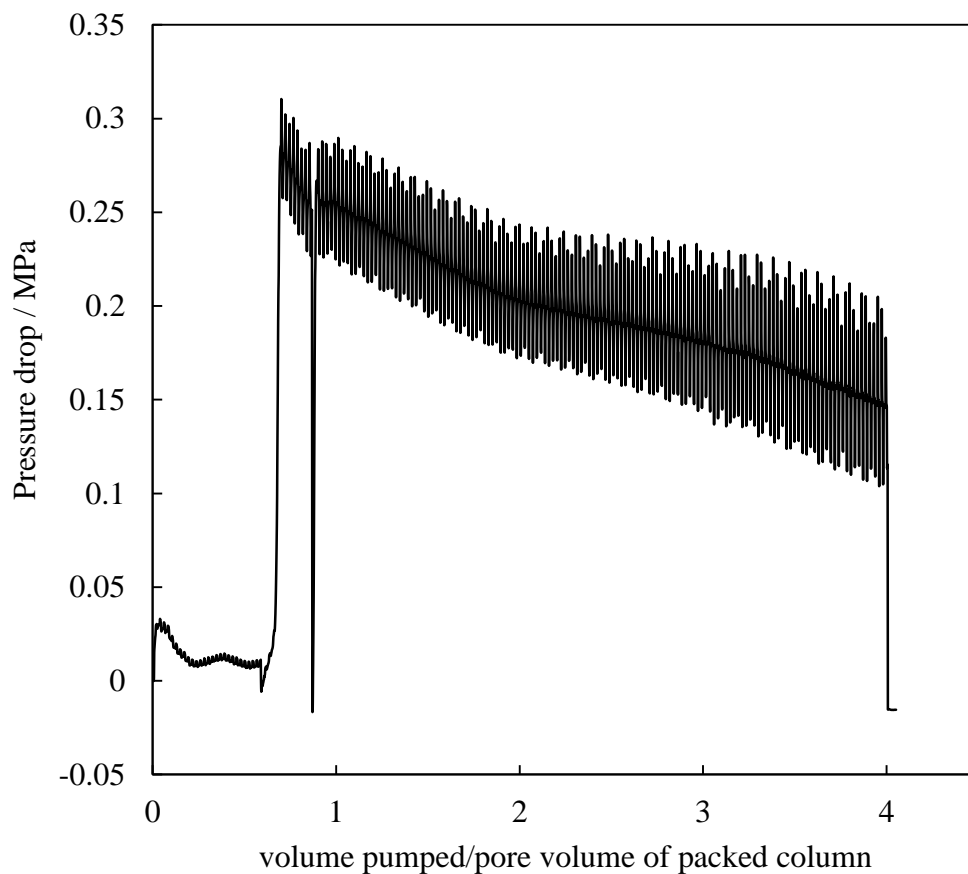
the internal workings of the pump and how the flow rate feed-back loop works is known. As this is beyond the scope of the work here, the trend is noted, but no further interpretation of why it happens will be made.

In Figure D2 where the AOT free concentration is in excess of the  $c_{\mu c}$ , a slightly different trend is seen past water breakthrough. In this system, a continuous increase in oil recovery is expected as with increasing pore volumes there will be an increase in recovery from the solubilisation and emulsification mechanism. Unlike the top plot in Figure D1, the pressure does not reach a plateau after 2 pore volumes but continuously decreases, presumably as more and more oil is removed.

Despite the irreproducibility of the pressure plots, a general trend is observed. For aqueous phases displacing oil, before water breakthrough at approximately 0.7-0.8 pore volumes, the driving pressure drop trend is not easily repeatable between similar floods. The pressure drops measured at this point of the flood are typically between -0.010 and 0.030 MPa, at least a factor 10 smaller than the Laplace (for higher interfacial tension floods) or capillary entry pressures. For floods where the oil-water interfacial tensions are lower, giving a lower Laplace pressure, the initial driving pressure readings are within a similar range as the Laplace pressure, though no correlation is possible due to the irreproducibility. For all aqueous floods displacing oil there is a sudden jump in the driving pressure drop at water breakthrough to a value between approximately 0.2 to 0.4 MPa, after which the majority of plots show two trends depending on if the surfactant concentration free is above or below the  $c_{\mu c}$ . When below the  $c_{\mu c}$ , the general trend of a decrease in pressure over a couple pore volumes to a constant value at residual oil saturation is observed. For system with a concentration above the  $c_{\mu c}$  a slow continuous decrease is observed as more and more oil is removed by the solubilisation and emulsification mechanisms.

As the aim of this work is to understand the effect of surfactant on the recovery of oil in terms of the surface chemistry modifications, no further work on interpreting the pressure plots will be discussed.

**Figure D2** Variation of pressure drop (between pressure sensor 2 and column exit) with volume of water containing 7 mM AOT and 10 mM Na<sub>2</sub>CO<sub>3</sub>, pumped at 0.005 ml min<sup>-1</sup> into an FC10 packed column with pore volume fraction 0.45 initially containing decane. (Oil-water tension = 0.33 mN m<sup>-1</sup>, contact angle through water = 0°,  $\Delta P_{\text{cap}} = -0.0041$  and  $\Delta P_{\text{flow}} = 0.044$  MPa.)



## D5 Conclusions

The driving pressures for single phase flow of either water or oil pumping through columns packed with calcite powders at different flow rates are shown to obey Darcy's law with pressure drops up to approximately 18 MPa. Above 27 MPa, a deviation from the linear trend is observed, the reason for which was determined to be due to an increase in the packing density of the calcite powder within the column, results in a lower permeability.

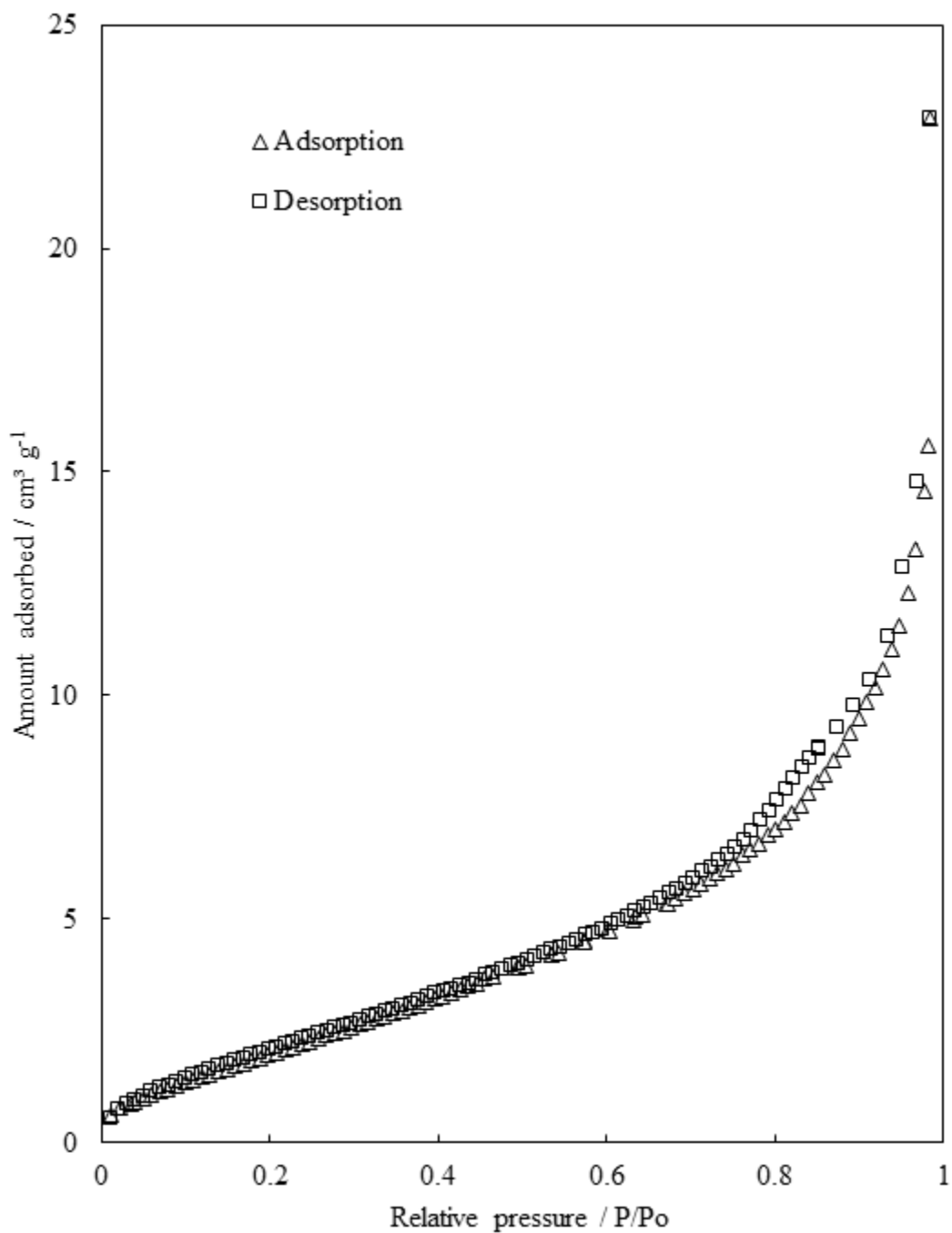
The pressure drops for oil displacing air at slow flow rates show some signs of the Laplace pressures lowering the driving pressure needed for flow to occur (as expected due to the negative sign of the Laplace pressure due to the  $0^\circ$  contact angle through the water). No simple quantitative analysis was possible due to irreproducibility between repeat runs.

Analysis of the driving pressure plots from the displacement of the oil by aqueous solutions of surfactant showed some irreproducibility between repeat and similar runs, particularly between 0 pore volumes and water breakthrough. Due to this, analysis of the plots was limited to the overall general trends that were seen for all displacement floods without in depth analysis of each change in the plots. Between 0 pore volumes and water breakthrough the driving pressure was often between -0.010 and 0.030 MPa (where the negative values were due to baseline corrections). These values are a factor 10 lower than the Laplace pressures expected for high oil-water interfacial tension systems, as such no link between the Laplace pressures and the driving pressures were possible to determine. At the point of water breakthrough (approximately 0.7-0.8 pore volumes), the driving pressure jumps to a value between approximately 0.2-0.4 MPa, where after the general trend was a slight decrease to a plateau after a couple of pore volumes for systems with surfactant free concentration below the  $c_{\mu c}$ , and a slow continuous decrease in pressure for systems with a surfactant free concentration above the  $c_{\mu c}$ . These high pressure drops are 10 times higher than the expected pressure drops for flowing pure water through the same column with water filled interstices. The difference between the two pressures were thought to be from relative permeability effects arising from the oil trapped in the pore space

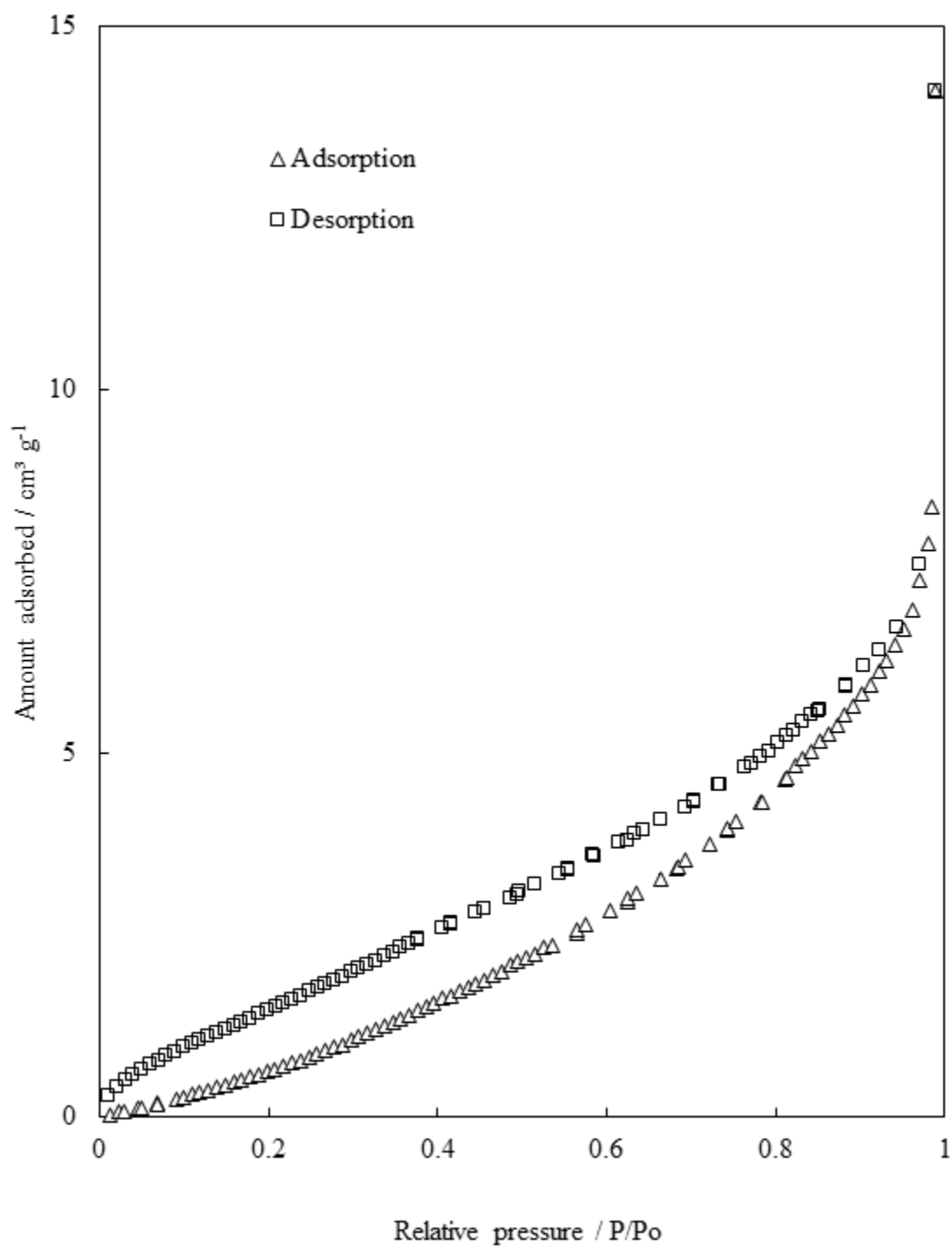
## APPENDIX E

### CALCITE BET NITROGEN ADSORPTION ISOTHERM PLOTS AND XRD PATTERNS

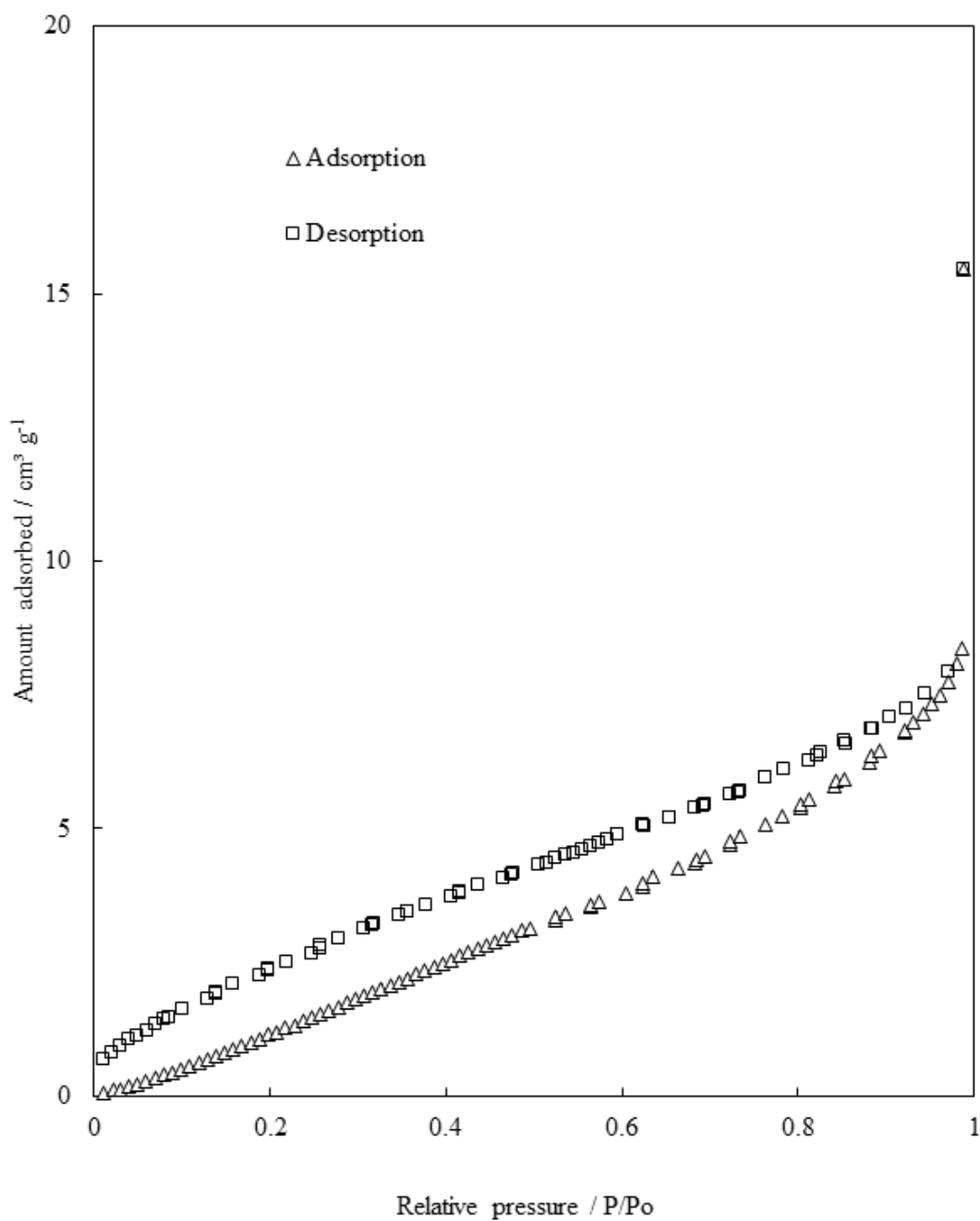
E1 Nitrogen adsorption isotherm for the BET analysis of the FordaCal 10 sample. The analysis was carried out using a Micromeritics TriStar 3000 at 77.300 K.



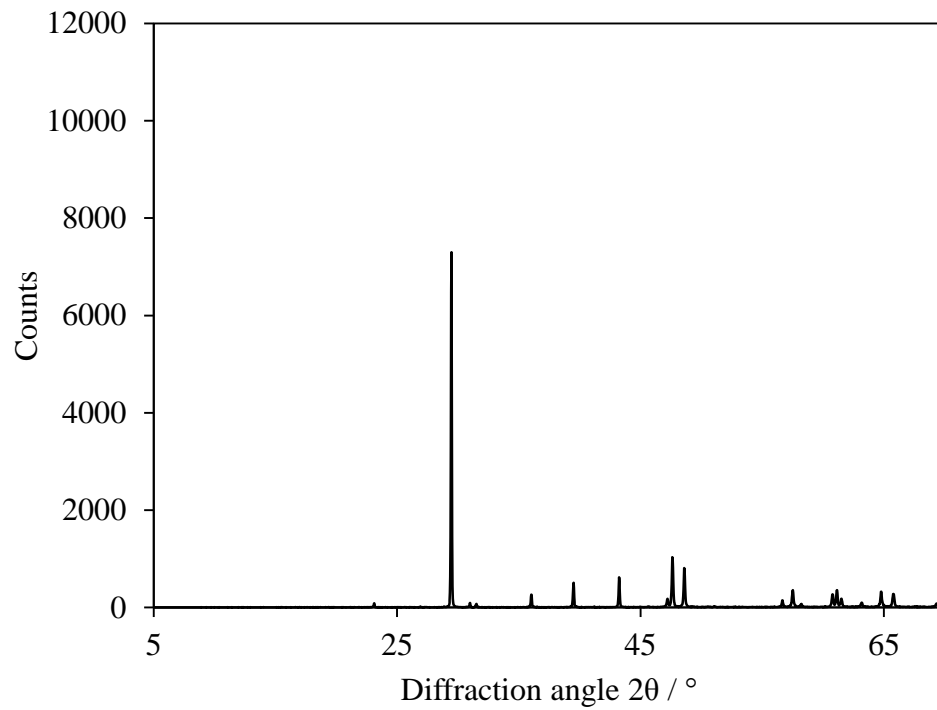
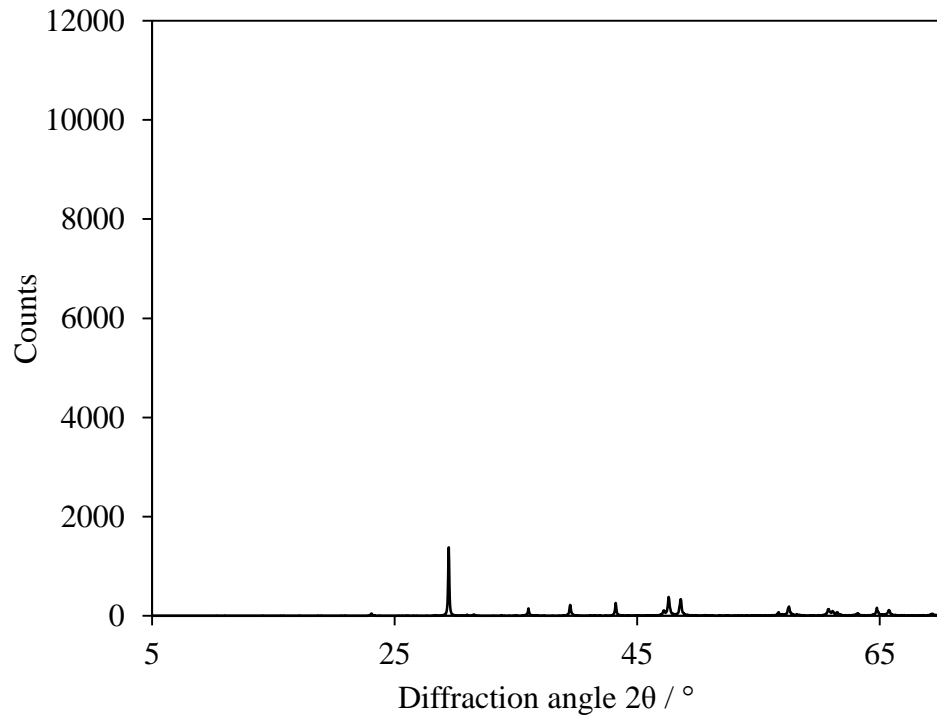
**E2** Nitrogen adsorption isotherm for the BET analysis of the FordaCal 30 sample. The analysis was carried out using a Micromeritics TriStar 3000 at 77.300 K.



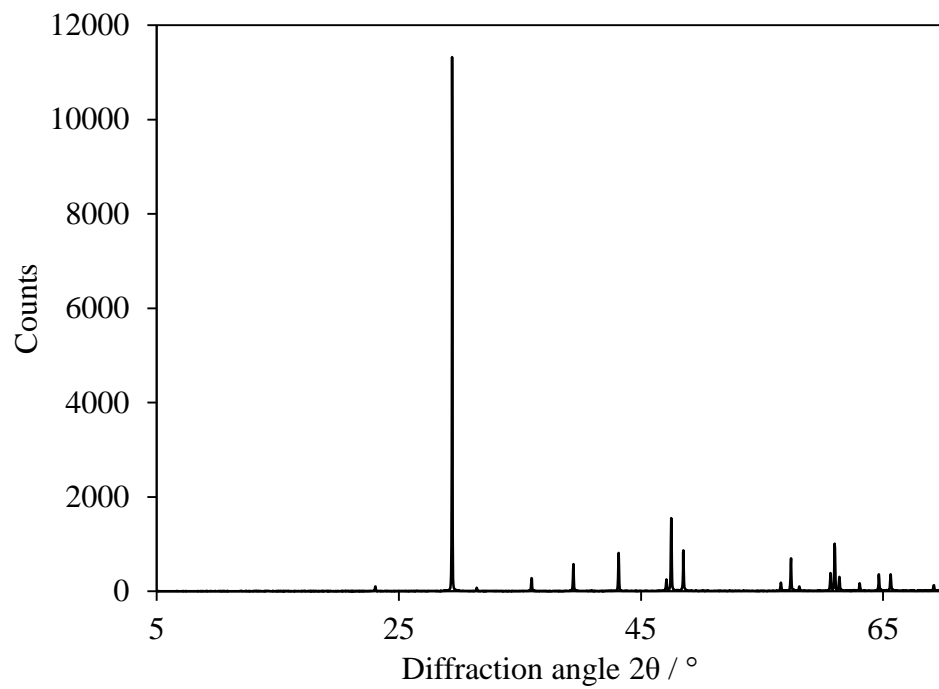
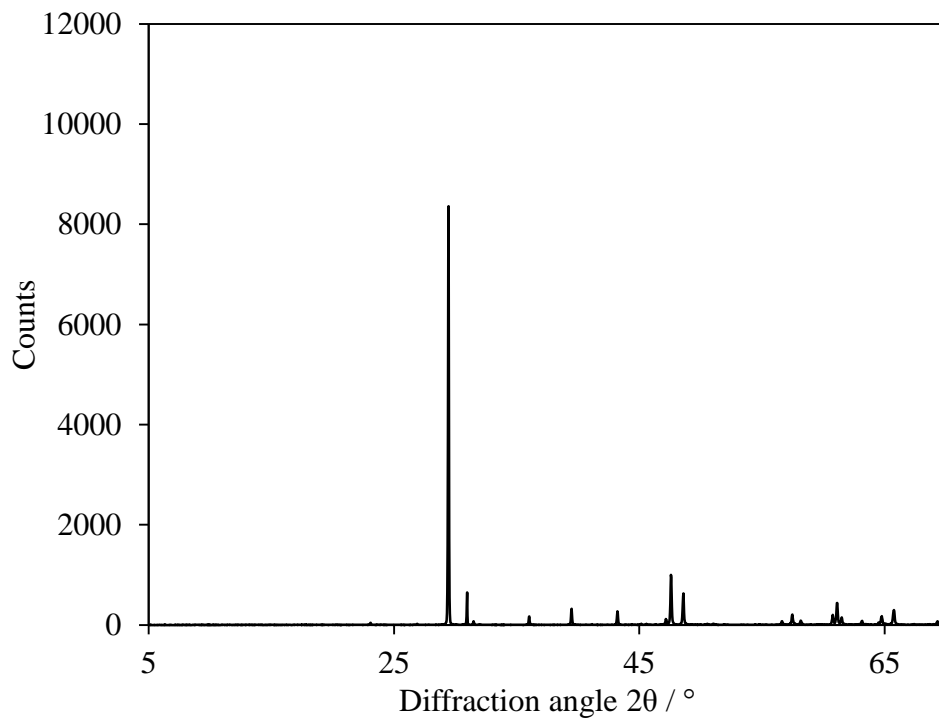
**E3** Nitrogen adsorption isotherm for the BET analysis of the FordaCal 200 sample. The analysis was carried out using a Micromeritics TriStar 3000 at 77.300 K.



**E4** Powder XRD pattern for the FC10 (top) and FC30 (bottom) calcium carbonate samples.



**E4** Powder XRD pattern for the FC200 calcium carbonate sample (top) and the ground up calcite crystal (bottom)



**E4** Comparison between the XRD pattern peak positions of the FC30 calcium carbonate sample and the spectrum in the high score database (Chapter 2).

